NOTICE

The quality of this microform is heavily dependent upon the quality of the original thesis submitted for microfilming. Every effort has been made to ensure the highest quality of reproduction possible.

If pages are missing, contact the university which granted the degree.

Some pages may have indistinct print especially if the original pages were typed with a poor typewriter ribbon or if the university sent us an inferior photocopy.

Reproduction in full or in part of this microform is governed by the Canadian Copyright Act, R.S.C. 1970, c. C-30, and subsequent amendments.

AVIS

La qualité de cette microforme dépend grandement de la qualité de la thèse soumise au microfilmage. Nous avons tout fait pour assurer une qualité supérieure de reproduction

S'il manque des pages, veuillez communiquer avec l'université qui a conféré le grade.

La qualité d'impression de certaines pages peut laisser à désirer, surtout si les pages originales ont été dactylographiées à l'aide d'un ruban usé ou si l'université nous a fait parvenir une photocopie de qualité inférieure

La reproduction, même partielle, de cette microforme est soumise à la Loi canadienne sur le droit d'auteur, SRC 1970, c. C-30, et ses amendements subséquents

Comprehensive Dynamic Analysis of a Bladed Disk-Turborotor-Bearing System

Ashok Kaushal

A Thesis

in

The Department of

Mechanical Engineering

Presented in Partial Fulfillment of the Requirements
for the Degree of Doctor of Philosophy at
Concordia University
Montréal, Québec, Canada

ISBN 0-315-73646-1

ABSTRACT

Comprehensive Dynamic Analysis of a Bladed-Disk-Turborotor-Bearing System

Ashok Kaushal, Ph.D
Concordia University, 1992

The dynamic behaviour of a bladed disk-turborotor-bearing system is studied employing analytical, numerical and experimental methods. The system consists of several subsystems such as turbine disk, blades, bearings, support pedestals etc. In order to completely understand the dynamic behaviour of the turborotor system an appropriate model for each individual component of the system is first developed. The individual components are modelled to include various design parameters and the effect of these parameters on the vibrational behaviour is studied. The vibration studies on the individual components are carried out using Rayleigh-Ritz method boundary characteristic orthogonal polynomials as assumed shape functions. The individual components are then assembled using the finite element technique. The turborotor system is studied from a system point of view and the natural frequencies and mode shapes are obtained for various rotational speeds. The results show that the natural frequencies of the system are different from those obtained by analyzing individual components, suggesting that a system

approach must be adopted for proper design of a turborotor system. The amplitude of vibration and stresses due to harmonic and centrifugal loading on the blades and the disk are also obtained. The results indicate that for the turborotor speed of operation, the centrifugal loading is the major factor in determining the critical stresses in comparison to the gas forces on the blade modelled as harmonic loading. Experimental validation of the analytical model is carried out and suggestions for future work are given.

DEDICATED TO MY PARENTS AND MY TEACHERS

ACKNOWLEDGEMENTS

The author expresses his indebtedness to his thesis supervisor Dr. R.B. Bhat for his excellent guidance, help and encouragement during the development of this thesis. His patience, understanding nature and technical excellence were the constant source of inspiration to the author throughout the course of the work.

Helpful suggestions by Dr.C.Rajalingham are greatly appreciated. The valuable assistance provided by Mr. Danny Juras in the author's experimental work, assistance by Babar Khan and discussions with Mr. Vineet Gupta are acknowledged with gratitude.

The financial support provided by the department of Mechanical Engineering of Concordia University is acknowledged.

Sincerest thanks are due to my special freind, Tara, for her constant emotional and moral support.

This work could not have been possible without the emotional support and understanding given by the authors's parents and his wife Abha. They were a constant source of strength and the author is grateful to them.

TABLE OF CONTENTS

LIST OF FIGURES

LIST OF TABLES

NOMENCLATURE

a	outer radius of disk
A_1	integration constant
A_2	integration constant
A_n	constant coefficients
A, A_D	area of disk
b	inner radius of disk
b_j	coefficient of starting function
B_n	constant coefficients
c	blade tip radius
c_j	coefficient of starting function
$[C]$	damping matrix
C_n	constant coefficients
C_{mn}	constant coefficients
D	flexural rigidity of the disk/plate
E	Young's modulus of elasticity
E_p	error
$F(t)$	sinusoidal force
F_x	force
$g(x)$	generating function
G	shear modulus of elasticity
h_p	thickness of plate
$h(r)$	disk thickness variation parameter
H_A	plate thickness at the outer periphery
H_B	plate thickness at the inner periphery
H_{sr}	frequency response function

H_{sr}^{G}	generated FRF
H_{sr}^{M}	measured FRF
I_x	moment of inertia
k_2	non dimensional parameter
K	shear coefficient
[K]	stiffness matrix
K_1	constant for disk thickness variation
K_2	constant for disk thickness variation
K_3	non dimensional parameter
K_4	non dimensional parameter
K_5	non dimensional parameter
K_{xx}	bearing stiffness
K_{yy}	bearing stiffness
l_p	length of plate
l_s	length of shaft
L	length of blade
L_1	Lagrangian
L_1	time averaged value of the Lagrangian
m	mass
M	bending moment
[M]	mass matrix
N_{rr}	stress resultant
$N_{\theta\theta}$	stress resultant
p	natural frequency
P_i	pole of ith mode
P^{*i}	complex conjugate

q_s	response
q	modal coordinates
r	non dimensional parameter
r_2	non dimensional parameter
R	disk radius
R	non dimensional parameter
R_1	radius of curvature
R_2	radius of curvature
R_3	radius of curvature
R_r	complex residue
S_{mn}	constant coefficients
T	kinetic energy
T^*	maximum kinetic energy
T_f	flexural kinetic energy
T_r	rotational kinetic energy
u	displacement vector
U	strain energy
w_p	width of plate
W	plate deflection
W_f	weight function
y	deflection
β_1	slope of elastic curve
δ	Kronecker delta
Δ	displacement
$\Delta(r)$	thickness variation parameter- radial direction
η_1	coordinate axis
ν	Poisson's ratio

ω	angular velocity of rotation
ψ	bending slope
ϕ	admissible function
ρ	density
σ_x	stress
σ_y	stress
τ	stress
θ	setting angle
ξ_1	coordinate axis
ξ_{xy}	shear deformation
ξ_{xx}	elongation
ξ_{yy}	elongation
Υ	phase angle
λ	non dimensional parameter
α	non dimensional parameter
η	non dimensional parameter
σ	non dimensional parameter
β	non dimensional parameter
θ	non dimensional parameter
Υ	phase angle
ς	damping

CHAPTER 1

INTRODUCTION, LITERATURE SURVEY AND OBJECTIVES

1.1 : General

Reliable operation of turbomachinery depends mainly on the designer's ability to accurately determine the stresses under actual operating conditions and keep them within safe limits. This requires a good understanding of the dynamic behaviour of the system. The recent trend in the design of turbomachinery is towards higher speeds and lower weight which seems more and more realizable in view of the improved methods available for predicting dynamic response of the turborotor. The turborotor system consists of several subsystems such as turbine and compressor blades, disks, bearings, mechanical couplings in shafts, etc. Centrifugal forces are set up in the disks and blades due to their rotation, which deflect the structure and at the same time cause in-plane strains resulting in the stiffening of the structure. In addition, the dynamic behaviour of the turborotor running in its bearings, mounted on supports which themselves may be flexible, will be quite complex. Since, the dynamics of the blades and disks as well as the rotor shaft and bearings are coupled, it is quite important that a comprehensive study of the dynamic behaviour is carried out from a system point of view, to arrive at a proper design.

Due to change in structural characteristics with the speed of rotation, the natural frequencies and associated modes of free vibration will be much different from those under non-rotating conditions. Also, the vibrational behaviour of individual components such as the blade, disk, shaft are coupled and this must be taken into consideration to determine the total behaviour of the turbo-rotor in operation.

1.2 : Scope of Literature Review

With the continually increasing use of tubomachinery at higher performance levels, especially in aircraft industry, the study of vibration problems arising in rotating structures has become increasingly important. Rotor shaft designers in the field of turbomachinery usually make the assumption that any disks attached to the shaft are rigid and adopt a lumped parameter representation. This assumption is generally satisfactory, but can be very optimistic if the disk is made thin in a weight minimizing effort, resulting in disk bending frequencies which may fall close to rotor operating frequency.

In addition, when a lumped parameter representation of the system is used, the number of obtainable critical speeds is equal to the number of the mass points selected. The lumped

parameter mathematical model does not represent the true physical model and consequently, does not accurately predict the higher critical speeds. Moreover, discretization of a continuous system lowers the natural frequencies from their true value [1] and if the analysis follows an energy approach, that will raise the natural frequencies above their true values. As a consequence, the designers cannot be certain about the reliability of the final result of an analysis which uses both discretization and energy approach.

Techniques for predicting the vibrational behaviour of a complete turbo-rotor system require a full understanding of the basic vibration characteristics of all the components such as blade, disk, rotor shaft mounted on bearings. It is usually the blades which are most seriously affected by vibrations. Probably as a result, much attention has been directed in the past to study the vibration behaviour of an individual blade, considered to be a cantilever beam and unaffected by the flexibility of the disc to which it is attached. Since the blades are idealized as beams when aspect ratios are high, and plates when aspect ratios are low, the vibration of rotating cantilever beams and plates have been studied in several investigations.

The methods of solution of such rotating structures can

broadly be classified as belonging to either the continuum model approach or the discrete model approach. In the continuum model approach, the potential energy method, the complementary energy principle or the Galerkin procedure have been employed for the solution of such structures. The resulting differential equations obtained using these methods are solved using Runge-Kutta procedure. In the discrete model approach, the Holzer-Myklestad, Stodola, polynomial frequency equation transformation, solution functions, finite difference and finite element methods are well developed. All these discrete model approaches suffer from the drawback of discretization of the distributed mass and elasticity, thus yielding lower bound solutions.

In view of the complexity of the problem, the review of the past literature on the subject is classified under the following categories and discussed in order to put the present study in proper perspective:

1) Vibration of blades with large aspect ratio.
2) Vibration of blades with small aspect ratio.
3) Vibration of disks.
4) Vibration of bladed disk assembly.
5) Bladed-Disk Assembly / Rotor Analyses

1.3 : Vibration of Blades with Large Aspect Ratio

Various investigators considered one or a combination of parameters such as rotational speed, pretwist, to determine their effects on the natural frequencies. A general survey of such studies is presented by Rao [2].

Energy expressions for a rotating beam undergoing transverse vibrations were derived by Carnegie [3] and he obtained the fundamental frequency using Rayleigh's method. Schilhansl [4] derived the equation of motion for the bending vibrations of a rotating cantilever beam with uniform cross-section and solved it by successive approximations to determine the effect of rotation on the fundamental frequency. He showed that the fundamental frequency of the beam increased with the inclusion of rotation. Pnuelli [5] investigated the vibrations of a rotating cantilever beam and found that the rotation of the beam tended to increase the natural frequencies of flexural vibration compared to those for the non-rotating beam. Subrahmanyam, Kulkarni and Rao [6] used Reissner method to obtain the natural frequencies of rotating blades having a symmetric aerofoil cross-section with allowance for shear deflection and rotary inertia. The Reissner method allows to determine accurately the stresses and the displacements as also the natural frequencies and

mode shapes simultaneously. They showed that the method gives results which are superior to those obtained by using the potential energy expression in the Ritz method. Kumar [7] used Myklestad method to obtain in-plane vibration frequencies of rotating beams with tip mass. Isabson and Eishley [8] used the extended Holzer-Myklestad procedure and Slypex [9] used the Stodola method to determine the natural frequencies of pretwisted cantilever blades. The method of Frobenius was used to solve for the natural frequencies and mode shapes of centrifugally stiffened beams by Wright, Smith, Thresher and Wang [10]. The effects of the hub radius and tip mass on the bending natural frequencies of rotating beams were studied by Handleman, Boyce and Cohen [11], Lo, Goldberg and Bogdanoff [12], and Boyce and Handlemann [13]. In these studies it was observed that the hub radius significantly influenced the bending natural frequencies . The effect of setting angle on the natural frequencies was studied by Wang et al [14]. An improved strain energy formulation in Rayleigh-Ritz method was used by Kaushal and Bhat [15] to obtain the natural frequencies of a rotating cantilever beam. In this formulation shear force distribution obtained from an assumed deflection shape, was integrated along the beam satisfying appropriate boundary conditions to obtain the moment distribution and using this information an improved expression for the strain energy was obtained. Bhat [16] studied the transverse

vibrations of a rotating cantilever beam with tip mass using beam-characteristic orthogonal polynomials in Rayleigh-Ritz method.

Finite element method was used by Putter and Manor [17] to solve for the natural frequencies in flexural vibrations of a rotating beam with tip mass. Hoa [18] also utilized the finite element technique to study the effect of setting angle and hub radii on a rotating beam with tip mass. The effect of root flexibility on the vibration characteristics of tapered blades was studied by Singh and Rawtani [19], and the coupled-bending vibrations were studied by Singh and Rawtani [20].

1.4 : Vibration of Blades with Small Aspect Ratio

A beam model will represent a turbine engine blade reasonably well if the blade is relatively long with respect to its width (i.e. large aspect ratio); and if the blade is reasonably thick, and only the first few vibration frequencies and mode shapes are needed. Unfortunately, these requirements are often not met. Blades in sections of turbomachinery have a small aspect ratio. Efficiency demands thin blades and dynamic response studies over a large frequency range require results for many modes, which cannot be approximated as beam modes.

The flexural vibration of rectangular plates by using beam vibration mode shapes as admissible functions in both the Rayleigh and Rayleigh-Ritz methods of analysis has been treated extensively by Young [21], Leissa [22], and Dickinson [23]. The convergence and accuracy of the Rayleigh-Ritz method has been discussed by various authors including Trefftz [24], Courant [25], and Collatz [26].

While Rayleigh-Ritz method is well known, it has not been used as much as might be expected for plate vibration problems. This is probably due, at least in part, to the great amount of computational labour which is required both to set up and solve the necessary equations. The amount of computation involved depends to a large extent upon the set of functions that are used to represent the plate deflection. For these functions, some investigators have used combinations of the characteristic functions which define the normal modes of vibration of a uniform beam. Gorman [27] obtained a general analytical solution for the vibration of rectangular plates supported on their lateral surface by symmetrically distributed point supports. Bassily and Dickinson [28] used degenerated beam functions to study flexure problems concerning static deflection or free vibration of plates involving free edges. An alternate set of admissible functions, derived from the mode shapes of vibration of plates

having two parallel edges simply supported and boundary conditions on the other two edges appropriate for the plate under consideration, was suggested by Dickinson and Li [29]. Even though these functions, which were called " the simply supported plate functions " provided superior results for plates supported in some manner along all four edges, they did not yield satisfactory results when some of the plate edges were free. Laura [30] used " polynomial co-ordinate functions " to approximate the fundamental natural frequencies of systems. Goldfracht and Rosenhouse [31] used a bipolynomial series to approximate the deflection shapes of plates and obtained the natural frequencies and mode shapes of plates with clamped boundaries with partial rotational flexibility of the edges employing Garlekin's method. They provided explicit algebraic expressions for the first nine modes. The deflection shapes defined by the bipolynomial series are not orthogonal to each other and hence the resulting expressions become quite cumbersome. Bhat [32] proposed a set of beam characteristic orthogonal polynomials that can be used as plate deflection functions to obtain the natural frequencies and mode shapes of rectangular plates in Rayleigh-Ritz method. He showed that the use of these orthogonal polynomials yields excellent results for the natural frequencies of several example plates having various boundary conditions. The excellence of the functions was further established by Dickinson and DiBlasio [33] who

conducted a convergence study of the method. They included the effect of special orthotropy and in-plane loading in their studies. These orthogonal polynomials for the beam are constructed using Gram-Schmidt process, the first member of the set satisfying both the geometrical and natural boundary conditions of the beam and all the rest satisfying the geometrical boundary conditions. Leissa, Lee and Wang [34] used shallow shell theory to determine the frequencies of a blade having camber and twist, rotating with non-zero angle of attack. The effect of camber on the natural frequencies was studied by Rawtani [35].

The stresses, natural frequencies and mode shapes of an existing thin blade have been studied using the finite element method by Barten et al [36]. A similar analysis has been done for thick blades by Ahmad et al [37] which was extended to rotating blades by Bossak and Zienkiewicz [38]. Dokainish and Rawtani [39] determined the natural frequencies and mode shapes of a cantilever plate mounted on the periphery of a rotating disk. From the results of computations carried out for various values of the aspect ratio, hub radii and setting angles, they derived empirical formulae giving the effect of these parameters on the natural frequencies. Henry and Lalanne [40] derived the total potential energy of a thin rotating

plate. They minimized the potential energy by using the finite element method and obtained the natural frequencies and mode shapes by simultaneous iterative technique. Macbain [41] used four node quadrilateral plate bending element (Cquad2) of Nastran to evaluate the natural frequencies of a fixed aspect ratio plate for different pre-twist conditions. Gupta and Rao [42] studied the effects of taper and twist on the natural frequencies of a blade. Jumaily and Faulkner [43] considered the thin shell theory for long hollow blades and compared the results with those obtained using beam theory and from laboratory tests. They showed that for higher frequency modes and thin, short blades it is inaccurate to model the blade as a beam. Also, the dynamic response studies require results for many modes, some of which cannot be approximated as beam modes. Gupta and Rao [44] used the thin shell theory to formulate energy expressions and derived differential equation for torsional vibrations .

1.5 : Vibration of Disks

The notable monograph by Leissa [45] contains a summary of all known results for the free vibration of many types of circular plates until 1965. For isotropic, circular plates of uniform thickness and subject to the classical boundary

conditions of clamped, free or simply supported, exact solutions in terms of Bessel functions exist. Natural frequency parameters and in some cases nodal patterns have been determined by several investigators. Among the investigators are Carrington [46], who studied clamped plates, Itao and Crandall [47], who tabulated natural frequency parameters and mode shapes for free plates and Leissa and Narita [48], who presented natural frequency parameters for simply supported plates. Vogel and Skinner [49] obtained exact solutions for the natural frequency parameters of isotropic annular plates with various combinations of the classical boundary conditions for a wide range of inside to outside radius ratios. The effects of rotary inertia and shear deflection on the natural frequencies of annular plates was studied by Rao and Prasad [50].

A disk having thickness which varies with radius has been treated by several researchers. Laura, Ficcadenti, Valerga and Greco [51] used the Rayleigh-Ritz method to study the effect of radially varying thickness on the fundamental frequency. The axisymmetric vibration with linearly varying thickness has been studied by Raju et al [52], who used the finite element method, and Soni and Amba Rao [53], who used the Chebyshev collocation method. The latter work is extended by Gupta and

Lal [54] to include the effect of in-plane force. The axisymmetrical vibration of such plates was further considered by Sankaranarayanan et al [55]. The natural frequency parameters for both axisymmetrical and non-axisymmetrical modes for disks with linearly varying thickness was obtained by Gorman, [56], using the finite element method. Exact analysis using Bessel functions for disks having parabolic and linear variations have been reported by Lenox, Conway, Becker [57], and Conway and Dubl [58], respectively.

The first analysis of solid circular spinning disks was by Lamb and Southwell [59]. They included results for a very slow rotating disk (negligible membrane forces) and an approximate solution for a case when both bending stiffness and membrane forces are important. Further, Southwell [60] generalized the results of [59] by obtaining solutions for a disk which is clamped at its inner radius and free at its outer edge. Simmonds [61] studied the spinning disk using membrane theory. Evesman and Dodson [62] solved the problem of a spinning disk which is clamped at its inner edge by using a series solution. Barasch and Chen [63] numerically integrated the system of differential equations in order to solve a similar problem. Mote [64] used the Rayleigh-Ritz technique to investigate the free vibration characteristics of centrally

clamped, variable thickness, axisymmetric disks with axisymmetric in-plane stress distributions. In plane stresses due to rotation, temperature and prestressing were considered. Sinha [65] determined the natural frequencies of a thick spinning disk using a numerical Rayleigh-Ritz trial function. Kirkhope and Wilson [66] and Kennedy and Gorman [67] used efficient annular finite elements to examine the vibrations of thin axisymmetric disks. The effects of variable thickness and temperature distributions were also included in their analyses. Mote [68] also considered the vibrations of non-axisymmetric disks using the finite element technique. Other studies such as those by Johnson [69], and Everson [70] deal with the spinning disk using membrane theory.

The stability characteristics of rotating disks have been studied by Iwan and Moeller [71]. They estimated the stability of a solid disk subject to a concentrated transverse load. Vibration and stability behaviour of rotating slicing blades with free inner and clamped outer edges was studied by Chonan and Sato [72]. They obtained the natural frequencies as a function of speed and discussed the types of instability that appear in the system. Benson and Boggy [73] studied the spinning disk problem with the objective of determining the transverse deflection due to spatially stationary loads.

Tobias and Arnold [74] presented a detailed investigation of the vibration of rotating disks with an emphasis on the critical speed instability phenomenon. Mote [75], and Mote and Neih [76] presented both theoretical and experimental investigations of this phenomenon.

1.6 : Bladed - Disk Assemblies / Rotor Analyses

Most of the previous studies on the vibration characteristics of turborotor system treat the various components of the system such as shaft, blades and disks as separate items. Very few studies have been done with regard to the effect of interaction of flexible disks and a rotor, and disk and blade vibration. A set of blades mounted on a rotor exhibit more complex vibration characteristics than do single or packeted cantilever blades.

Armstrong et al [77] used a coupling procedure to combine the constituent parts of the bladed-disk assembly to determine the natural frequencies of the system. Ewins [78] studied the basic vibration characteristics of bladed disk assemblies to predict the natural frequencies. A finite element model has been developed by Kirkhope and Wilson [79] considering the effects of rotation and temperature distribution, and by Dye

and Henry [80].

The earliest extensive work on the problem of non-synchronous whirl of a flexible rotor with a rigid disk including gyroscopic forces was by Green [81]. Sann [82] studied a flexible-disk supported by a shaft which had angular and axial flexibility, but no mass. Dopkin and Shoup [83] studied the effect of disk flexibility and gyroscopic forces on the resonant frequencies of an axisymmetric rotating shaft with multiple disks and bearings. They found that disk flexibility can significantly reduce the rotor resonant speeds, particularly at low speed. Dynamic unbalance response of an axisymmetrically mounted rotor with the influence of the flexible disk has been studied by Hagiwara and Yoneyama [84]. They found that due to the asymmetry of the rotor the shaft motion is elliptical rather than circular and this has remarkable influence on the response of the shaft and disk. Eshleman and Eubanks [85] investigated the effect of gyroscopic moments on the critical speeds of a shaft-disk system mounted in short end bearings. Hagiwara, Sakata, Takayanagi, Kikuchi and Gyobu [86] studied the vibration of a rotor shaft system coupled with flexible impellers based on the transfer matrix method. They found that impeller flexibility can reduce the critical speed of a rotor. Also, components whose effect on the vibration characteristics

is very important are the various types of connections which may be made between adjacent blades referred to as 'shrouding' (tip shrouds and lacing wires). The effect of these connections has been studied by Bielawa, Srinivasan, Rimkunas, and Craig [87-90]. These studies concentrated on the various types of damping mechanisms to account for any energy dissipation due to the vibratory rubbing at shroud interfaces which in turn influences the extent of mechanical coupling between the blades. Finally, the subject of 'mistuned' blades i.e. differences in tuning on the vibration properties of bladed disk assemblies has been studied by Whitehead, Kaza, and Bendiksen [91-93]. These studies concluded that aerodynamic mistuning is generally very beneficial, resulting in significantly decreased maximum amplitude blade response.

1.7 : Scope of the Present Investigation

The objectives of the present investigation are:

i) To develop suitable models for each individual component of a turborotor system and study their dynamic behaviour.

ii) To develop a comprehensive model of the turborotor system by assembling each individual component using the finite element technique and study its dynamic behaviour. Also, to study the effect of disk, support and blade flexibility on the system dynamic behaviour.

iii) To obtain the response due to harmonic and centrifugal loading using the finite element model of the turborotor system.

iv) To obtain the stresses due to steady harmonic and centrifugal loading.

v) To conduct modal testing of a shaft disk system and compare the natural frequencies with those obtained from the analytical results.

In the present study, Chapter 2 deals with the dynamic analysis of a turborotor blade using beam characteristic orthogonal polynomials in the Rayleigh-Ritz method. Depending on the aspect ratio, the blades are idealized either as beams or plates. The setting angle of the blade with respect to the plane of rotation and the radius of the hub on which the structure is mounted are taken into account in the formulation. The effects of shear deflection and rotary inertia are also studied. The variation of the natural frequencies and mode shapes with the speed of rotation are obtained for several combinations of the setting angle, hub radius and aspect ratio.

In Chapter 3, axisymmetrical and antisymmetrical vibrations of a turbine disk with varying thickness is studied. Characteristic orthogonal polynomials are employed as

deflection functions in the Rayleigh-Ritz method. The variation of the natural frequencies with speed of rotation are presented for several parameter combinations such as the ratio of inner/outer radii, ratio of inner/outer thickness.

Chapter 4, presents a finite element model of the bladed-disk assembly. Natural frequencies and mode shapes are presented for various values of the setting angle.

In Chapter 5, a complete model of the turborotor system is developed using the finite element technique and the natural frequencies and mode shapes are obtained for various rotational speeds.

In Chapter 6, response analysis of a complete turborotor system subjected to steady sinusoidal and centrifugal loading is carried out. The stresses and amplitudes of vibration for a typical turborotor system are obtained.

Chapter 7 presents an experimental validation of the analytical model used to study the effect of rotation on the natural frequencies of a disk of a turborotor system.

Finally, conclusions, highlights, and recommendations for future work are presented in Chapter 8.

CHAPTER 2

DYNAMIC ANALYSIS OF ROTATING BEAM AND PLATE TYPE STRUCTURES

2.1 : General

A turbomachine blade, depending on its aspect ratio, can be treated either as a cantilever beam or a cantilever plate mounted on the periphery of a rotating disk at a setting angle. A beam model will represent a turbine blade reasonably well if the blade is slender (i.e. large aspect ratio), is reasonably thick, and only the first few vibrational frequencies and mode shapes are needed accurately. Unfortunately, these conditions are often not met. Many blades in sections of turbomachinery have a small aspect ratio, efficiency demands thin blades and dynamic response studies require results for many modes, some of which cannot be approximated as beam modes.

Centrifugal forces are set up in the blade due to rotation, which cause in-plane strains, resulting in the stiffening of the blade. Coriolis effects are also present which modify the dynamic behaviour. Due to change in structural characteristics with the speed of rotation, the natural frequencies of the structure will change and it is imperative that the speed of operation be away from the natural frequencies for satisfactory operation.

In this chapter, the dynamics of a rotating blade is studied using Rayleigh Ritz method. The blade is modelled as a rotating beam initially and then as a rotating plate. The setting angle of the blade with respect to plane of rotation and radius of the hub on which the blade is mounted are considered in the formulation. The effects of shear deformation and rotary inertia are also included. The variation of the natural frequencies and mode shapes with the speed of rotation are obtained for several combinations of setting angle and hub radius parameters.

2.2 : Rayleigh - Ritz method

The Rayleigh-Ritz method is widely used to obtain approximate values for the natural frequencies and mode shapes of structures. The method is based on the principle of conservation of energy in undamped structures undergoing vibration and provides upper bound values for the system natural frequencies.

In this method, a deflection shape of the form,

$$y = \sum_{n=1}^{N} C_n \phi_n \qquad (2.1)$$

is assumed initially, where ϕ_n are admissible functions satisfying at least the geometrical boundary conditions and

C_1, C_2, ...C_n are arbitrary constant coefficients. The functions ϕ_n must form a complete set to represent all the modes of vibrations. In limiting this set to a finite number of functions, the analysis can be interpreted as approximating a continuous system into a multidegree of freedom discrete system. The coefficients are adjusted by minimizing the frequency with respect to each of the coefficients. This results in N algebraic equations in terms of the N unknown coefficients, C_n , involving p^2, the frequency of vibration. The solution of these equations then gives the natural frequencies and associated mode shapes of the system.

For a conservative system, the maximum kinetic energy in the system undergoing vibration is equal to the maximum strain energy. However since the assumed mode shapes are not exact, T_{max} will not be equal to U_{max} and hence,

$$F(C_n, p) = T_{max} - U_{max} \tag{2.2}$$

will be the error term. The coefficients C_n must be chosen so as to minimize the error and hence,

$$\frac{dF}{dC_n} = \frac{d}{dC_n}(T_{max} - U_{max}) = 0 \tag{2.3}$$

$$\frac{\partial T^*_{max}}{\partial C_n} p^2 + T^*_{max} \frac{\partial p^2}{\partial C_n} - \frac{\partial U_{max}}{\partial C_n} = 0 \tag{2.4}$$

where $T_{max} = p^2 T^*_{max}$. Since p^2 must be stationery with respect to C_n , $\partial p^2/\partial C_n = 0$ and hence,

$$p^2 [A] + [B] = 0$$

$$where\ [A] = \frac{\partial T^*_{max}(C_n)}{\partial C_n}\ ;\ [B] = \frac{\partial U_{max}(C_n)}{\partial C_n}\ n=1,2,.....N$$

(2.5)

This is a standard eigen-value problem and the solution yields the natural frequencies and the corresponding coefficients C_n can be used in equation (2.1) to obtain the approximate mode shapes.

2.2.1 : Assumed Shape Functions in Rayleigh - Ritz Method

In order to apply the Rayleigh-Ritz method it is necessary to use shape functions satisfying at least the geometrical boundary conditions. These shape functions when substituted in the kinetic and potential terms produce cross terms in the mass and stiffness matrices. When more number of these terms are considered the matrices become ill conditioned and pose numerical problems in solving for eigenvalues.

To overcome this problem beam characteristic orthogonal polynomials proposed by Bhat [16,32] can be employed as admissible functions in the Rayleigh-Ritz method. Construction

of such beam characteristic functions are discussed in the following section.

2.3 : Orthogonal Functions

2.3.1 : Definition of Orthogonality

Two functions $\Phi_m(x)$ and $\Phi_n(x)$ are said to be mutually 'orthogonal' in the interval $a \leq x \leq b$ with respect to the weight function (or weighting function) $W_f(x)$ if

$$\int_a^b W_f \, \phi_m(x) \, \phi_n(x) \, dx = \begin{cases} 0 & m \neq n \\ \delta_{mn} & m = n \end{cases} \qquad (2.6)$$

where, δ_{mn} is called "Kronecker delta' and is defined as 0 if $m \neq n$ and 1 if $m = n$ and $W_f(x)$ is non-negative and integrable in the interval $a \leq x \leq b$ [94], such that,

$$\int_a^b W_f \, dx > 0 \qquad (2.7)$$

When each member of a set of functions $\phi_k(x)$ is orthogonal to every other member of the set, in the interval (a,b) with respect to the weight function $W_f(x)$, the set of functions is called 'an orthogonal set of functions'. For the orthogonal set of functions equation (2.6) can be generalized as,

$$\int_a^b W_f \phi_m(x) \phi_n(x)\, dx = c_m \delta_{mn} \quad m,n=1,2,3.... \tag{2.8}$$

where, c_m is a constant . When m=n, and $\phi_m(x) \neq 0$, the integrand in equation (2.8) is positive and consequently $C_m > 0$ or,

$$\int_a^b W_f(x)\, \phi_m^2\, dx \neq 0 \tag{2.9}$$

The norm of the function ϕ_m is $\sqrt{C_m}$.

2.3.2 : Generation of Orthogonal Polynomials

When a set of orthogonal functions is constructed only with polynomials and the difference between the degrees (the term of highest degree in each member) of any two consecutive member polynomials is just 1, a number of relationships are known to exist [94,95]. Among them, one of the most important relationships is the recurrence relation,

$$\phi_2(x) = (A_1 x - B_1)\, \phi_1(x) \tag{2.10}$$

$$\phi_{n+1} = (A_n x - B_n)\, \phi_n(x) - C_n \phi_{n-1}(x) \quad n=2,3.... \tag{2.11}$$

where, A_n, B_n and C_n are constants and $\phi_1(x)$ is unity. Further, when A_n is 1 or the coefficient of the term

containing the highest degree in the member is unity, the polynomial is called a monic polynomial [94]. For monic polynomials the constants B_n and C_n are given as [94,95],

$$B_n = \int_a^b W_f(x)\, x\, \phi_n^2(x)\, dx \;/\; \int_a^b W_f(x)\, \phi_n^2(x)\, dx \qquad (2.12)$$

$$C_n = \int_a^b x W_f(x)\, \phi_n \phi_{n-1}\, dx \;/\; \int_a^b W_f(x)\, \phi_{n-1}^2(x)\, dx \qquad (2.13)$$

The recurrence relation (2.8) is generalized by replacing the first term in the right hand side with g(x) [96] as,

$$\phi_2(x) = (A_1 x - B_1)\, \phi_1(x) \qquad (2.14)$$

$$\phi_{n+1} = \{g(x) - B_n\}\, \phi_n(x) - C_n\, \phi_{n-1}(x) \qquad n=2,3\ldots \qquad (2.15)$$

Using this recurrence relation , a set of orthogonal polynomials can be generated. In this set, the difference in degree between successive polynomials depends on the form of g(x) and the recurrence relation given by equation (2.11) remains valid with the inclusion of g(x) [96].

2.4 : Beam Characteristic Orthogonal Polynomials

Numerous sets of orthogonal polynomials in a given interval with respect to a weight function can be obtained by using the recurrence relation (2.12) and taking different

starting or the generating function. With the generating function $g(x)=x$ and starting function unity, a number of well known polynomials are obtained. Some such polynomials are:

Legendre polynomials obtained with $W_f(x) = 1$ on the interval $-1 \leq x \leq 1$; Chebyshev polynomials of the first kind with $W_f(x) = (1 - x^2)^{-1/2}$ in $-1 \leq x \leq 1$; Laguerre polynomials with $W_f(x)= e^{-x}$ in $0 \leq x \leq \infty$;

Bhat [32] proposed a set of beam characteristic orthogonal polynomials for use in Rayleigh-Ritz method as the admissible functions for dynamic and static problems of beams or rectangular plates with classical boundary conditions. The starting function Φ_1 is chosen as the simplest polynomial of the least degree that satisfies at least the geometrical boundary conditions of the beam, and the higher members of the set are constructed using the generating function $g(x)=x$. However, if the starting polynomial $\phi_1(x)$ is made to satisfy both geometrical and natural boundary conditions, the results will improve for a given number of terms. Even though $\phi_1(x)$ is also made to satisfy natural boundary conditions , it is easy to check that higher members will satisfy only geometrical boundary conditions when $g(x)=x$. Higher members also can be constructed so as to satisfy natural boundary conditions in some cases by choice of $g(x)$ [96].

2.5 : Beam Model

The cantilever beam considered is mounted on the periphery of a rotating disc as shown in Fig. 2.1 . The xyz coordinate frame is chosen such that x and y axes are in the plane of beam cross-section and are the principal centroidal axes of inertia in that plane. The z-axis is along the beam. XYZ is another orthogonal cartesian frame where Z axis is along the beam and XZ plane contains the plane of disc rotation. Origin of both xyz and XYZ coordinate systems are at the root of the beam where it is fixed to the disc. The angle θ between the Y and x axes is the setting or the stagger angle.

2.6 : Strain energy

The strain energy U may be written as [97] ,

$$U_{max} = \frac{1}{2} \int \frac{M^2}{EI_x} \, dz = \frac{1}{2} \int EI_x \left(\frac{d^2y}{dz^2}\right)^2 dz \qquad (2.16)$$

where the integration is carried out along the length of the beam.

Let $\acute{z} = z/L$ be the non - dimensional axial length. Substituting this in equation (2.16) and integrating along the length of the beam, the expression for strain energy is,

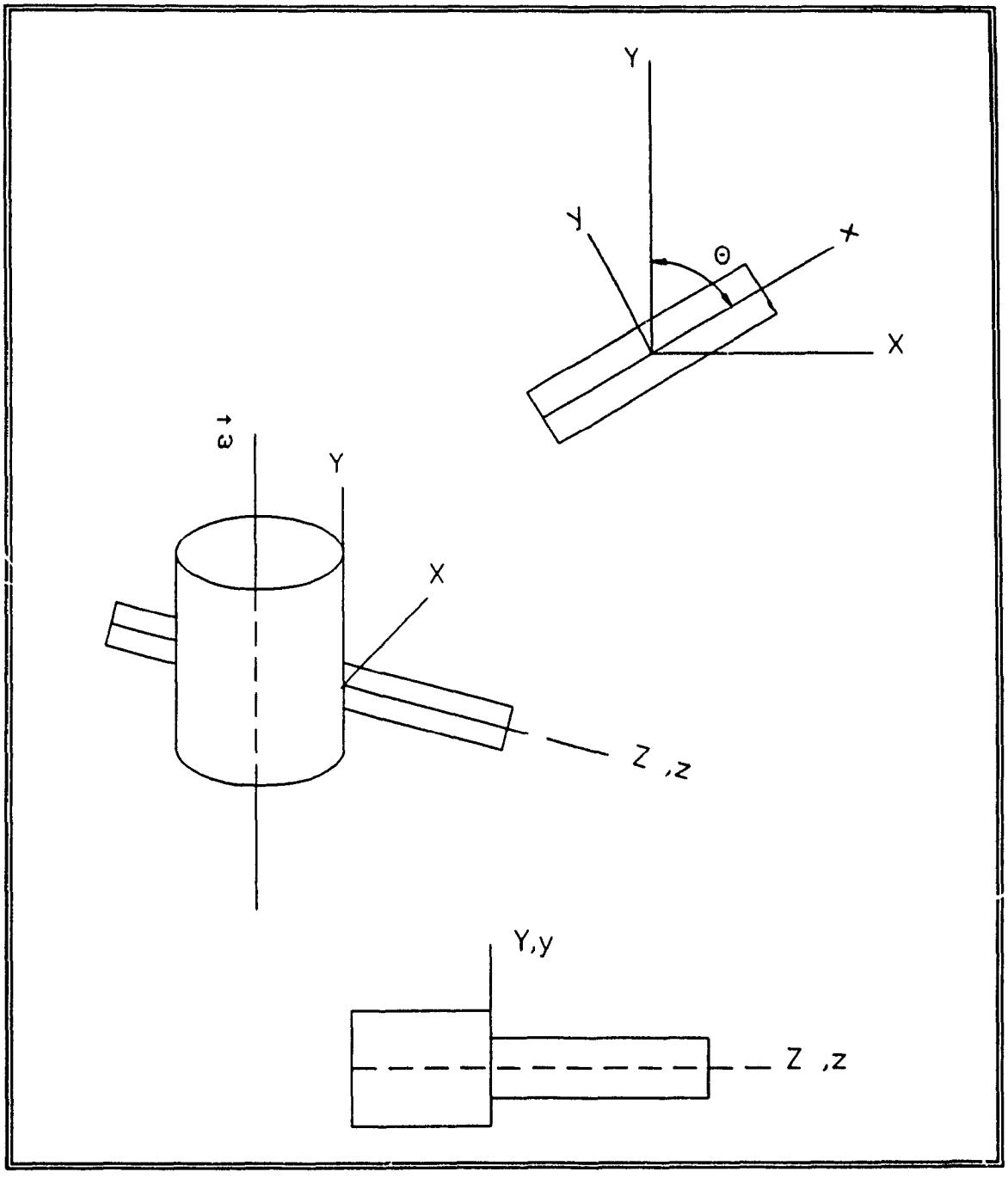

Figure 2.1 : Rotating Cantilever Beam

$$U_{max} = \frac{1}{2L^3} \int_0^1 EI_x \left(\frac{d^2y}{d\tilde{z}^2}\right)^2 d\tilde{z} \qquad (2.17)$$

2.7 : Kinetic Energy

The total kinetic energy of the system is the sum of the kinetic energy due to flexural motion of the beam, T_f, and that due to rotation T_r. Since the rotational motion induces centrifugal loads and the consequent energy stored in the beam can be treated as a strain energy, some prefer to treat the kinetic energy due to rotation, T_r as strain energy due to rotation.

2.7.1 : Flexural Kinetic Energy

The total kinetic energy of the blade in flexural vibration can be considered to be made up of two parts. They are the translational kinetic energy, T_b, and that due to rotation T_t. (rotation about a transverse axis, rotary inertia contribution)

For an element dz, the translational kinetic energy dT_b of the mass concentrated at the centroid is given by

$$dT_b = \frac{1}{2}\, m\dot{y}^2\, dz \qquad (2.18)$$

where m = ρA.

Hence the total kinetic energy T_b is,

$$T_b = \frac{1}{2}\, m \int_0^L \dot{y}^2\, dz \qquad (2.19)$$

The rotational kinetic energy, dT_t, due to rotation of the element about its centroid is,

$$dT_t = \frac{\rho I_x dz (\dot{y}')^2}{2} \qquad (2.20)$$

Therefore, the total instantaneous kinetic energy T_t, becomes

$$T_t = \frac{1}{2} \int_0^L \rho\, I_x\, (\dot{y}')^2\, dz \qquad (2.21)$$

The combined kinetic energy T_f, is the sum of the translational and rotational kinetic energy and can be written from equations (2.19) and (2.21) as,

$$T_f = \frac{1}{2} \int_0^L [\, \rho A\dot{y}^2 + \rho I_x (\dot{y}')^2]\, dz \qquad (2.22)$$

2.7.2 : Kinetic energy due to rotation

Fig. 2.2 shows the blade mounted on the periphery of the rotating disc. For a short element dz, each view shows both the rest position A and the deflected position B, displacements occurring in both $\eta_1 z$ plane (Fig. 2.2(a)) and $\xi_1 z$ plane (Fig. 2.2(b)).

When the blade deflects in the $\xi_1 z$ plane, Fig. 2.2(b), the line of action of the centrifugal force, dF, on the element dz remains parallel to the z axis. Hence the force component dF_ξ in the ξ_1 is zero and the kinetic energy dT_ξ stored by the element is also zero. Thus,

$$dT_\xi = 0 \tag{2.23}$$

With the element dz in the deflected position B, Fig. 2.2(a), the force dF can be resolved into two components dF_η and dF_z, in the circumferential and radial directions η_1 and z respectively. The circumferential component dF_η of the centrifugal force dF is given by,

$$dF_\eta = dF \sin \beta_1 \tag{2.24}$$

where,

$$dF = m\,\omega^2 (R+z)\, dz \tag{2.25}$$

and

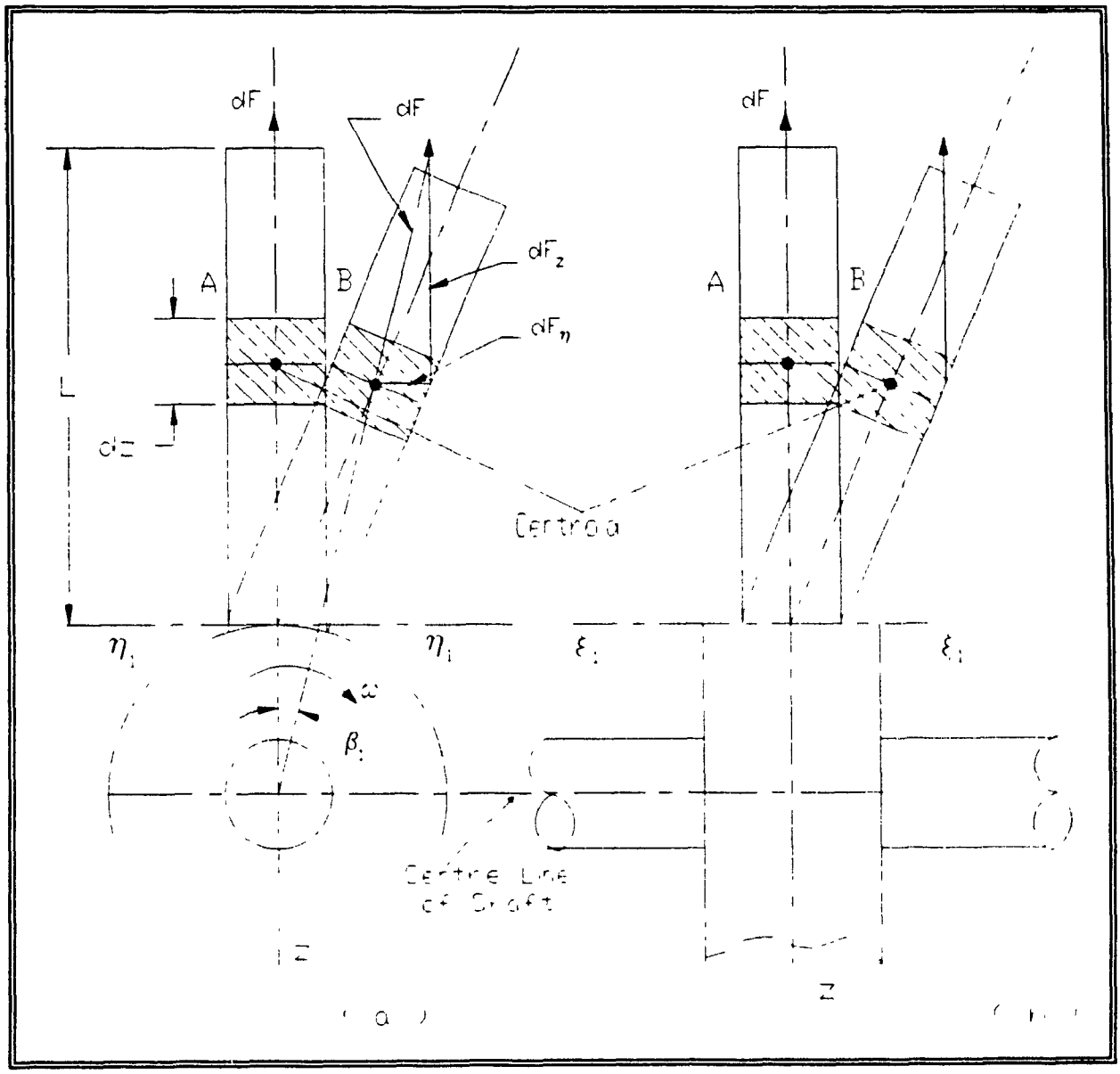

Figure 2.2 : Beam - Hub Radii Assembly

$$\sin \beta_1 = \frac{\eta_1}{(R+z)} \tag{2.26}$$

In the above equations, R is the disc radius, ω is the angular velocity of rotation of disc and m is the mass of blade per unit length.

Substitution of equations (2.25) and (2.26) into (2.24) gives,

$$dF_\eta = m\,\omega^2\,\eta_1 dz \tag{2.27}$$

Since the η_1 component of the centrifugal force, dF_η, increases linearly from zero at the position A, regarded as datum, to a value given by equation (2.27) at B, the average force during a displacement η_1 is $dF_\eta/2$. With the force and motion in the same direction, the corresponding gain of the kinetic energy dT_η is given by,

$$dT_\eta = \frac{dF_\eta\,\eta}{2} = \frac{m\,\omega^2\,\eta_1^2\,dz}{2} \tag{2.28}$$

and for the entire blade,

$$T_\eta = \int_0^L \frac{m\,\omega^2\,\eta_1^2\,dz}{2} \tag{2.29}$$

The centrifugal force dF acting on the element in the undeflected position A is given by (2.25). In the deflected position B the force component dF_z in the z direction is,

$$dF_z = dF \cos \beta_1 \tag{2.30}$$

For small displacements, cos β_1 approaches unity; the force component in the z direction can, thus, be regarded as constant and is given by equation (2.25).

The z component of the kinetic energy dT_z stored by the element can be written as,

$$dT_z = -dF_z\Delta \approx -dF\Delta \tag{2.31}$$

where Δ is the total displacement of the element dz in moving from rest position A to deflected position B.

To determine Δ from Fig. 2.3,

$$dz^2 = d\delta^2 + (dz-d\Delta)^2$$

where,

$$d\delta = [d\xi_1^2 + d\eta_1^2]^{\frac{1}{2}} \tag{2.32}$$

represents the increase of total transverse displacement δ. From (2.32),

$$dz^2=d\delta^2+(dz^2+d\Delta^2-2dzd\Delta) \tag{2.33}$$

Since $d\Delta$ is small, neglecting higher order terms involving $d\Delta$, equation (2.33) can be written as,

$$d\Delta = \frac{1}{2}\left(\frac{d\delta}{\partial z}\right)^2 dz \tag{2.34}$$

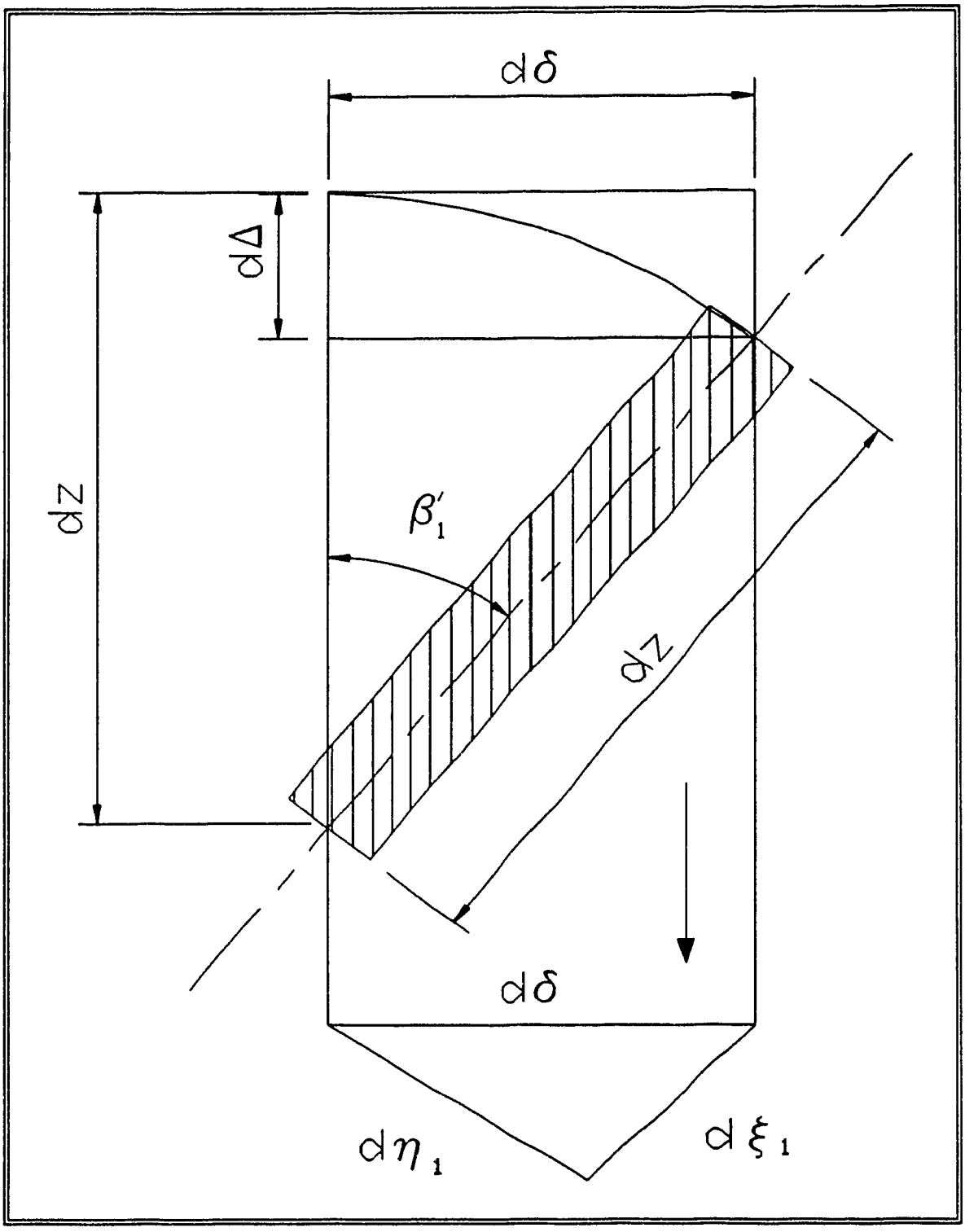

Figure 2.3: Beam Element Before and After Deflection Showing the Relative Displacement dΔ of the Ends

Combining equations (2.32) and (2.34),

$$d\Delta = \frac{1}{2}\left(\left(\frac{\partial \xi_1}{\partial z}\right)^2 + \left(\frac{\partial \eta_1}{\partial z}\right)^2 \right) dz \qquad (2.35)$$

and the total displacement Δ, of the element at z, is thus, given by

$$\Delta = \frac{1}{2}\int_0^z \left(\left(\frac{\partial \xi_1}{\partial z}\right)^2 + \left(\frac{\partial \eta_1}{\partial z}\right)^2 \right) dz \qquad (2.36)$$

Assuming small displacements, and making use of equations (2.25) and (2.36), equation (2.31) can be rewritten as,

$$dT_z = -\frac{m\omega^2}{2}(R+z)\,dz \int_0^z \left(\left(\frac{\partial \xi_1}{\partial z}\right)^2 + \left(\frac{\partial \eta_1}{\partial z}\right)^2 \right) dz \qquad (2.37)$$

Thus, for the entire blade the kinetic energy T_z, becomes

$$T_z = -\frac{\omega^2}{2}\int_0^L \left[m(R+z) \int_0^z \left(\left(\frac{\partial \xi_1}{\partial z}\right)^2 + \left(\frac{\partial \eta_1}{\partial z}\right)^2 \right) dz \right] dz \qquad (2.38)$$

The total kinetic energy due to centrifugal effects is given by,

$$T_R = T_\xi + T_\eta + T_z \qquad (2.39)$$

which can be expressed as,

$$T_R = -\frac{\omega^2}{2}\int_0^L \left[m(R+z) \int_0^z \left(\left(\frac{\partial \xi_1}{\partial z}\right)^2 + \left(\frac{\partial \eta_1}{\partial z}\right)^2 \right) dz - m\eta_1^2 \right] dz \qquad (2.40)$$

Let,

$$\frac{d}{dz}(F.\Delta) = \Delta\left(\frac{dF}{dz}\right) + F\left(\frac{d\Delta}{dz}\right)$$

where Δ is given by equation (2.36) . Integrating this equation with respect to z from 0 to L, the left hand side becomes zero and hence,

$$\int_0^L \Delta \frac{dF}{dz} = -\int_0^L F\frac{d\Delta}{dz}dz \qquad (2.41)$$

Using the relationship ,

$$\frac{d}{dz}\int_z^L F(z)\,dz = -F(z) \qquad (2.42)$$

and using equations (2.41) and (2.42), equation (2.40) can be written as,

$$T_R = \frac{\omega^2}{2}\int_0^L [\langle (\frac{\partial \xi_1}{\partial z})^2 + (\frac{\partial \eta_1}{\partial z})^2 \rangle \int_z^L (m(R+z))dz + m\eta_1^2]\,dz \qquad (2.43)$$

Now, using the relationships,

$$\eta_1 = y\cos\theta - x\sin\theta$$

$$\xi_1 = y\sin\theta + x\cos\theta \qquad (2.44)$$

equation (2.43), can be written as,

$$T_R = \frac{\rho A \omega^2}{2}\,[\int_0^L \langle (x^2\sin^2\theta - 2xy\sin\theta\cos\theta + y^2\cos^2\theta)$$

$$-\langle (\frac{\partial x}{\partial z})^2 + (\frac{\partial y}{\partial z})^2 \rangle)dz \int_z^L (R+z)\,dz] \qquad (2.45)$$

The in plane deflections x and y are small as compared to the bending deflection z. Hence neglecting coupling of x and y deflections and ignoring higher order terms involving x and y,

$$T_R = \frac{\rho A \omega^2}{2} \left[\int_0^L y^2 Cos^2\theta \, dz - \int_0^L \left(\frac{\partial y}{\partial z}\right)^2 \left(RL + \frac{L^2}{2} - Rz - \frac{z^2}{2}\right) dz \right] \quad (2.46)$$

The total kinetic energy of the system in terms of the non - dimensional parameter $\tilde{z}$ is,

$$T_{TOTAL} = T_f + T_R$$

i.e.

$$T_{TOTAL} = \frac{L}{2} \int_0^1 \rho A (\dot{y}')^2 d\tilde{z} + \frac{1}{2L} \int_0^1 \rho I_x (\dot{y}')^2 d\tilde{z}$$

$$+ \frac{\rho A \omega^2}{2} \left[L \int_0^1 y^2 Cos^2\theta \, d\tilde{z} - \frac{1}{L} \int_0^1 (y')^2 \left(RL + \frac{L^2}{2} - RL\tilde{z} - \frac{L^2\tilde{z}^2}{2}\right) d\tilde{z} \right]$$

(2.47)

where a dot represents differentiation with respect to time and $( )'$ indicates differentiation with respect to $\tilde{z}$.

Rayleigh-Ritz analysis can be applied at this stage to obtain the natural frequencies and mode shapes. This can be done by following the procedure outlined in section 2.2.1 or alternatively, using the time averaged Lagrangian as follows.The Lagrangian is given as,

$$L_1 = T-U \tag{2.48}$$

Assuming harmonic motion,

$$y = Y\exp(jpt) \tag{2.49}$$

the time averaged value of the Lagrangian is given by,

$$\bar{L_1} = \int_0^{\frac{2\pi}{p}} L_1 dt \tag{2.50}$$

Incorporating the following dimensionless parameters,

$$\tilde{R} = \frac{R}{L} \; ; \; \tilde{r}^2 = \frac{I_x}{AL^2} \; ; \; \lambda = \frac{\rho AL^4}{EI_x} \; ; \; \alpha^2 = \lambda\omega^2 \; ; \; \eta^2 = \lambda p^2 \tag{2.51}$$

the time averaged value of the Lagrangian can be written as,

$$\bar{L_1} = \frac{\pi EI_x}{2pL^3} \int_0^1 [\eta^2 Y^2 + \eta^2 \tilde{r}^2 (Y')^2 + \alpha^2 Y^2 Cos^2\theta$$

$$-\alpha^2 Y'^2 \{\tilde{R}(1-\tilde{z}) + \frac{1}{2}(1-\tilde{z}^2)\} - (Y'')^2] \, d\tilde{z} \tag{2.52}$$

To apply the Rayleigh - Ritz method, the shape function is assumed in the form,

$$Y = \sum A_m \phi_m(\tilde{z}) \tag{2.53}$$

where ϕ_m ($\tilde{z}$) are the assumed admissible shape functions in the form of beam characteristic orthogonal polynomials in the z direction, and A_m are the arbitrary coefficients. To determine the first member of the set satisfying the clamped - free condition, consider the function,

$$\phi_1(\tilde{z}) = b_1 + b_2\tilde{z} + b_3\tilde{z}^2 + b_4\tilde{z}^3 + b_5\tilde{z}^4 \tag{2.54}$$

The boundary conditions for such a beam are that at $\tilde{z} = 0$ the deflection and slope are zero and for $\tilde{z} = 1$ the moment and shear force are equal to zero,

$$i.e. \phi_i(0) = \phi_i'(0) = \phi_i''(1) = \phi_i'''(1) = 0 \tag{2.55}$$

(The prime denotes differentiation with respect to $\tilde{z}$)
Substituting the boundary conditions in (2.55),

$$\phi_i(\tilde{z}) = b_5(6\tilde{z}^2 - 4\tilde{z}^3 + \tilde{z}^4) \tag{2.56}$$

The coefficient b_5 is chosen appropriately so as to normalize ϕ_1 ($\tilde{z}$) such that,

$$\int_0^1 \phi_1^2(\tilde{z})\, d\tilde{z} = 1 \tag{2.57}$$

Therefore, the starting function in the z direction is taken as,

$$\phi_1(\bar{z}) = \sum_{j=1}^{5} b_j \bar{z}^{j-1} \tag{2.58}$$

where the b_j are given in Table 2.1.The other members of the orthogonal set are generated using the procedure outlined in sections 2.3 and 2.4.

However since the assumed mode shapes are not exact and hence minimizing the time averaged Lagrangian with respect to the arbitrary coefficients A_m, [6], following homogenous simultaneous equations are obtained,

$$\frac{\partial \bar{L}}{\partial A_m} = 0 \quad i = 1,2,3,.....N \tag{2.59}$$

which can be cast in the form of a standard eigenvalue problem,

$$\eta^2 [A] - [B] = 0 \tag{2.60}$$

Natural frequencies and mode shapes can be obtained by solving this set of equations.

A computer algorithm is developed to solve (2.60) for several parameter combinations of setting angle, hub radius and rotational speeds.

2.8 : Effect of Shear Deflection and Rotary Inertia

The beam model is refined further to include the effect of shear deflection and rotary inertia. Denoting the dynamic deflection and bending slope by y and ψ respectively, the potential and kinetic energy in sections 2.6 and 2.7 can be rewritten as [6],

$$U_{max} = \frac{L}{2}\int_0^1 [EI_x(\psi')^2 + KAG(y'-\psi)^2]\, d\tilde{z} \qquad (2.61)$$

$$T_f = \frac{L}{2}\int_0^1 (\rho A\dot{y}^2 + \rho I_x\psi^2)\, d\tilde{z} \qquad (2.62)$$

$$T_R = \frac{\rho A\omega^2 L}{2}\left[\int_0^1 y^2 Cos^2\theta\, d\tilde{z} - \int_0^1 (y')^2\left(RL + \frac{L^2}{2} - RL\tilde{z} - \frac{L^2\tilde{z}^2}{2}\right) d\tilde{z}\right] \qquad (2.63)$$

In the above equations the shear deflection is taken into account, where K is the shear coefficient and G is the shear modulus of elasticity.

The total kinetic energy is,

$$T = T_f + T_R \qquad (2.64)$$

and the Lagrangian is given by,

$$L_1 = T - U \tag{2.65}$$

The time averaged value of the Lagrangian is obtained as,

$$\bar{L_1} = \int_0^{\frac{2\pi}{p}} L dt \tag{2.66}$$

Introducing the following additional non dimensional parameters,

$$\tilde{k_2} = \frac{GK}{E} \; ; \; \tilde{r}_2 = \frac{I_x}{AL^2} \; ; \; \sigma = \frac{\tilde{r}_2}{\tilde{k}_2} \tag{2.67}$$

and following the procedure outlined in section 2.7.2 the natural frequencies and mode shapes can be obtained.

2.9 : Plate Model

Rotating structures in many applications cannot be strictly modelled as beams (i.e. when the aspect ratio is small) and must be modelled as flat or curved plates. In this section, the vibrational behaviour of a rotating plate is studied using Rayleigh-Ritz method. A class of beam

characteristic orthogonal polynomials [32], constructed using the Gram-Schmidt process are employed as deflection functions for plates in the Rayleigh-Ritz method to obtain their natural frequencies. The variation of the natural frequencies with the speed of rotation are obtained for several parameter combinations of setting angle and hub radius.

2.9.1 : Cantilever Plate

Rotating blade with low aspect ratio can be idealized as a cantilever plate. A simplified model of a rotating blade is shown in Fig. 2.4 . The blade is represented as a plate having one edge rigidly clamped and the other three free. The planform is rectangular having length l_p, width w_p and thickness h_p. As depicted, the blade rotates with angular velocity ω about an axis located at some distance R from the blade root. The figure is drawn for setting angle,θ, equal to 90° , that is the xy plane is perpendicular to the rotation axis.

In general, the setting angle can vary between 0° and 90° .

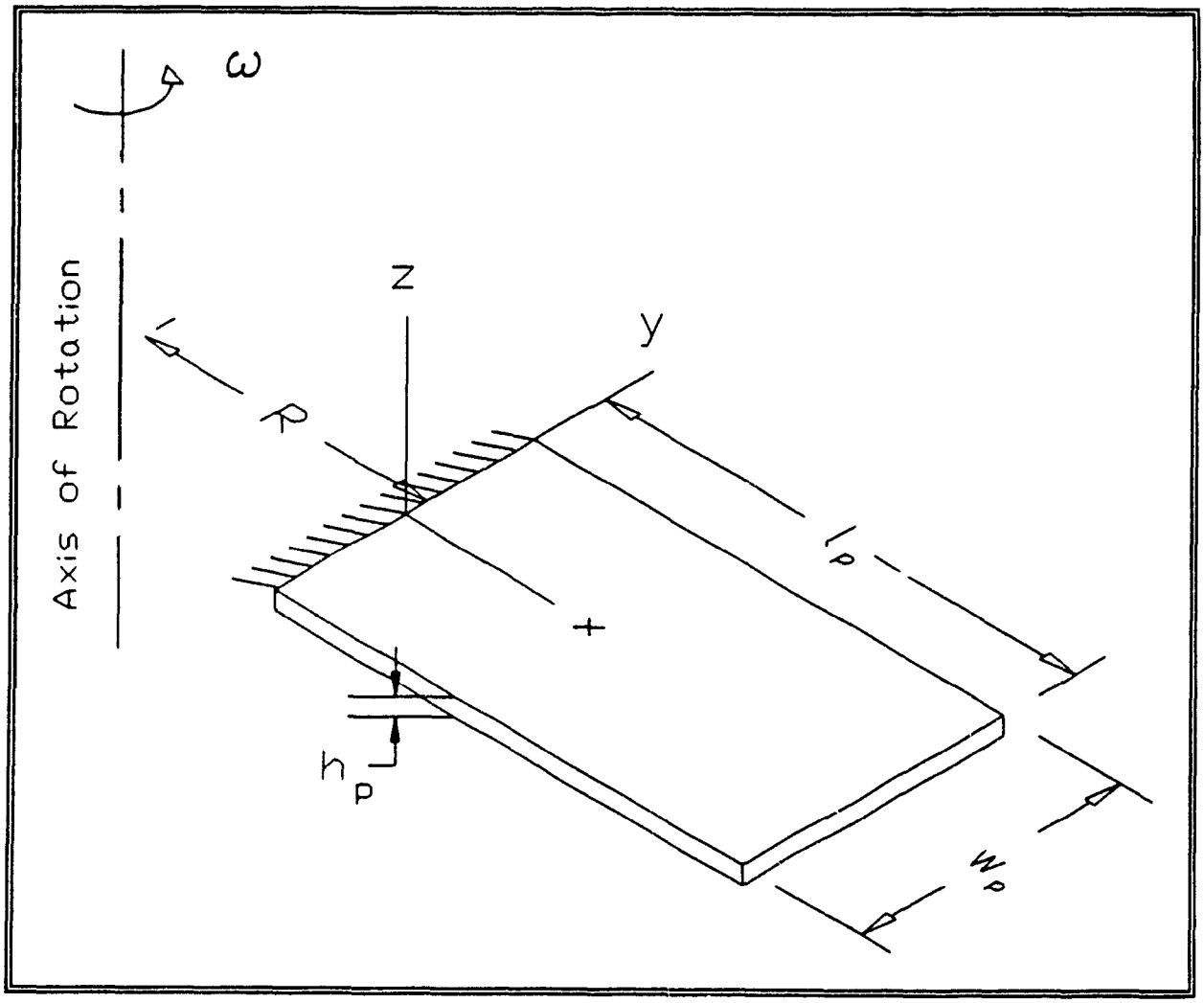

Figure 2.4 : Rotating Cantilever Plate

2.9.2 : Strain Energy

2.9.2.1 : Bending Strain Energy

The bending strain energy of the plate is given by,

$$U_b = \iiint dU_b = \frac{D}{2} \iint \left[\left(\frac{\partial^2 W}{\partial x^2} \right)^2 + \left(\frac{\partial^2 W}{\partial y^2} \right)^2 + 2\nu \frac{\partial^2 W}{\partial x^2} \frac{\partial^2 W}{\partial y^2} + 2(1-\nu) \left(\frac{\partial^2 W}{\partial x \partial y} \right)^2 \right] dx dy \tag{2.68}$$

2.9.2.2 : Strain Energy Due to Rotation

Energy due to rotation is included as strain energy here. It should be noted that this energy can also be considered as kinetic energy. In either case, it does not contain the vibration dependent frequency p^2. If W is the deflection of an arbitrary point on the middle surface of the plate, its instantaneous co-ordinates during vibration can be taken as (x,y,W). The components of the centrifugal force per unit volume of the plate along the xyz axes are given by,

$$F_x = \rho\omega^2 (x+R) \tag{2.69}$$

$$F_y = \rho\omega^2 (y\cos^2\theta - W\sin\theta\cos\theta) \tag{2.70}$$

$$F_z = \rho\omega^2 (-y\sin\theta\cos\theta + W\sin^2\theta) \tag{2.71}$$

These distributed in-plane forces F_x and F_y produce in plane stresses on the middle surface of the plate. The force F_x is independent of the displacement but the force F_y has a component proportional to the displacement W. If the vibrations are assumed to be of small amplitude, the component of the stresses dependent on W may be taken to be small as compared to the stresses produced by the forces independent of W. Thus, the stresses in the middle surface are those produced by the distributed forces, [39]

$$F_x = \rho\omega^2(X+R) \tag{2.72}$$

$$F_y = \rho\omega^2 y Cos^2\theta \tag{2.73}$$

The strain energy developed during vibrational deformation due to the presence of initial stress resultants N_x° , N_y°, N_{xy}° (i.e. forces per unit length), which are caused by the rotational body forces given in Equations (2.72 and 2.73), is given by,

$$U_{r1} = \frac{1}{2}\int_{\frac{-w_p}{2}}^{\frac{w_p}{2}}\int_{0}^{l_p}\left(N_x^\circ\left[\frac{\partial W}{\partial x}\right]^2 + N_y^\circ\left[\frac{\partial W}{\partial y}\right]^2 + 2N_{xy}^\circ\frac{\partial W}{\partial x}\frac{\partial W}{\partial y}\right)dxdy \tag{2.74}$$

With a reasonable first approximation, using strength of

materials type assumption gives the initial stress resultants as,

$$N_x^\circ = \frac{\rho h_p \omega^2}{2} [(R+l_p)^2 - (R+x)^2] \tag{2.75}$$

$$N_y^\circ = \frac{\rho h_p \omega^2 Cos^2\theta}{2} [(\frac{w_p}{2})^2 - y^2] \tag{2.76}$$

$$N_{xy}^\circ = 0 \tag{2.77}$$

Using Equations (2.75, 2.76, and 2.77) in Equation (2.74) gives,

$$U_{r1} = \frac{1}{2}\rho h_p \frac{\omega^2}{2} \int_{\frac{-w_p}{2}}^{\frac{w_p}{2}} \int_0^{l_p} [[(R+l_p)^2 - (R+x)^2] (\frac{\partial W}{\partial x})^2$$

$$+ Cos^2\theta ((\frac{w_p}{2}) - y^2) (\frac{\partial W}{\partial Y})^2] dxdy \tag{2.78}$$

The strain energy due to the displacement dependent force F_z which for the case given by Equation (2.71) (neglecting the deflection in the y direction) becomes,

$$U_{r2} = \frac{1}{2}\rho h_p \frac{\omega^2}{2} Sin^2\theta \int_{\frac{-w_p}{2}}^{\frac{w_p}{2}} \int_0^{l_p} W^2 dxdy \tag{2.79}$$

Hence, the total strain energy is,

$$U_{total} = U_b + U_{r1} + U_{r2} \tag{2.80}$$

2.9.3 : Kinetic Energy

The kinetic energy of the plate is given by,

$$T = \frac{\rho h_p}{2} \int_{\frac{-w_p}{2}}^{\frac{w_p}{2}} \int_0^{l_p} [\frac{\partial W}{\partial t}]^2 dxdy \tag{2.81}$$

The equations of motion can be derived directly from the energy expressions by using the Lagrangian,

$$L_1 = T - U \tag{2.82}$$

Assuming harmonic motion,

$$W(x, y, t) = W_o Sinpt \tag{2.83}$$

and incorporating the following dimensionless parameters,

$$\hat{x} = \frac{x}{l_p} \; ; \; \hat{y} = \frac{y}{w_p} \; ; \; \alpha_1 = \frac{l_p}{w_p} \; ;$$

$$\tilde{R} = \frac{R}{l_p} \; ; \; \lambda = \frac{\rho h_p l_p^4}{D} \; ; \; \beta^2 = \lambda \omega^2 \; ; \; \eta^2 = \lambda p^2 \tag{2.84}$$

the Lagrangian can be written as,

$$L = \int_{-\frac{1}{2}}^{\frac{1}{2}} \int_{0}^{1} \{ (W_o^2 \eta^2) - \{ [(W_o)_{\hat{x}\hat{x}} + \alpha_1^4 (W_o)_{\hat{y}\hat{y}}^2 + 2\nu\alpha_1^2 (W_o)_{\hat{x}\hat{x}} (W_o)_{\hat{y}\hat{y}}$$

$$+2(1-\nu)\alpha_1^2 (W_o)_{\hat{x}\hat{y}}^2] + \frac{\omega^2}{2} [(1-\hat{x}^2+2\hat{R}(1-\hat{x})) (W_o)_{\hat{x}}^2$$

$$+Cos^2\theta (\frac{1}{4}-\hat{y}^2) (W_o)_{\hat{y}}^2] + \omega^2 Sin^2\theta [(W_o)^2] \} d\hat{x}d\hat{y} \qquad (2.85)$$

To apply the Rayleigh - Ritz method, the deflection for a plate undergoing free flexural vibration is assumed as,

$$W_o(x,y) = \sum_m \sum_n A_{mn} \phi_m(\hat{x}) \psi_n(\hat{y}) \qquad (2.86)$$

Fig. 2.5 shows that the cantilever plate consists of beam problems with clamped free and free-free boundary conditions. The starting function in the $\hat{x}$ direction is taken as,

$$\phi_1(\hat{x}) = \sum_{j=1}^{5} b_j \hat{x}^{j-1} \qquad (2.87)$$

Similarly, the starting function in the $\hat{y}$ direction is

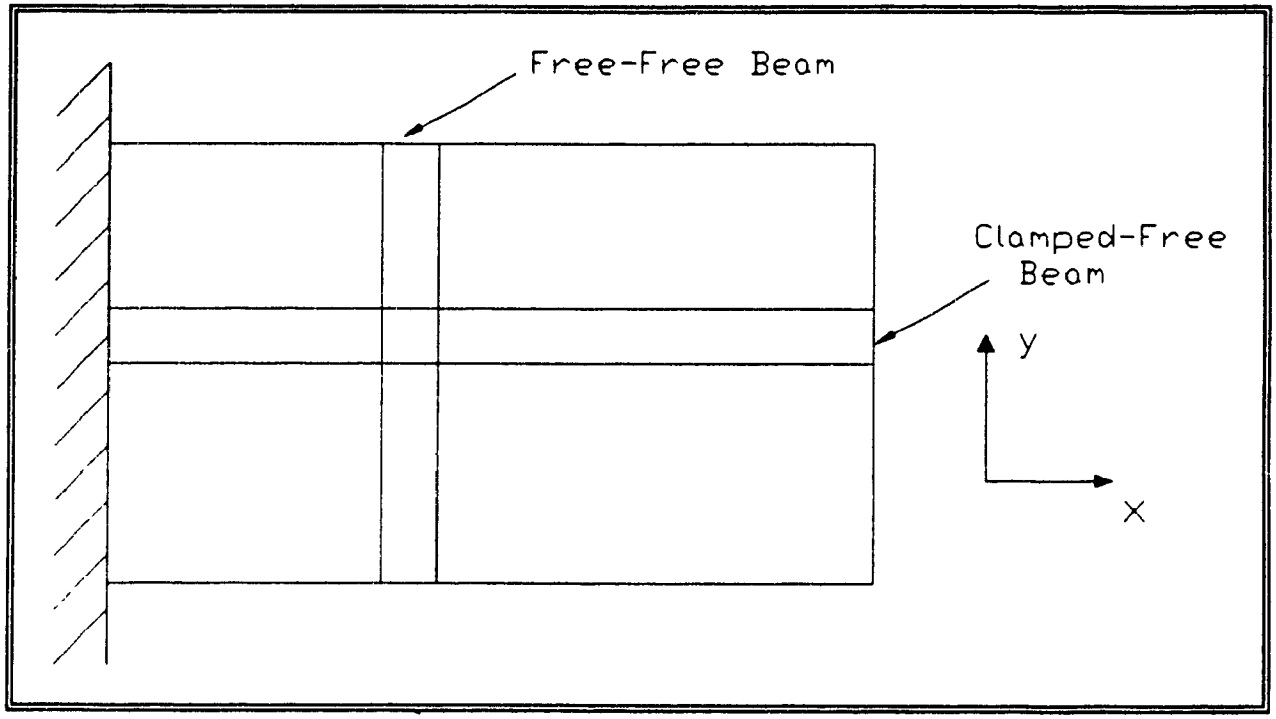

Figure 2.5 : Free-Free and Clamped-Free Beams used to Model the Cantilever Plate

taken as,

$$\psi_1(\hat{y}) = \sum_{j=1}^{5} c_j \hat{y}^{j-1} \qquad (2.88)$$

where the b_j and c_j for different boundary condition are given in Table 2.1.

The other members of orthogonal set are generated using the procedure outlined in sections 2.3 an 2.4.

2.10 : Discussion of Results

2.10.1 : Beam Model

The first three of beam characteristic orthogonal polynomials constructed using the Gram - Schmidt process are shown in Fig. 2.6.

Natural frequencies and mode shapes are obtained for a rotating beam at various rotational speeds for different values of setting angle and hub radii.

A convergence test was made by varying the number of terms considered in the shape function. The results are shown in Table 2.2. The results converge quite fast, for example, the first frequency converged up to 3 decimal with four terms. The variation of fundamental and second natural frequency for various values of hub radii and setting angle are presented in Tables 2.3 through 2.8. The results are also plotted in Figs. 2.7 through 2.12.

Variation of the natural frequency, η, with rotational speed , α, for the first mode for various values of setting angle and hub radii is shown in Figs. 2.7 through 2.12. The increase in natural frequency is larger for higher setting angles and for any setting angle the increase is linear at

higher rotational speeds.

The effect of hub radii, R, on the natural frequency is plotted against the rotational speed for setting angles of zero and 90°. With higher value of, R, the natural frequencies are higher and increase faster with the rotational speed. The results are compared with those from Hoa [18] .

Fig. 2.13 shows the mode shape of a standstill blade. The variation of the fundamental mode shape with rotational speed is shown in Fig. 2.14. The mode shapes are normalized to a value of unity at the tip. It is observed that as the rotational speed α, increases, the beam tries to straighten itself more and more. The variation of the shape of second mode with rotational speed is shown in Fig. 2.15. The beam has the tendency to straighten itself as the rotational speed increases as in the case of the fundamental mode.

The following numerical values are used to compare the results with [6] :

$$L=9.1948x10^{-2}m; \quad A=8.258x10^{-5}m^2;$$

$$G=82.74Gpa; \quad \rho=7.83x10^3\frac{Kg}{m^3};$$

$$E=206.85x10^9Pa; \quad I_x=5.7729x10^{-10};$$

$$\omega=540.35\frac{rad}{sec}; \quad R=2.63652x10^{-1}m; \qquad (2.89)$$

ν, is Poisson's ratio and is taken to be 0.3 in the calculations. Table 2.9 shows the theoretical classical frequencies for Euler - Bernoulli beams [98] for the blade parameters specified above. Two cases of setting angle are considered, that is $\theta = 0^\circ$ and $\theta = 90^\circ$; the results are presented and compared with [6] and [99] in Table 2.10. The present results are compared with Kaushal and Bhat [15] in Table 2.11. From Table 2.11 it can be seen that the shear and rotary inertia effects when taken into account, lower the frequency values of the rotating blade, such reduction being more predominant at higher modes.

2.10.2 : Plate Model

Natural frequencies and mode shapes are obtained for the rotating plate at various rotational speeds for different values of the setting angle, hub radii and aspect ratio.

Natural frequencies of the rotating plate for various combinations of the setting angle, hub radii and aspect ratio are presented in Tables 2.12 through 2.15. From these tables it can be seen that for a fixed rotational speed, increasing θ yields increasing values for all the frequencies and increasing hub radii increases the values for all the frequencies.

The present results are compared with the results of a finite element model [39] in Table 2.16.

Variation of the natural frequency, η, with rotational speed , α, for a fixed value of hub radii, aspect ratio and various values of setting angle is shown in Figs. 2.16 through 2.18. The increase in natural frequency is larger for higher setting angles . The effect of hub radii, R, on the natural frequency is plotted against the rotational speed for setting angles of 0 and 90° in Figs. 2.19 through 2.22. With higher value of, R, the natural frequencies are higher and increase

faster with the rotational speed.

The first six mode shapes of the cantilever plate are presented in Fig. 2.23.

2.11 : Summary

The dynamics of a rotating blade modelled as a beam and a plate is studied using beam characteristic orthogonal polynomials in the Rayleigh-Ritz method. Natural frequencies and mode shapes are obtained for different rotational speeds and for different parametric combinations. The natural frequencies increase with increase in setting angle. Also, for a fixed value of the setting angle the natural frequencies increase with increase in hub radii.

In the following chapter, dynamic analysis of a disk with varying thickness, exhibiting axisymmetrical and antisymmetrical vibrations is studied.

Table 2.1 : Coefficients of Starting Functions for Cantilever Plates

Boundary Conditions	b_1	b_2	b_3	b_4	b_5
Clamped (inner) Free (outer)	0	0	6	-4	1
	c_1	c_2	c_3	c_4	c_5
Free Free	1	0	0	0	0

Table 2.2 : Convergence of Natural Frequency with Number of Terms (Neglecting Shear Deflection and Rotary Inertia)

Setting Angle $\theta = 90°$

Angular Velocity $\alpha = 0$

Hub Radius $\tilde{R} = 0$

Natural Frequency $\eta = p\sqrt{\lambda}$					
No. of terms	Mode 1	Mode 2	Mode 3	Mode 4	Mode 5
2	3.527	34.8069			
3	3.5170	22.2333	118.1444		
4	3.5160	22.1578	63.3467	281.5692	
5	3.5160	22.0351	63.2397	128.5194	562.7075

Table 2.3 : Variation of Fundamental Frequency for $\tilde{R}$ = 0.0 and Various Values of Setting Angle

Angular Velocity α	Natural Frequency $\eta = p\sqrt{\lambda}$			
	$\tilde{R}$ = 0.0			
	$\theta = 0°$	$\theta = 30°$	$\theta = 60°$	$\theta = 90°$
0	3.516	3.516	3.516	3.516
1	3.543	3.578	3.647	3.681
2	3.621	3.757	4.014	4.137
3	3.744	4.033	4.557	4.797
4	3.898	4.381	5.214	5.585
5	4.074	4.780	5.945	6.449
6	4.263	5.213	6.721	7.360
7	4.459	5.669	7.526	8.299
8	4.657	6.139	8.348	9.256
9	4.854	6.619	9.182	10.225
10	5.049	7.106	10.024	11.202

Table 2.4 : Variation of Fundamental Frequency for $\tilde{R} = 1.0$ and Various Values of Setting Angle

Angular Velocity α	Natural Frequency $\eta = p \sqrt{\lambda}$			
	$\tilde{R} = 1.0$			
	$\theta = 0°$	$\theta = 30°$	$\theta = 60°$	$\theta = 90°$
0	3.516	3.516	3.516	3.516
1	3.731	3.764	3.829	3.862
2	4.370	4.483	4.699	4.805
3	5.253	5.462	5.859	6.046
4	6.266	6.577	7.158	7.430
5	7.349	7.762	8.526	8.8884
6	8.469	8.983	9.312	10.373
7	9.609	10.226	11.357	11.883
8	10.763	11.480	12.794	13.403
9	11.925	12.743	14.239	14.931
10	13.092	14.011	15.689	16.4658

Table 2.5 : Variation of Fundamental Frequency for $\tilde{R}$ = 10.0 and Various Values of Setting Angle

Angular Velocity α	Natural Frequency $\eta = p\sqrt{\lambda}$			
	$\tilde{R}$ = 10.0			
	$\theta = 0°$	$\theta = 30°$	$\theta = 60°$	$\theta = 90°$
0	3.516	3.516	3.516	3.516
1	5.278	5.301	5.348	5.371
2	8.603	8.661	8.775	8.832
3	12.223	12.314	12.495	12.584
4	15.918	16.043	16.289	16.412
5	19.642	19.800	20.112	20.266
6	23.381	23.572	23.949	24.136
7	27.129	27.354	27.797	28.016
8	30.887	31.143	31.652	31.902
9	34.649	34.939	35.513	35.796
10	38.417	38.740	39.738	39.694

Table 2.6 : Variation of Second Natural Frequency for $\tilde{R} = 0.0$ and Various Values of Setting Angle

Angular Velocity α	Natural Frequency $\eta = p \sqrt{\lambda}$			
	$\tilde{R} = 0.0$			
	$\theta = 0°$	$\theta = 30°$	$\theta = 60°$	$\theta = 90°$
0	22.035	22.035	22.035	22.035
1	22.138	22.186	22.198	22.206
2	22.417	22.429	22.496	22.687
3	23.109	23.187	23.264	23.311
4	23.832	24.045	24.181	24.264
5	24.741	25.066	25.213	25.463
6	26.108	26.292	26.512	26.810
7	27.348	27.670	28.104	28.326
8	28.702	29.178	29.620	29.988
9	30.365	30.795	31.346	31.766
10	32.109	32.505	33.164	33.630

Table 2.7 : Variation of Second Natural Frequency for $\tilde{R}$ = 1.0 and Various Values of Setting Angle

Angular Velocity α	Natural Frequency $\eta = p \sqrt{\lambda}$			
	$\tilde{R}$ = 1.0			
	$\theta = 0°$	$\theta = 30°$	$\theta = 60°$	$\theta = 90°$
0	22.035	22.035	22.035	22.035
1	22.343	22.347	22.360	22.366
2	23.271	23.282	23.335	23.357
3	24.737	24.744	24.873	24.918
4	26.651	26.715	26.872	26.974
5	28.918	29.015	29.237	29.380
6	31.456	31.587	31.868	32.025
7	34.206	34.320	34.739	34.914
8	37.113	37.436	37.753	37.964
9	40.140	40.381	40.864	410136
10	43.260	43.492	44.109	44.401

Table 2.8 : Variation of Second Natural Frequency for $\tilde{R}$ = 10.0 and Various Values of Setting Angle

Angular Velocity α	Natural Frequency $\eta = p\sqrt{\lambda}$			
	$\tilde{R}$ = 10.0			
	$\theta = 0°$	$\theta = 30°$	$\theta = 60°$	$\theta = 90°$
0	22.035	22.035	22.035	22.035
1	24.014	24.011	24.022	24.026
2	29.149	29.136	29.201	29.218
3	36.034	36.062	36.128	36.159
4	43.795	43.831	43.832	43.968
5	52.008	52.004	52.167	52.247
6	60.476	60.621	60.682	60.762
7	69.102	69.180	69.357	69.455
8	77.835	77.925	78.122	78.245
9	86.643	86.742	86.866	87.109
10	95.509	95.619	95.832	96.030

Table 2.9 : Theoretical Natural Frequencies of the Standstill Blade (rad/sec)

Mode Number	1	2	3
Uncorrected Classical Value P_s	5654.07	35436.00	99231.82
Corrected for Shear and Rotary Inertia Effects [98]	5608.84	33664.20	87323.28

Table 2.10 : Comparison of Rotating Blade Frequencies

$P_R^2 = (P_T / P_S)^2$

$$= \frac{\text{Theoretical Frequency of Rotating blade}}{\text{Classical Uncorrected Frequency (Standstill blade)}}$$

ω = 540.35 rad/sec

R = 2.86743

Mode Number	θ	Present Results $(P_R)^2$	[6] $(P_R)^2$	[99] Neglecting Shear and Rotary Inertia
1	0.0	1.026794	1.036679	1.0523
2	0.0	0.910737	0.911519	1.0073
3	0.0	0.804313	0.816706	1.0027
1	47.7	1.031798	1.032815	1.0482
2	47.7	0.910863	0.911519	1.0072
3	47.7	0.804329	0.816706	1.0027

Table 2.11 : Effect Of Shear Deflection and Rotary Inertia on the Natural Frequency

Setting Angle $\theta = 90°$ Angular Velocity $\alpha = 0$ Hub Radius $R = 0.0$ $r^2 = 8.2686 \times 10^{-4}$ $\sigma = 2.4329 \times 10^{-3}$ Present Results = P.R. (inclusion of Rotary Inertia and Shear deflection)							
Natural Frequency							
Mode 1		Mode 2		Mode 3		Mode 4	
P.R.	[15]	P.R.	[15]	P.R.	[15]	P.R.	[15]
3.48	3.48	20.96	22.02	55.28	61.63	100.67	120.42
Setting Angle $\theta = 90°$ Angular Velocity $\alpha = 10$ Hub Radius $R = 0.0$ $r^2 = 8.2686 \times 10^{-4}$ $\sigma = 2.4329 \times 10^{-3}$ Present Results = P.R.							
P.R.	[15]	P.R.	[15]	P.R.	[15]	P.R.	[15]
11.1	11.2	32.53	33.63	68.58	74.60	115.74	134.36

Table 2.12 : Variation of Natural Frequency for $\tilde{R} = 0$; α_1=1.0 and Various Values of Setting Angle

Angular Velocity α	Natural Frequency $\eta = p \sqrt{\lambda}$					
	$\tilde{R} = 0.0$; $\alpha_1 = 1.0$					
	$\theta = 0°$			$\theta = 90°$		
	0,0	0,1	0,2	0,0	0,1	0,2
0	3.49	8.55	21.47	3.49	8.55	21.47
1	3.51	8.55	21.59	3.66	8.67	21.62
2	3.60	8.57	21.94	4.12	9,03	22.05
3	3.72	8.60	22.52	4.78	9.59	22.75
4	3.88	8.64	23.29	5.57	10.33	23.69
5	4.06	8.69	24.23	6.44	11.21	24.86
6	4.25	8.75	25.32	7.35	12.19	26.21
7	4.45	8.82	26.49	8.29	13.26	27.71
8	4.65	8.89	27.69	9.25	14.39	29.35
9	4.85	8.97	28.78	10.22	15.57	31.09
10	5.05	9.06	29.64	11.20	16.80	32.91

Table 2.13 : Variation of Natural Frequency for $\tilde{R}$ = 1.0 ; α_1= 4.0 and Various Values of Setting Angle

Angular Velocity α	Natural Frequency $\eta = p\sqrt{\lambda}$					
	$\tilde{R}$ = 1.0 ; α_1 = 4.0					
	θ = 0°			θ = 90°		
	0,0	0,1	0,2	0,0	0,1	0,2
0	3.43	21.49	27.69	3.43	21.49	27.69
1	3.68	21.81	27.72	3.81	21.83	27.76
2	4.34	22.75	27.82	4.78	22.83	27.96
3	5.24	24.23	27.99	6.04	24.41	28.31
4	6.28	26.16	28.21	7.45	26.46	28.78
5	7.39	28.46	28.50	8.92	28.89	29.37
6	8.53	28.85	31.03	10.43	30.07	31.60
7	6.70	29.26	33.82	11.96	30.88	34.54
8	10.88	29.71	36.77	13.51	31.79	37.63
9	12.07	30.22	39.85	15.06	32.79	40.86
10	13.27	30.77	43.03	16.62	33.87	44.18

Table 2.14 : Variation of Natural Frequency for $\tilde{R}$ = 5.0; α_1= 4.0 and Various Values of Setting Angle

Angular Velocity α	Natural Frequency $\eta = p\sqrt{\lambda}$					
	$\tilde{R} = 5.0$; $\alpha_1 = 4.0$					
	$\theta = 0°$			$\theta = 90°$		
	0,0	0,1	0,2	0,0	0,1	0,2
0	3.43	21.49	27.69	3.43	21.49	27.69
1	4.45	22.56	27.85	4.56	22.60	27.88
2	6.61	25.56	28.31	6.91	25.64	28.45
3	9.11	29.06	29.87	9.59	29.37	30.02
4	11.71	30.08	35.02	12.38	30.61	35.25
5	14.36	31.33	40.68	15.21	32.12	40.98
6	17.23	32.77	46.65	18.06	33.85	47.03
7	19.72	34.38	52.82	20.92	35.78	52.28
8	22.41	36.14	59.12	23.80	37.86	59.66
9	25.12	38.00	55.51	26.68	40.08	66.12
10	27.83	39.97	71.95	29.57	42.41	72.64

Table 2.15 : Variation of Natural Frequency for $\tilde{R}$ = 10.0; α_1= 4.0 and Various Values of Setting Angle

Angular Velocity α	Natural Frequency $\eta = p\sqrt{\lambda}$					
	$\tilde{R}$ = 10.0 ; α_1 = 4.0					
	$\theta = 0°$			$\theta = 90°$		
	0,0	0,1	0,2	0,0	0,1	0,2
0	3.43	21.49	27.69	3.43	21.49	27.69
1	5.26	23.50	27.99	5.35	23.52	28.04
2	8.63	28.69	28.91	8.86	28.76	29.05
3	12.31	30.35	35.68	12.67	30.64	35.80
4	16.06	32.23	43.59	16.55	32.72	43.77
5	19.85	34.47	51.97	20.47	35.59	52.21
6	23.65	36.99	60.62	24.41	37.95	60.92
7	27.47	39.73	69.42	28.35	40.94	69.74
8	33.30	42.64	78.31	32.31	44.11	78.72
9	35.14	45.68	87.25	36.28	47.42	87.71
10	38.98	48.83	96.22	40.25	50.83	96.74

Table 2.16 : Comparison of Rotating Plate Frequencies

	Setting Angle	$\theta = 0°$
	Angular Velocity	$\alpha = 3.472$
	Hub Radius	$\tilde{R} = 0.0$
	Aspect Ratio	$\alpha_1 = 1.0$
	Natural Frequency	
Mode Number	Present Results	[39] 3 x 3 mesh
1	5.142	5.091
2	9.919	9.902
3	23.166	23.182
	Setting Angle	$\theta = 45°$
	Angular Velocity	$\alpha = 3.472$
	Hub Radius	$\tilde{R} = 1.0$
	Aspect Ratio	$\alpha_1 = 1.0$
Mode Number	Present	[39] 3 x 3 mesh
1	10.822	10.826
2	14.158	13.864
3	32.230	29.212

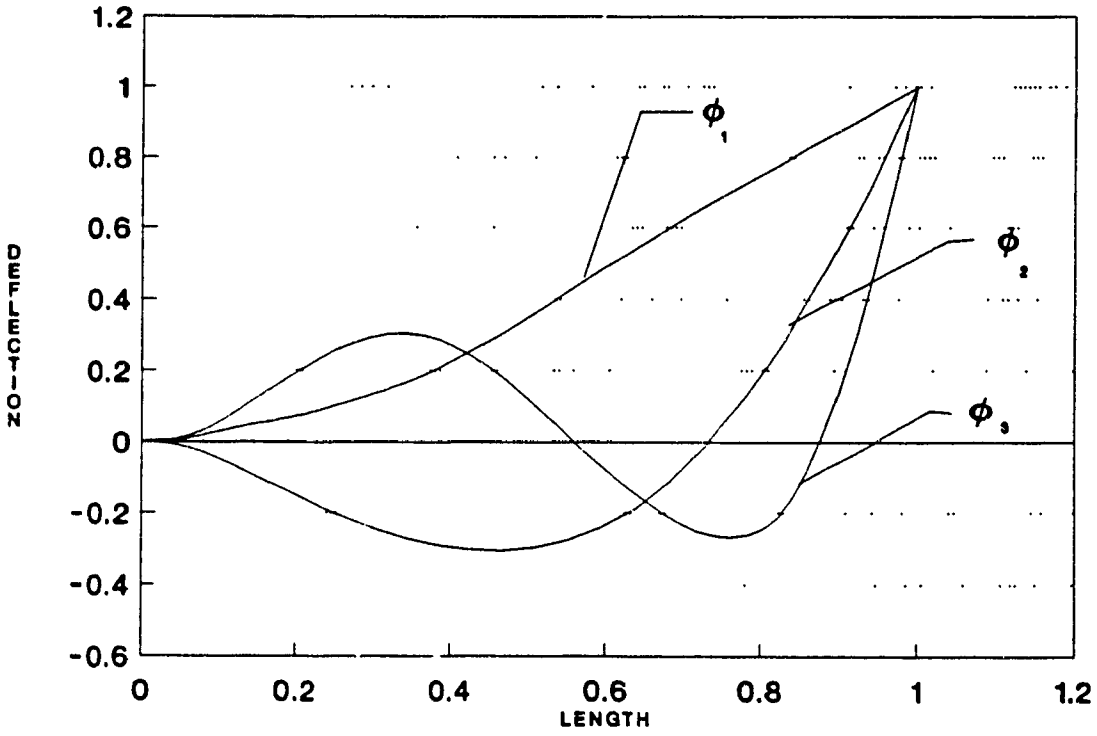

Fig. 2.6 : Orthogonal Polynomial Deflection Functions for Clamped- free beam

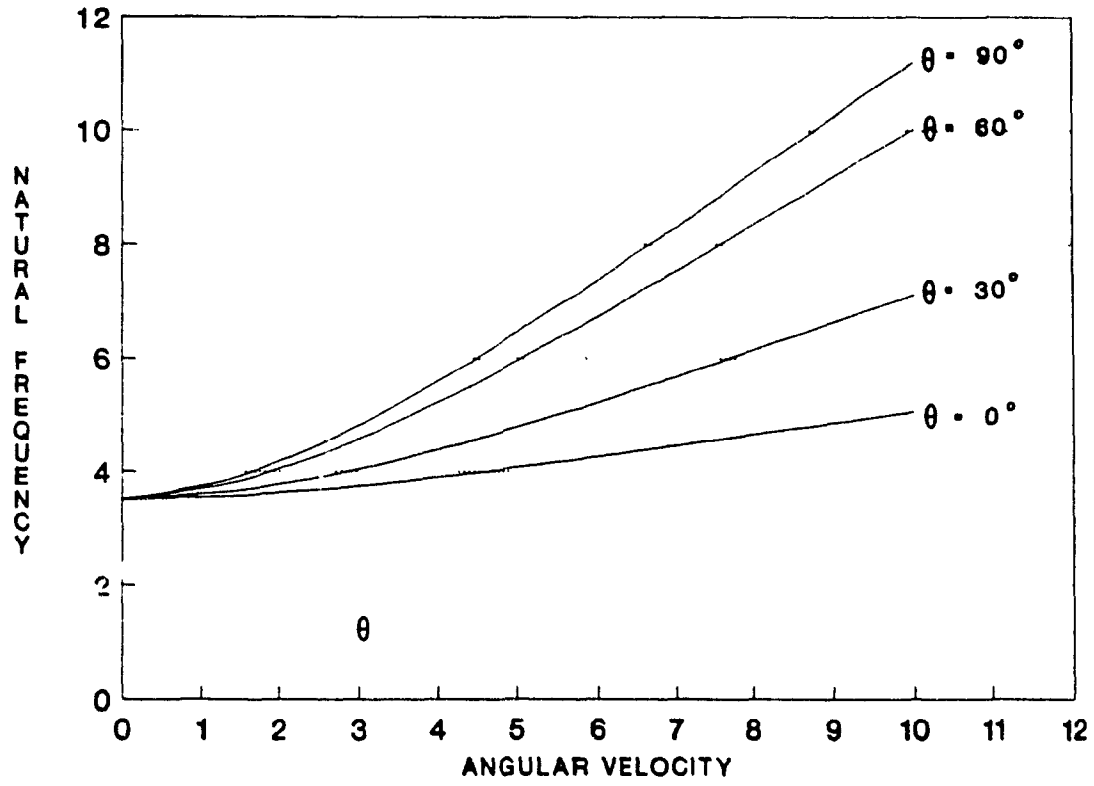

Fig. 2.7 : Variation of First Natural Frequency with Speed for Different Setting Angles (R = 0.0)

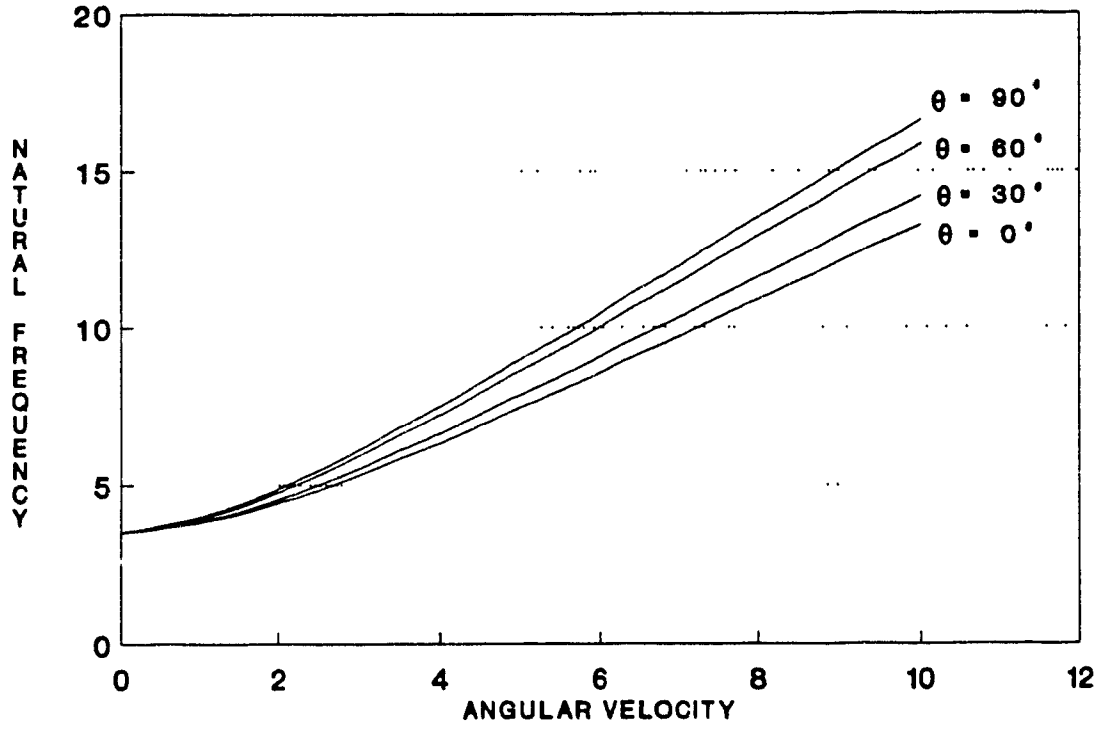

Fig. 2.8 : Variation of First Natural Frequency With Speed For Different Setting Angles (R = 1.0)

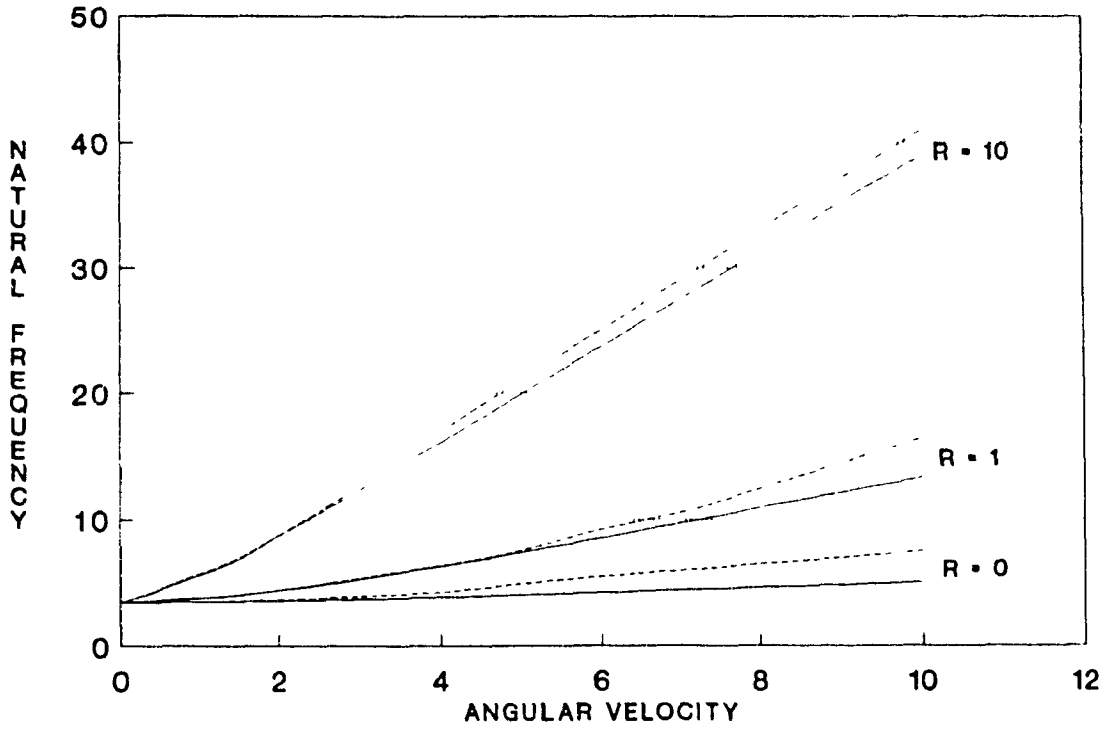

Fig. 2.9 : Variation of First Natural Frequency With Speed for Different Hub Radii ($\theta = 0^{c}$)

(----- [18])

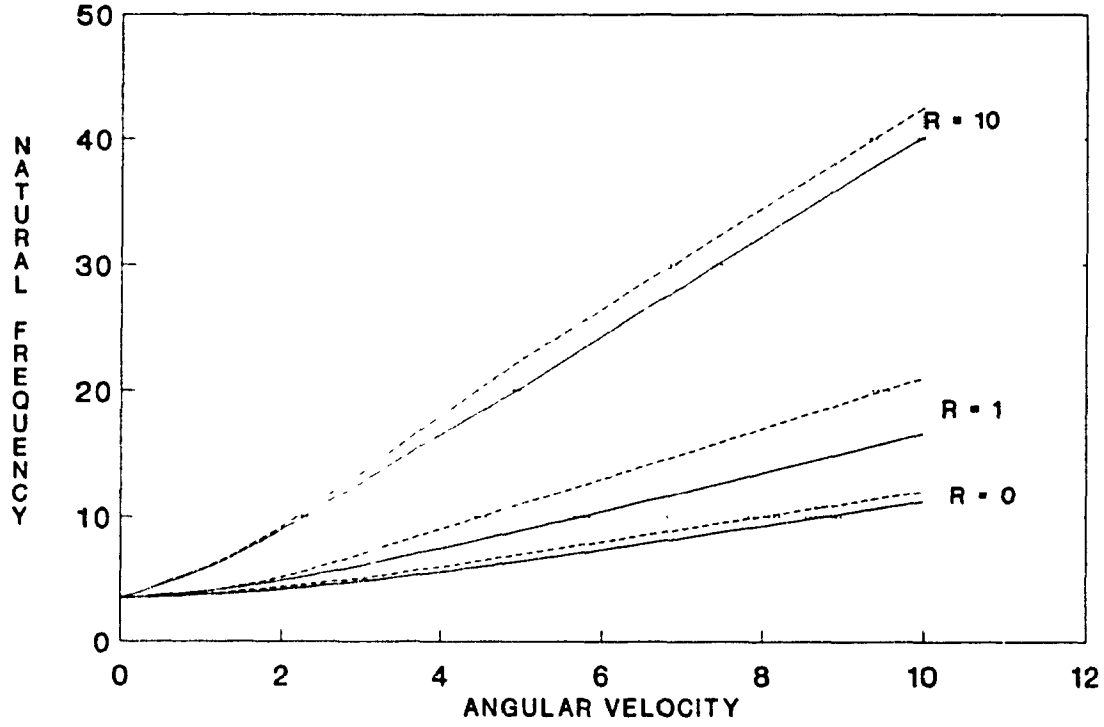

Fig 2.10 : Variation of First Natural Frequency With Speed for Different Hub Radii (θ = 90°)

(---- [18])

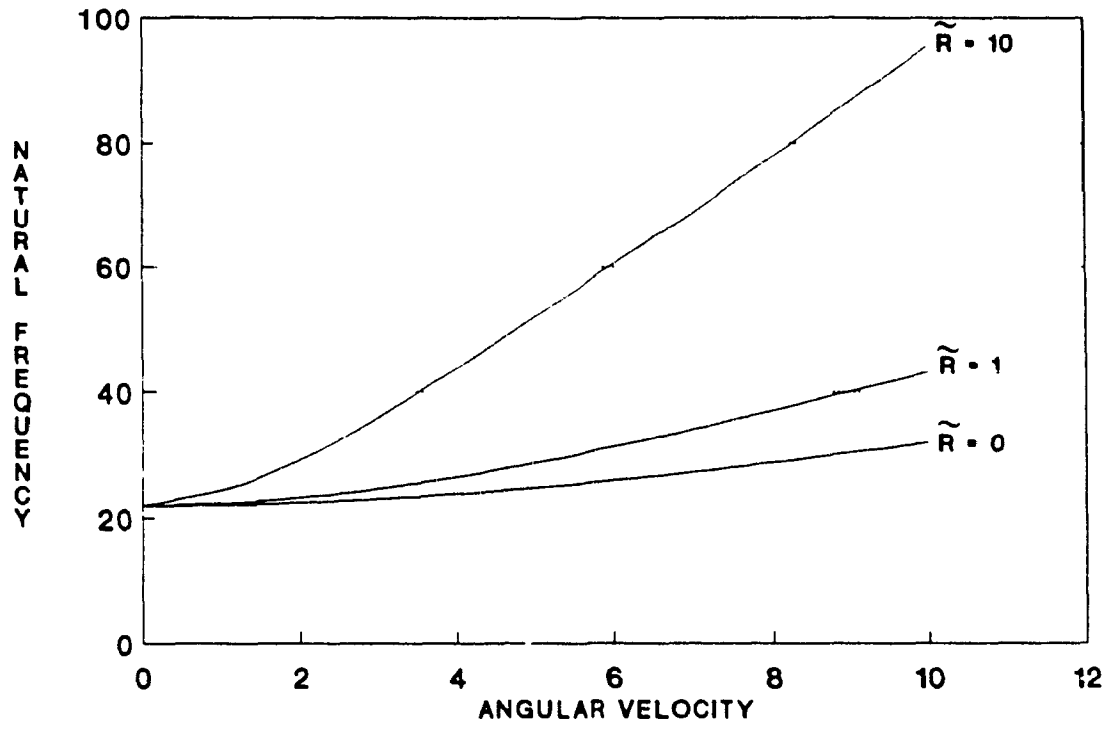

Fig. 2.11 : Variation of Second Natural Frequency with Speed for Various Hub Radii ($\theta = 0°$)

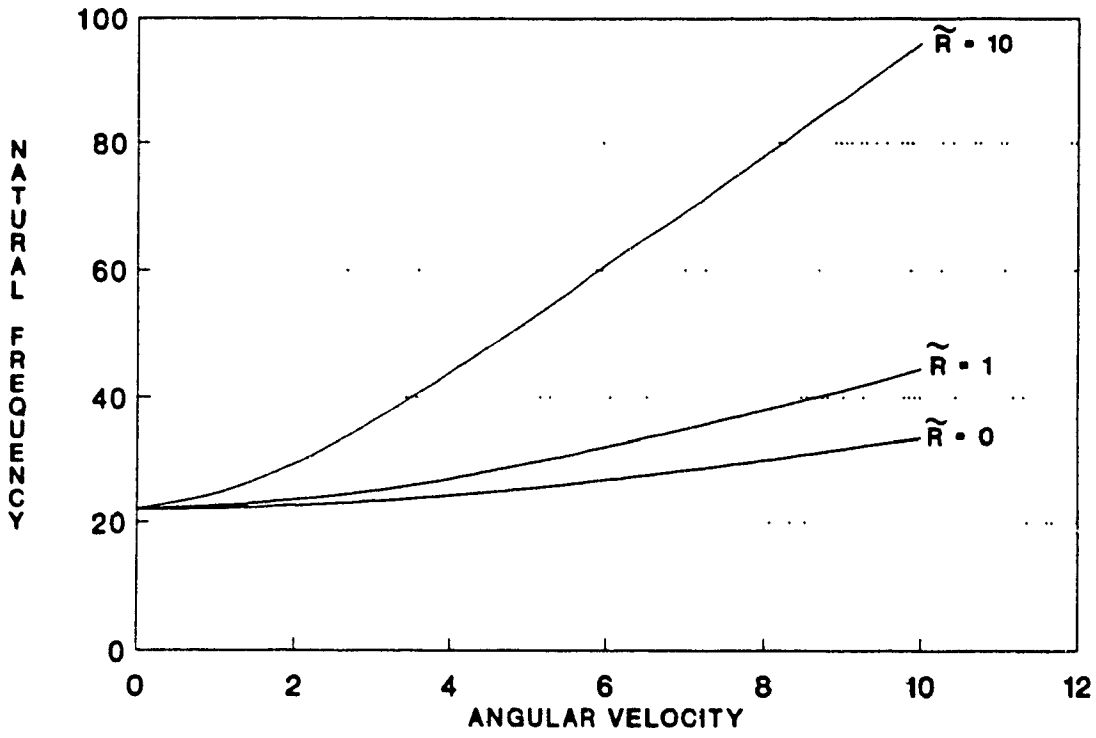

Fig.2.12 : Variation of Second Natural Frequency with Speed for Various Hub Radii ($\theta = 90°$)

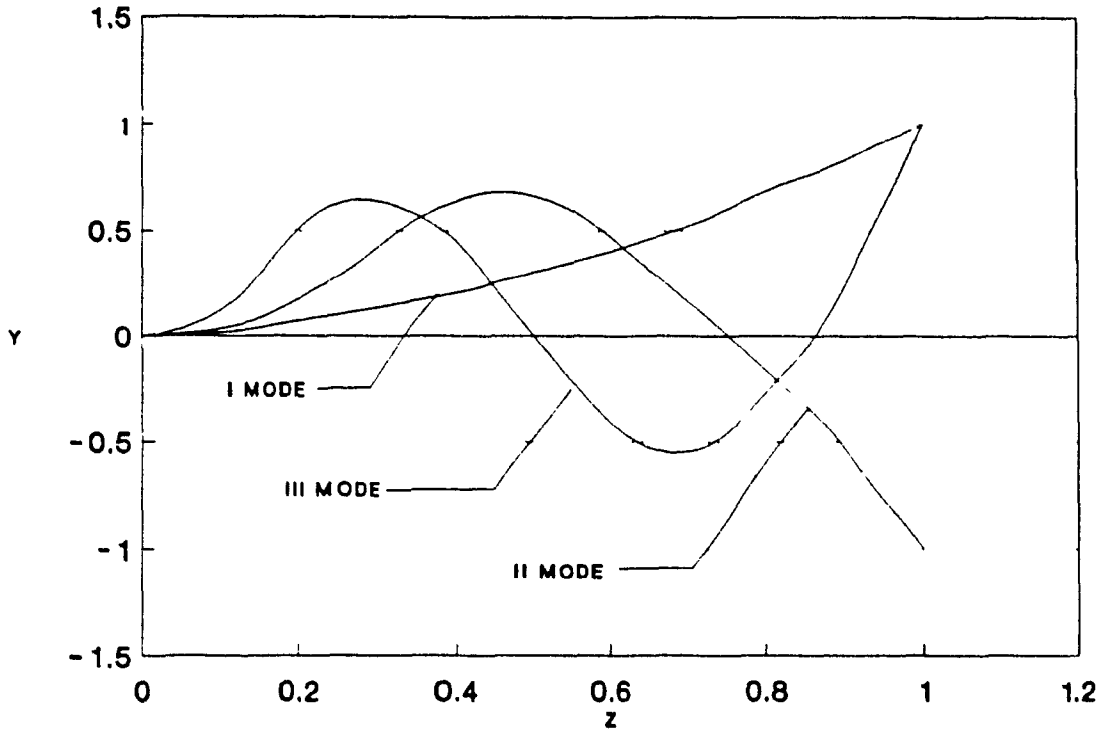

Fig 2.13 : Flexural Mode Shapes for the Standstill Blade

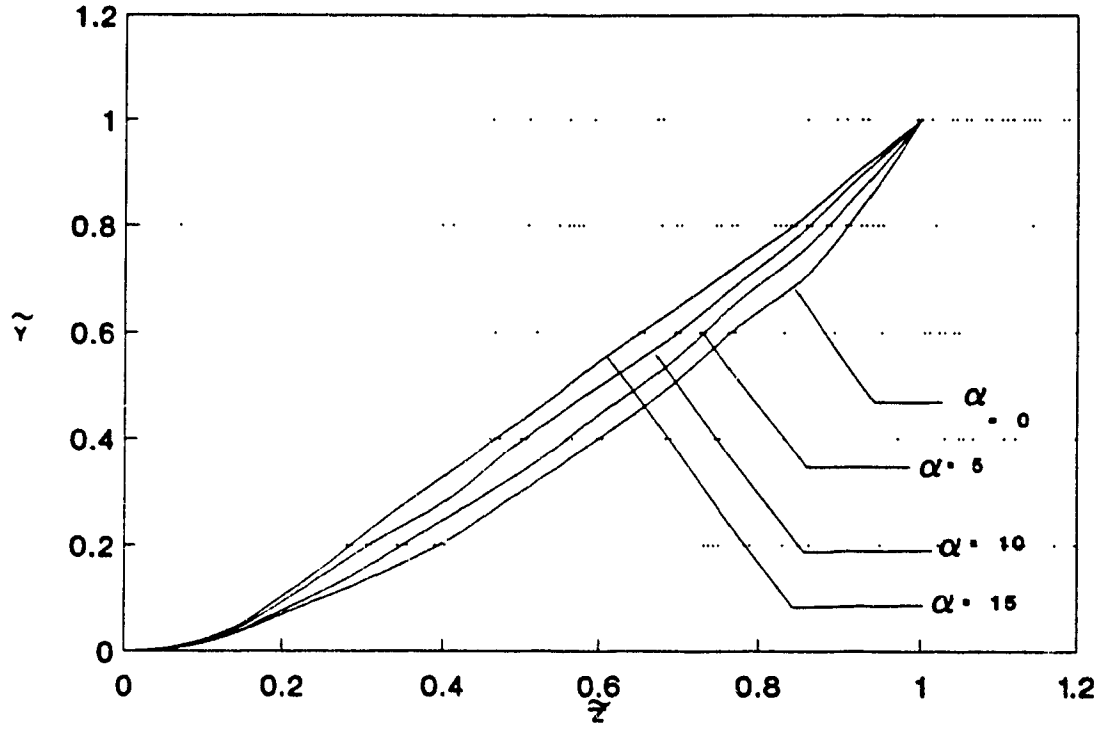

Fig. 2.14 : Variation of First Mode Shape with Speed
($\tilde{R}$ = 0.0 θ = 90°)

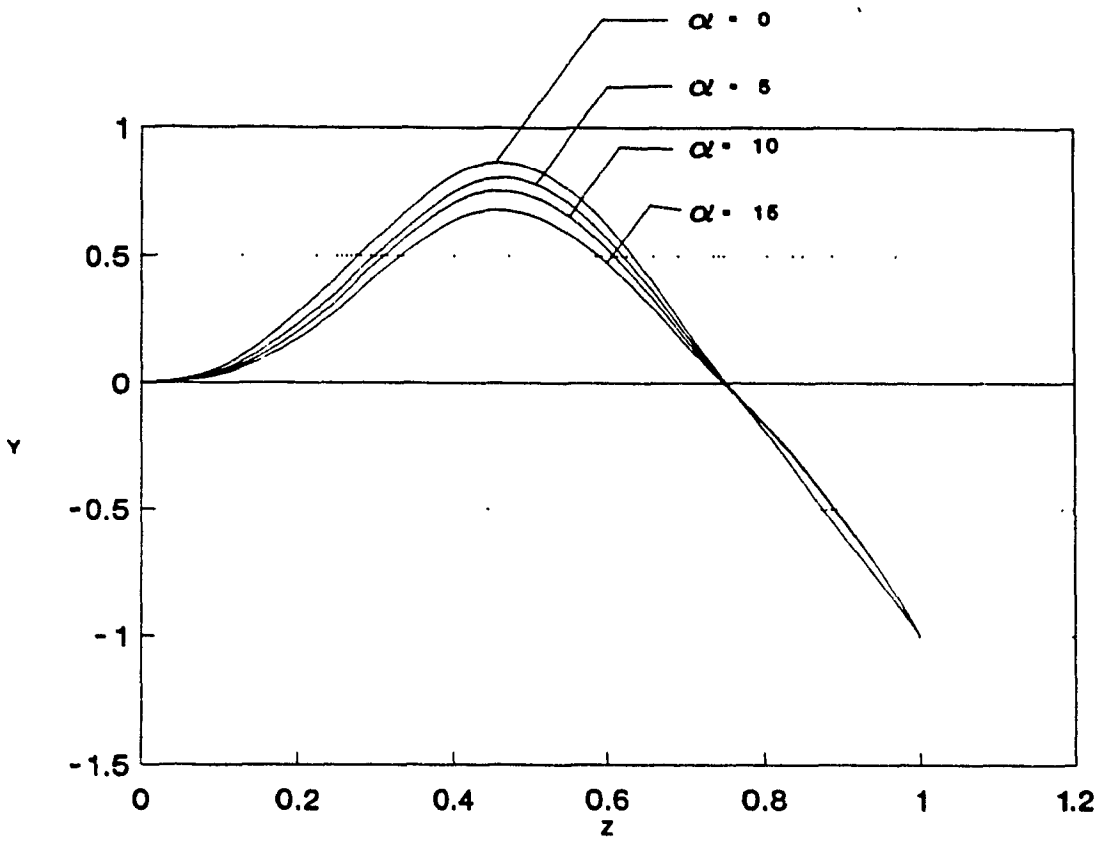

Fig. 2.15 : Variation of Second Mode Shape with Speed
($\tilde{R}$ = 0.0 θ = 90°)

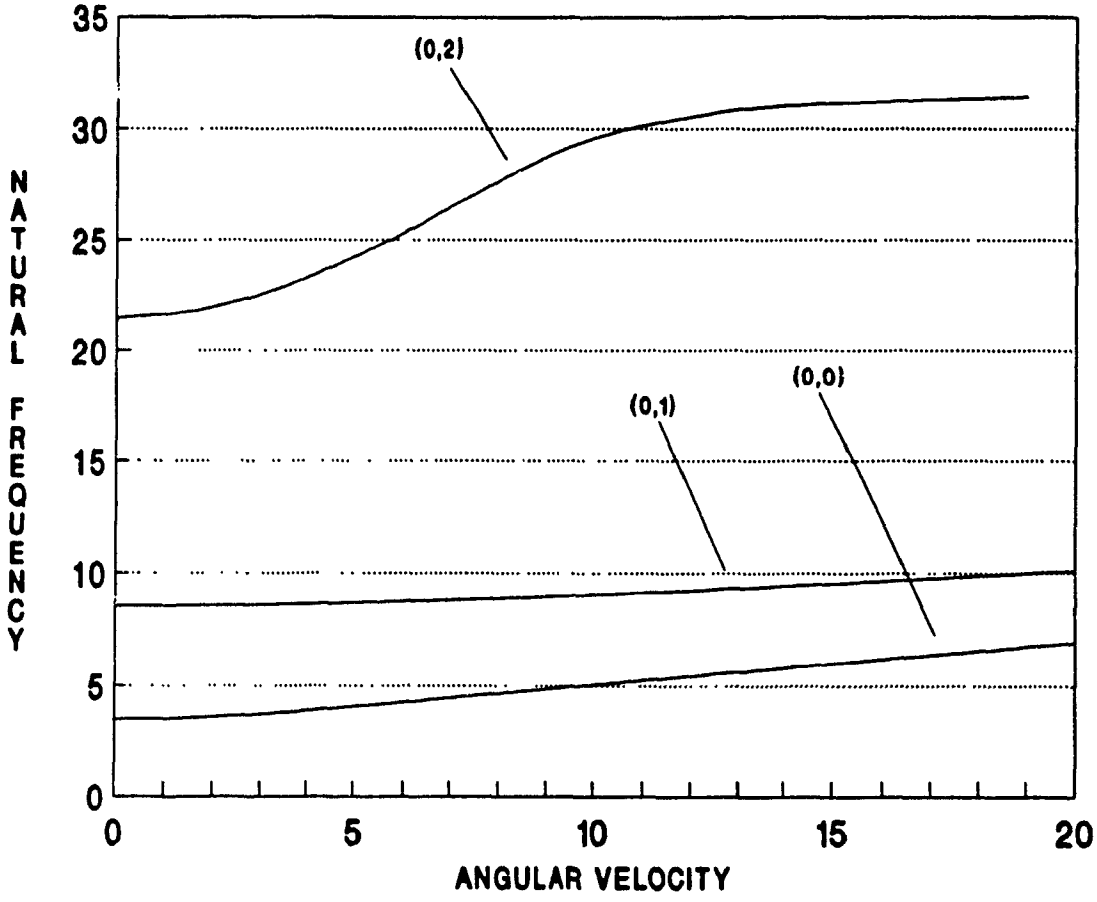

Fig. 2.16 : Variation of Plate Frequency with Speed

($\tilde{R}$ = 0.0 ; α_1 = 1.0 ; θ = 0°)

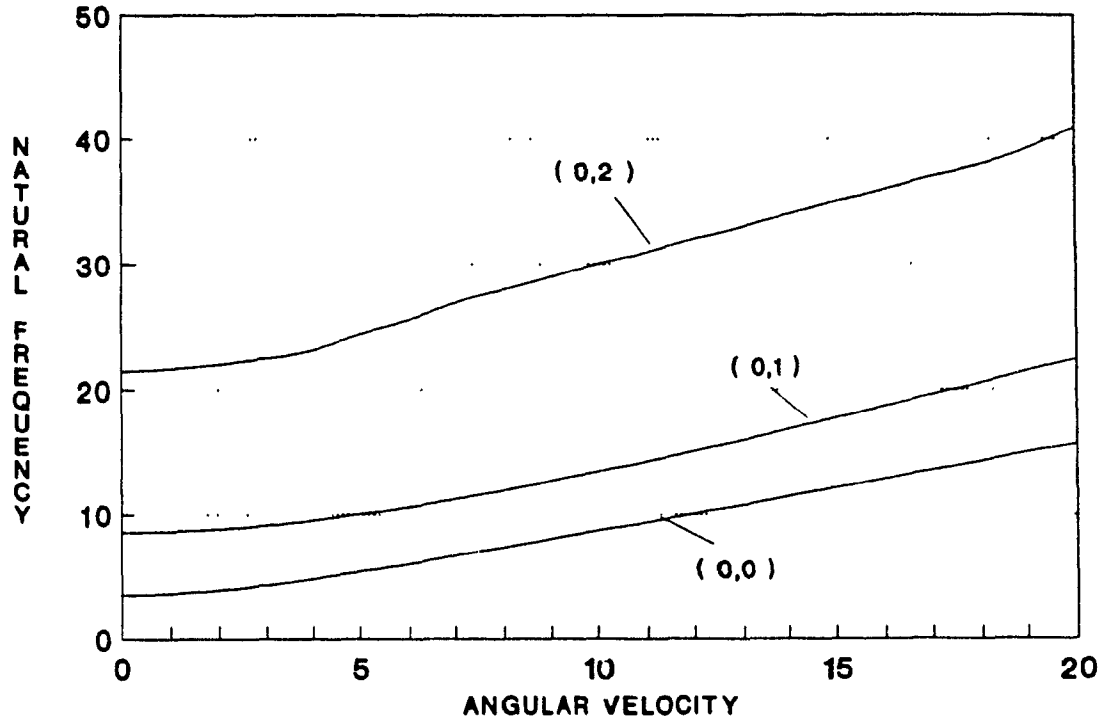

Fig 2.17 : Variation of Plate Natural Frequency with Speed

($\tilde{R}$ = 0.0 ; α_1 = 1.0 ; θ = 45°)

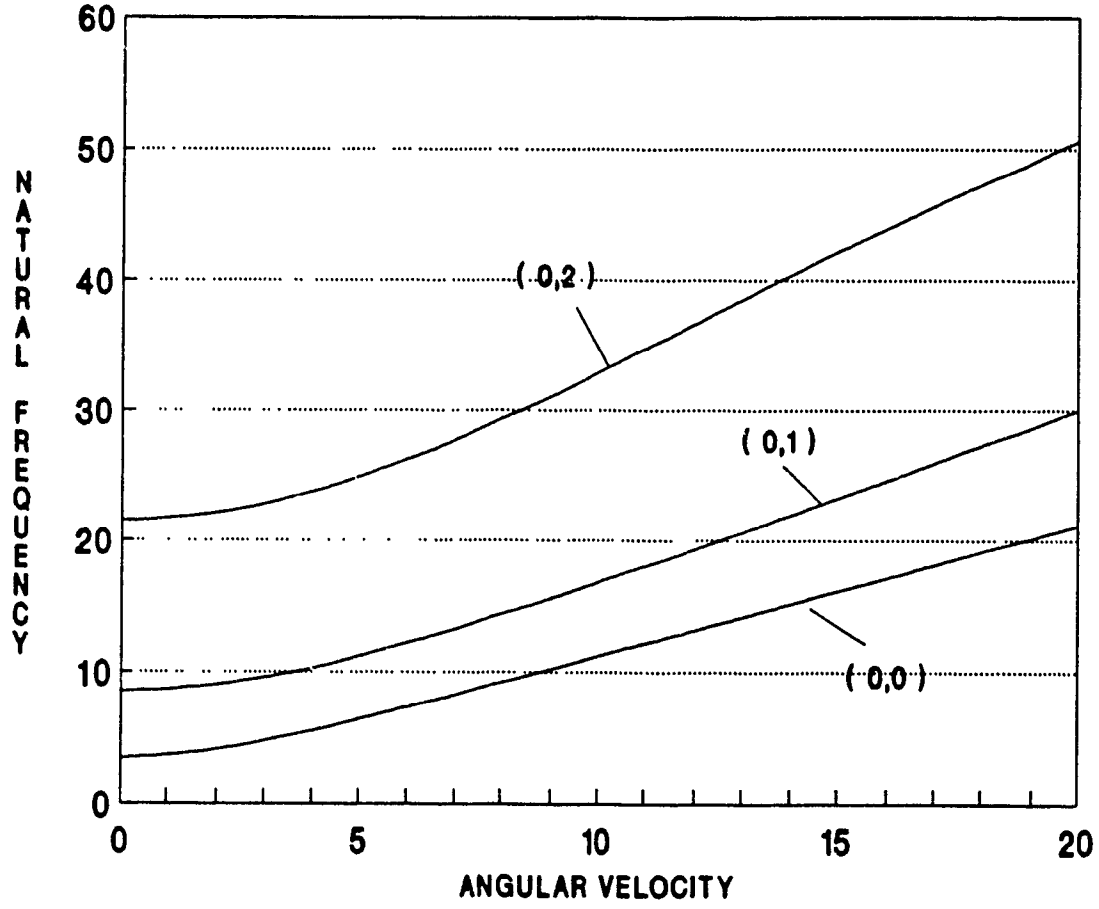

Fig 2.18 : Variation of Plate Natural Frequency with Speed

($\tilde{R}$ = 0.0 ; α_1 = 1.0 ; θ = 90°)

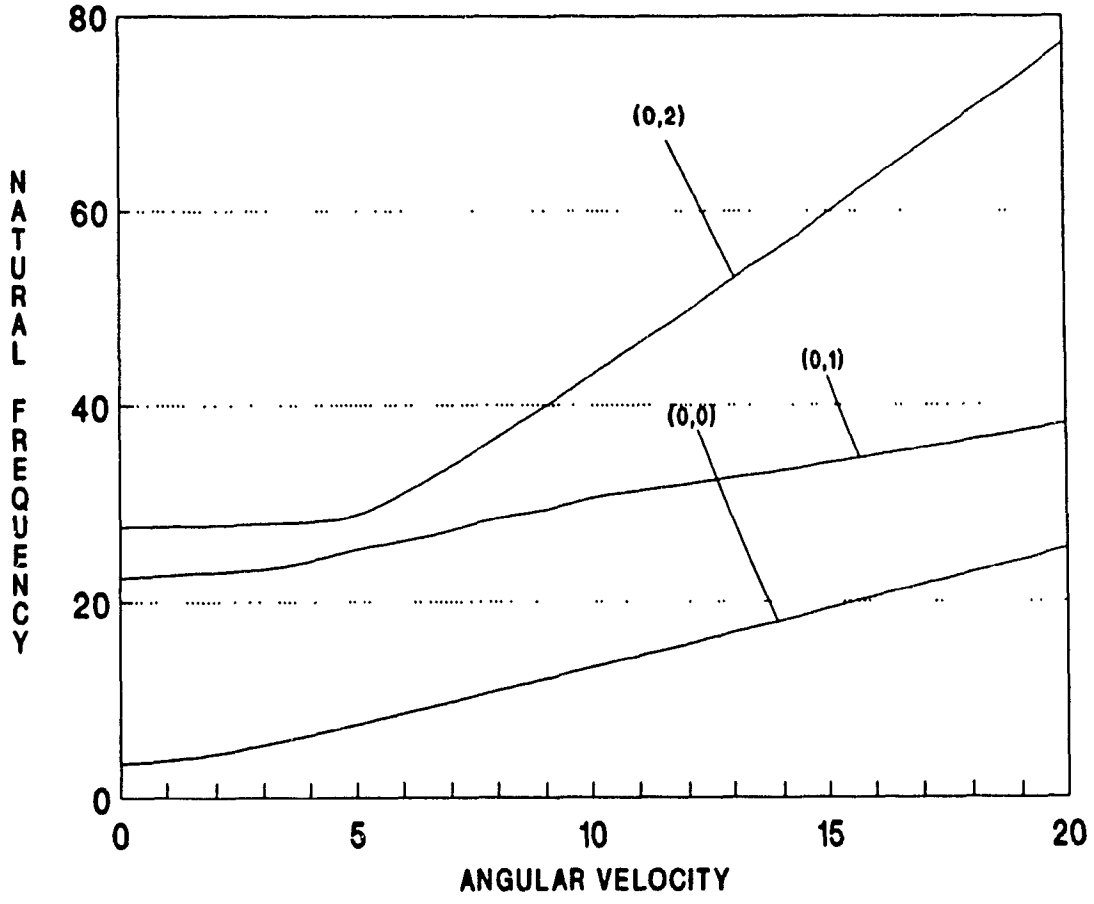

Fig 2.19 : Variation of Plate Natural Frequency with Speed

($\widetilde{R}$ = 1.0 ; α_1 = 4.0 ; θ = 0°)

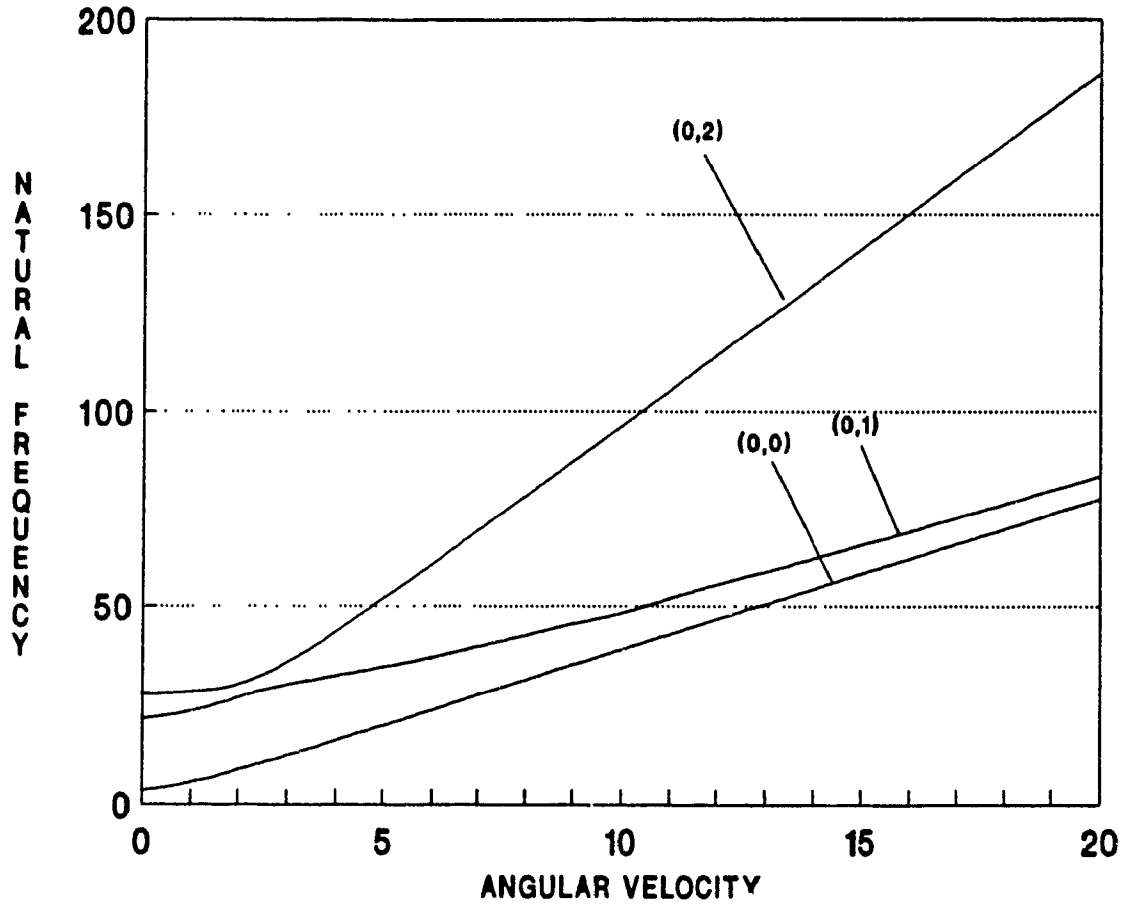

Fig. 2.20 : Variation of Plate Natural Frequency with Speed

($\tilde{R}$ = 10.0 ; α_1 = 4.0 ; θ = 0°)

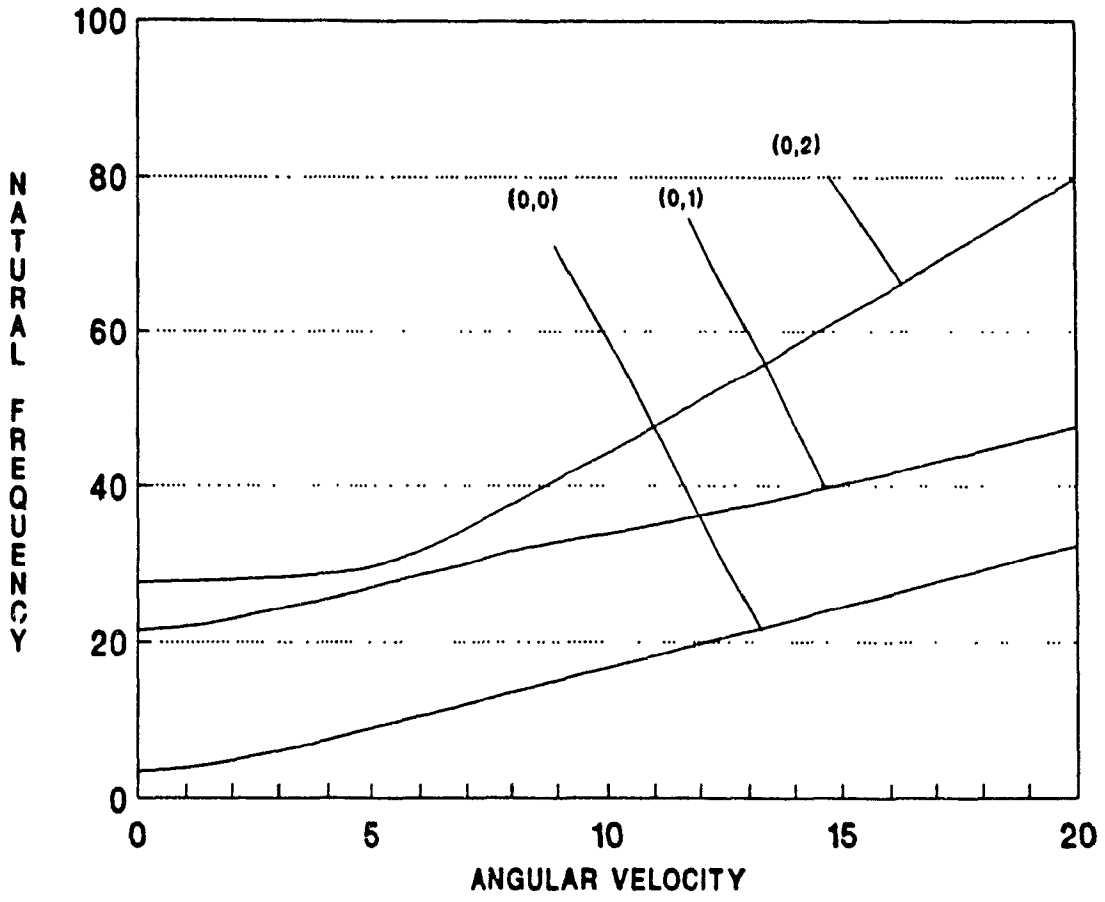

Fig. 2.21 : Variation of Plate Natural Frequency with Speed

($\tilde{R}$ = 1.0 ; α_1 = 4.0 ; θ = 90°)

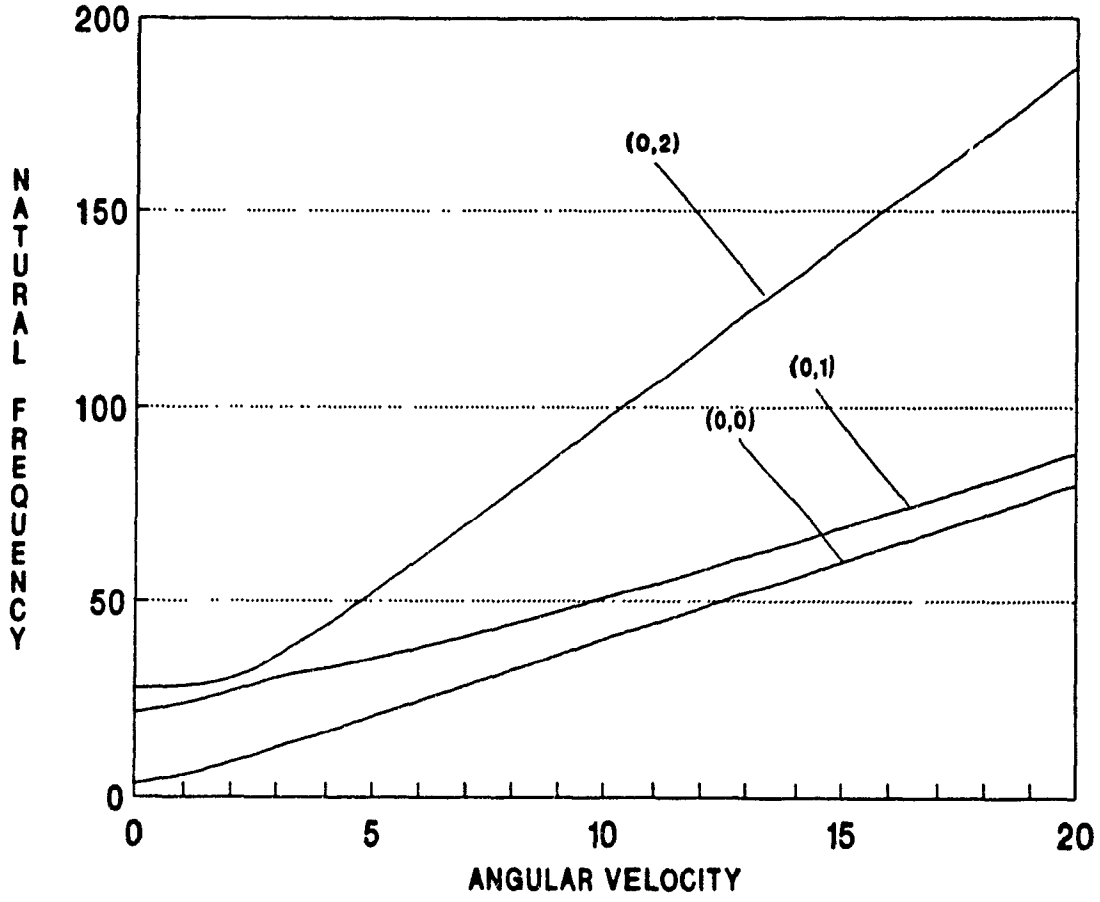

Fig. 2.22 : Variation of Plate Natural Frequency with Speed

($\hat{k} = 10.0$; $\alpha_1 = 4.0$; $\theta = 90°$)

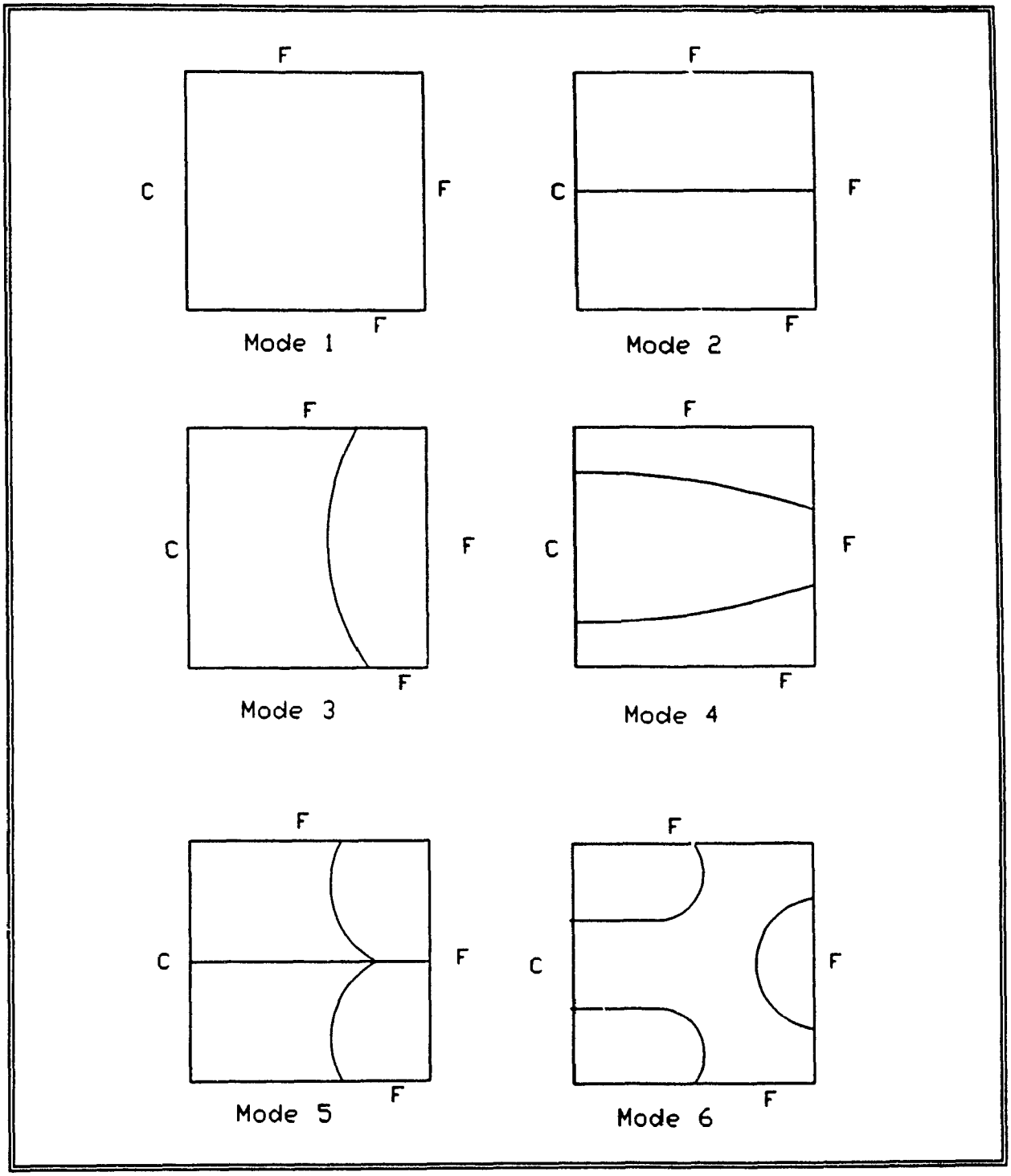

Figure 2.23 : Nodal Lines for Cantilevered Plate

CHAPTER 3

DYNAMIC ANALYSIS OF ROTATING DISKS

3.1 : General

The blades in a turbine or impeller are mounted on a disk and hence the disk is a key component of turbo-machinery. A successful design of the disk necessitates a good understanding of its vibrational characteristics . The natural frequency of free vibrations of a rotating disk will be different from those under non-rotating conditions because of the additional stiffening of the disk due to rotation.

In this chapter free vibrational behaviour of a rotating disk with radially varying thickness exhibiting axisymmetrical and nonaxisymmetrical vibrations is studied. Beam Characteristic Orthogonal polynomials are employed as deflection functions in the Rayleigh-Ritz method to obtain their natural frequencies. The variation of natural frequencies with speed of rotation is obtained for several parameter combinations such as the ratio of inner/outer radii, ratio of inner/outer thickness.

3.2 Analysis

The potential and the kinetic energy expressions for the rotating disk can be obtained in polar coordinates by

transforming the corresponding energy expressions for the rotating rectangular plate, derived in Eqs. (2.77) and (2.90) in Chapter 2. By taking the coordinates shown in Fig.3.1 a small increment dx along x direction can be expressed in the radial and angular coordinates as,

$$dr = dx\cos\theta, \quad d\theta = -\frac{dx\sin\theta}{r} \tag{3.1}$$

Considering the deflection w as a function of r and θ, the slope along the x direction can be expressed in r and θ coordinates as,

$$\frac{dw}{dx} = \frac{\partial w}{\partial r}\frac{\partial r}{\partial x} + \frac{\partial w}{\partial \theta}\frac{\partial \theta}{\partial x} = \frac{\partial w}{\partial r}\cos\theta - \frac{\partial w}{\partial \theta}\frac{\sin\theta}{r} \tag{3.2}$$

Similarly, the slope along the y direction can be expressed in r and θ coordinates as,

$$\frac{\partial w}{\partial y} = \frac{\partial w}{\partial r}\sin\theta + \frac{\partial w}{\partial \theta}\frac{\cos\theta}{r} \tag{3.3}$$

The second derivatives of w with resect to x and y are obtained, respectively as,

$$\frac{\partial^2 w}{\partial x^2} = \left(\frac{\partial}{\partial r}Cos\theta - \frac{\partial}{\partial \theta}\frac{\sin\theta}{r}\right)\left(\frac{\partial w}{\partial r}Cos\theta - \frac{\partial w}{\partial \theta}\frac{\sin\theta}{r}\right) \tag{3.4}$$

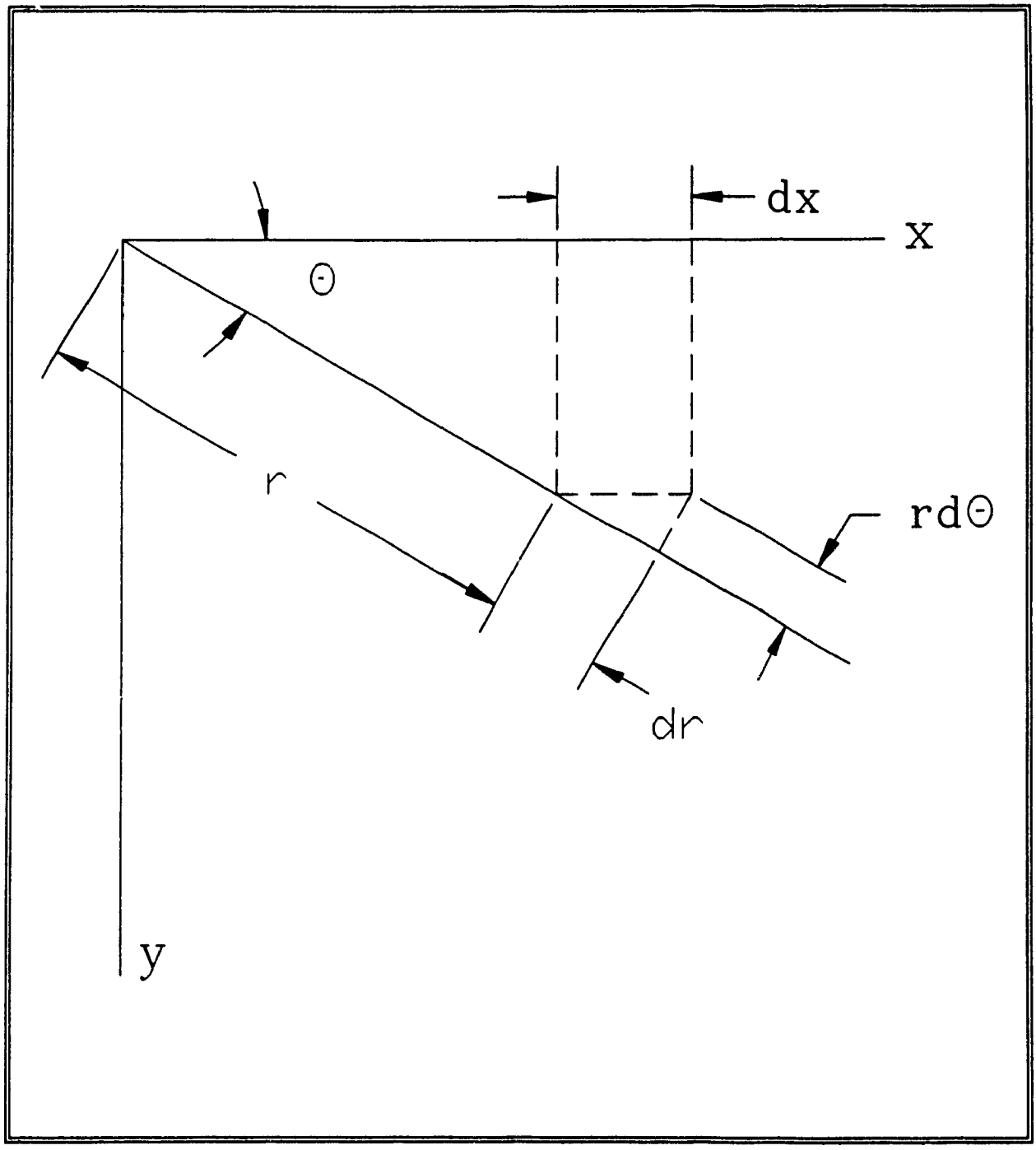

Fig. 3.1 : Transformation of Coordinates from Cartesian to Cylindrical

$$= \frac{\partial^2 w}{\partial r^2}\cos^2\theta - 2\frac{\partial^2}{\partial\theta\partial r}\frac{\sin\theta\cos\theta}{r} + \frac{\partial w}{\partial r}\frac{\sin^2\theta}{r}$$

$$+2\frac{\partial w}{\partial\theta}\frac{\sin\theta\cos\theta}{r^2} + \frac{\partial^2 w}{\partial\theta^2}\frac{\sin^2\theta}{r^2} \qquad (3.5)$$

$$\frac{\partial^2 w}{\partial y^2} = \frac{\partial^2 w}{\partial r^2}\sin^2\theta + 2\frac{\partial^2 w}{\partial\theta\partial r}\frac{\sin\theta\cos\theta}{r} + \frac{\partial w}{\partial r}\frac{\cos^2\theta}{r}$$

$$-2\frac{\partial w}{\partial\theta}\frac{\sin\theta\cos\theta}{r^2} + \frac{\partial^2 w}{\partial\theta^2}\frac{\cos^2\theta}{r^2} \qquad (3.6)$$

$$\frac{\partial^2 w}{\partial x\partial y} = \frac{\partial^2 w}{\partial r^2}\sin\theta\cos\theta + \frac{\partial^2 w}{\partial r\partial\theta}\frac{\cos 2\theta}{r} - \frac{\partial w}{\partial\theta}\frac{\cos 2\theta}{r^2}$$

$$-\frac{\partial w}{\partial r}\frac{\sin\theta\cos\theta}{r} - \frac{\partial^2 w}{\partial\theta^2}\frac{\sin\theta\cos\theta}{r^2}$$

(3.7)

Consequently, the following derivative expressions with respect to x and y appearing in the energy expressions, can be expressed in r and θ coordinates as,

$$\frac{\partial^2 w}{\partial x^2} + \frac{\partial^2 w}{\partial y^2} = \frac{\partial^2 w}{\partial r^2} + \frac{1}{r}\frac{\partial w}{\partial r} + \frac{1}{r^2}\frac{\partial^2 w}{\partial \theta^2}$$

$$\frac{\partial^2 w}{\partial x^2}\frac{\partial^2 w}{\partial y^2} - \left(\frac{\partial^2 w}{\partial x \partial y}\right)^2 = \frac{\partial^2 w}{\partial r^2}\left(\frac{1}{r}\frac{\partial w}{\partial r} + \frac{1}{r^2}\frac{\partial^2 w}{\partial \theta^2}\right) - \left\{\frac{\partial}{\partial r}\left(\frac{1}{r}\frac{\partial w}{\partial \theta}\right)\right\}^2$$

(3.8)

Substituting in Eq. (2.68), the bending strain energy of the disk is expressed in r and θ coordinates as,

$$U_1 = \int_{A_D} \frac{D}{2}\left\{\left(\frac{\partial^2 w}{\partial r^2} + \frac{1}{r}\frac{\partial w}{\partial r} + \frac{1}{r^2}\frac{\partial^2 w}{\partial \theta}\right)^2\right.$$

$$\left. - 2(1-\nu)\frac{\partial^2 w}{\partial r^2}\left(\frac{1}{r}\frac{\partial w}{\partial r} + \frac{1}{r^2}\frac{\partial^2 w}{\partial \theta^2}\right) + 2(1-\nu)\left\{\frac{\partial}{\partial r}\left(\frac{1}{r}\frac{\partial w}{\partial \theta}\right)\right\}^2\right\} dA$$

(3.9)

3.3 Axisymmetrical Vibrations

3.3.1 Analysis

Consider the circular plate depicted in Fig. 3.2 . The total (maximum) potential energy of the rotating circular plate is given by,

$$U = (U_1) + (U_2) \qquad (3.10)$$

where (U_1) corresponds to the potential energy in bending of a standstill disk and (U_2) corresponds to the additional bending energy due to the rotational effects.

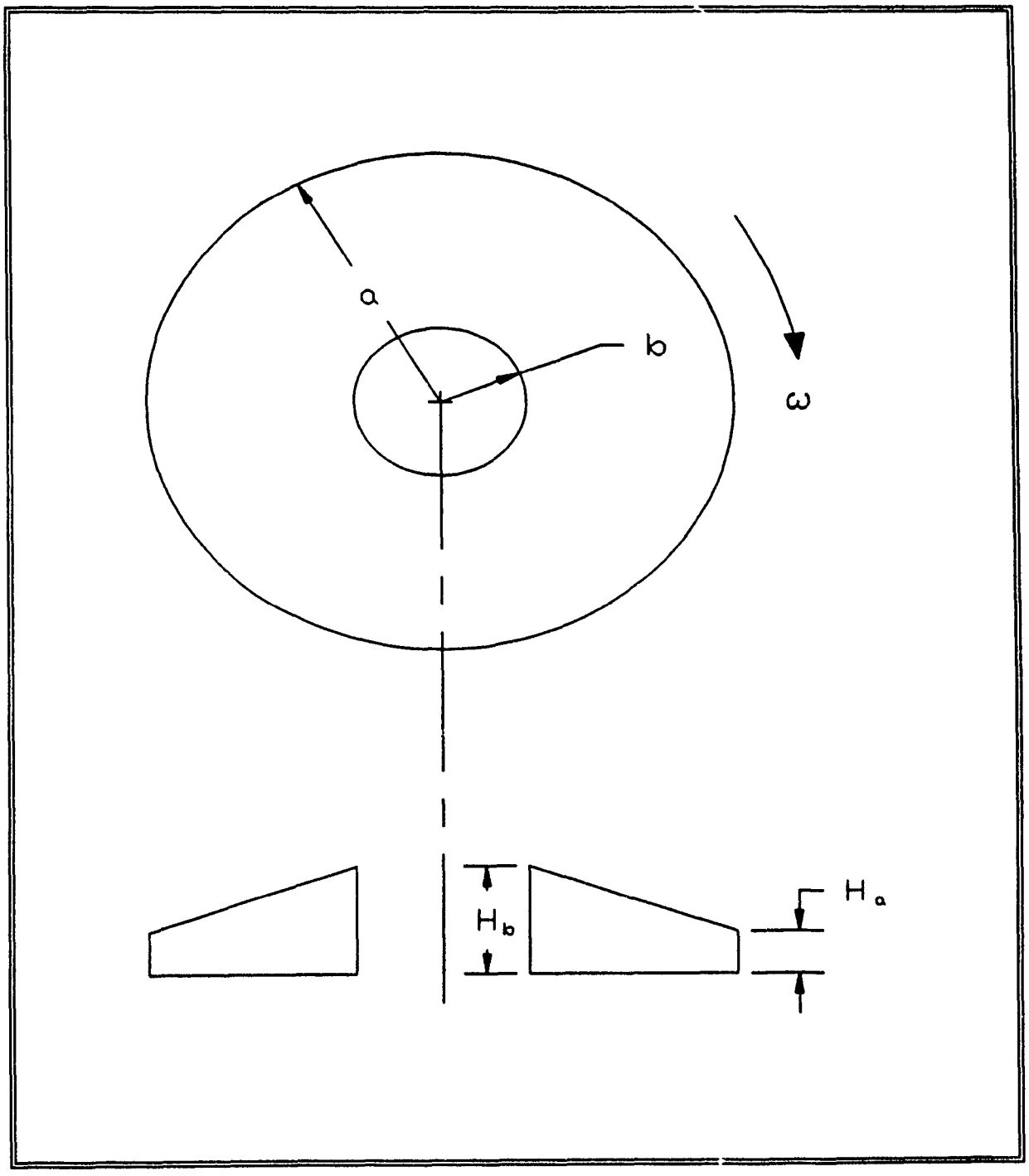

Fig. 3.2. Rotating Circular Plate with Varying Thickness

When the deflection of the plate is symmetrical about the centre, W will be a function of r only and Eq.(3.9) becomes,

$$U_1 = \pi \int_b^a D\{(\frac{\partial^2 w}{\partial r^2} + \frac{1}{r}\frac{\partial w}{\partial r})^2 - 2(1-\gamma)\frac{\partial^2 w}{\partial r^2}\frac{1}{r}\frac{\partial w}{\partial r}\} r dr \qquad (3.11)$$

The limits of integration a, b are the outer and inner radii of the circular plate respectively, $D = Eh^3 / 12(1 - \nu^2)$ is the flexural rigidity of the circular plate and h(r) is the plate thickness which varies along the radial direction.

In considering the vibration of a rotating disk, not only the energy due to the deformation but also the energy corresponding to work during deflection by the centrifugal forces must be taken into consideration. To calculate the work done by the centrifugal forces consider an element cut out from the disk by two cylindrical surfaces of the radii r and r + dr, as shown in Fig. 3.3.

The radial displacement of the element towards the centre due to the deflection will be,

$$du_r = \frac{1}{2}\int_b^r (\frac{\partial w}{\partial r})^2 dr \qquad (3.12)$$

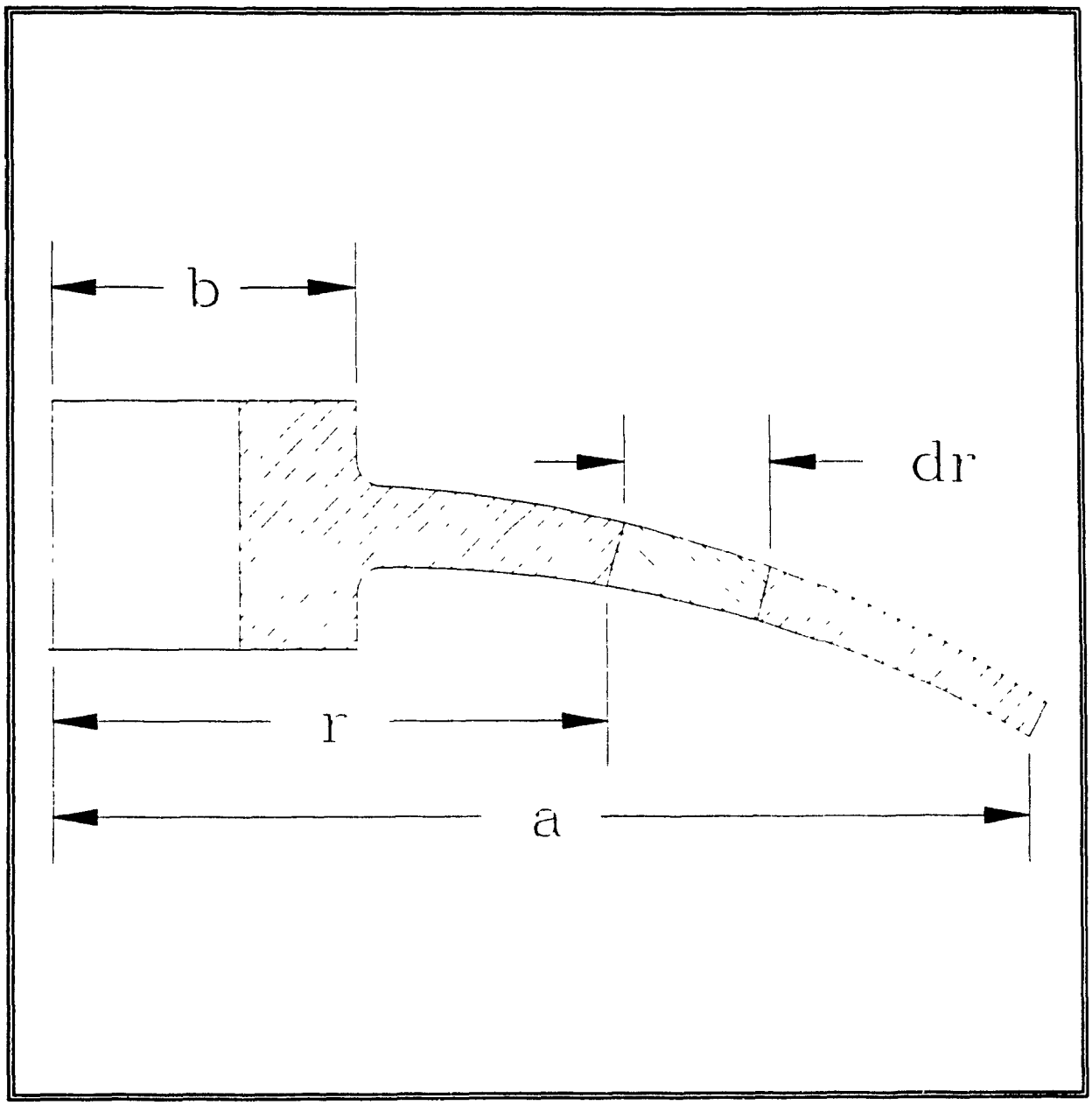

Fig. 3.3 : Rotating Disk Element

The mass of the element is,

$$dm = 2\pi r \rho h dr \tag{3.13}$$

where ρ is the material density. The energy which is the negative work done during the deflection by the centrifugal forces acting in this element is,

$$dU_2 = 2\pi r^2 \omega^2 \rho h dr \frac{1}{2} \int_b^r \left(\frac{\partial w}{\partial r}\right)^2 dr \tag{3.14}$$

The energy U_2, corresponding to the work of the centrifugal forces can be obtained by summation of such elements and is given by,

$$U_2 = \pi \omega^2 \rho h \int_b^a r^2 \left(\int_b^r \left(\frac{\partial w}{\partial r}\right)^2 dr \right) dr \tag{3.15}$$

The maximum kinetic energy is given by,

$$T = \pi \rho p^2 \int_b^a h w^2 r dr \tag{3.16}$$

where p is the frequency of harmonic vibration.

The following non-dimensional parameters are introduced:

$$f = \frac{r}{a} ; \beta = \frac{b}{a} ; K_1 = \frac{H_B}{H_A} ; K_2 = \frac{A_a^2}{H_A}$$

$$\lambda = \frac{\rho H_A a^4}{D_o} ; \eta^2 = \lambda p^2 ; \alpha^2 = \lambda \omega^2 \qquad (3.17)$$

where,

$$D_o = \frac{E H_A^3}{12(1-\nu^2)} \qquad (3.18)$$

H_B - Plate thickness at the inner periphery

H_A - Plate thickness at the outer periphery

A class of thickness variations are considered in the form,

$$h(\hat{f}) = H_a \Delta(\hat{f}) \qquad (3.19)$$

where $\Delta(\hat{f})$ describes the variation in thickness along the radial direction. It may be noted that for a plate with uniform thickness, $h(\hat{r})$ becomes unity.

For plates having thickness varying in a quadratic

fashion the thickness can be expressed as,

$$h(r) = A\,r^2 + B\,r + C \tag{3.20}$$

$\Delta(r)$ can be expressed as

$$\Delta(\hat{r}) = K_2\hat{r}^2 + C_1\hat{r} + C_o \tag{3.21}$$

where,

$$C_1 = \left(\frac{(1-K_1)}{(1-\beta)} - K_2(1+\beta)\right) \tag{3.22}$$

$$C_0 = 1 - K_2 - \left(\frac{(1-K_1)}{(1-\beta)} - K_2(1+\beta)\right) \tag{3.23}$$

With appropriate K_1 and K_2 values the thickness variation can be made linear or quadratic as shown in Fig. 3.4. For example, a uniform plate will have the values $K_1 = 1$ and $K_2=0$.

The deflection w can be expressed in the form

$$w = W_o(\hat{r})\sin pt \tag{3.24}$$

where,

$$W_o(\hat{r}) = \sum A_i\phi_i(\hat{r}) \tag{3.25}$$

and $\phi_i(r)$ are the assumed admissible functions which satisfy

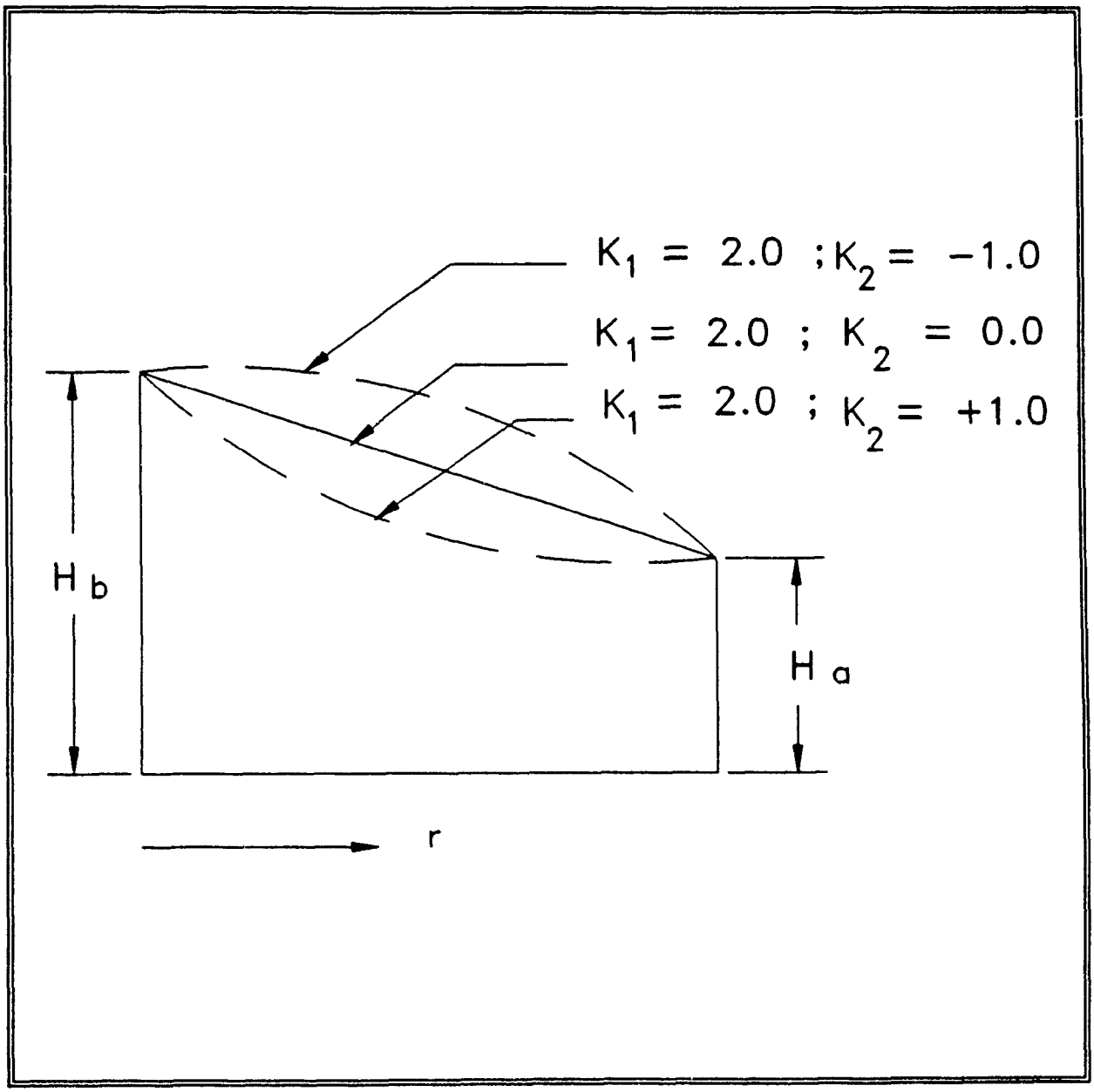

Fig. 3.4 : Parameters for Thickness Variation in the Disk

at least the geometrical boundary conditions of the circular plate.

Substituting Eqs. (3.21), (3.24), and (3.25) into the energy expressions (3.11), (3.15), (3.16) and minimizing with respect to the coefficients A_m, the equations of motion in terms of non-dimensional parameters is obtained as,

$$\eta^2 \int_{\beta}^{1} [\hat{r}\Delta(\hat{r}) W_o \frac{\partial W_o}{\partial A_i} d\hat{r}$$

$$- \int_{\beta}^{1} \hat{r}\Delta(\hat{r})^3 \{ (W_o'') \frac{\partial^2 W_o''}{\partial A_i} + \frac{1}{\hat{r}^2} (W_o') \frac{\partial W_o'}{\partial A_i}$$

$$+ \frac{W_o}{\hat{r}} [\frac{\partial^2 W_o''}{\partial A_i} W_o' + (W_o'') \frac{\partial W_o'}{\partial A_i}] d\hat{r} \}$$

$$- \alpha^2 \int_{\beta}^{1} [\![(W_o') \frac{\partial W_o'}{\partial A_i} [\![\{ \frac{1}{3} + \frac{K_2}{5} + \{ \frac{(1-K_1)}{(1-\beta)} - K_2(1+\beta) \} \frac{1}{4}$$

$$- \frac{K_2}{3} - [\frac{(1-K_1)}{(1-\beta)} - K_2(1-\beta)] \frac{1}{3}]\!]$$

$$-\left[\frac{f^3}{3}+K_2\frac{f^5}{5}+\left\{\frac{(1-K_1)}{(1-\beta)}-K_2(1+\beta)\right\}\frac{f^4}{4}-\frac{K_2 f^3}{3}\right.$$

$$\left.-\left\{\frac{(1-K_1)}{(1-\beta)}-K_2(1+\alpha)\right\}\frac{f^3}{3}\right]\Big]d\hat{r}=0 \qquad (3.26)$$

This is the standard eigen value problem in the form,

$$\eta^2[A]-[B]=0 \qquad (3.27)$$

The solution of Eq.(3.27) yields the natural frequencies of the vibration of the plate. The validity and accuracy of the solution depends upon the choice of the functions $\Phi_1(r)$.

Considering the boundary conditions at r = b, a (i.e at $\hat{r}$ = b/a , 1) the starting functions for the circular plate can be written as,

$$\Phi_1=\sum_{j=1}^{5} a_j f^{j\,1} \qquad (3.28)$$

where a_j for different boundary conditions considered are presented in Table (3.1).

For comparison purposes a circular annular plate with free-free boundary is also studied.

3.4 : Nonaxisymmetrical Vibrations

3.4.1 : Analysis

Fig.3.5 shows a turbine disk rotating with a constant angular speed ω. Two co-ordinate frames are introduced. One is the frame (r, θ) rotating with the blade, and the other one is the (r, Λ) frame fixed in space. θ and Λ are related through $\theta + \Lambda = \omega t$.

The maximum potential energy of the rotating disk is given by,

$$U = U_1 + U_2 \tag{3.29}$$

where, as before U_1 corresponds to the potential energy without considering rotational effects given by,

$$U_1 = \int_{A_D} \frac{D}{2} \{ (\frac{\partial^2 w}{\partial r^2} + \frac{1}{r} \frac{\partial w}{\partial r} + \frac{1}{r^2} \frac{\partial^2 w}{\partial \theta})^2$$

$$- 2(1-\nu) \frac{\partial^2 w}{\partial r^2} (\frac{1}{r} \frac{\partial w}{\partial r} + \frac{1}{r^2} \frac{\partial^2 w}{\partial \theta^2}) + 2(1-\nu) \{ \frac{\partial}{\partial r} (\frac{\partial}{\partial r} (\frac{1}{r} \frac{\partial w}{\partial \theta}))^2 \} dA$$

(3.30)

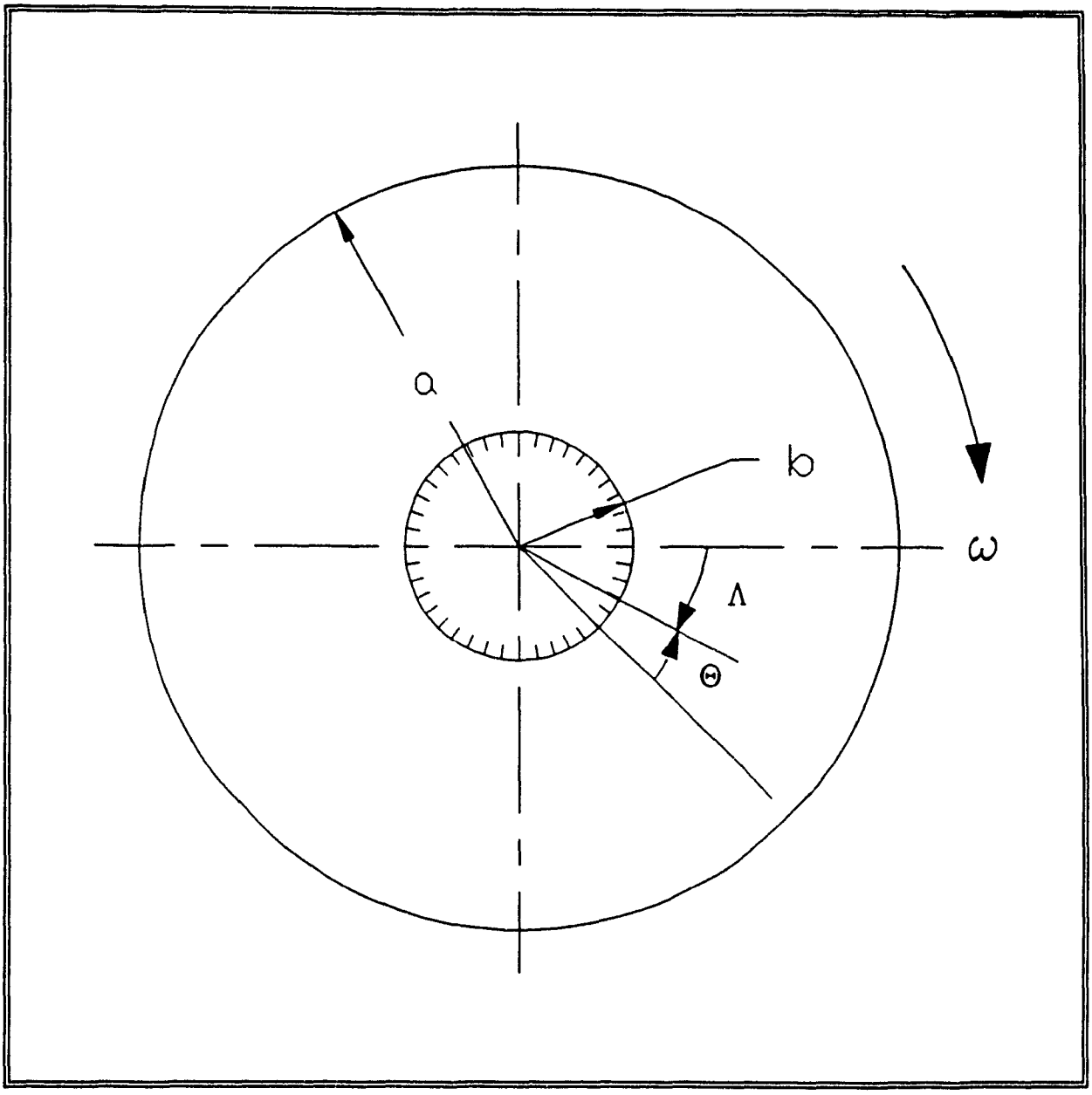

Fig. 3.5 Rotating Circular Plate

and the potential energy U_2 , corresponds to the strain energy due to bending in the presence of in-plane centrifugal forces given by,

$$U_2 = \frac{1}{2}\int_{A_D} h(r)\,[N_{rr}\,(\frac{\partial w}{\partial r})^2 + \frac{N_{\theta\theta}}{r^2}\,(\frac{\partial w}{\partial \theta})^2]\,dA \qquad (3.31)$$

where the integral is taken over the area A_D of the disk, and N_{rr} and $N_{\theta\theta}$ are the stress resultants.

The kinetic energy of the blade is,

$$T = \frac{\rho h}{2}\int_{A_D} (\frac{Dw}{Dt})^2\,dA \qquad (3.32)$$

where,

$$\frac{Dw}{Dt} = \frac{\partial w}{\partial t} + \frac{\partial w}{\partial \theta}\frac{\partial \theta}{\partial t} \qquad (3.33)$$

3.4.2 : <u>Stress Resultants</u>: N_{rr} and $N_{\theta\theta}$

The stress distribution in rotating circular disks is of practical importance. If the thickness of the disk is small compared to its radius, the variation of the radial and tangential stresses over the thickness may, as a first approximation, be neglected. This is equivalent to a plane

stress assumption.

For a disk rotating at constant angular velocity ω, the radial and tangential stresses are given by

$$N_{rr} = \frac{E}{(1-\nu^2)} \left[\frac{-(3+\nu)(1-\nu^2)}{8E} \rho \omega^2 r^2 + (1+\nu) A_1 - (1-\nu) \frac{A_2}{r^2} \right]$$

$$N_{\theta\theta} = \frac{E}{(1-\nu^2)} \left[- \frac{(1+3\nu)(1-\nu^2)}{8E} \rho \omega^2 r^2 + (1+\nu) A_1 + (1-\nu) \frac{A_2}{r^2} \right]$$

(3.34)

where ρ is the mass density, ν is the Poissons ratio, E is the Young's Modulus of Elasticity and A_1 and A_2 are constants of integrations which can be evaluated on the basis of the boundary conditions.

Applying the boundary conditions of the disk, (i.e. at outer edge $N_{rr} = 0$ at $r = a$, and displacement $U_r = 0$ at $r = b$) the stress resultants can be rewritten as,

$$N_{rr} = \rho\omega^2 a^2 \frac{(1+\nu)}{8}\left[\frac{(1-\nu)\left(\frac{b}{a}\right)^4+(3+\nu)}{(1-\nu)\left(\frac{b}{a}\right)^2+(1+\nu)}\right]$$

$$+\frac{(1-\nu)}{(1+\nu)}\left\{\frac{-(1+\nu)\left(\frac{b}{a}\right)^2+(3+\nu)}{(1-\nu)\left(\frac{b}{a}\right)^2+(1+\nu)}\right\}\frac{\left(\frac{b}{a}\right)^2}{\left(\frac{r}{a}\right)^2}-\frac{(3+\nu)}{(1+\nu)}\left(\frac{r}{a}\right)^2\Bigg] \tag{3.35}$$

$$N_{\theta\theta} = \rho\omega^2 a^2 \frac{(1+\nu)}{8}\left[\frac{(1-\nu)\left(\frac{b}{a}\right)^4+(3+\nu)}{(1-\nu)\left(\frac{b}{a}\right)^2+(1+\nu)}\right]$$

$$-\frac{(1-\nu)}{(1+\nu)}\left\{\frac{-(1+\nu)\left(\frac{b}{a}\right)^2+(3+\nu)}{(1-\nu)\left(\frac{b}{a}\right)^2+(1+\nu)}\right\}\frac{\left(\frac{b}{a}\right)^2}{\left(\frac{r}{a}\right)^2}-\frac{(1+3\nu)}{(1+\nu)}\left(\frac{r}{a}\right)^2\Bigg] \tag{3.36}$$

The above stress resultants can be used in Eq.(3.31).

Incorporating the following non-dimensional parameters,

$$\hat{r} = \frac{r}{a} \; ; \; \theta = \frac{\theta}{2\pi} \; ; \; \beta = \frac{b}{a} \; ; \; \lambda = \frac{\rho a h^4}{D}$$

$$\alpha^2 = \lambda \omega^2 \; ; \; \eta^2 = \lambda p_s^2 \; ; \; K_3 = \frac{(1-\nu)(\beta^4) + (3+\nu)}{(1-\nu)(\beta^2) + (1+\nu)}$$

$$K_4 = \frac{(1-\nu)}{(1+\nu)} \beta^2 \; ; \; K_5 = \frac{-(1+\nu)(\beta^2) + (3+\nu)}{(1-\nu)(\beta^2) + (1+\nu)} \qquad (3.37)$$

The Lagrangian can be written as,

$$L_l = T - U \qquad (3.38)$$

$$= \frac{2\pi D a^2}{2a^4} \left[\int_0^1 \int_\beta^1 \left[w^2 \eta^2 + \left(\frac{\partial w}{\partial \theta} \right)^2 \frac{\alpha^2}{4\pi^4} + \frac{w}{\pi} \eta \alpha \left(\frac{\partial w}{\partial \theta} \right) \right] \right.$$

$$- \left[\left(\frac{\partial^2 w}{\partial \hat{r}^2} \right)^2 + \frac{1}{\hat{r}^2} \left(\frac{\partial w}{\partial \hat{r}} \right)^2 + \frac{1}{16\pi^4 \hat{r}^4} \left(\frac{\partial^2 w}{\partial \theta^2} \right)^2 + \frac{2}{\hat{r}^3 4\pi^2} \left(\frac{\partial w}{\partial \hat{r}} \right) \left(\frac{\partial^2 w}{\partial \theta^2} \right) \right.$$

$$+ \frac{2\nu}{\hat{r}} \left(\frac{\partial w}{\partial \hat{r}} \right) \left(\frac{\partial^2 w}{\partial \hat{r}^2} \right) + \frac{2\nu}{4\pi^2 \hat{r}^2} \left(\frac{\partial^2 w}{\partial \hat{r}^2} \right) \left(\frac{\partial^2 w}{\partial \theta^2} \right)$$

$$\left. \left. + \frac{2}{\hat{r}^2 4\pi^2} \left(\frac{\partial^2 w}{\partial \hat{r} \partial \theta} \right)^2 + \frac{2}{4\pi^2 \hat{r}^4} \left(\frac{\partial w}{\partial \theta} \right)^2 - \frac{4}{4\pi^2 \hat{r}^3} \left(\frac{\partial^2 w}{\partial \hat{r} \partial \theta} \right) \left(\frac{\partial w}{\partial \theta} \right) \right] \right]$$

$$-\frac{2\nu}{\hat{r}^2 4\pi^2}\left(\frac{\partial^2 w}{\partial \hat{r}\partial\hat{\theta}}\right)^2-\frac{2\nu}{4\pi^2\hat{r}^4}\left(\frac{\partial w}{\partial\hat{\theta}}\right)^2+\frac{4\nu}{4\pi^2\hat{r}^3}\left(\frac{\partial^2 w}{\partial\hat{r}\partial\hat{\theta}}\right)\left(\frac{\partial w}{\partial\hat{\theta}}\right)]$$

$$+\left(\frac{1+\nu}{8}\right)\alpha^2[(K_3+\frac{(K_4+K_5)}{\hat{r}^2}-\frac{(3+\nu)}{(1+\nu)}\hat{r}^2)\left(\frac{\partial w}{\partial\hat{r}}\right)^2$$

$$+\frac{1}{\hat{r}^2 4\pi^2}(K_3-\frac{K_4K_5}{\hat{r}^2}-(\frac{1+3\nu}{1+\nu})\hat{r}^2)\left(\frac{\partial w}{\partial\hat{\theta}}\right)^2]]\hat{r}d\hat{r}d\hat{\theta}]] \qquad (3.39)$$

A rotating circular disk has two natural frequencies for each mode of vibration when it is observed from the reference frame fixed in space [72]. They are the frequencies of the flexural waves travelling on the rotating disk in the forward and backward directions corresponding to the direction of rotation and hence having different propagation speeds when observed from outside. On the other hand if the disk is observed in a rotating frame of reference it will exhibit only one frequency [65].

For free vibration the displacement w is expressed as,

$$w(\hat{r},\hat{\theta},t)=\sum_m\sum_n[C_{mn}(t)\,Cos2\pi n\hat{\theta}+S_{mn}(t)\,Sin2\pi n\hat{\theta}]\,\phi_m(\hat{r}) \qquad (3.40)$$

where,

$$C_{mn}(t) = C_{mn}^{(1)} \cos p_s t + C_{mn}^{(2)} \sin p_s t \qquad (3.41)$$

$$S_{mn}(t) = S_{mn}^{(1)} \cos p_s t + S_{mn}^{(2)} \sin p_s t \qquad (3.42)$$

and Φ_m (r) are the assumed admissible functions which satisfy at least the geometrical boundary conditions of the plate.

For a conservative system, U_{max} (C_{mn}, S_{mn}) and T_{max} (C_{mn}, S_{mn}) must be equal which implies that,

$$T_{max} - U_{max} = 0 \qquad (3.43)$$

However since the assumed mode shapes are not exact, T_{max} will not be equal to U_{max} and hence,

$$F(C_{mn}, S_{mn}, \eta) = T_{max} - U_{max} \qquad (3.44)$$

will be an error term. The coefficients C_{mn} and S_{mn} must be chosen so as to minimize the error and hence,

$$\frac{\partial F}{\partial C_{mn}} = \frac{\partial}{\partial C_{mn}} (T_{max} - U_{max}) = 0 \qquad (3.45)$$

and

$$\frac{\partial F}{\partial S_{mn}} = \frac{\partial}{\partial S_{mn}} (T_{max} - U_{max}) = 0 \qquad (3.46)$$

Substituting equation, (3.40) in (3.29) and minimizing with respect to the coefficients C_{mn} and S_{mn} according to equations (3.45) and (3.46) leads to a complex eigenvalue problem in 2mn equations given by,

$$\eta^2 [A] + \eta [B] + [C] = 0 \qquad (3.47)$$

The above equation can be separated into two sets of mn equations and the solution of equation (3.47) results in the complex eigenvalues of the disk.

3.5 : Discussion of Results

3.5.1 : Axisymmetrical Vibrations

Natural frequencies are obtained for a rotating disk with varying thickness at various rotational speeds for different ratios of inner/outer radii and inner/outer thickness.

The effect of inner/outer radii ratio, ß, are presented and compared with [57], [96] in Table 3.2. From Table 3.2 it can be seen that as the inner/outer radii ratio is increased the natural frequency increases, such increase being more predominant at higher modes.

The variation of the natural frequencies for various ratios of the inner/outer radii and inner/outer thickness are presented in Tables 3.3 through 3.8. From these tables it can be seen that the natural frequencies increase with the increase in the inner/outer thickness ratio for a fixed value of the inner/outer radii.

Natural frequencies of the rotating disk for different rotational speeds and several parametrical combinations shown in Tables 3.3 through 3.8 are presented in Figs. 3.6 through 3.9. Natural frequency increases with the increase in the inner/outer radii value and decreases with the increase in the thickness parameter K_2.

Variation of the first natural frequency, η, with rotational speed, α, for a constant value of inner/outer radii is shown in Fig 3.6 for linear and parabolic thickness variations. The natural frequency increases with increase in the inner/outer thickness parameter K_1 (Curve 1 and Curve 2) and for a constant inner/outer radii ratio the natural frequency decreases with the increase in the parameter K_2. Also, from Figs. 3.6 and 3.8 it can be seen that for a fixed value of the thickness parameters K_1 and K_2 the natural

frequency increases with the increase in the inner/outer radii ratio.

The variation of the second natural frequency with speed for different parametrical combinations are shown in Figs 3.7 and 3.9. The natural frequency increases with an increase in inner/outer radii ratio for a fixed value of the thickness parameters K_1 and K_2 . Also, the natural frequency increases with the increase in inner/outer thickness parameter K_1 and decreases with the increase in the thickness parameter K_2.

3.5.2 : Nonaxisymmetrical Vibrations

Natural frequencies of a rotating disk undergoing nonaxisymmetrical vibrations are obtained for different combinations of the inner/outer radii ratio, ß, at various rotational speeds.

The variation of the natural frequencies in the rotating frame of reference (i.e. no pseudo damping term in Eq.3.47) are presented in Tables 3.9 through 3.11. From these tables it can be seen that as the rotational speed increases the natural frequencies increase and for a given rotational speed, increase in the inner/outer radii ratio increases the natural frequencies.

Variation of natural frequencies with the speed of rotation for various values of inner/outer radii ratio are shown in Figs 3.10 through 3.12. From these figures it can be seen that the natural frequency increases with an increase in the inner/outer radii ratio.

Variation of the natural frequencies in the fixed frame of reference are shown in Fig 3.13 .The first two modes have no critical speeds while for mode 3 its lower frequency curve decreases and intersects the lateral axis. After the intersection it again increases as the rotation speed increases. The speed at the intersection point is the critical speed. It must be noted that the physical interpretation of this zero frequency critical point is dependent on the reference frame. If the motion is viewed in an inertial frame this critical speed appears as a spatially fixed deflection. In an axis system rotating with the disk this is not a zero frequency vibration, but rather one with a frequency same as the rotational speed. This is a wave travelling backward at the rotational speed, which then appears spatially fixed. The upper frequency curve, on the other hand, increases with the increase in rotational speed.

3.6 : Summary

Free vibrational behaviour of a rotating disk with varying thickness exhibiting axisymmetrical and nonaxisymmetrical vibrations is studied using characteristic orthogonal polynomials in the Rayleigh-Ritz method. The variation of the natural frequencies with speed of rotation are obtained for several parameter combinations of the ratio of inner/outer radii and inner/outer thickness. The natural frequencies increase with increase in the inner/outer thickness ratio . Also, the natural frequencies increase with increase in rotational speed and for a given rotational speed increase in the inner/outer radii ratio increases the natural frequency.

In Chapter 4, a finite element model of a bladed-disk assembly is developed to study its dynamic behaviour.

Table 3.1 : Coefficients of Starting Functions for Circular Plates

Boundary Conditions	a_0	a_1	a_2	a_3	a_4
Clamped (inner) Free (outer)	$\beta^2(6-8\beta+3\beta^2)$	$-4\beta(3-3\beta+\beta^2)$	6	-4	1
Free(inner) Free (outer)	1	0	0	0	0

Table 3.2 : Comparison of Natural Frequency for Axisymmetrical Modes of Circular Plate

$\eta = p\sqrt{\lambda}$							
P.R. = Present Results							
Mode 1		Mode 2		Mode 3		Mode 4	
P.R.	[96]	P.R.	[96]	P.R.	[96]	P.R.	[96]
Clamped (inner) ; Free (outside)							
$\beta = 0.001$; $H_a = 1.0$; $K_1 = 1.0$; $K_2 = 0.0$; $\alpha = 0.0$							
3.75	3.752	20.92	20.92	60.69	60.70	119.96	120.7
$\beta = 0.1$; $H_a = 1.0$; $K_1 = 1.0$; $K_2 = 0.0$; $\alpha = 0.0$							
4.23	4.237	25.26	25.26	73.90	-	146.69	-
Free (inner) ; Free (outside)							
$\beta = 0.1$; $K_1 = .01$; $K_2 = 1.0$; $\alpha = 0.0$							
P.R	[57]	P.R	[57]	P.R	[57]	P.R	[57]
0.00	0.00	4.204	4.20	9.107	9.09	16.927	17.11

Table 3.3 : Variation of Natural Frequency with Rotational Speed for Axisymmetrical Modes of Circular Plates of Uniform Thickness

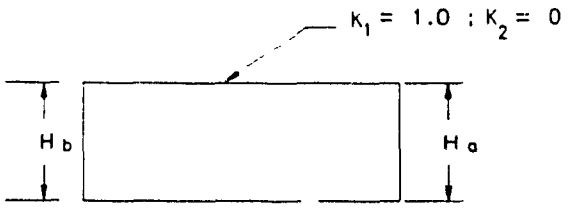

Angular Velocity α	Natural Frequency $\eta = p \sqrt{\lambda}$			
	$\beta = 0.00$; $H_a = 1.0$; $K_1 = 1.0$; $K_2 = 0.0$;			
	Mode 1	Mode 2	Mode 3	Mode 4
0	3.75	20.92	60.69	119.96
1	3.89	21.14	60.97	120.29
2	4.29	21.81	61.81	121.29
3	4.87	22.86	63.16	122.92
4	5.59	24.25	64.99	125.14
5	6.38	25.92	67.23	127.90
6	7.23	27.80	69.83	131.14
7	8.11	29.85	72.73	134.82
8	9.02	32.04	75.88	138.86
9	9.95	34.32	79.24	143.22
10	10.89	36.69	82.76	147.85

Table 3.4 : Variation of Natural Frequency with Rotational Speed for Axisymmetrical Modes of Circular Plate with Linear Thickness Variation

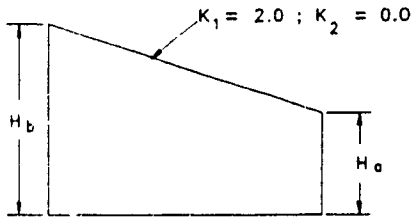

Angular Velocity α	Natural Frequency $\eta = p \sqrt{\lambda}$			
	$\beta = 0.00$; $H_a = 1.0$; $K_1 = 2.0$; $K_2 = 0.0$;			
	Mode 1	Mode 2	Mode 3	Mode 4
0	7.25	34.48	92.05	178.17
1	7.33	34.59	92.18	178.31
2	7.56	34.92	92.55	178.73
3	7.93	35.45	93.17	179.43
4	8.42	36.19	94.03	180.39
5	9.00	37.12	95.12	181.63
6	9.67	38.22	96.43	183.12
7	10.39	39.48	97.95	184.86
8	11.16	40.88	99.67	186.85
9	11.97	42.42	101.59	189.07
10	12.81	44.06	103.67	191.51

Table 3.5 : Variation of Natural Frequency with Rotational Speed for Axisymmetrical Modes of Circular Plate

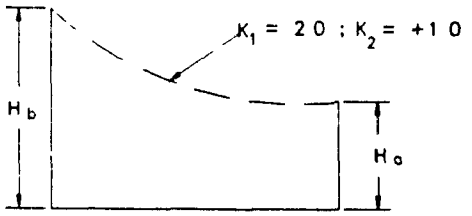

Angular Velocity α	Natural Frequency $\eta = p\sqrt{\lambda}$			
	$\beta = 0.00$; $H_a = 1.0$; $K_1 = 2.0$; $K_2 = 1.0$;			
	Mode 1	Mode 2	Mode 3	Mode 4
0	6.38	30.19	80.75	156.56
1	6.47	30.32	80.90	156.72
2	6.75	30.70	81.33	157.20
3	7.17	31.33	82.04	157.99
4	7.73	32.18	83.03	159.09
5	8.38	33.25	84.28	160.50
6	9.11	34.51	85.77	162.20
7	9.89	35.94	87.51	164.17
8	10.71	37.53	89.46	166.41
9	11.57	39.24	91.61	168.91
10	12.44	41.07	93.94	171.65

Table 3.6 : Variation of Natural Frequency with Rotational Speed for Axisymmetrical Modes of Circular Plate

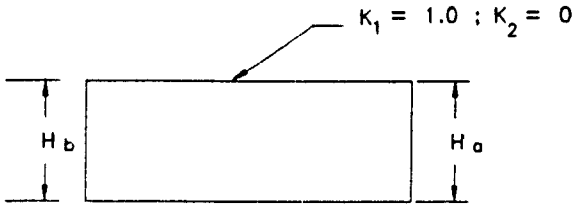

Angular Velocity α	Natural Frequency $\eta = p \sqrt{\lambda}$			
	$\beta = 0.1 ; H_a = 1.0 ; K_1 = 1.0; K_2 = 0.0 ;$			
	Mode 1	Mode 2	Mode 3	Mode 4
0	4.24	25.26	73.90	146.69
1	4.38	25.46	74.13	146.95
2	4.79	25.05	74.82	147.73
3	5.39	27.01	75.95	149.00
4	6.14	28.29	77.49	150.76
5	6.98	29.85	79.42	152.98
6	7.88	31.63	81.69	155.63
7	8.83	33.61	84.27	158.68
8	9.79	35.74	87.12	162.09
9	10.79	37.99	90.21	165.85
10	11.79	40.34	93.49	169.91

Table 3.7 : Variation of Natural Frequency with Rotational Speed for Axisymmetrical Modes of Circular Plate

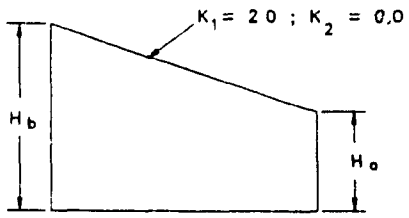

Angular Velocity α	Natural Frequency $\eta = p\sqrt{\lambda}$			
	$\beta = 0.1$; $H_a = 1.0$; $K_1 = 2.0$; $K_2 = 0.0$;			
	Mode 1	Mode 2	Mode 3	Mode 4
0	8.42	41.72	112.023	218.13
1	8.50	41.82	112.34	218.25
2	8.73	42.11	112.66	218.59
3	9.09	42.60	113.19	219.16
4	9.59	43.27	113.92	219.97
5	10.18	44.12	114087	220.97
6	10.86	45.13	116.00	222.21
7	11.60	46.30	117.34	223.66
8	12.41	47.61	118.85	225.33
9	13.25	49.05	120.53	227.18
10	14.13	50.62	122.39	229.25

Table 3.8 : Variation of Natural Frequency with Rotational Speed for Axisymmetrical Modes of Circular Plate

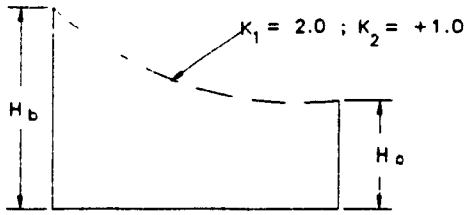

Angular Velocity α	Natural Frequency $\eta = p \sqrt{\lambda}$			
	β = 0.1 ; H_a = 1.0 ; K_1 = 2.0; K_2 = 1.0 ;			
	Mode 1	Mode 2	Mode 3	Mode 4
0	7.72	37.54	101.07	196.77
1	7.81	37.80	101.69	196.90
2	8.07	38.14	101.92	197.28
3	8.46	38.53	102.15	197.92
4	9.00	39.29	102.98	198.81
5	9.64	40.24	104.03	199.95
6	10.37	41.37	105.31	201.33
7	11.17	42.67	106.79	202.95
8	12.01	44.12	108.48	204.80
9	12.90	45.71	110.3.	206.88
10	13.82	47.42	112.40	209.16

Table 3.9 : Variation of Natural Frequency with Rotational Speed for Nonaxisymmetrical Modes of Circular Plate

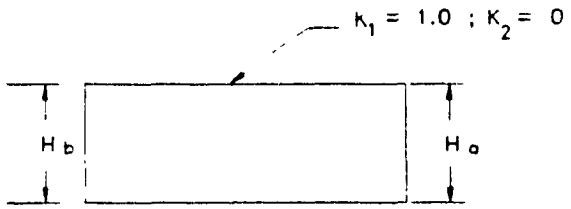

Angular Velocity α	Natural Frequency $\eta = p \sqrt{\lambda}$		
	$\beta = 0.25$		
	Mode 1	Mode 2	Mode 3
0	5.63	5.84	7.14
1	5.75	5.94	7.30
2	6.10	6.20	7.76
3	6.62	6.64	8.47
4	7.16	7.33	9.38
5	7.79	8.13	10.43
6	8.50	9.01	11.59
7	9.27	9.95	12.82
8	10.07	10.93	14.11
9	10.91	11.95	15.44
10	11.77	12.98	16.8

Table 3.10 : Variation of Natural Frequency with Rotational Speed for Nonaxisymmetrical Modes of Circular Plate

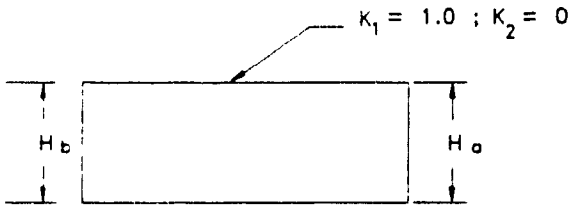

Angular Velocity α	Natural Frequency $\eta = p \sqrt{\lambda}$		
	$\beta = 0.5$		
	Mode 1	Mode 2	Mode 3
0	13.02	13.29	14.71
1	13.11	13.38	14.80
2	13.36	13.64	15.08
3	13.77	14.07	15.54
4	14.32	14.64	16.17
5	15.00	15.36	16.93
6	15.78	16.18	17.82
7	16.68	17.11	18.82
8	17.65	18.11	19.91
9	18.68	19.18	21.08
10	19.77	20.32	22.31

Table 3.11 : Variation of Natural Frequency with Rotational Speed for Nonaxisymmetrical Modes of Circular Plate

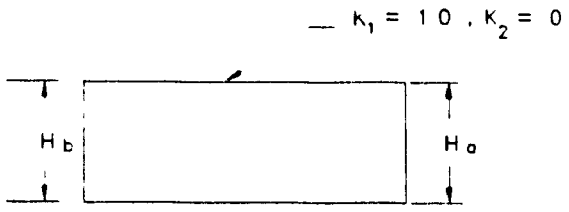

Angular Velocity α	Natural Frequency $\eta = p \sqrt{\lambda}$		
	$\beta = 0.75$		
	Mode 1	Mode 2	Mode 3
0	53.62	54.23	56.13
1	53.67	54.28	56.18
2	53.83	54.43	56.33
3	54.08	54.69	56.58
4	54.44	55.04	56.93
5	54.89	55.49	57.38
6	55.44	56.04	57.92
7	56.09	56.68	58.56
8	56.82	57.41	59.28
9	57.64	58.23	60.09
10	58.54	59.13	60.98

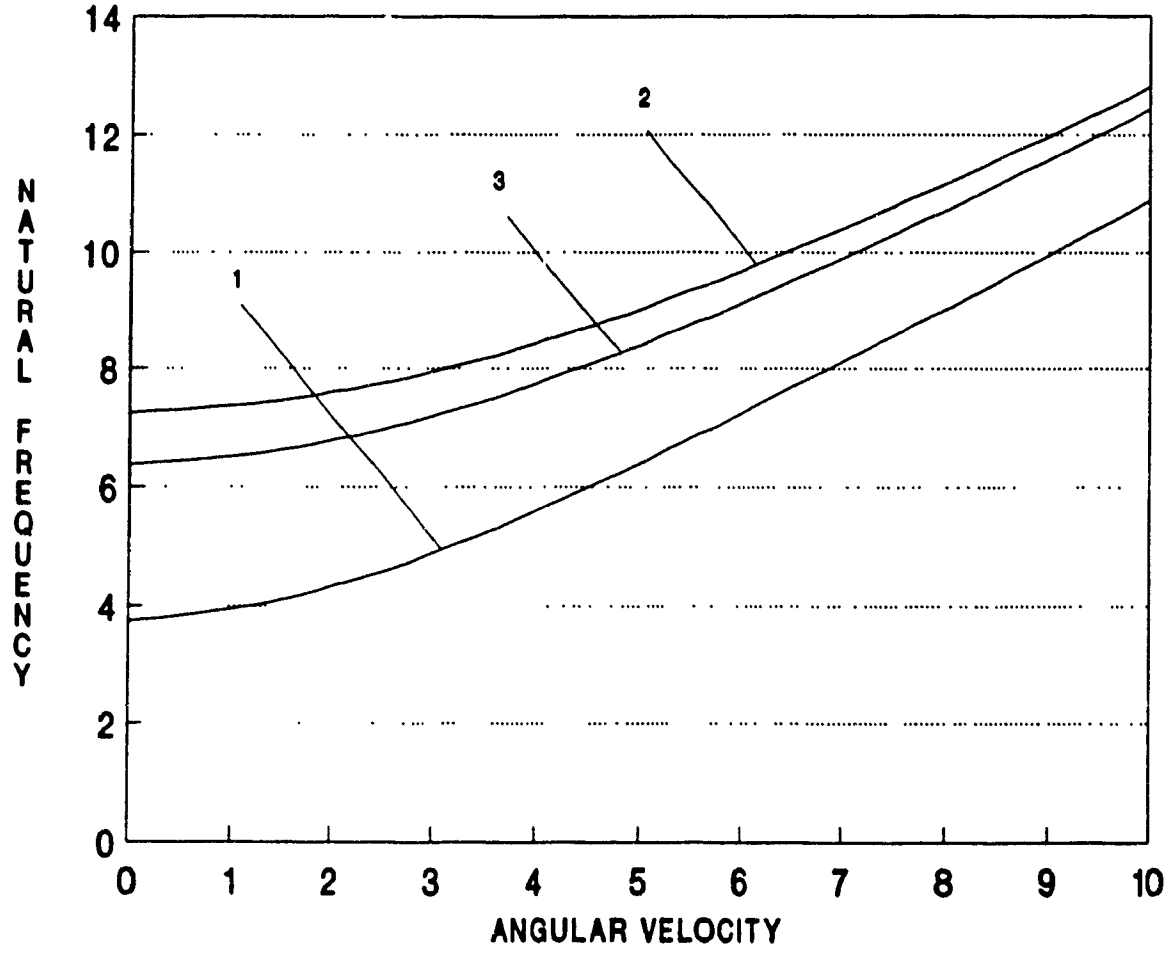

Fig.3.6 : Variation of First Natural Frequency with Speed (β=0.0)

Curve 1 : K_1=1.0 K_2=0.0 Curve 2 K_1=2.0 K_2=0.0 Curve 3 : K_1=2.0 K_2=1.0

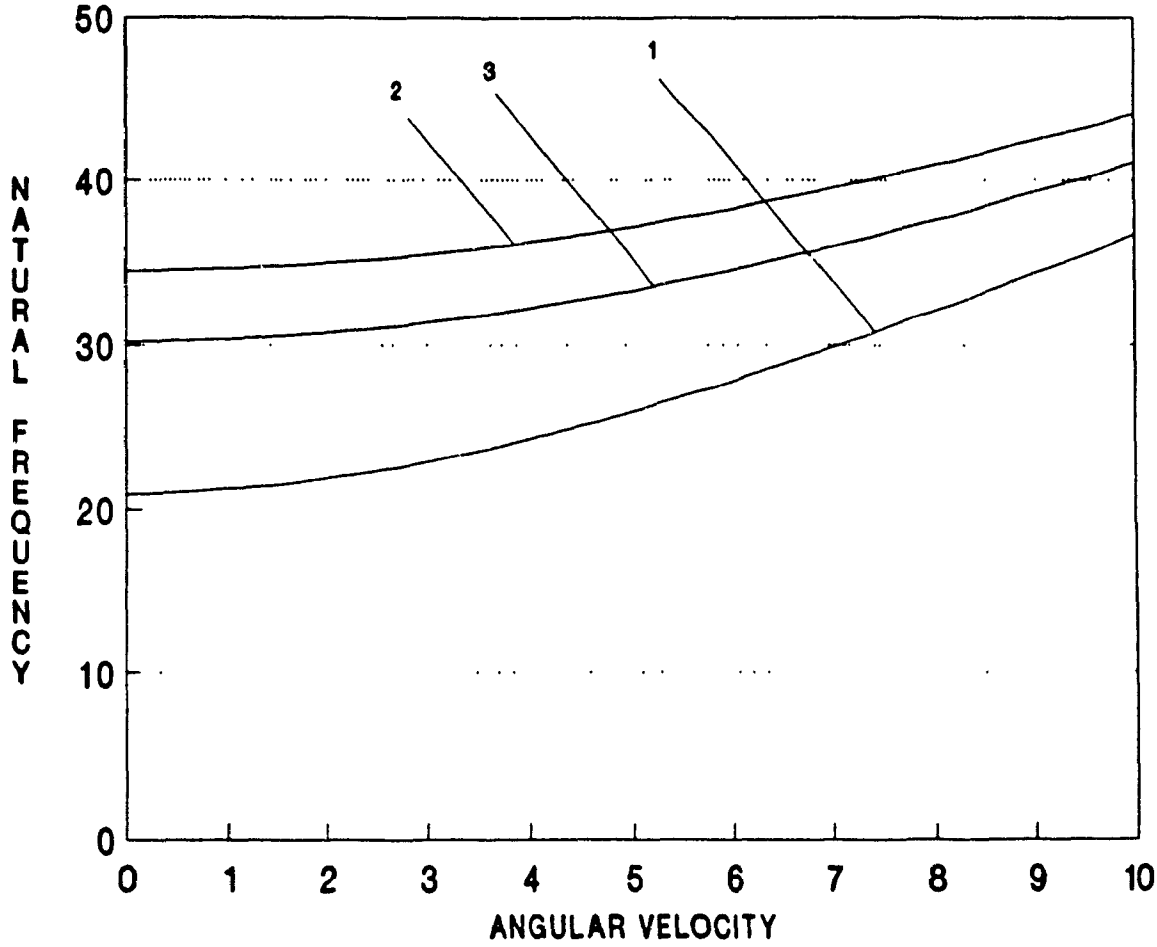

Fig 3.7: Variation of Second Natural Frequency with Speed (ß=0.0)

Curve 1: K_1=1.0 K_2=0.0 Curve 2 : K_1=2.0 K_2=0.0 Curve 3 : K_1=2.0 K_2=1.0

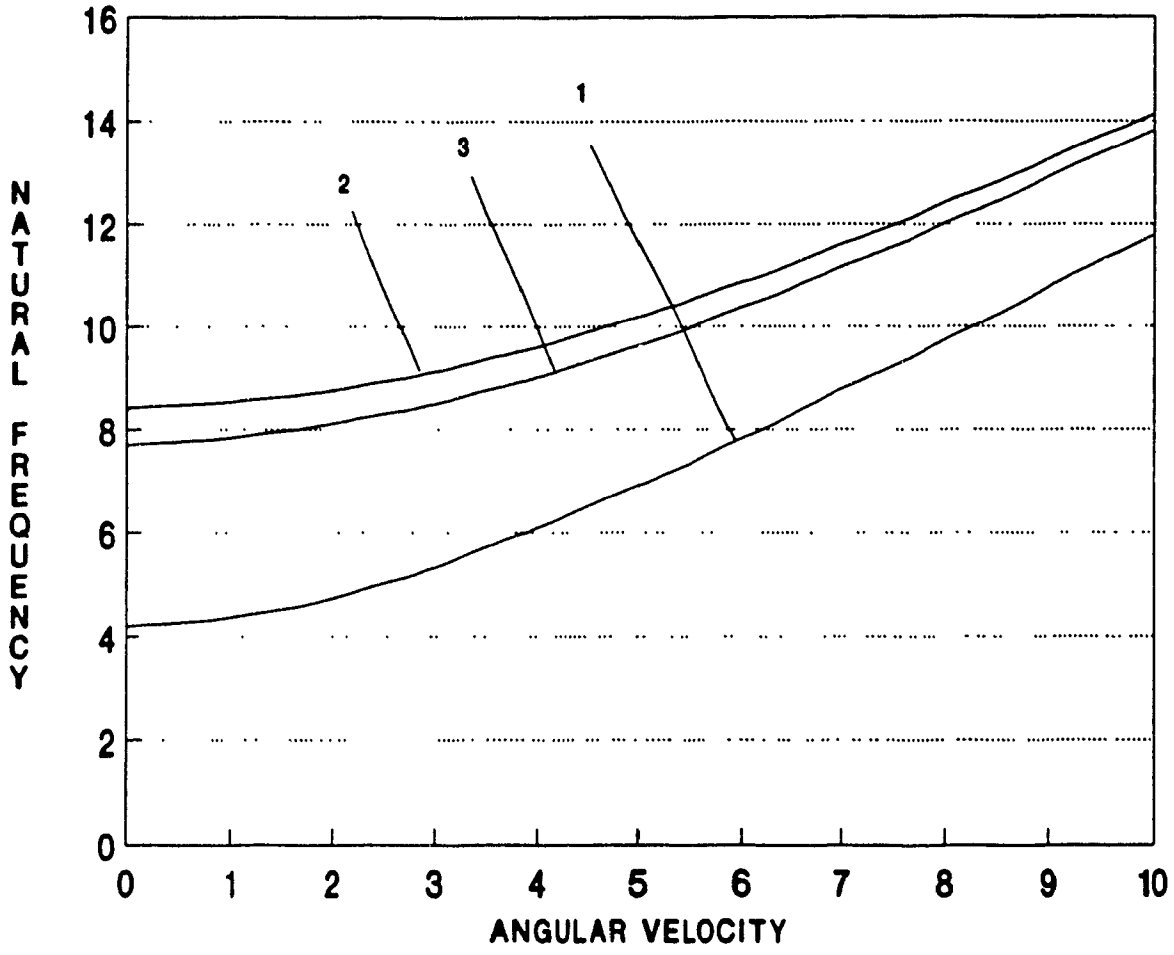

Fig 3.8 : Variation of First Natural Frequency with Speed (β=0.1)

Curve 1: K_1=1.0 K_2=0.0 Curve 2: K_1=2.0 K_2=0.0 Curve 3: K_1=2.0 K_2=1.0

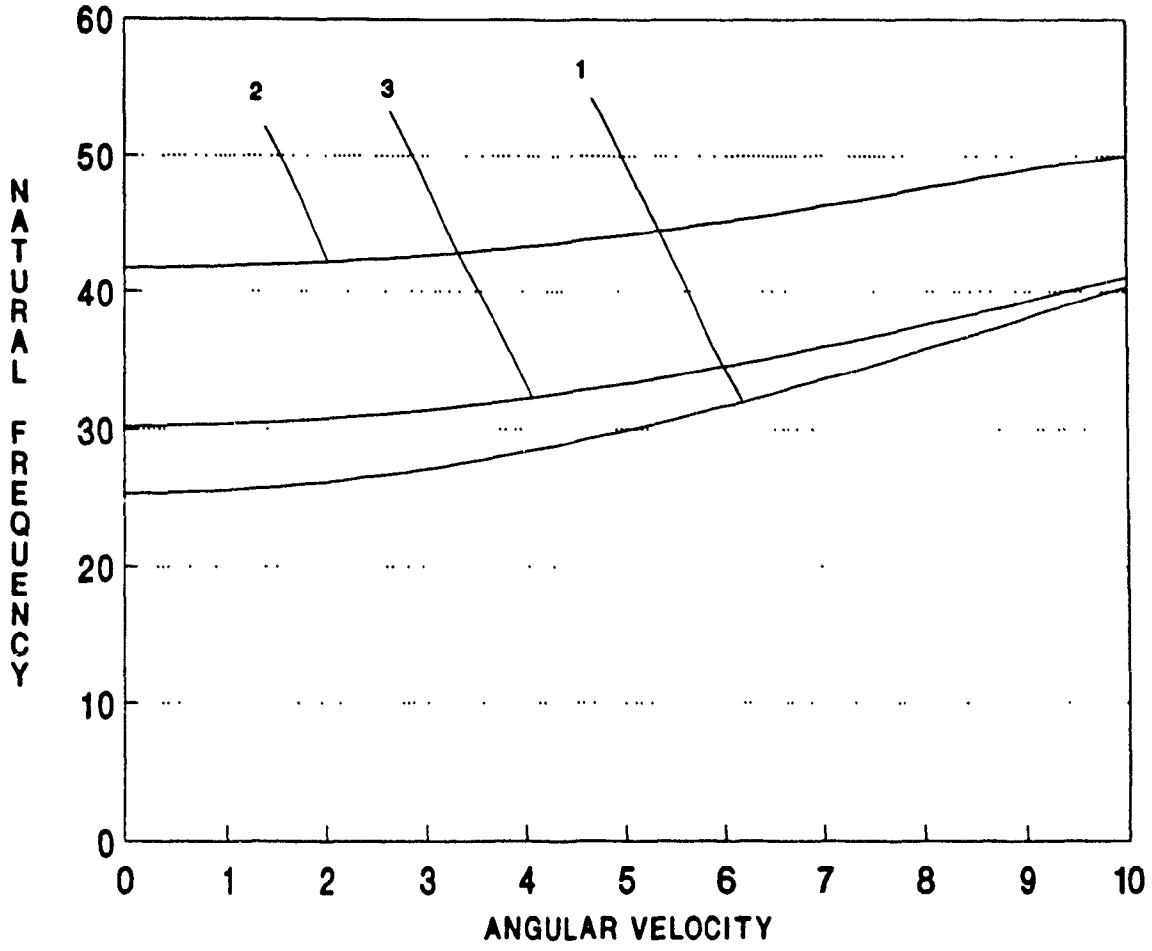

Fig 3.9: Variation of Second Natural Frequency with Speed (ß=0.1)

Curve 1: K_1=1.0 K_2=0 Curve 2: K_1=2.0 K_2=0.0 Curve 3: K_1=2.0 K_2=1.0

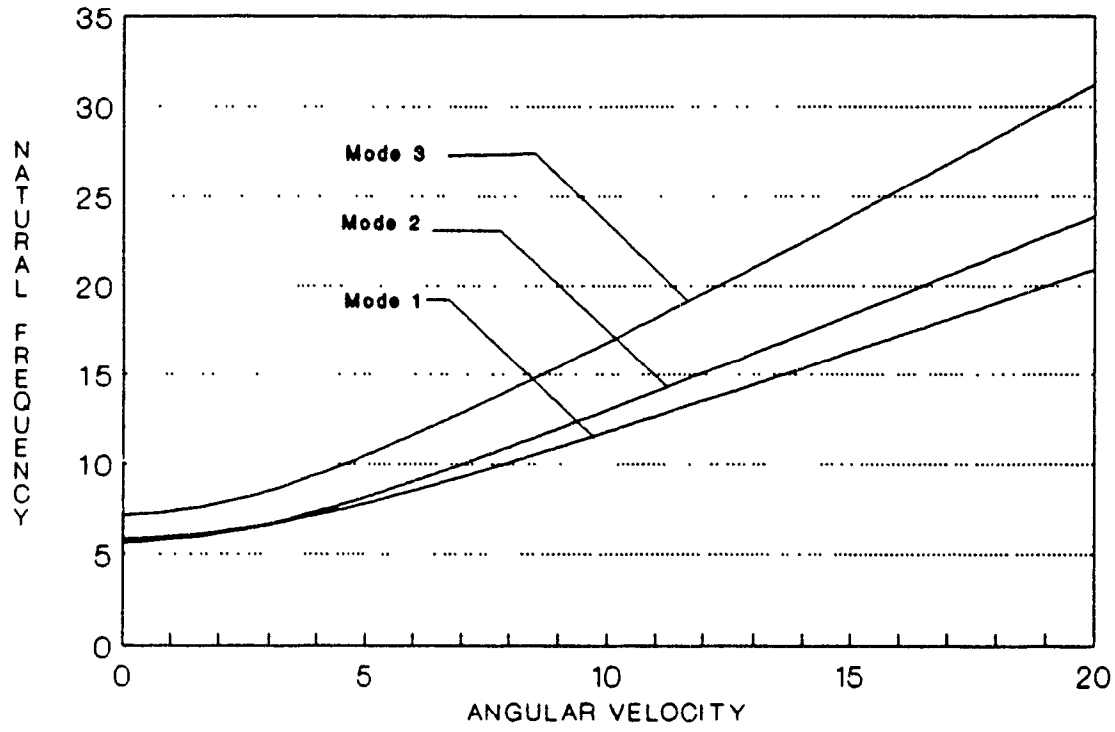

Fig. 3.10 : Variation of the Natural Frequency with Speed (β = 0.25)

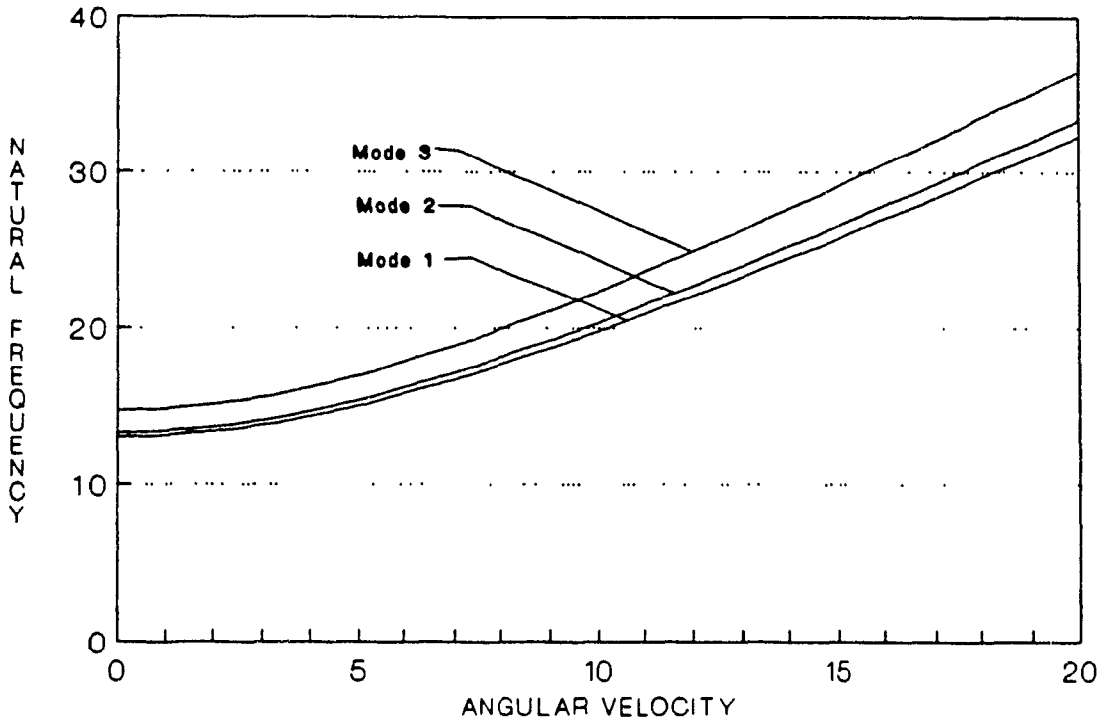

Fig. 3.11: Variation of Natural Frequency with Speed (ß = 0.5)

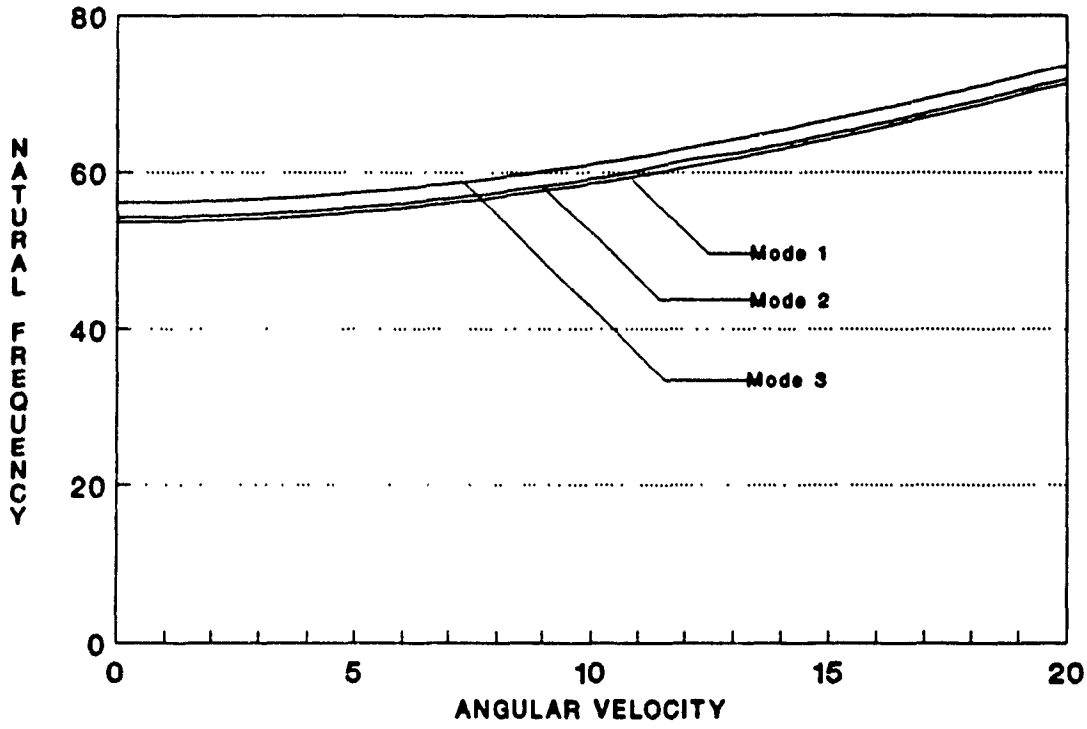

Fig 3.12.: Variation of Natural Frequency with Speed
(β = 0.75)

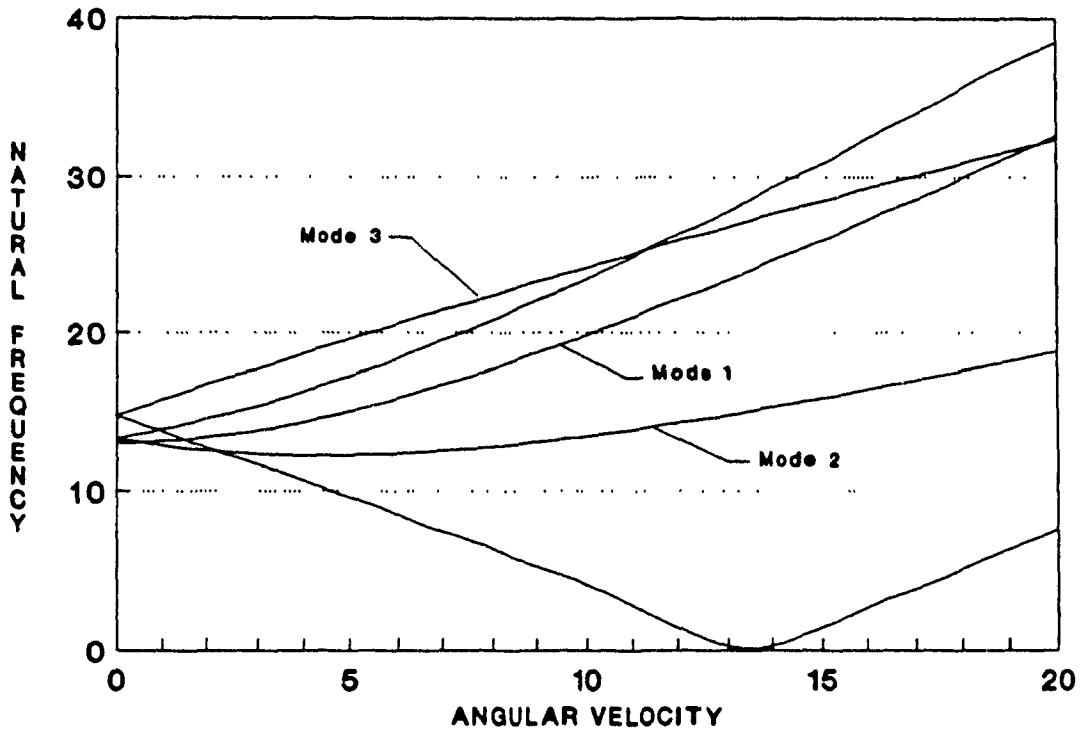

Fig. 3.13 : Variation of Natural Frequency with Speed
(β = 0.5)

CHAPTER 4

DYNAMIC ANALYSIS OF BLADED-DISK ASSEMBLY

4.1 : General

The determination of the natural frequencies of bladed disks is important in the design of turbomachines in order to prevent harmful resonances and ensure reliable operation of the turbine engine. The vibration of the turbo-machines is a coupled motion involving both the blades and the disk. The interaction between the blades and the disk will significantly effect the frequencies of the system depending upon the relative stiffness of the disk and the blades. Hence, it is essential to study the bladed disk system to understand the free vibration characteristics of the system.

In this chapter free vibrational behaviour of a bladed - disk assembly is studied using the finite element program, ANSYS [100]. Pertinent description of the finite element analysis program is provided in this chapter. The variation of the natural frequencies and mode shapes with speed are obtained for a typical bladed-disk system.

4.2 : ANSYS Finite Element Analysis Program

The ANSYS finite element program [100] is a large scale general purpose program which has the capabilities for linear and non-linear static and dynamic analyses. It can handle small and large displacements, as well as solve problems involving elastic, plastic, creep and swelling effects. It utilizes the matrix displacement method for the analysis and the wavefront method for matrix reduction and solution. The program contains many routines, which are all inter-related. An extensive element library makes it feasible to analyze two or three dimensional structures.

There are basically three phases involved in an ANSYS solution. Figure 4.1 and Figure 4.2 show the flow chart of the analysis methodology for any type of problem and the main routines involved in them.

The pre-processing is generally carried out using the Prep7 module either interactively or by inputting the model data from a CAD finite element modelling pre-processor. User interaction in this module is done by using a command language

specific to this module. Each module performs a different operation and contains a unique set of commands. The basic Prep7 flow chart is shown in Figure 4.3. Each file mentioned in the figure is intended to store the data whether it be for the solution phase, for plotting the geometry, or for the resumption of data. Any one of the different analyses shown in Figure 4.2 can be specified in this module before the model is sent for analysis. After the analysis stage, there are a number of post-processors available within ANSYS for the plotting and sorting of the data. Post12 is a general database processor for selecting, sorting, printing, and displaying results .

Based on this brief description of the ANSYS finite element package, in the next section the finite element model of the bladed - disk assembly is developed.

PREPROCESSING PHASE	SOLUTION PHASE	POSTPROCESSING PHASE
Mesh Generation	Element Matrix Formulation	Post Solution Operations
Geometry Definition		
Material Definition	Overall Matrix Triangularization	Post Data Printout
Constraint Definition		
Load Definition	Displacement, Stress, Etc.,	Post Data Displays
Model Display	Calculations	

Fig. 4.1 : Typical Phases of an Analysis in ANSYS

PREP 7	ANALYSIS TYPES	POST 26-30
General Mesh Generation and Model Definition	0 - Static 1 - Buckling 2 - Modal 3 - Harmonic 4 - Non Linear Dynamic etc.	Graph Displays Solution Combinations Tabular Printout

Fig. 4.2 : Basic ANSYS Routines Associated with the Three Phases

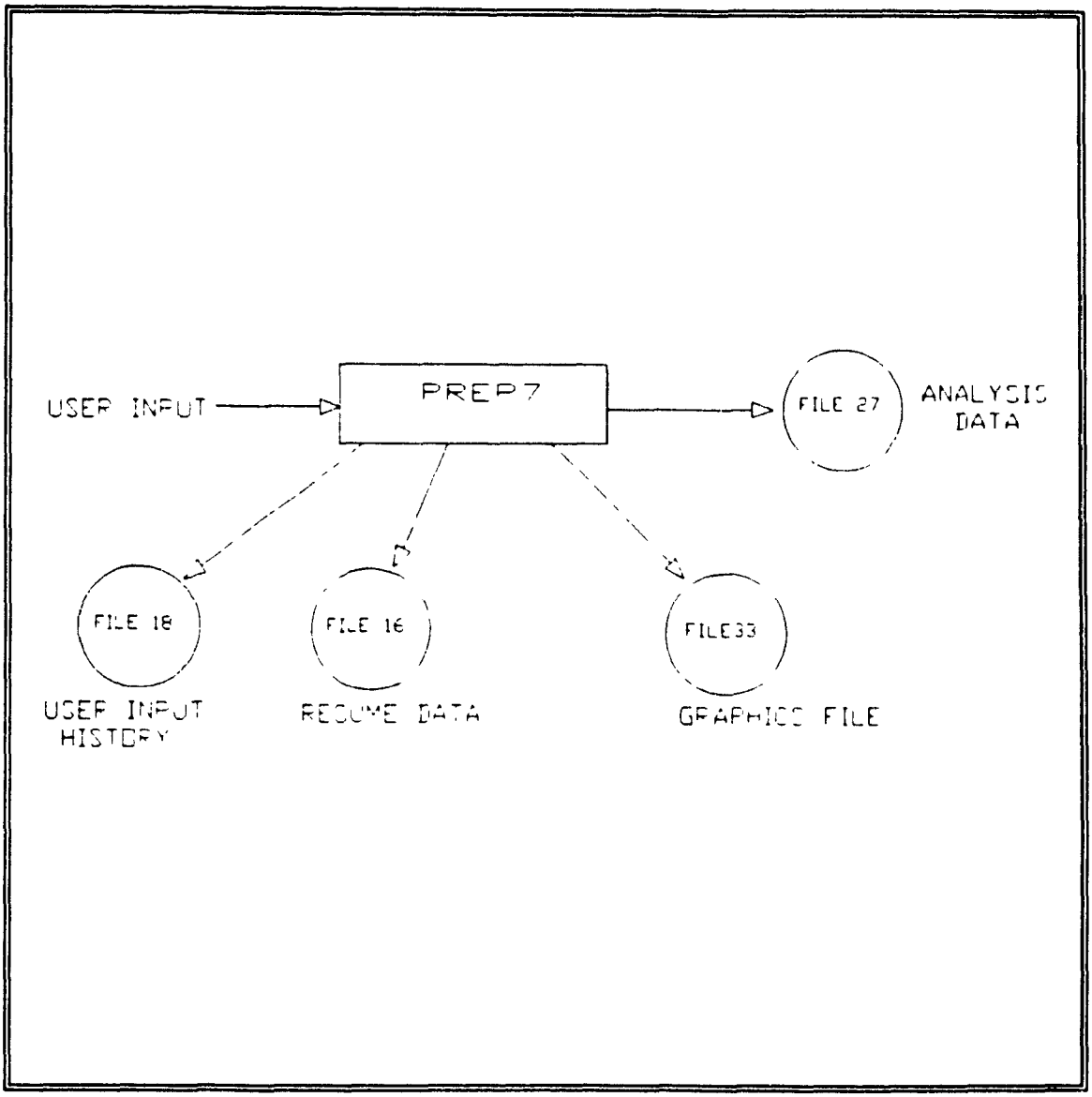

Fig. 4.3. : Basic Prep7 Data Flow Diagram

4.3 : Finite Element Model of the Bladed - Disk Assembly

The bladed-disk assembly is shown in Fig 4.4. The assembly consists of a disk with 12 blades mounted on it, having identical geometric, material and constraint properties. The disk is assumed to be clamped at the center. The system rotates with constant angular velocity ω, about the z-axis.

Figures 4.5 and 4.6 show the finite element models of the bladed-disk assembly as displayed using some of the commands in the Prep7 module of ANSYS. Fig. 4.5 also shows the boundary conditions at the inner periphery of the disk. Elastic quadrilateral shell elements of different geometric properties are used to model the assembly. The assembly is composed of 444 nodes and 360 elements. Standard steel material properties were input into ANSYS for analysis purposes.

Table 4.1 shows the dimensions and material properties that are used for the analysis of the bladed-disk assembly:

Table 4.1 : Bladed-Disk Assembly Parameters

Modulus of Elasticity	= 206.85 x 10^{9} N/m^2
Density	= 7.83 x 10^{-3} Kg/m^3
Poisson's Ratio	= 0.3
Disk Inner Radius (a)	= 5.08 x 10^{-2} m
Disk Outer Radius (b)	= 18.03 x 10^{-2} m
Blade Tip Radius (c)	= 24.64 x 10^{-2} m
Disk Thickness	= 0.635 x 10^{-2} m
Blade Thickness	= 0.3175 x 10^{-2} m
Blade Width	= 3.1475 x 10^{-2} m

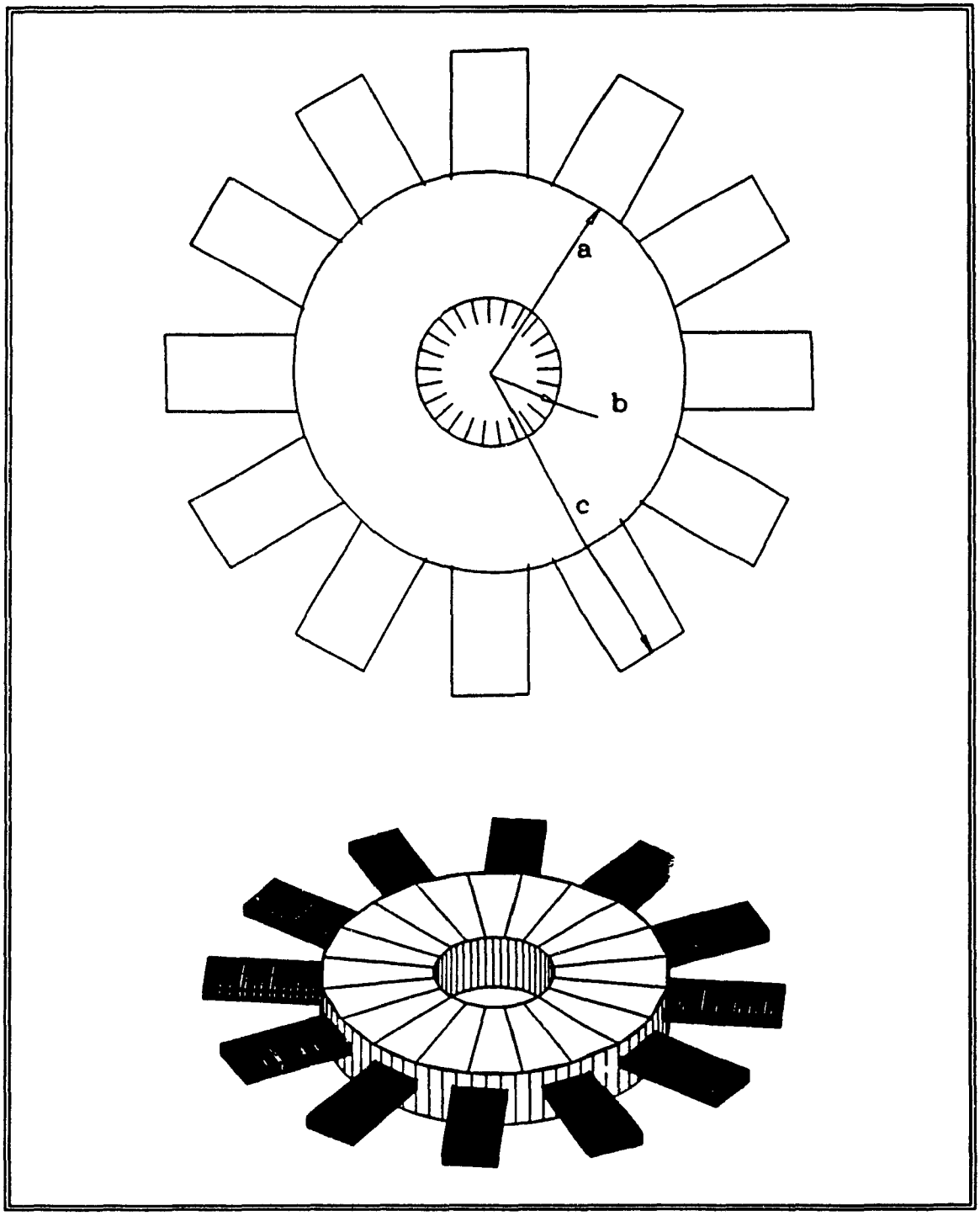

Figure 4.4 : Bladed-Disk Assembly

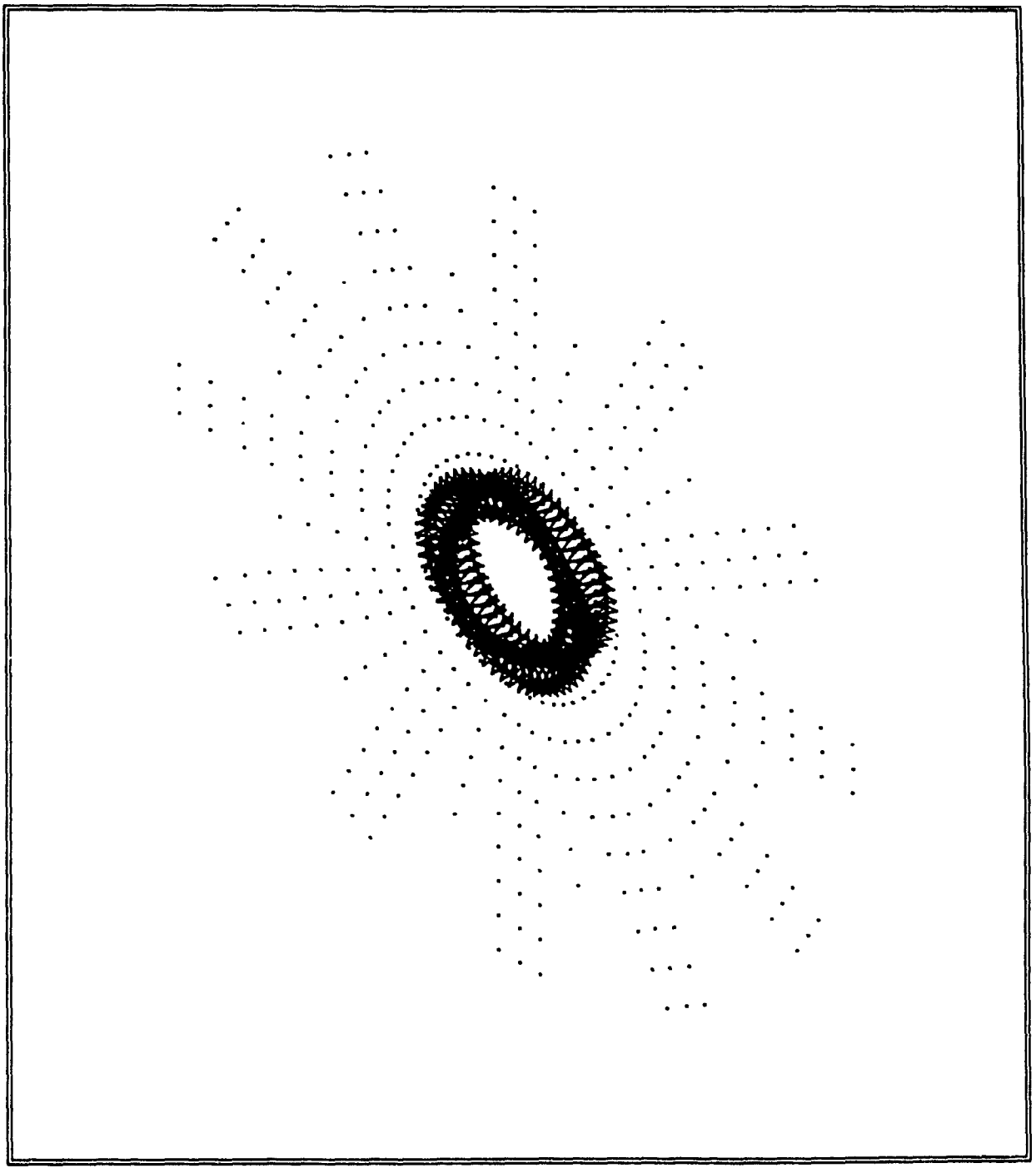

Figure 4.5 : Finite Element Model of the Bladed-Disk Assembly (Node Plot)

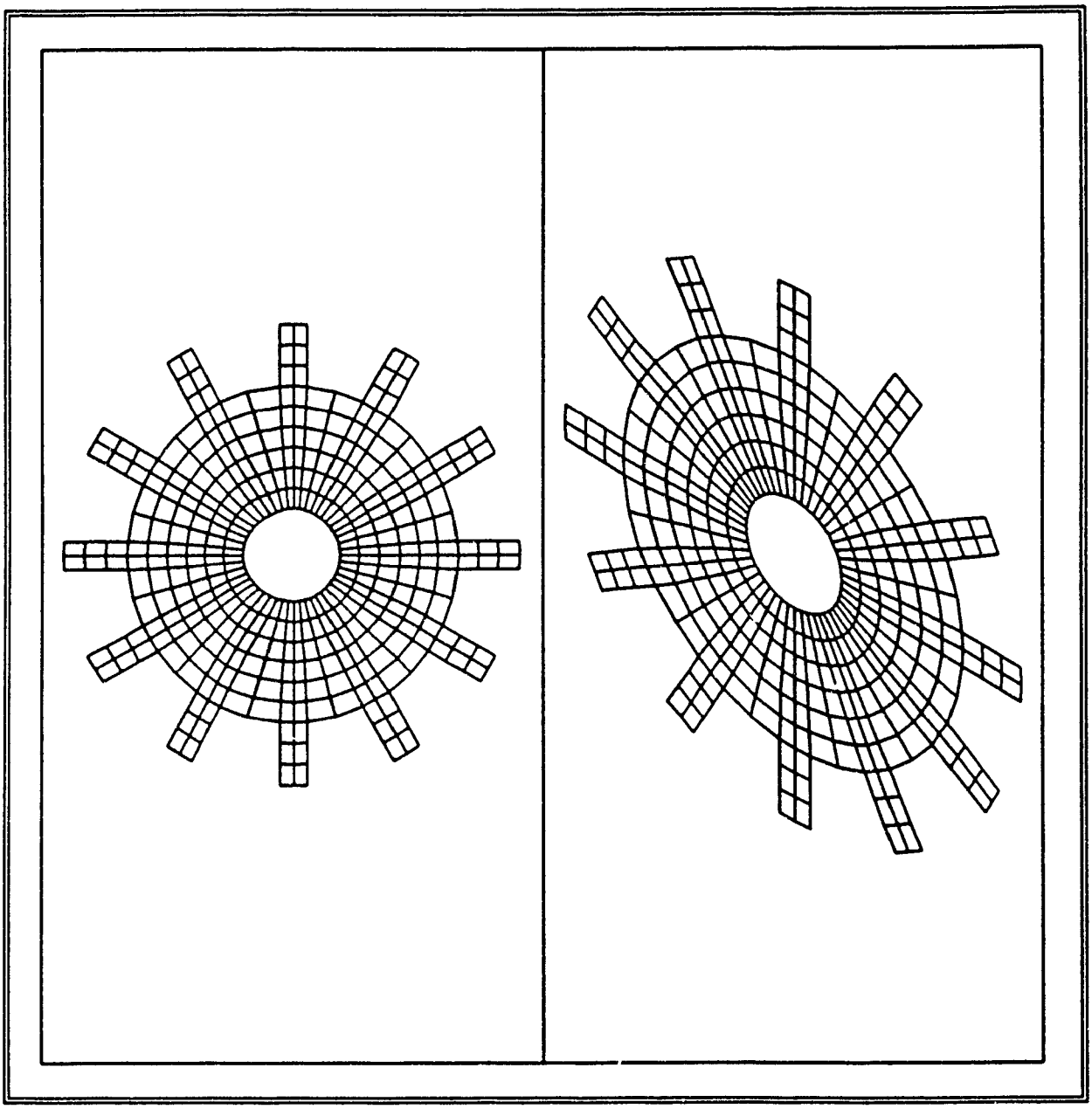

Figure 4.6 : Finite Element Model of the Bladed-Disk Assembly (Element Plot)

Modal Analysis is carried out in the solution phase of the ANSYS program invoking KAN=2 subroutine to obtain the natural frequencies and mode shapes.

The governing equation for free, undamped vibrations is,

$$M\ddot{u} + Ku = 0 \qquad (4.1)$$

where M and K are the mass and stiffness matrices, respectively, and u is the displacement vector.

For a linear structure undergoing free vibration the displacements are harmonic of the form,

$$u = U_0 \cos pt \qquad (4.2)$$

Substituting in (4.1) it implies,

$$(K - p^2 M)\, U_0 = 0 \qquad (4.3)$$

where p is the frequency of vibration.

This is a standard eigenvalue problem and the natural frequencies and mode shapes are obtained by solving this equation.

Since the number of degrees of freedom in a 360 node

bladed-disk assembly could be about 2160, it is not economical to conduct a modal analysis with so many degrees of freedom. Therefore, one of the features of the ANSYS program, namely, the Guyan reduction, is utilized by specifying the master degrees of freedom. The mass and stiffness matrices may be full or they may be reduced by the Guyan reduction scheme to contain only selected master degrees of freedom. The purpose of specifying such a subset is to reduce the complexity of the analysis by including those degrees of freedom which are sufficient to characterize the behaviour of the structure. The master degrees of freedom may be specified explicitly by the user, selected automatically by ANSYS or chosen by a combination of both. Commands are so chosen in the program such that the bending direction of the blade disk assembly is specified as a master degree of freedom and other master degrees of freedom are selected automatically by the program. Guyan reduction is a static reduction scheme and the influence of this reduction on the results of the dynamic analysis of rotating structures is not studied in this thesis but it is a potential area for future investigation.

Natural Frequencies and mode shapes of the bladed-disk assembly are obtained for various values of the setting angle using the reduced modal analysis procedure. Figure 4.7 shows the solution flow chart for the reduced modal analysis.

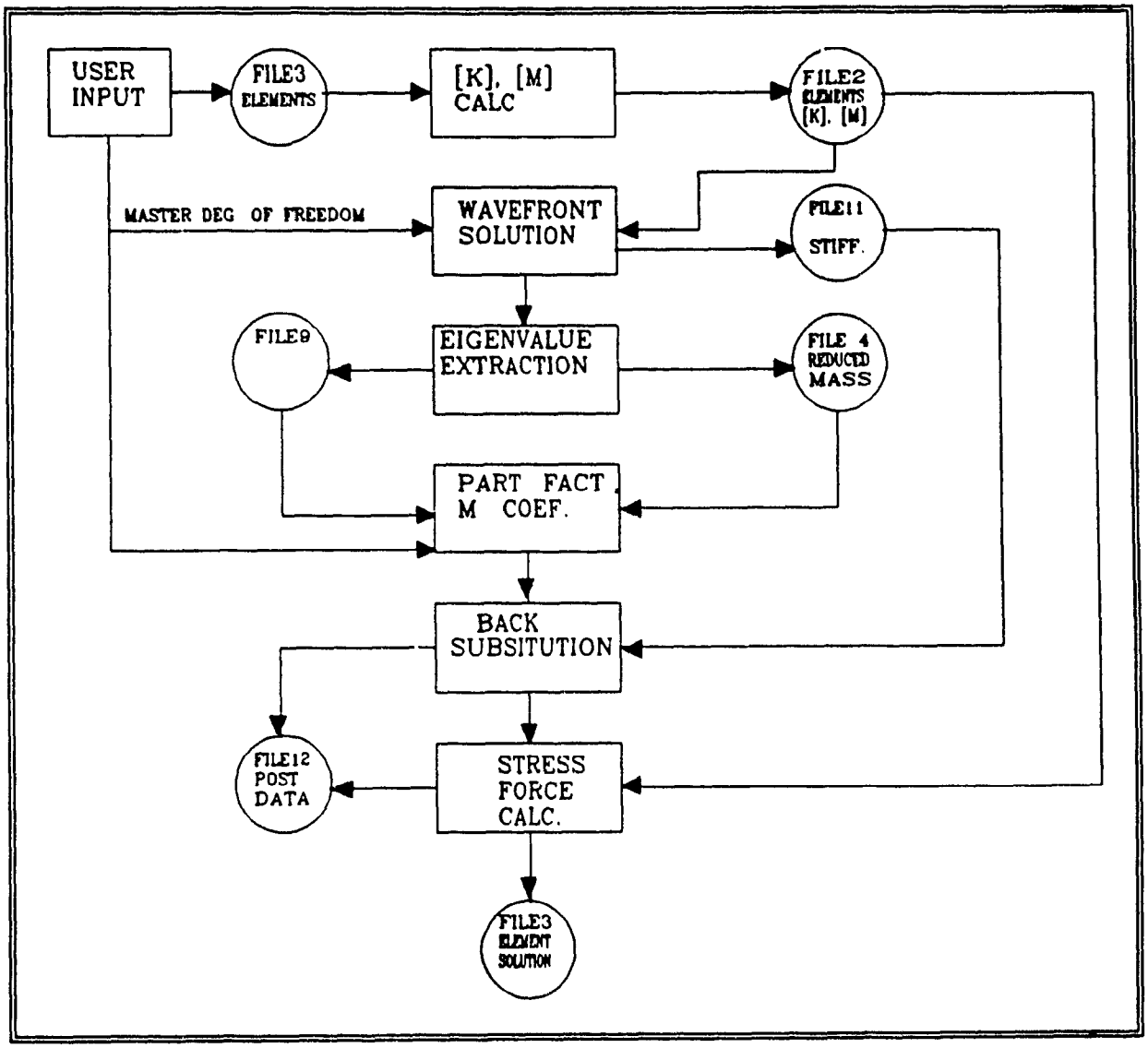

Fig. 4.7. Reduced Modal (KAN=2) Analysis Solution Flow Chart

4.4 : Discussion of results

Natural frequencies and mode shapes for a bladed disk assembly are obtained at different rotational speeds and setting angle.

The variation of the natural frequency with rotational speed for the first fifteen modes is presented in Tables 4.2 and 4.3. From these tables it can be seen that as the rotational speed is increased the natural frequencies increase.

Variation of natural frequencies with speed for the first three modes of vibration for a bladed disk and a disk are presented in Figs. 4.8 through 4.10. It can be seen from these figures that with the inclusion of the blades the natural frequencies decrease. This is understandable because the increase in mass due to the blades does not increase the stiffness of the bladed disk proportionately. This is illustrated using a simple model consisting of two beams with different geometrical properties as shown in Fig 4.11. From this simple model it can be seen that the fundamental frequency decreases with the inclusion of the smaller second beam thus illustrating the reduction of natural frequencies in

the bladed disk model.

The effect of the setting angle on the natural frequency is shown in Fig. 4.12. It can be seen that for a constant rotational speed the increase in the setting angle of the blade has no significant effect on the natural frequency of the bladed disk assembly.

The mode shapes of the bladed disk assembly are presented in Figs. 4.13 through 4.22. The solid lines represent the original shape and the dashed lines are the displaced shape. From Figs. 4.13 and 4.14 it can be seen that there is a nodal line in the radial direction and the bladed disk on one side bends in an opposite direction relative to the other side. Figs.4.15 through 4.22 show the same behaviour of the bladed disk assembly with nodal lines in the radial and angular directions.

4.5 : Summary

The dynamics of a bladed disk assembly is studied using the finite element package ANSYS. Natural frequencies and mode shapes are obtained for different rotational speeds and for different setting angles. The results are compared to a single

disk analysis.

In the following chapter, dynamic analysis of a complete turborotor system with the inclusion of the support bearings is studied using the finite element package ANSYS.

Table 4.2:Variation of Natural Frequency with Rotational Speed

Mode Number	Angular Velocity (Hz)				
	0.0	83.3	166.6	249.9	333.2
1	229.2	250.9	301.4	364.9	436.9
2	229.2	251.2	305.9	379.5	462.6
3	236.0	254.7	306.2	380.2	463.8
4	269.5	296.1	363.1	453.5	556.3
5	269.7	296.2	363.2	453.8	556.5
6	398.1	424.1	492.3	587.8	699.2
7	398.1	424.2	492.4	588.1	699.7
8	490.5	517.6	590.4	692.5	811.1
9	490.8	517.6	590.8	693.0	811.7
10	525.1	553.4	630.5	738.6	863.8
11	525.9	554.3	631.3	739.3	864.5
12	534.4	563.2	641.4	751.3	878.7
13	664.0	703.7	790.3	918.8	1069.6
14	668.9	714.7	805.3	937.4	1095.9
15	670.1	715.1	805.6	939.3	1098.4

Table 4.3:Variation of Natural Frequency with Rotational Speed

Mode Number	Angular Velocity (Hz)				
	416.8	583.1	666.5	749.8	833.
1	513.8	676.3	759.4	843.3	927.9
2	551.1	737.3	832.5	928.6	1025.5
3	552.9	740.7	836.8	933.9	1031.7
4	665.8	895.8	1013.9	1133.3	1253.5
5	666.2	898.4	1017.1	1137.0	1257.9
6	820.0	1077.6	1210.6	1345.3	1481.3
7	820.7	1078.1	1211.2	1346.1	1482.3
8	939.0	1210.8	1351.1	1493.2	1636.8
9	939.9	1211.4	1351.7	1493.9	1637.6
10	998.2	1280.5	1425.3	1571.7	1719.3
11	998.9	1281.0	1425.8	1572.1	1719.7
12	1015.4	1301.5	1448.0	1595.8	1744.7
13	1235.4	1606.5	1794.7	1985.9	2179.4
14	1271.2	1650.8	1849.0	2050.8	2255.2
15	1274.2	1663.5	1864.1	2068.5	2275.5

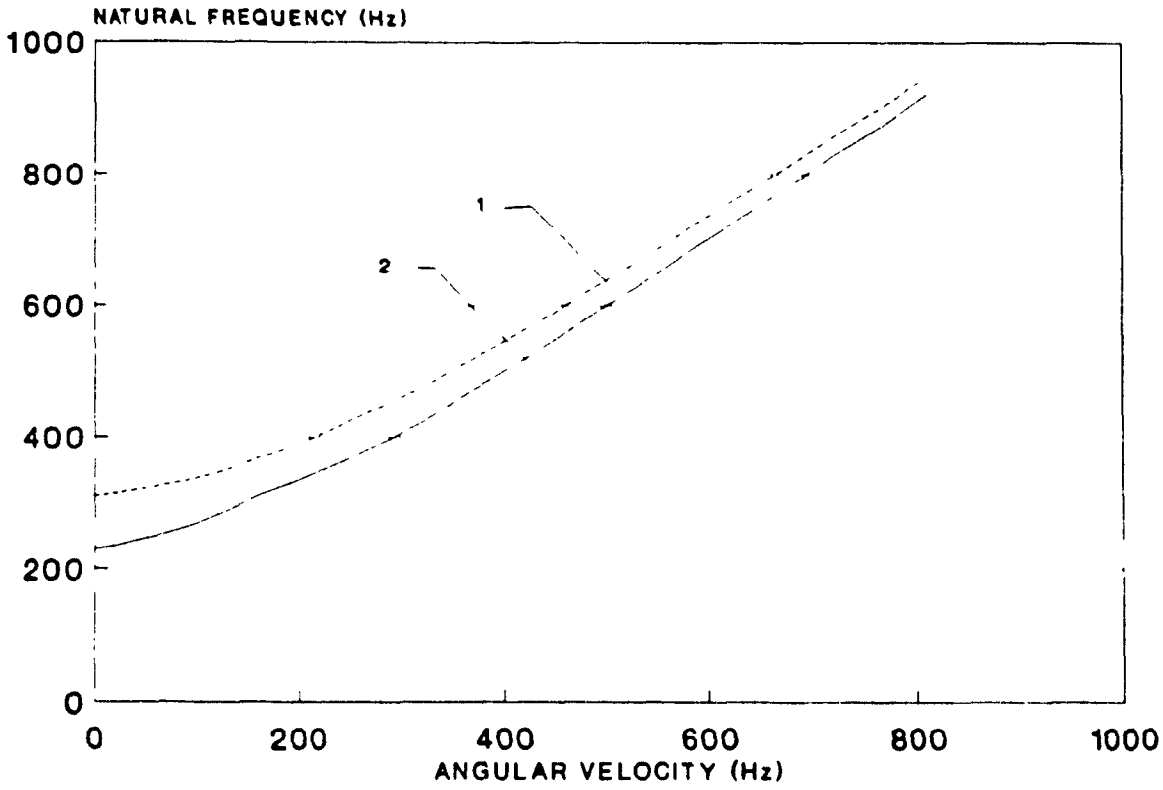

Fig 4.8 : Variation of First Natural Frequency with Speed

Curve 1 : Disk Frequency

Curve 2 : Bladed-Disk Assembly Frequency

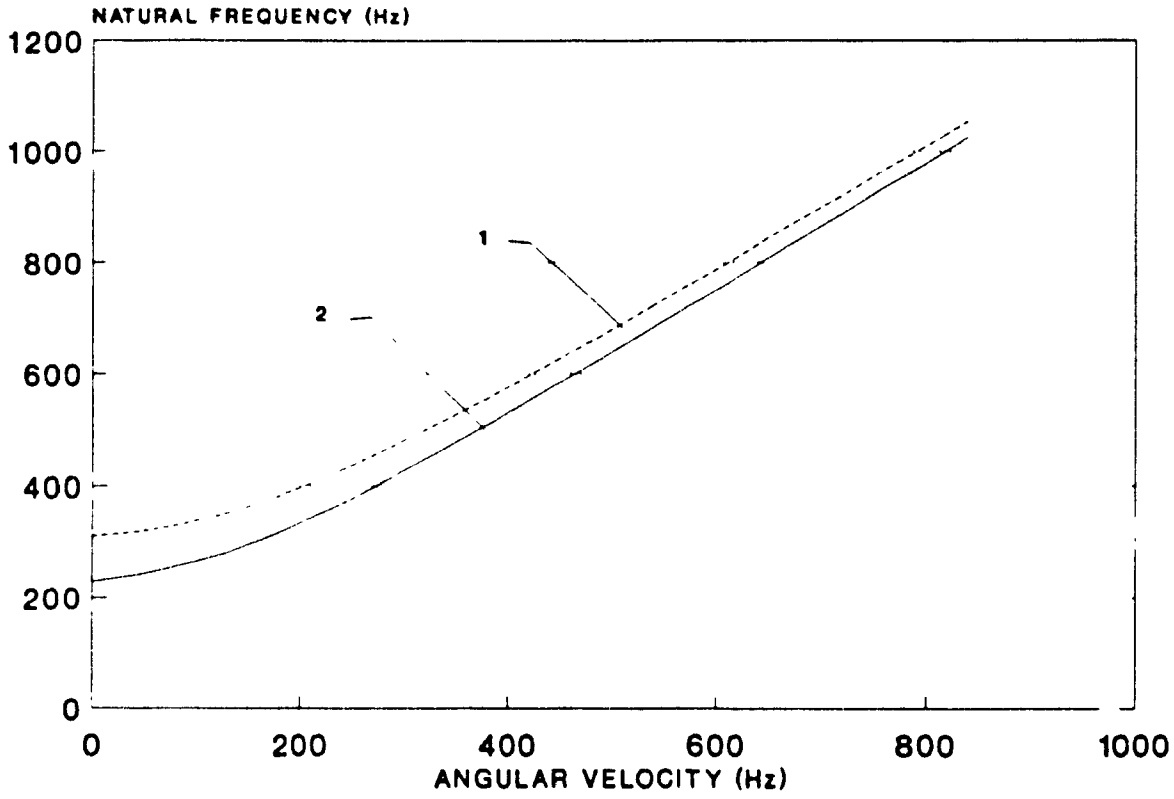

Fig 4.9 : Variation of Second Natural Frequency with Speed

Curve 1 : Disk Frequency

Curve 2 : Bladed-Disk Assembly Frequency

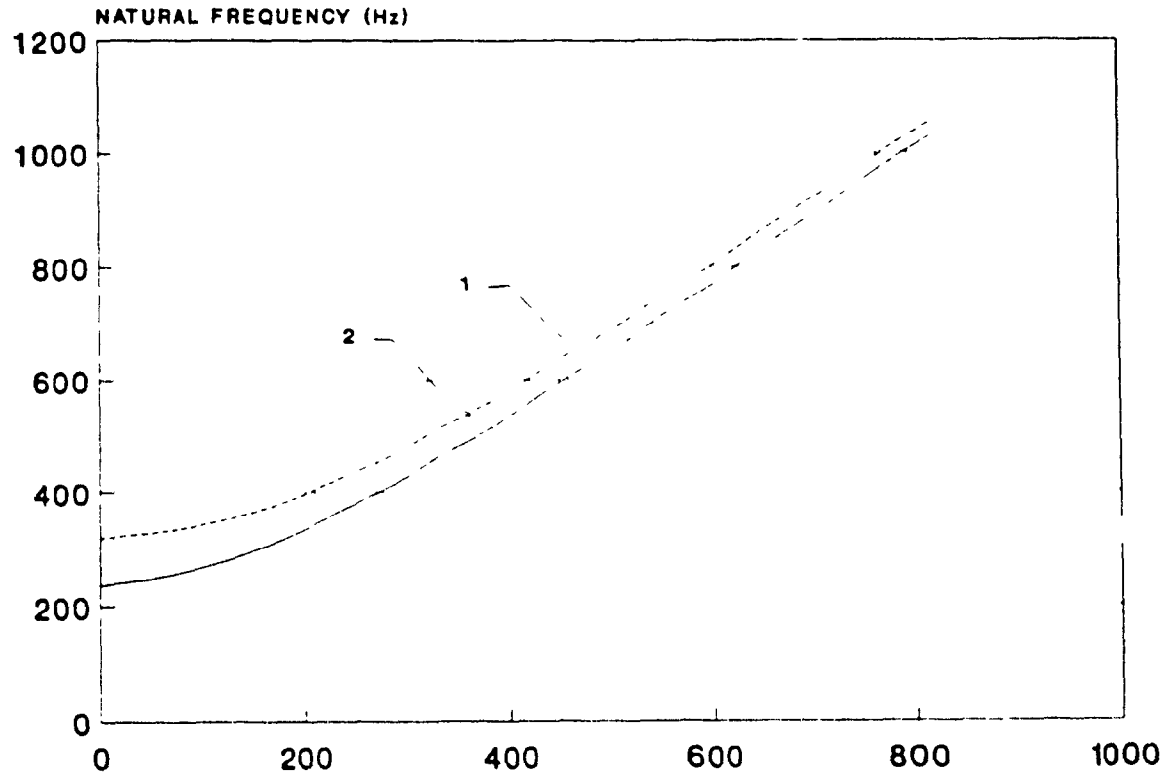

Fig 4.10 : Variation of Third Natural Frequency with Speed

Curve 1 : Disk Frequency

Curve 2 : Bladed-Disk Assembly Frequency

Beam Parameters:

$a=18.03 \times 10^{-2}m$ $c=24.64 \times 10^{-2}m$

$I_1=1.34318 \times 10^{-9}m^4$ $I_2=8.3940 \times 10^{-11}m^4$

$A_1=19.9866 \times 10^{-5}m^2$ $A_2=9.9933 \times 10^{-5}m^2$

$M_1=1.5589548$ kg/m $M_2=7.794774 \times 10^{-1}$ kg/m

Fundamental Frequency = 1.09×10^3 rad/sec

If only First Beam Present:

Fundamental Frequency = 1.836×10^3 rad/sec

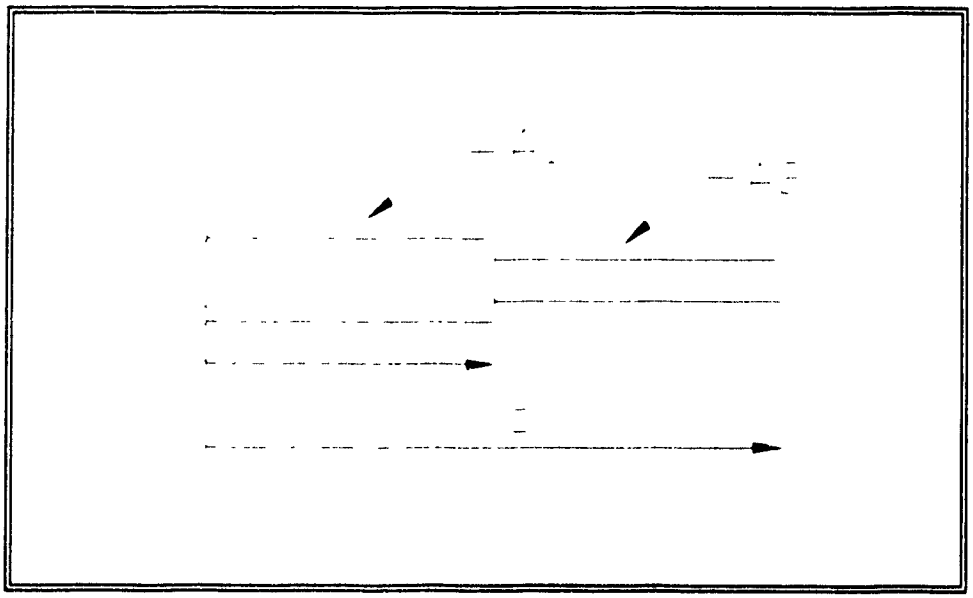

Fig. 4.11 : Beam Analogy Using Rayleigh-Ritz Method

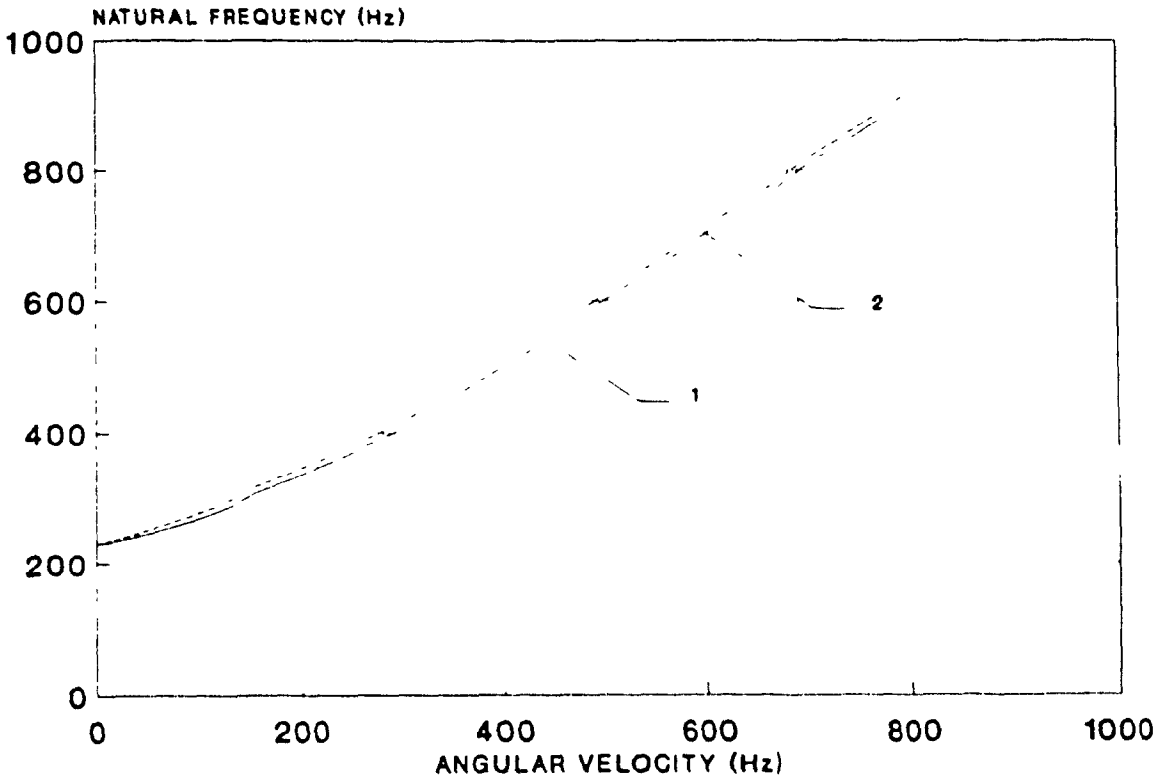

Fig. 4.12 : Variation of First Natural Frequency with speed for Different Values of the Setting Angle

Curve 1 : $\theta = 0°$ Curve 2 : $\theta = 60°$

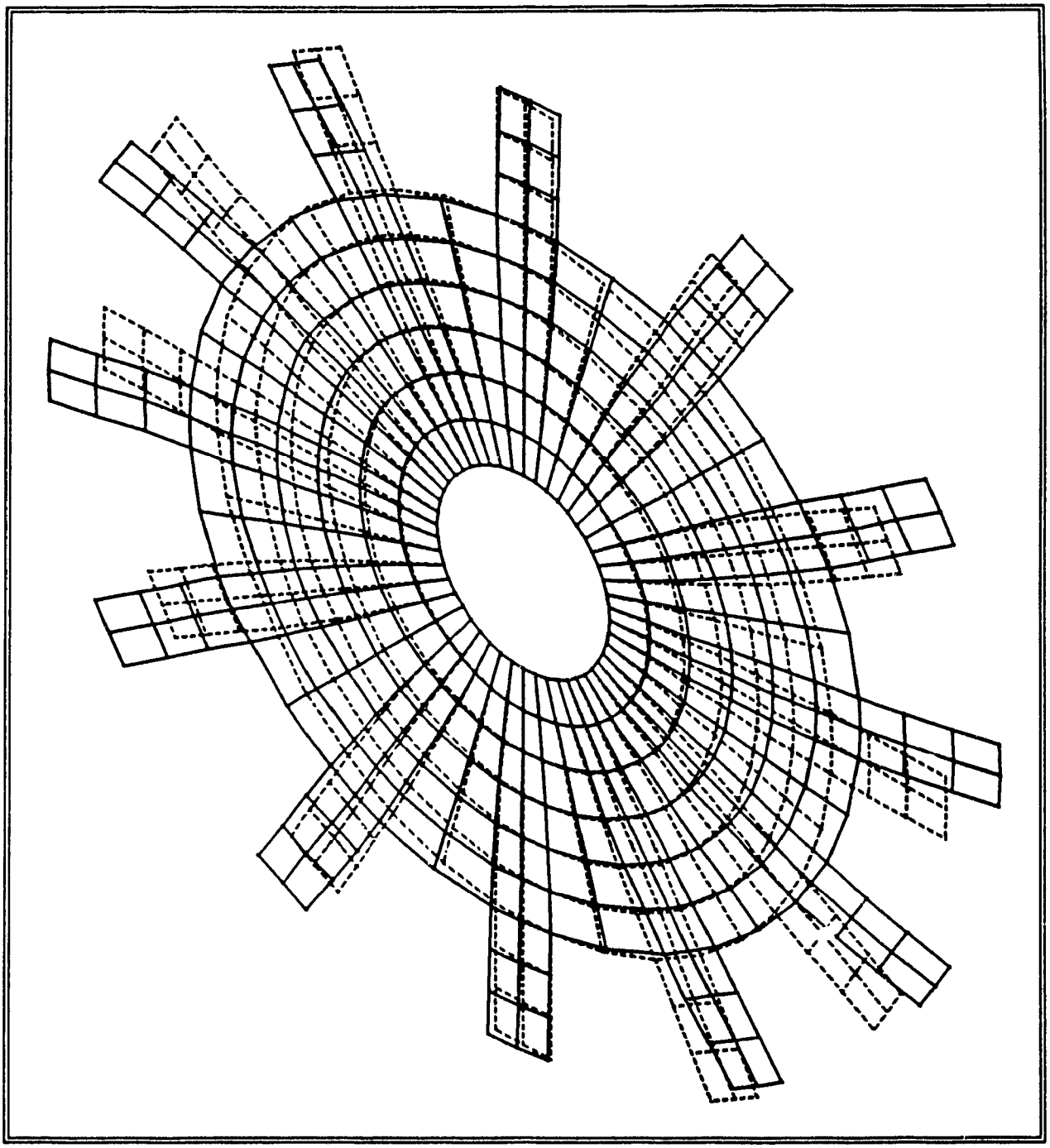

Fig.4.13 : Mode Shape of the Bladed-Disk Assembly
(at 229.21 Hz)

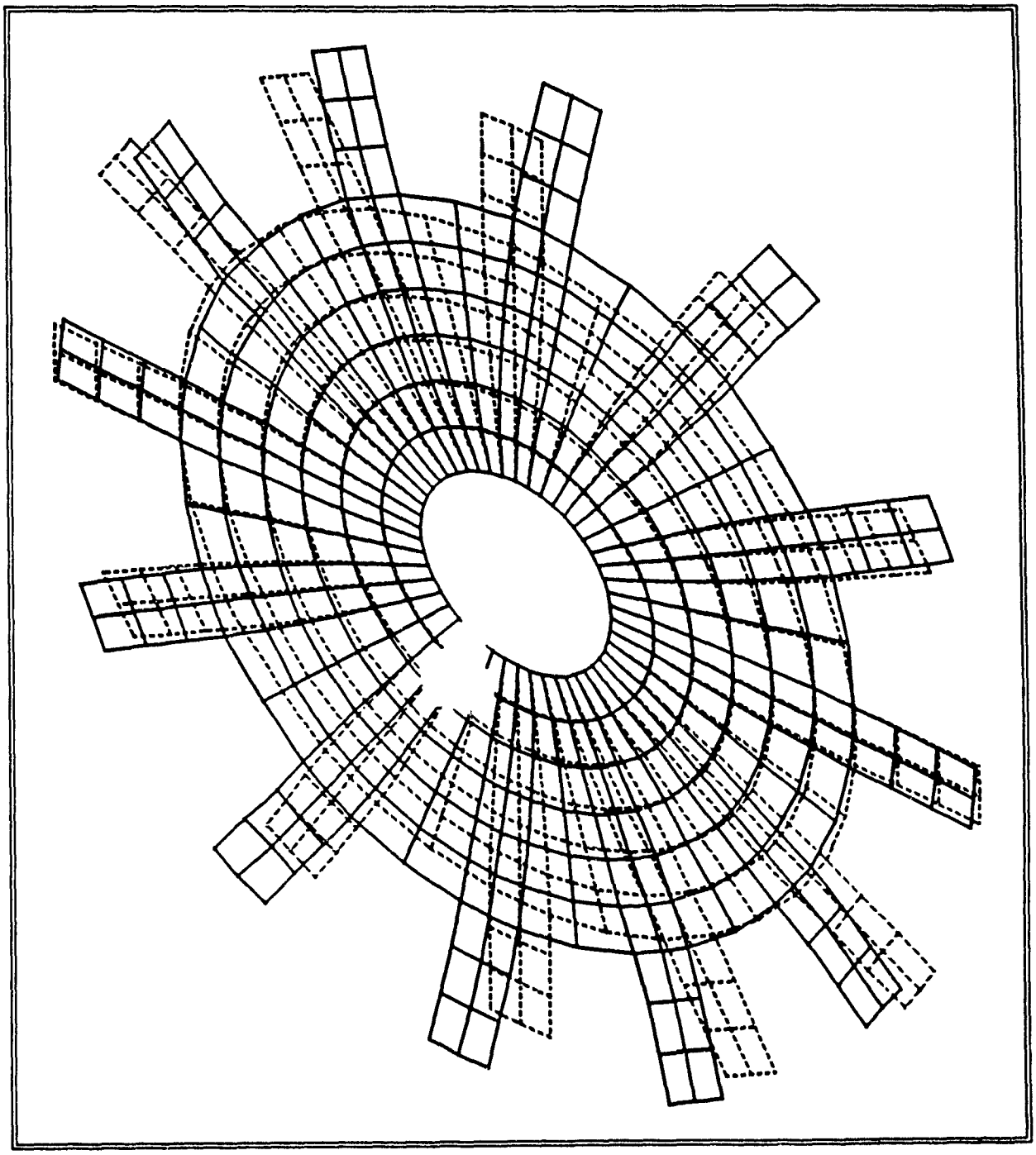

Fig.4.14 : Mode Shape of the Bladed-Disk Assembly
(at 229.23 Hz)

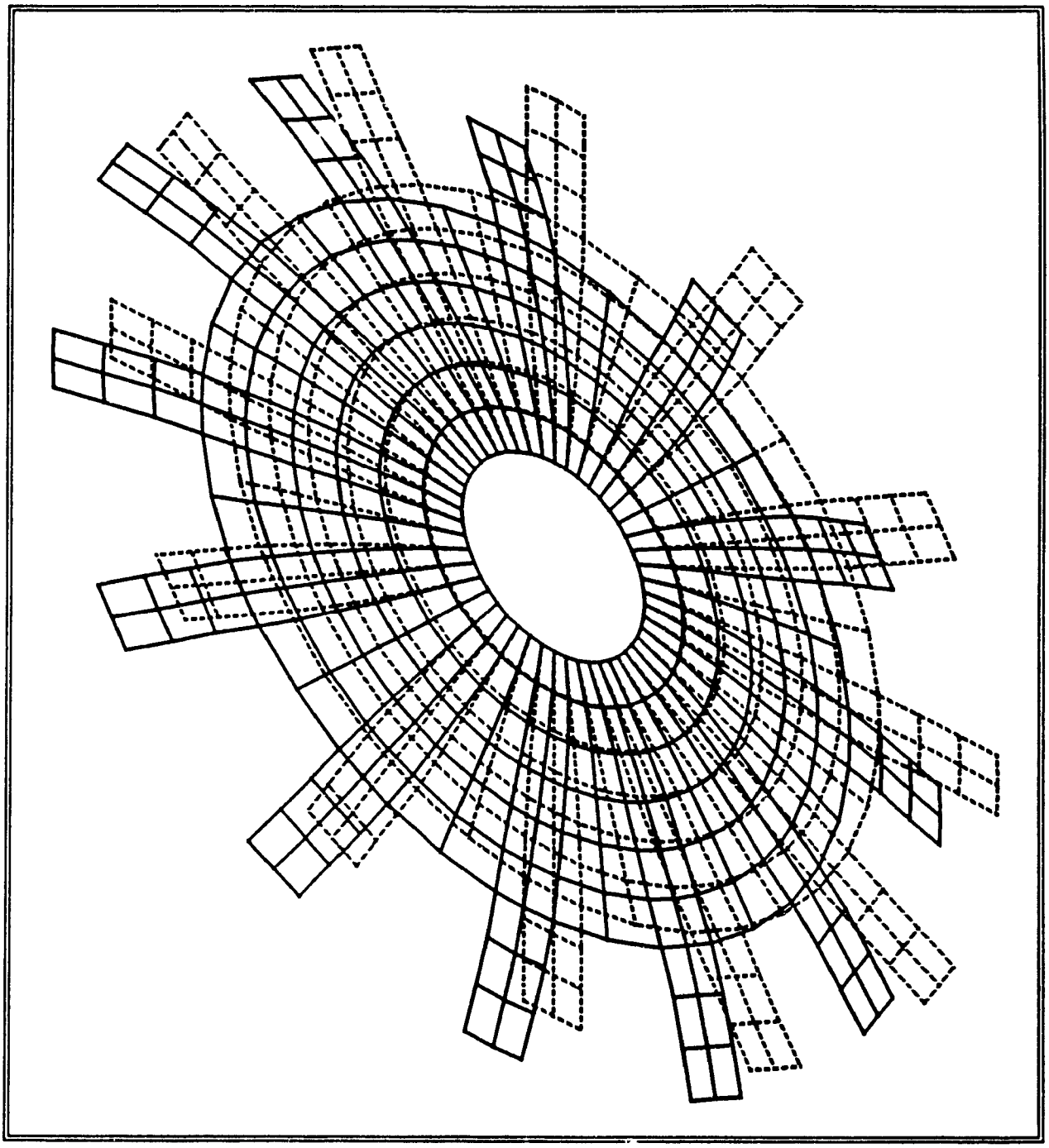

Fig.4.15 : Mode Shape of the Bladed-Disk Assembly
(at 236.05 Hz)

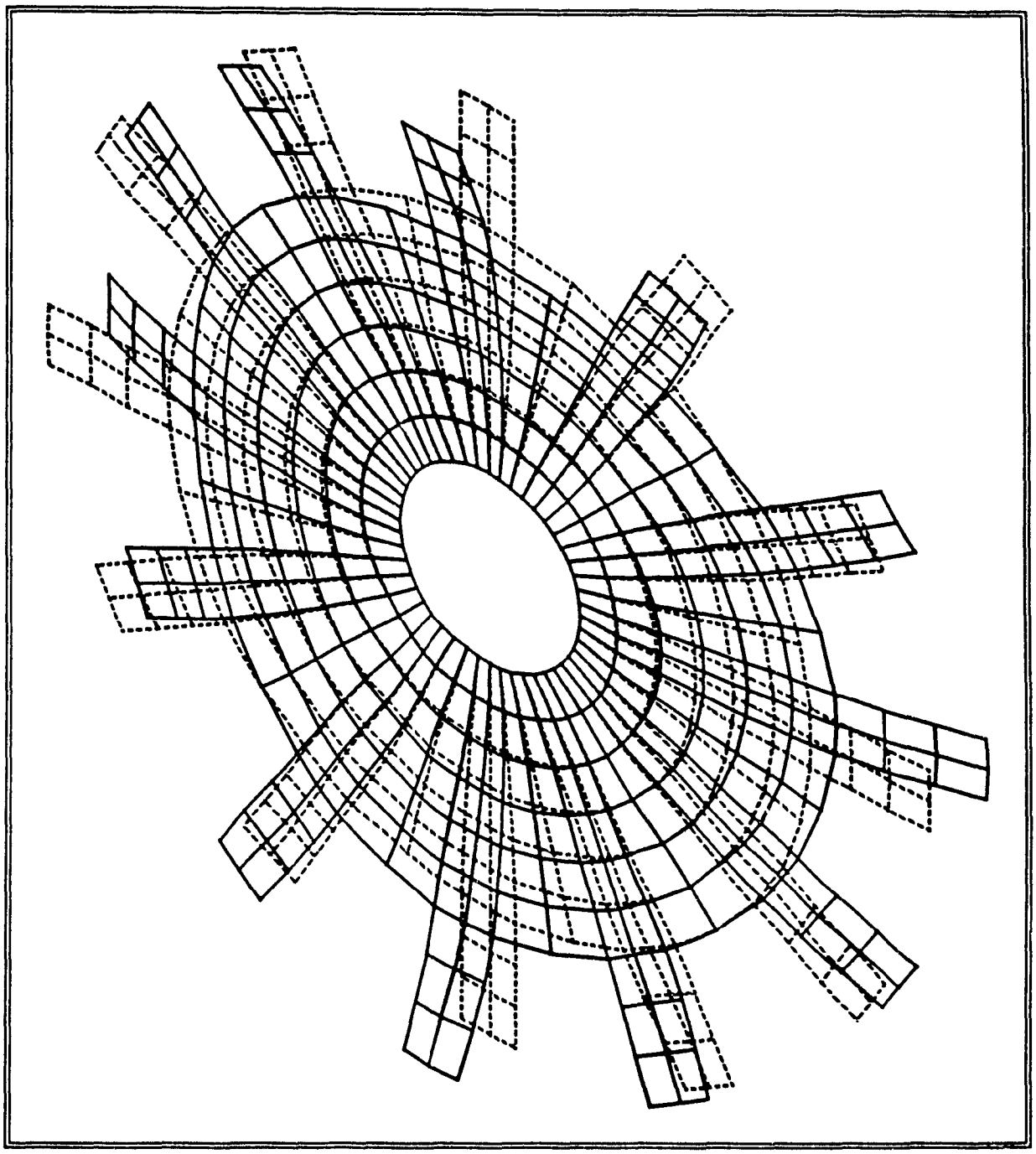

Fig.4.16 : Mode Shape of the Bladed-Disk Assembly
(at 269.50 Hz)

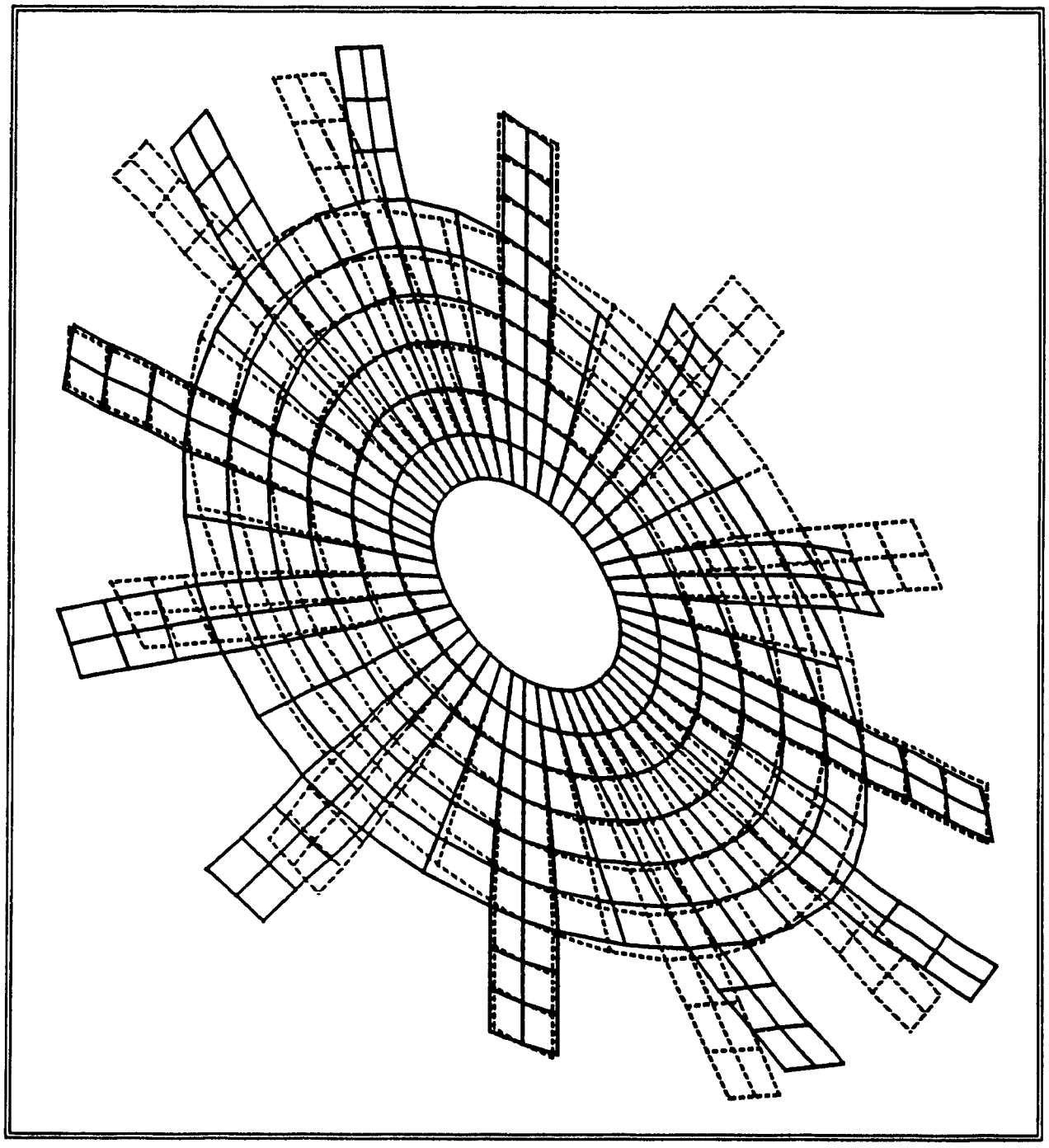

Fig.4.17 : Mode Shape of the Bladed-Disk Assembly
(at 269.79 Hz)

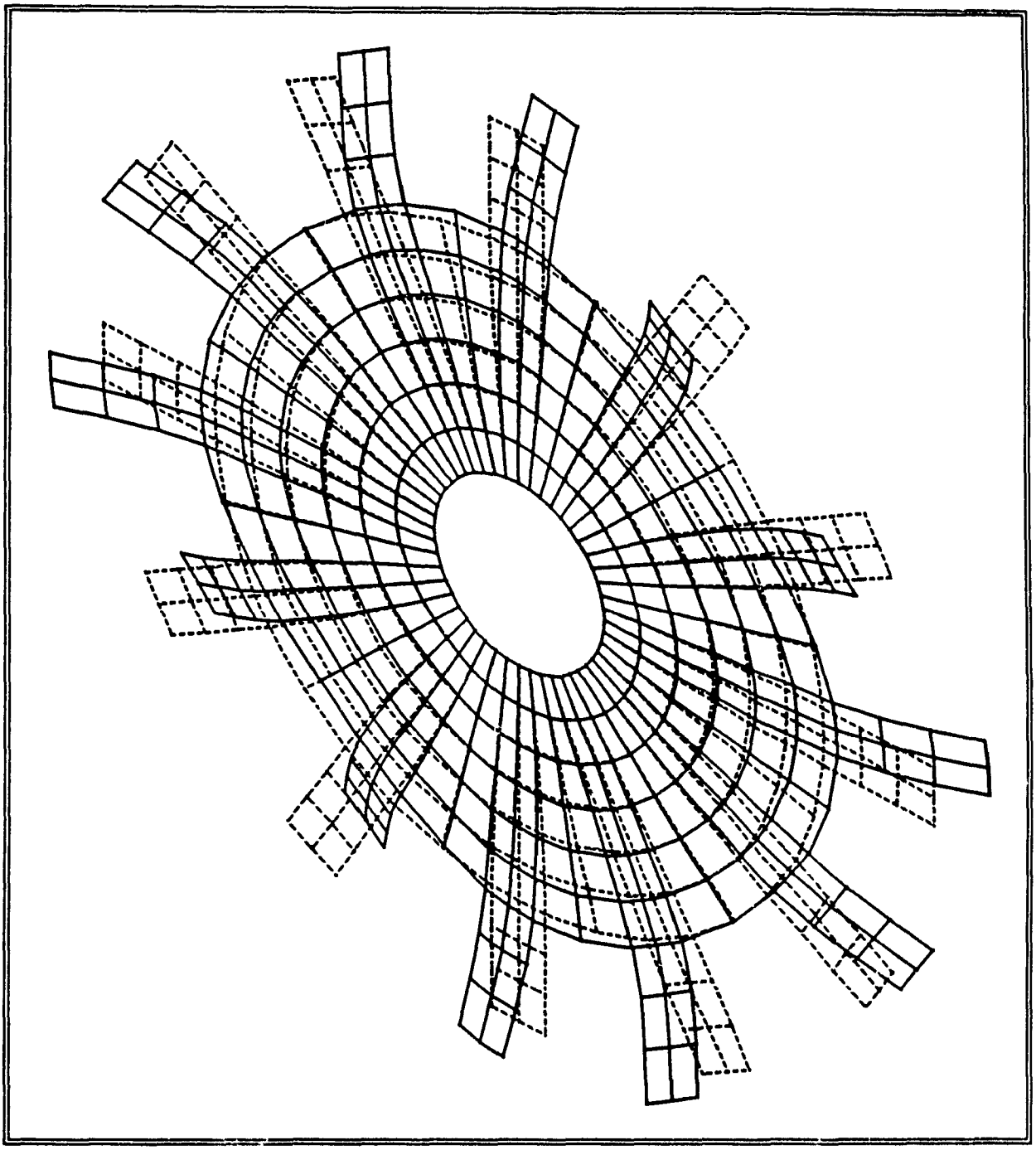

Fig.4.18 : Mode Shape of the Bladed-Disk Assembly
(at 398.13 Hz)

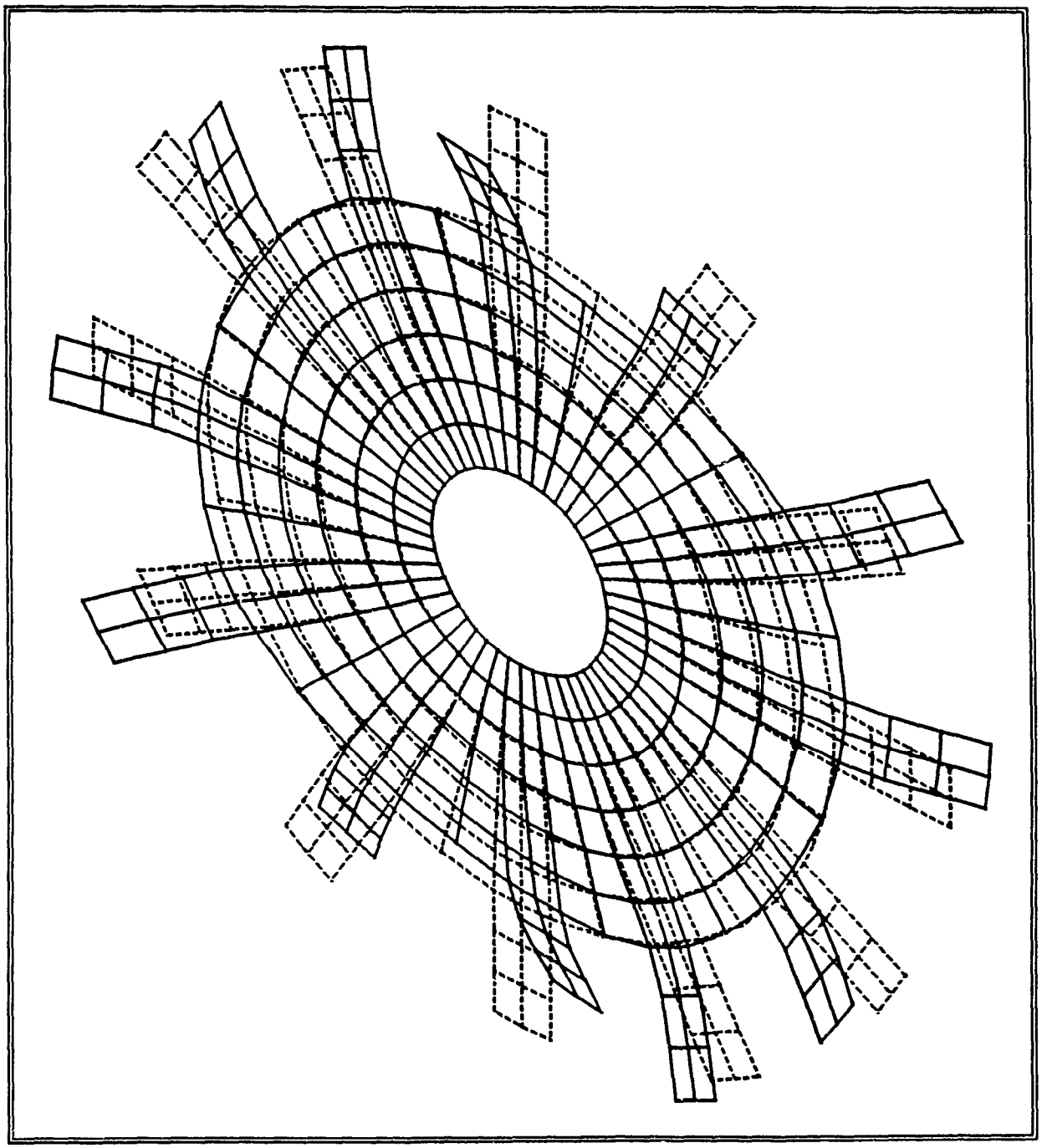

Fig.4.19 : Mode Shape of the Bladed-Disk Assembly (at 398.16 Hz)

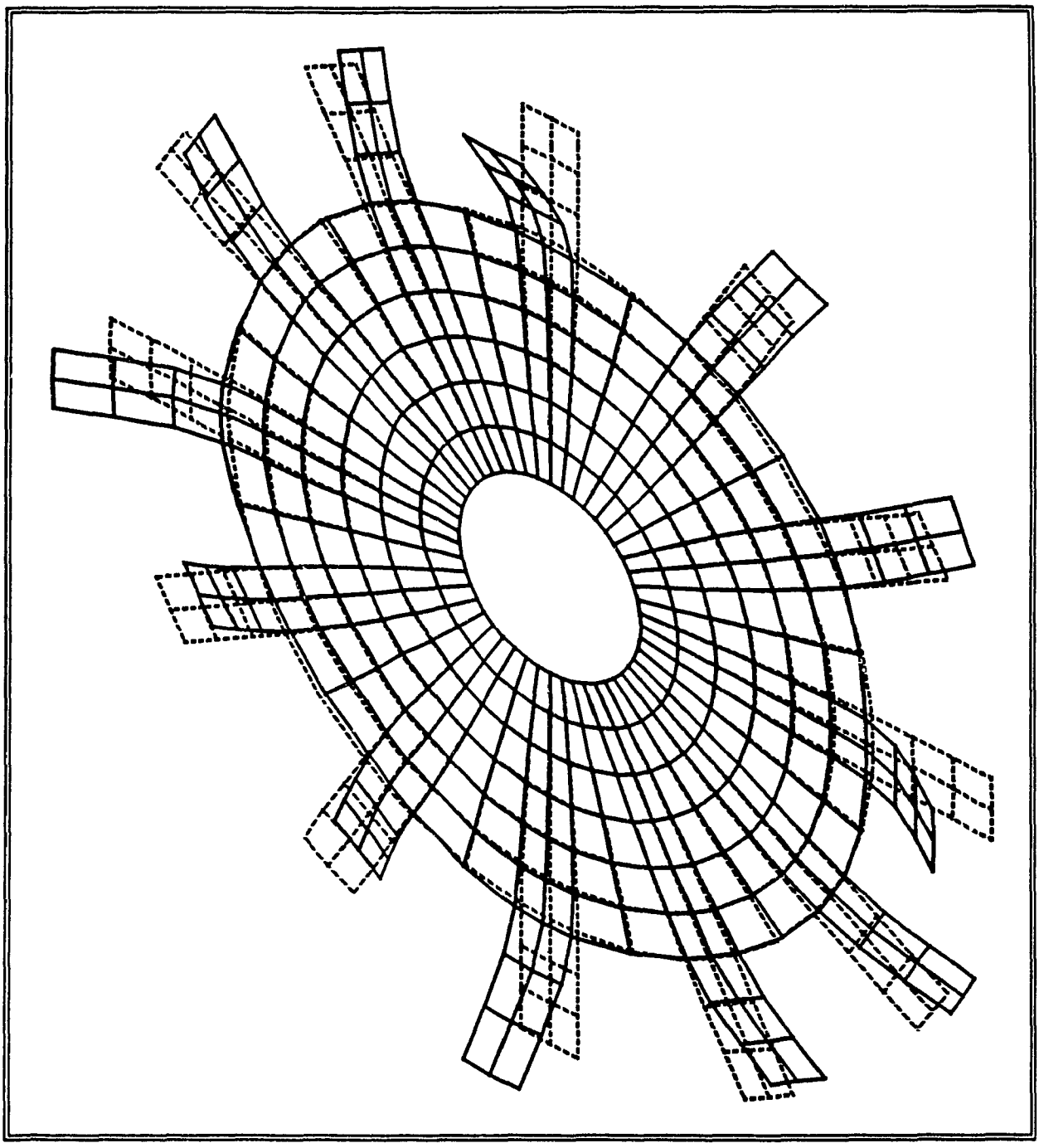

Fig.4.20 : Mode Shape of the Bladed-Disk Assembly (at 490.54 Hz)

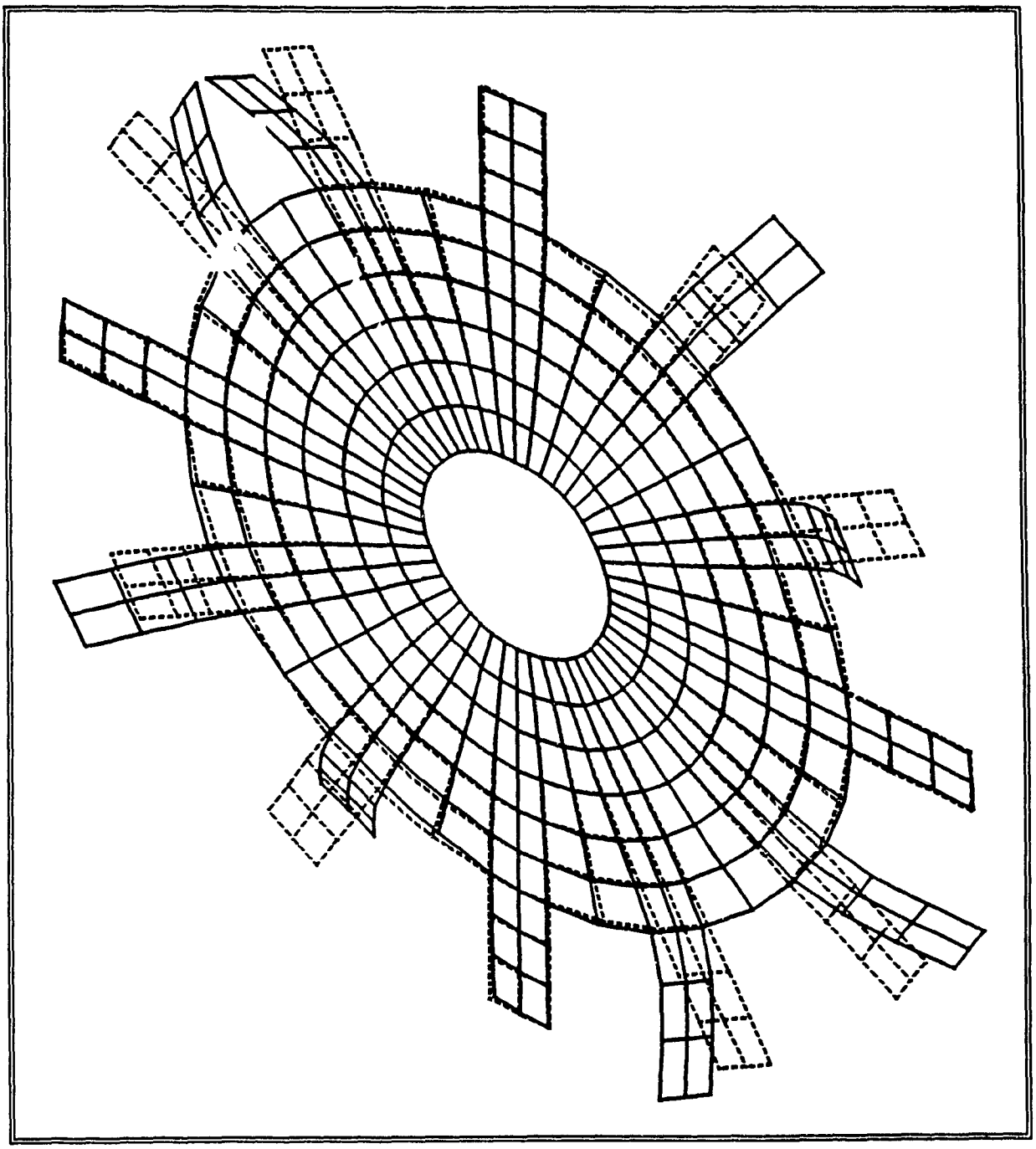

Fig.4.21 : Mode Shape of the Bladed-Disk Assembly (at 490.84)

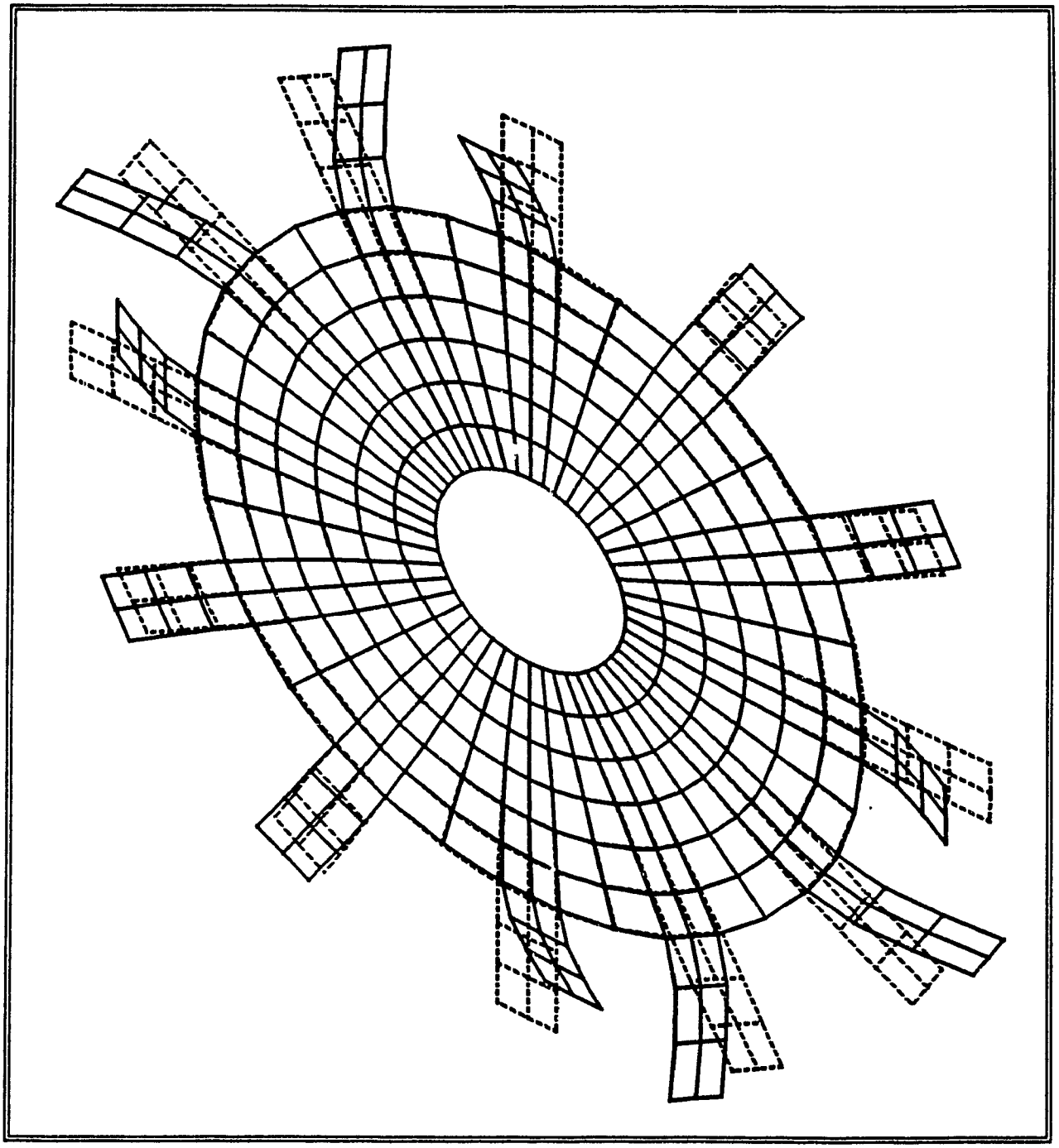

Fig. 4.22 : Mode Shape of the Bladed-Disk Assembly (at 525.03 Hz)

CHAPTER 5

DYNAMIC ANALYSIS OF A TURBOROTOR SYSTEM

5.1 : General

Rotor shaft designers in the field of turbomachinery usually make the assumption that any disks attached to the shaft are rigid. This assumption is generally a satisfactory approximation, but can be very optimistic if a disk is thin enough to have a disk bending frequency comparable to the rotor resonant frequency. In addition, the coupling between the blade, disk as well as the rotor shaft and the bearings on which the turborotor is supported further complicates the dynamics of the total system. Hence, to ensure reliable operation of the turborotor system, it is very important that a dynamic analysis of the complete system, including the coupling between its various components, be carried out.

In this chapter free undamped vibrations of a complete turborotor system is studied using the finite element program ANSYS. A real system would consist of some damping, which would be added as modal damping when the harmonic responses are evaluated in the next chapter. Pertinent descriptions of the finite element analysis program are described in Chapter 4. The variation of the natural frequencies and mode shapes with speed are obtained for a typical turborotor system.

5.2 : Finite Element Model of the Turborotor Assembly

The turborotor assembly is shown in Fig 5.1. The assembly consists of a rotating shaft mounted on bearings with linear stiffness parameters and having a disk with 12 blades mounted on it. The blades have identical geometric, material and constraint properties. The disk is assumed to be at the center point of the shaft and the system rotates with constant angular velocity ω, about the z-axis.

Figures 5.2 and 5.3 show the finite element models of the assembly as displayed using some of the commands in the Prep7 module of ANSYS. The bearings on which the turborotor assembly is mounted are modelled using a spring element having up to three degrees of freedom at each node. The rotating shaft is modelled using three dimensional beam elements having 6 degrees of freedom at each node, which are the translations in the nodal X, Y, Z directions and rotations about the nodal X, Y, and Z axes. Elastic quadrilateral shell elements having 6 degrees of freedom at each node with different geometric properties are used to discretize the bladed-disk assembly. The bladed -disk assembly is mounted at the center of the shaft and is coupled to the shaft through constraint equations.

The turborotor assembly is composed of 173 nodes and 109 elements. Standard steel material properties were input into ANSYS for analysis purposes.

Table 5.1 shows the dimensions and material properties that are used for the analysis of the turborotor assembly:

Table 5.1 : Turborotor Assembly Parameters

Modulus of Elasticity	= 206.85 x 10^{9} N/m^{2}
Density	= 7.83 x 10^{-3} Kg/m^{3}
Poisson's Ratio	= 0.3
Disk Inner Radius (a)	= 5.08 x 10^{-2} m
Disk Outer Radius (b)	= 18.03 x 10^{-2} m
Blade Tip Radius (c)	= 25.64 x 10^{-2} m
Disk Thickness	= 0.635 x 10^{-2} m
Blade Thickness	= 0.3175 x 10^{-2} m
Blade Width	= 3.1475 x 10^{-2} m
Shaft Length	= 2.0 m
Bearing Stiffness	= 1.75 x 10^{7} N/m

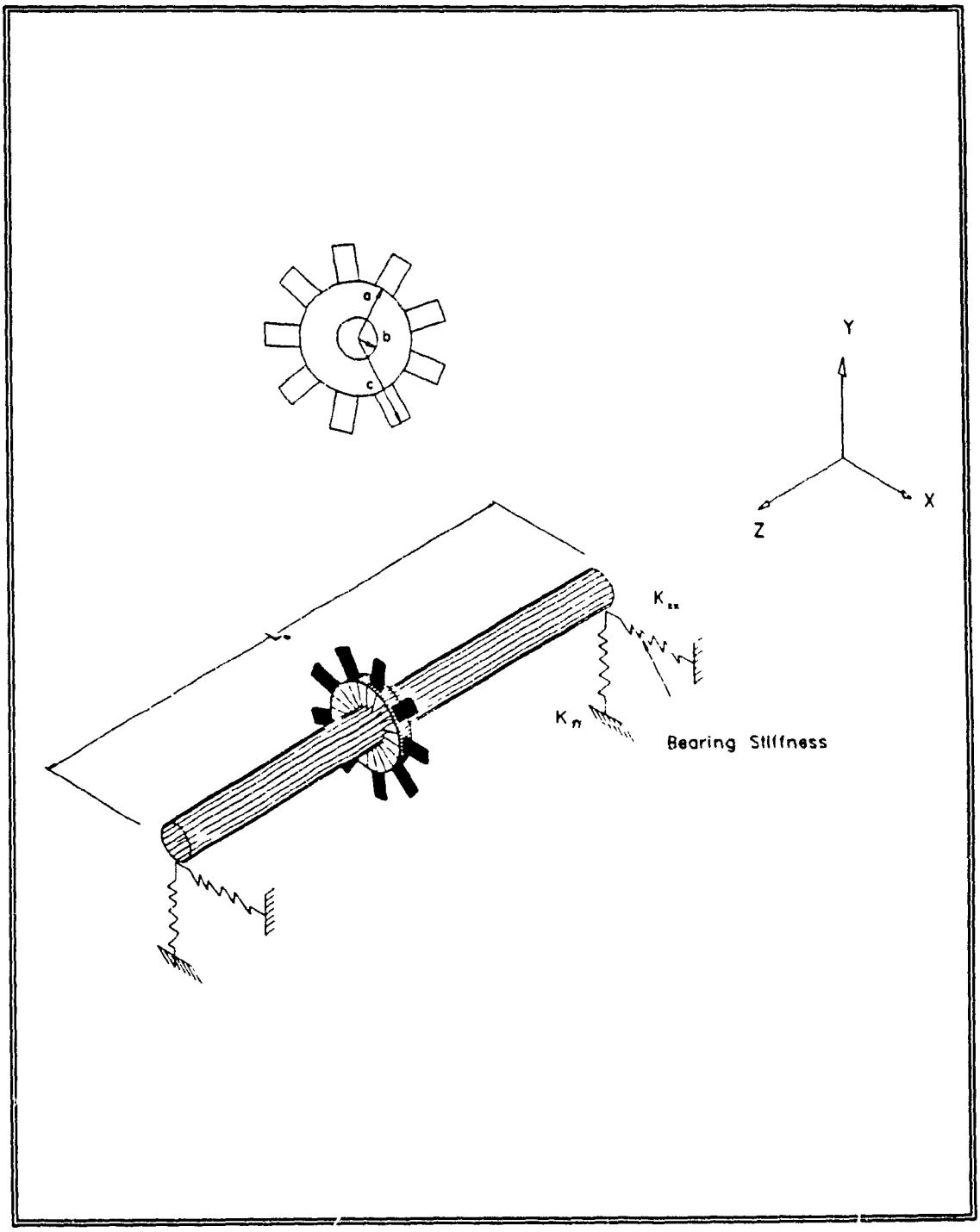

Figure 5.1 : Turborotor Assembly

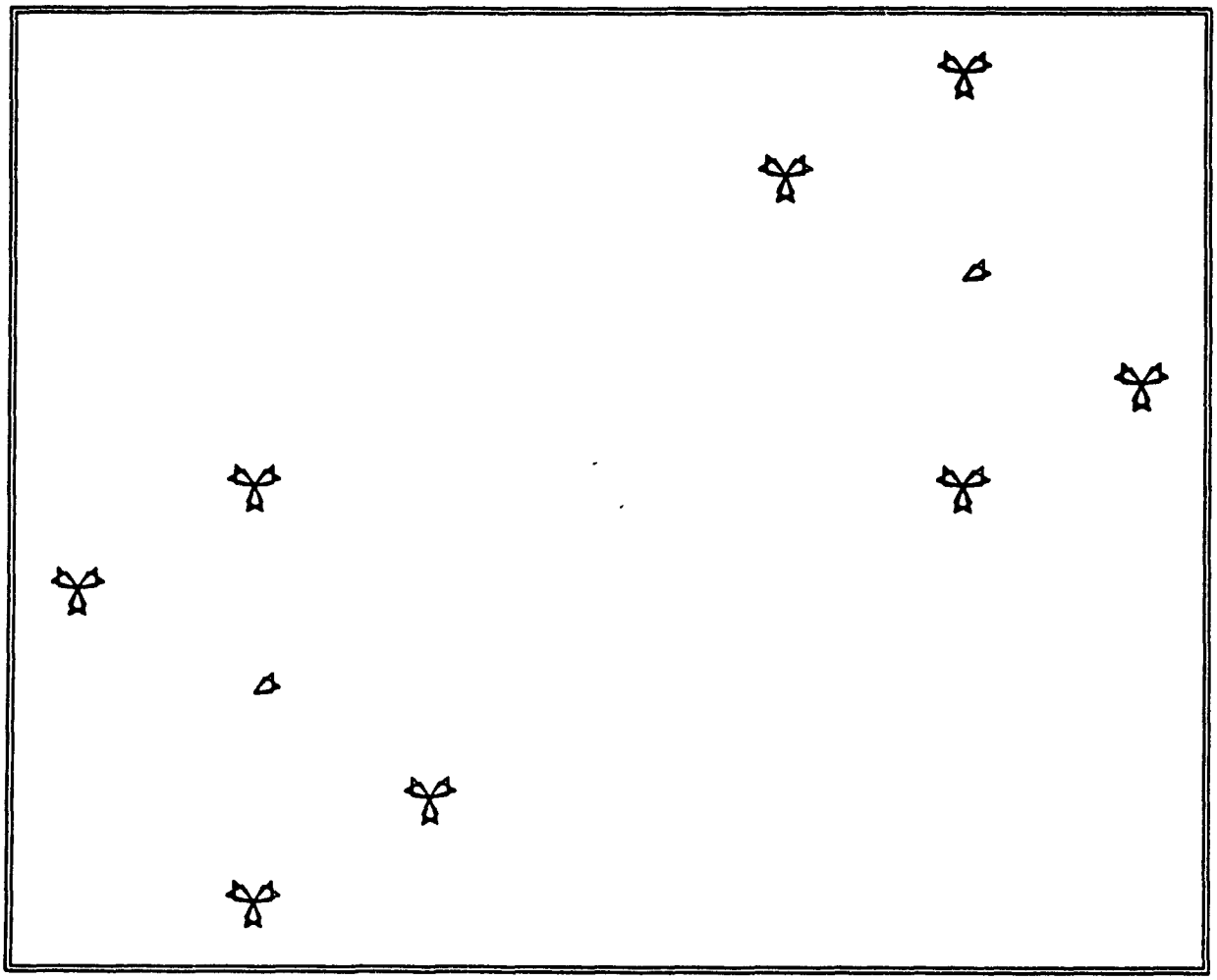

Figure 5.2 : Finite Element Model of the Turborotor Assembly (Node Plot)

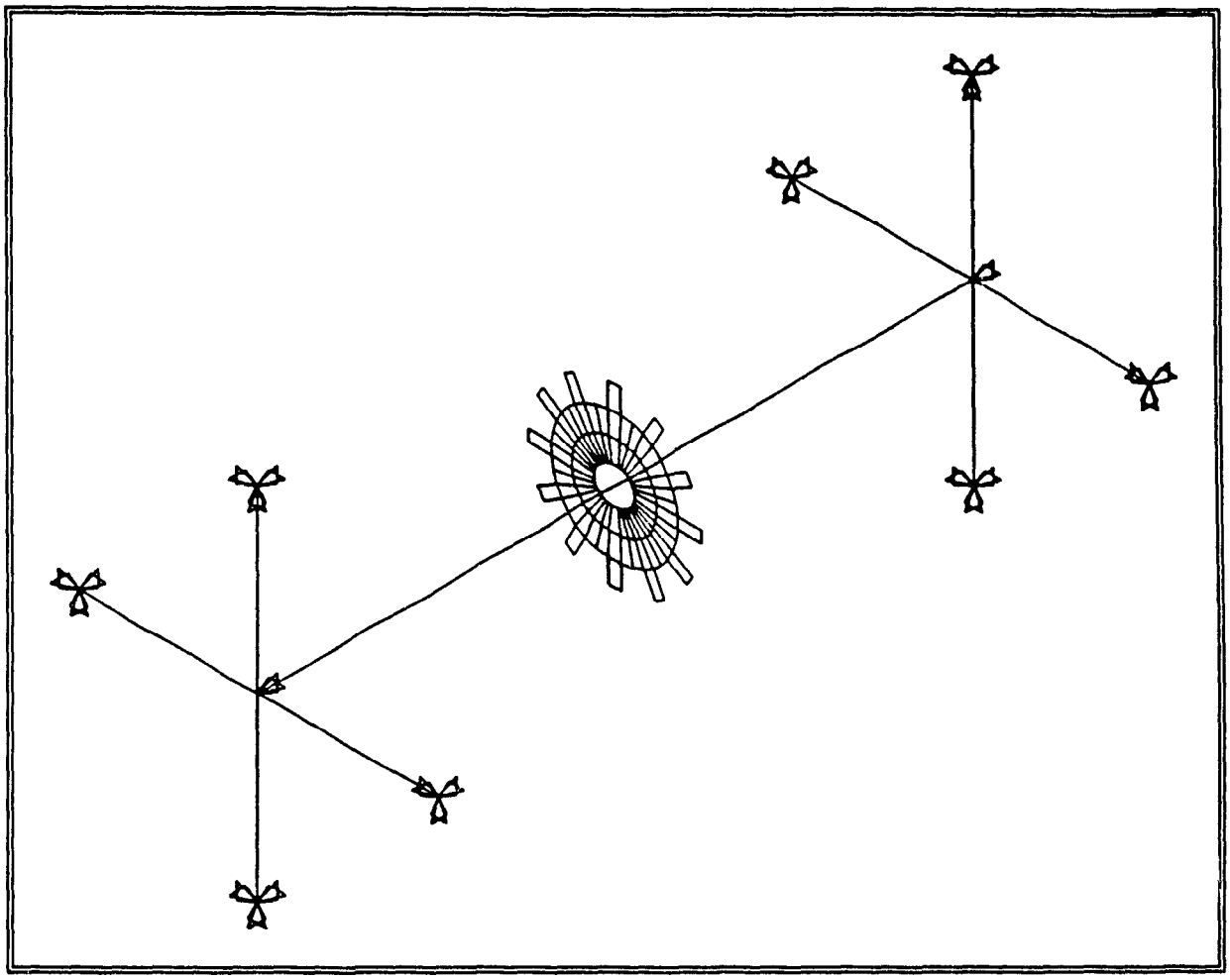

Figure 5.3 : Finite Element Model of the Turborotor Assembly (Element Plot)

As mentioned in Chapter 4 the natural frequencies and mode shapes of the turborotor system are obtained by carrying out the Modal Analysis in the solution phase of the ANSYS program invoking KAN=2 subroutine.

The governing equation for free, undamped vibrations is,

$$M\ddot{u}+Ku=0 \tag{5.1}$$

For a linear structure undergoing free vibration the displacements are harmonic of the form,

$$u=U_c\cos pt \tag{5.2}$$

Substituting in (5.1),

$$(K-p^2M)\,U_0=0 \tag{5.3}$$

where p is the frequency of vibration.

This is a standard eigenvalue problem and the natural frequencies and mode shapes are obtained by solving this equation.

Since the number of degrees of freedom in a 173 node turborotor assembly could be about 1038, it is not economical to conduct a modal analysis with so many degrees of freedom. As mentioned in Chapter 4, the Guyan reduction technique is utilized by specifying the master degrees of freedom. Commands are so chosen in the program such that the bending of the blade, disk and the shaft account for 61 specified master degrees of freedom. The program itself is allowed to select another 89 master degrees of freedom to make sure that any modes are not missed. This automatic selection of the additional master degrees of freedom is done by the program for points having a small K/M ratio.

Natural Frequencies and mode shapes of the turborotor assembly are obtained for various values of the rotational speed using the reduced modal analysis procedure outlined in Chapter 4.

5.3 : Discussion of Results

Natural frequencies and mode shapes of a turborotor assembly are obtained at various rotational speeds.

Natural frequencies of the turborotor for different rotational speeds are presented in Tables 5.2 and 5.3. From these tables it can be seen that as the rotational speed increases some of the natural frequencies increase while the others remain constant. The constant frequencies are the shaft frequencies which are unaffected by rotation while the disk and blade frequencies increase with increasing rotational speed.

The variation of shaft natural frequencies with rotational speed are presented in Figure 5.4. It has been observed that the rotational speed has no significant effect on these frequencies. This is understandable since the influence of centrifugal effects due to shaft rotation on its flexural motion is negligible.

Variation of the first natural frequency with rotational speed for a disk, bladed-disk and the turborotor assembly is shown in Figure 5.5. From this figure it can be seen that with

the inclusion of the blades the natural frequency of the disk decreases. Also, from a system point of view the first natural frequency of the turborotor assembly corresponds to the shaft bending frequency which is significantly lower than the bladed disk assembly and is unaffected by the rotation.

The effect of the bearing flexibility on the natural frequencies of the turborotor system are shown in Table 5.4. As it can be seen from the table, that for a higher value of the stiffness the natural frequency increases.

The first ten mode shapes of the turborotor assembly are shown in Figs. 5.6 through 5.15. As before the solid lines represent the original shape and the dashed lines are the displaced shape. From these figures it can seen that the first four modes correspond to the shaft bending. Modes 5, 6 and 7 are the bending of the bladed-disk assembly. Modes 8 and 9 correspond to shaft bending and mode 10 is again the bending of the bladed-disk assembly.

5.5 : Summary

The dynamics of a turborotor system is studied using the finite element package ANSYS. The natural frequencies and mode shapes are obtained at various rotational frequencies and the

results compared to disk and bladed-disk analysis.

In Chapter 6, response analysis is carried out on a typical turborotor assembly to obtain its amplitude of displacement and stress levels.

Table 5.2:Variation of Natural Frequency with Rotational Speed

Mode Number	Angular Velocity (Hz)				
	0.0	83.3	166.6	249.9	333.2
1	46.7	46.8	46.8	46.8	46.8
2	46.7	46.8	46.8	46.8	46.8
3	167.1	167.1	167.3	167.3	167.4
4	167.1	167.1	167.3	167.3	167.4
5	236.9	259.5	261.6	261.6	261.6
6	236.7	259.7	261.6	261.6	261.6
7	246.7	261.6	314.9	379.5	435.9
8	261.6	261.6	316.4	391.3	435.9
9	261.6	266.3	316.7	391.9	452.2
10	269.1	297.3	368.2	436.9	476.9
11	270.3	298.5	369.4	436.9	477.9
12	407.9	436.5	436.6	461.8	566.9
13	407.9	436.5	436.6	463.5	569.3
14	436.4	437.7	514.0	616.7	706.4
15	436.4	437.7	514.1	616.9	706.4

Table 5.3:Variation of Natural Frequency with Rotational Speed

Mode Number	Angular Velocity (Hz)				
	416.8	583.1	666.5	749.8	833.0
1	46.7	46.8	46.8	46.8	46.8
2	46.7	46.8	46.8	46.8	46.8
3	167.4	167.5	167.5	167.6	167.6
4	167.4	167.5	167.5	167.6	167.6
5	261.6	261.6	261.6	261.6	261.6
6	261.6	261.6	261.6	261.6	261.6
7	436.3	436.5	436.6	436.7	436.7
8	436.3	436.5	436.6	436.7	436.7
9	529.3	689.1	706.4	706.4	706.4
10	566.2	706.4	706.4	706.4	706.4
11	567.7	706.4	769.6	849.9	849.9
12	678.3	753.6	849.7	946.7	946.7
13	681.7	756.5	853.3	951.1	951.2
14	706.4	910.8	1029.8	1149.9	1149.9
15	706.4	916.8	1037.3	1158.9	1158.9

Table 5.4 : Effect of Bearing Flexibility on the Natural Frequencies

Mode Number	Natural Frequency (Hz) Angular Velocity = 0.0	
	Bearing Stiffness 1.75×10^7 N/m	Bearing Stiffness 1.75×10^{14} N/m
1	46.7	50.3
2	46.7	50.3
3	167.1	223.8
4	167.1	223.8
5	236.9	238.7
6	236.7	238.7
7	246.7	246.7
8	261.6	268.9

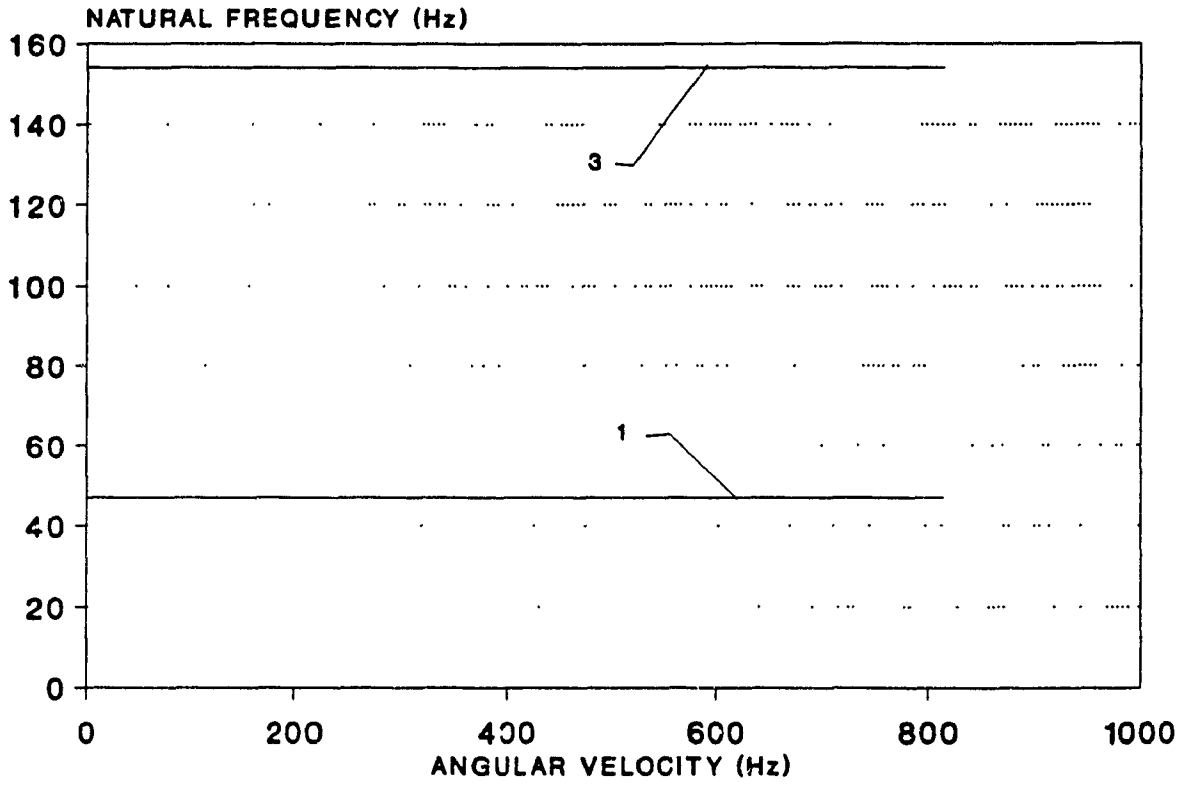

Fig. 5.4 : Variation of Natural Frequency with Speed

Curve 1 : First Natural Frequency

Curve 3 : Third Natural Frequency

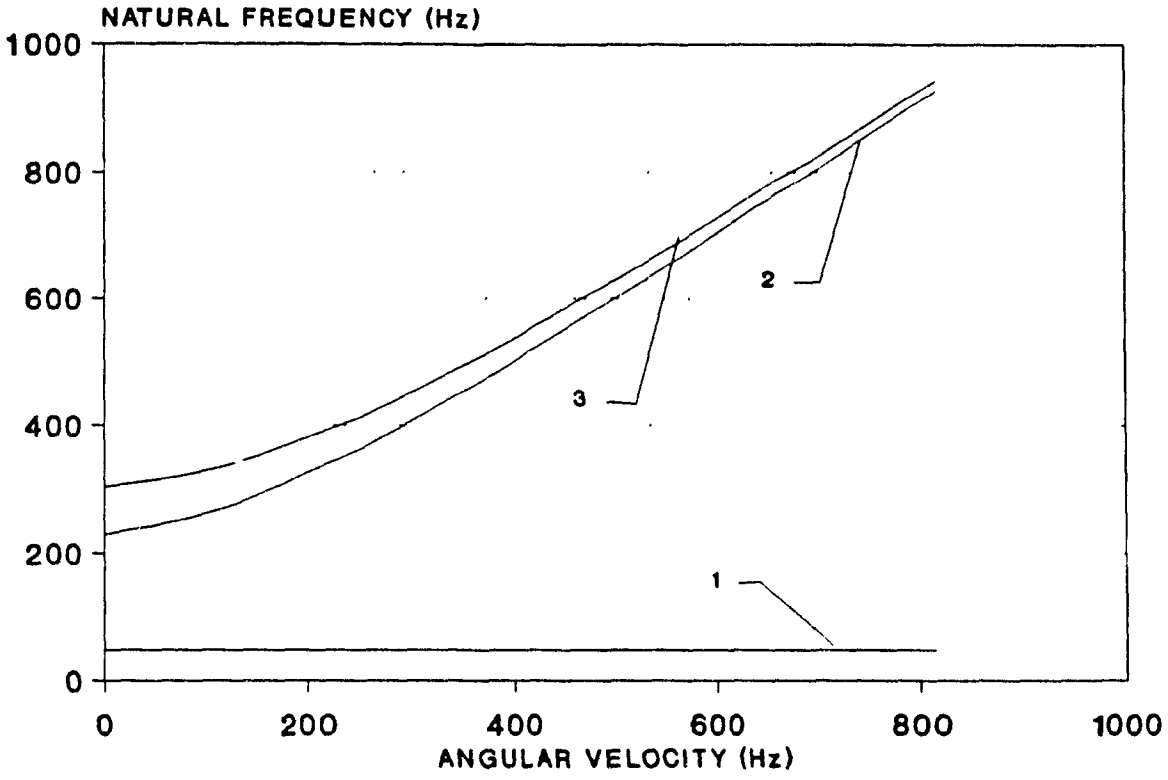

Fig. 5.5 : Comparison of the First Natural Frequency

Curve 1 : Turborotor Assembly Natural Frequency
Curve 2 : Disk-Blade Natural Frequency
Curve 3 : Disk Natural Frequency

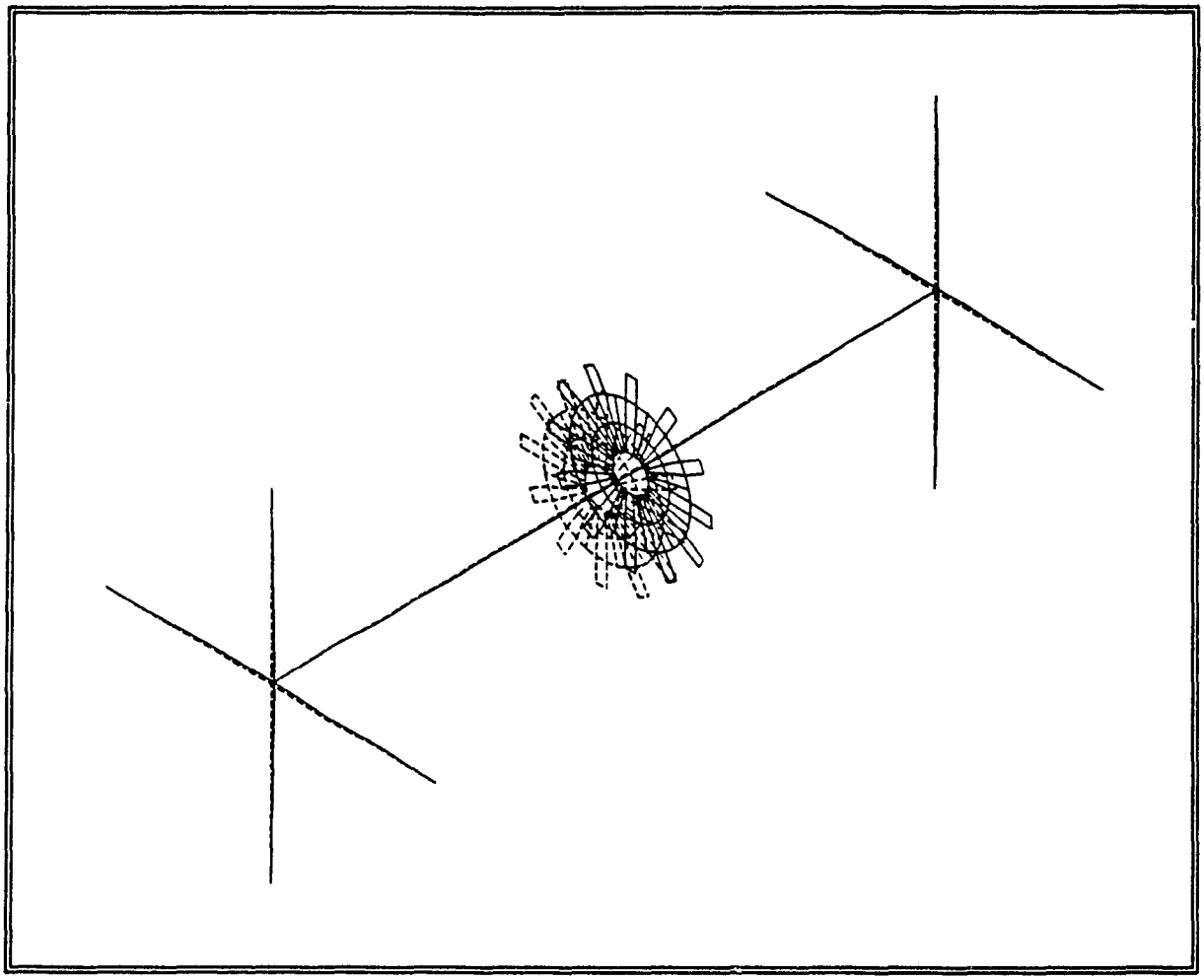

Fig. 5.6 : Mode Shape of the Turborotor Assembly (at 46.7 Hz)

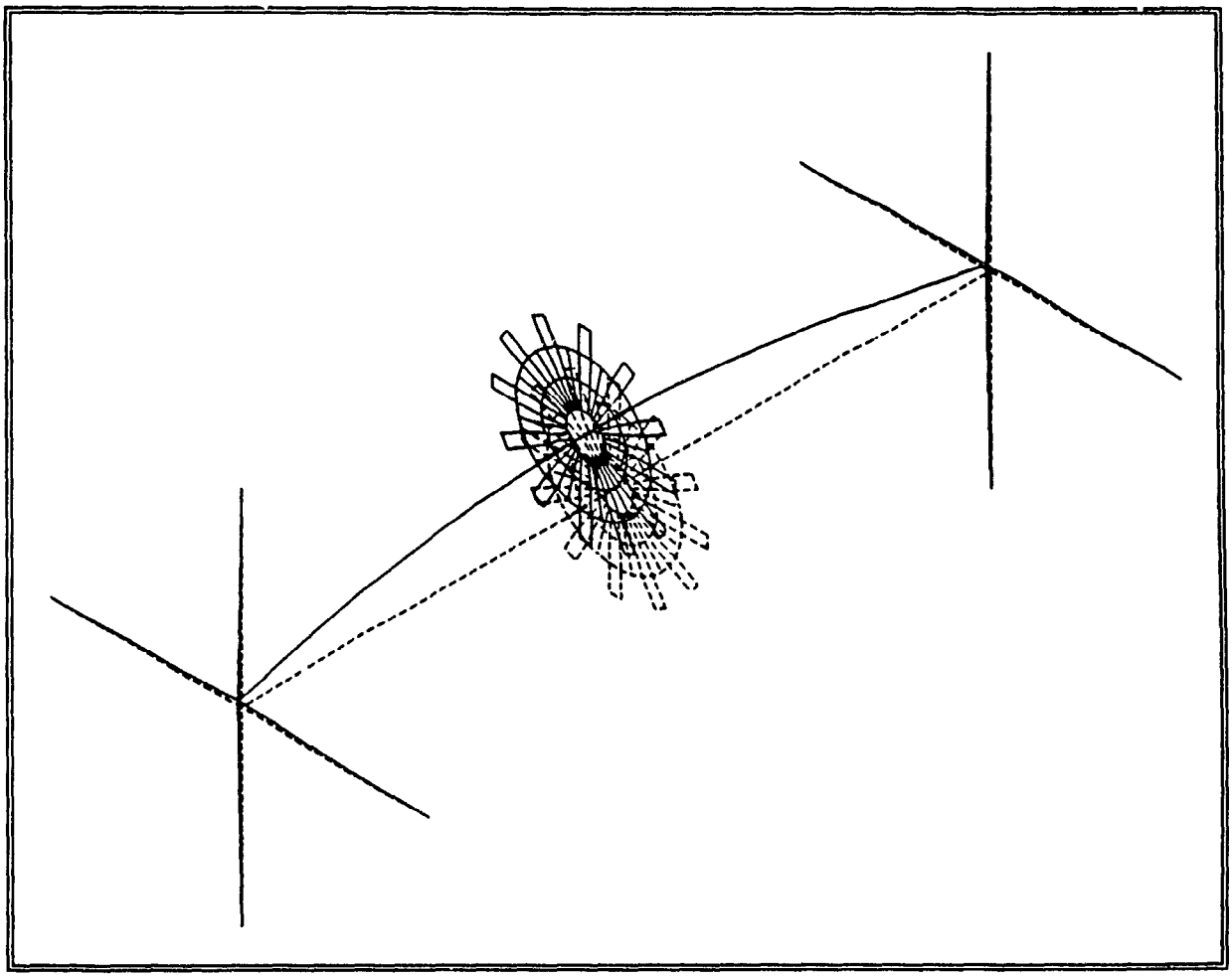

Fig. 5.7 : Mode Shape of the Turborotor Assembly
(at 46.7 Hz)

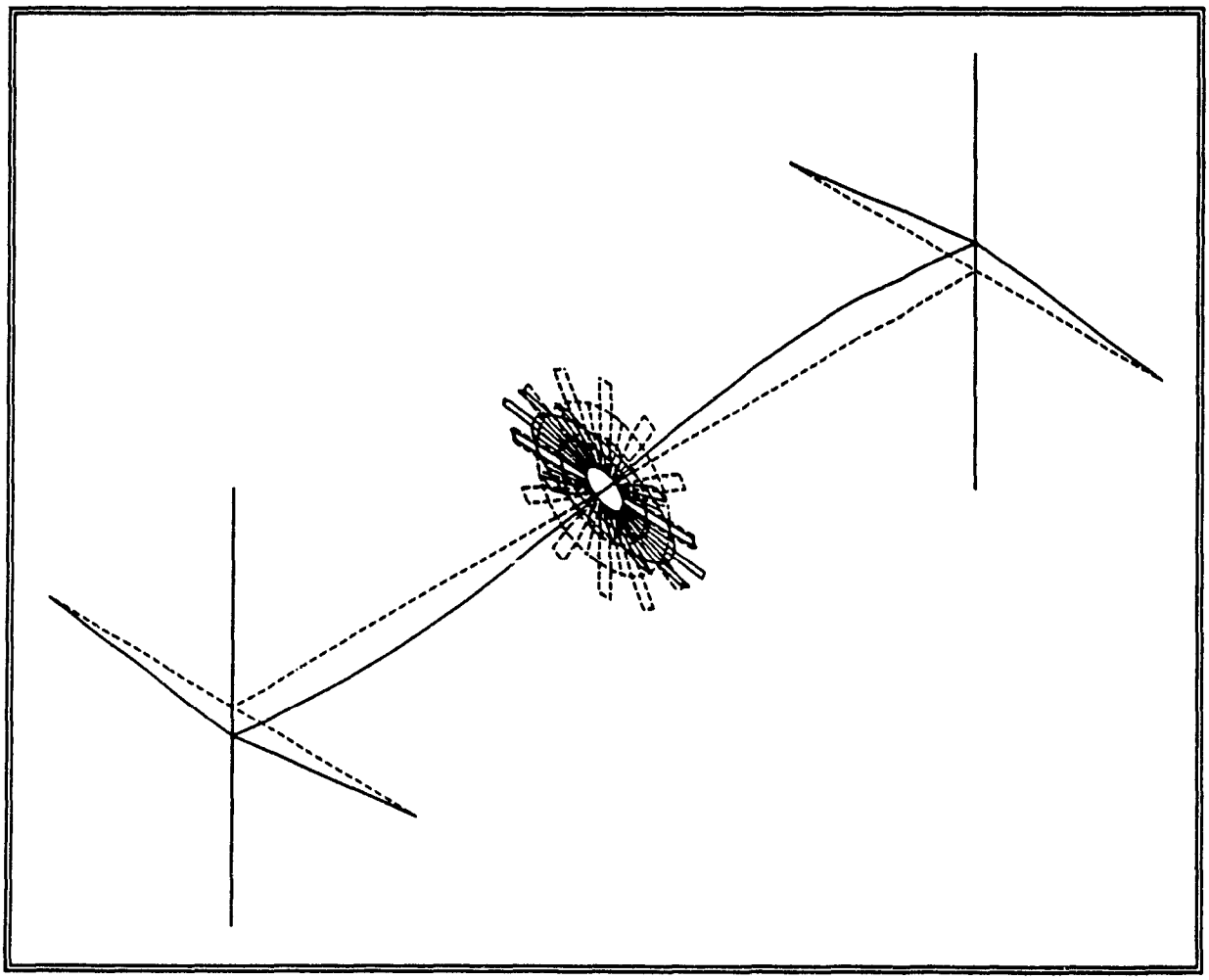

Fig. 5.8 : Mode Shape of the Turborotor Assembly (at 167.1 Hz)

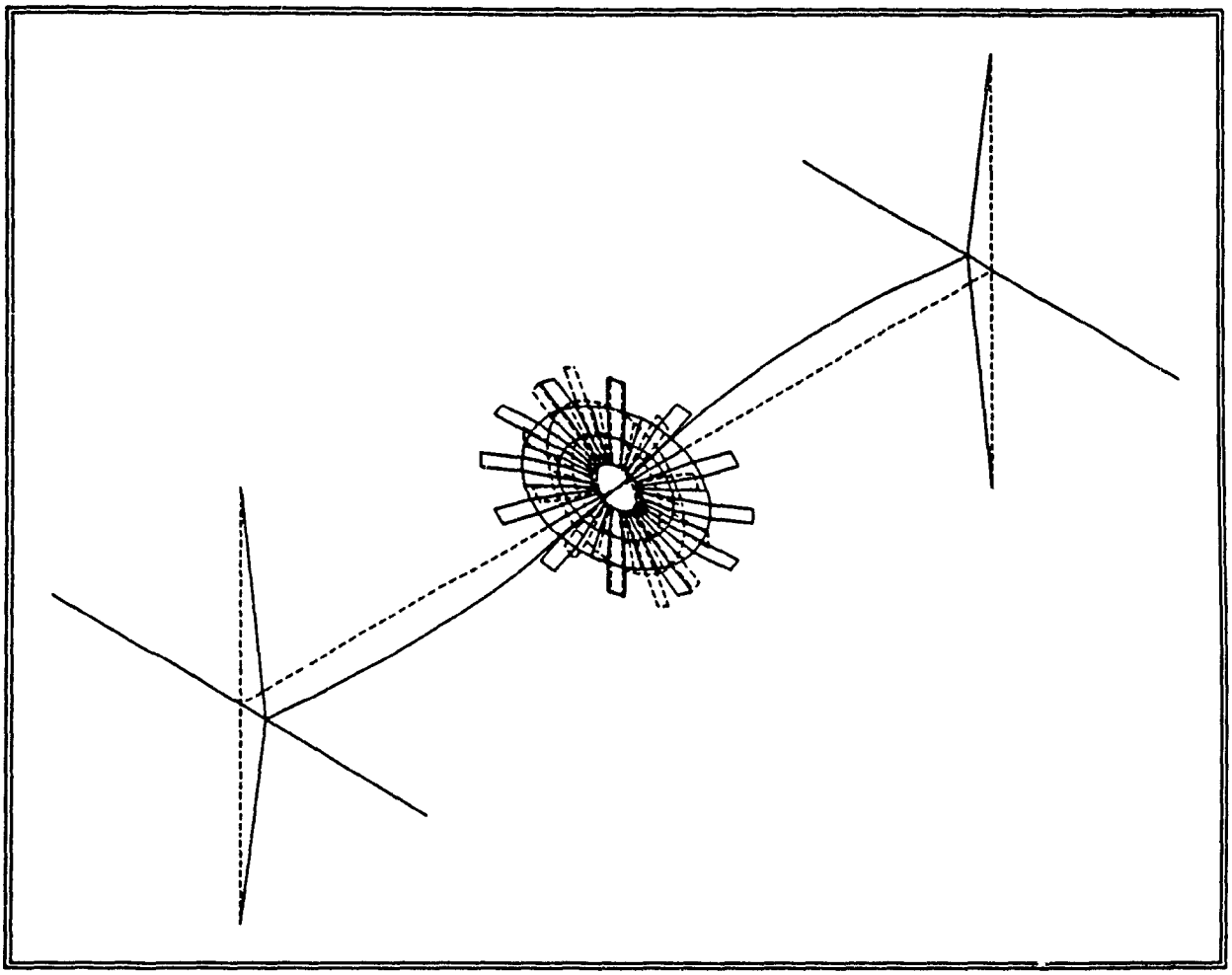

Fig. 5.9 : Mode Shape of the Turborotor Assembly (at 167.1 Hz)

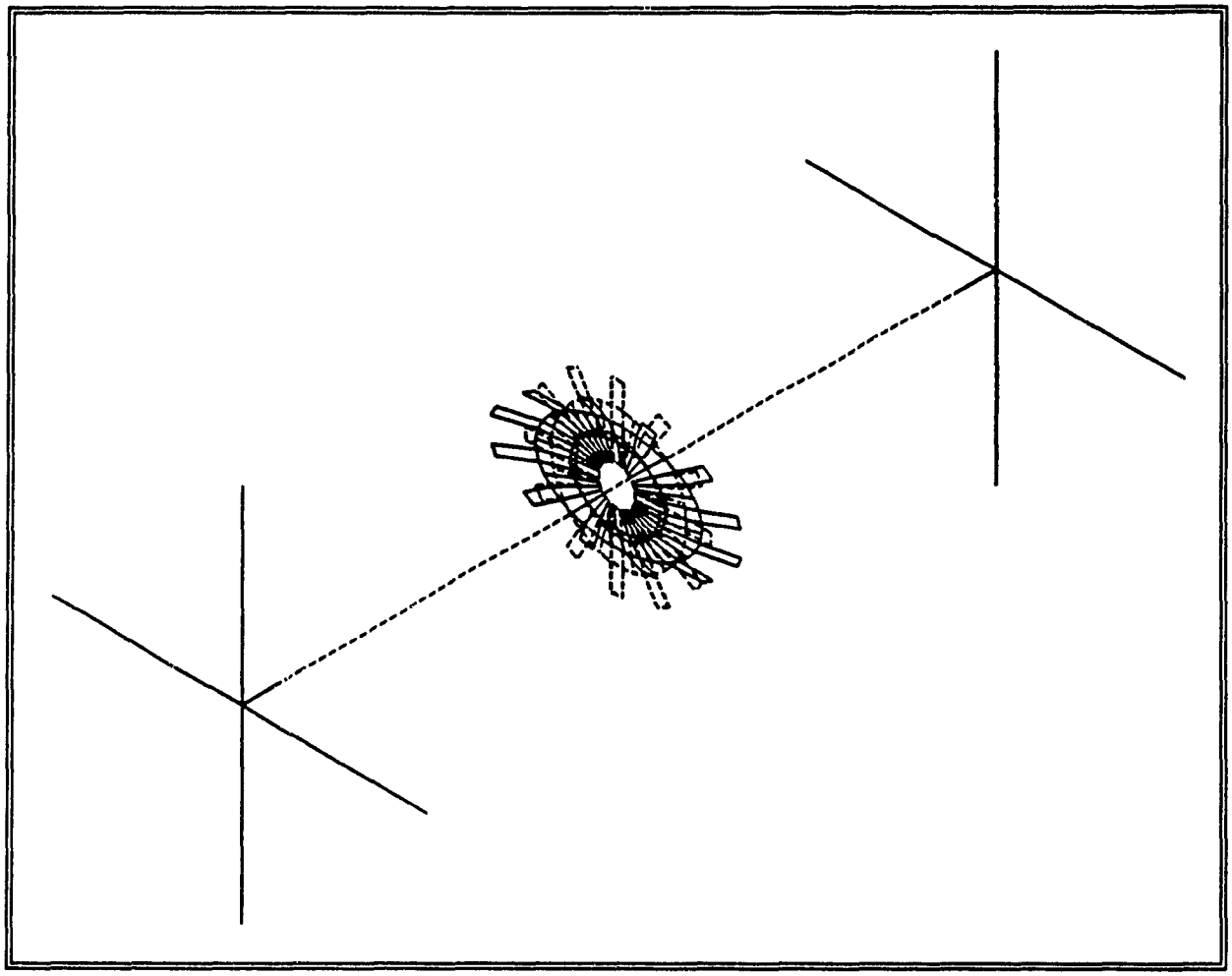

Fig. 5.10 : Mode Shape of the Turborotor Assembly
(at 236.9 Hz)

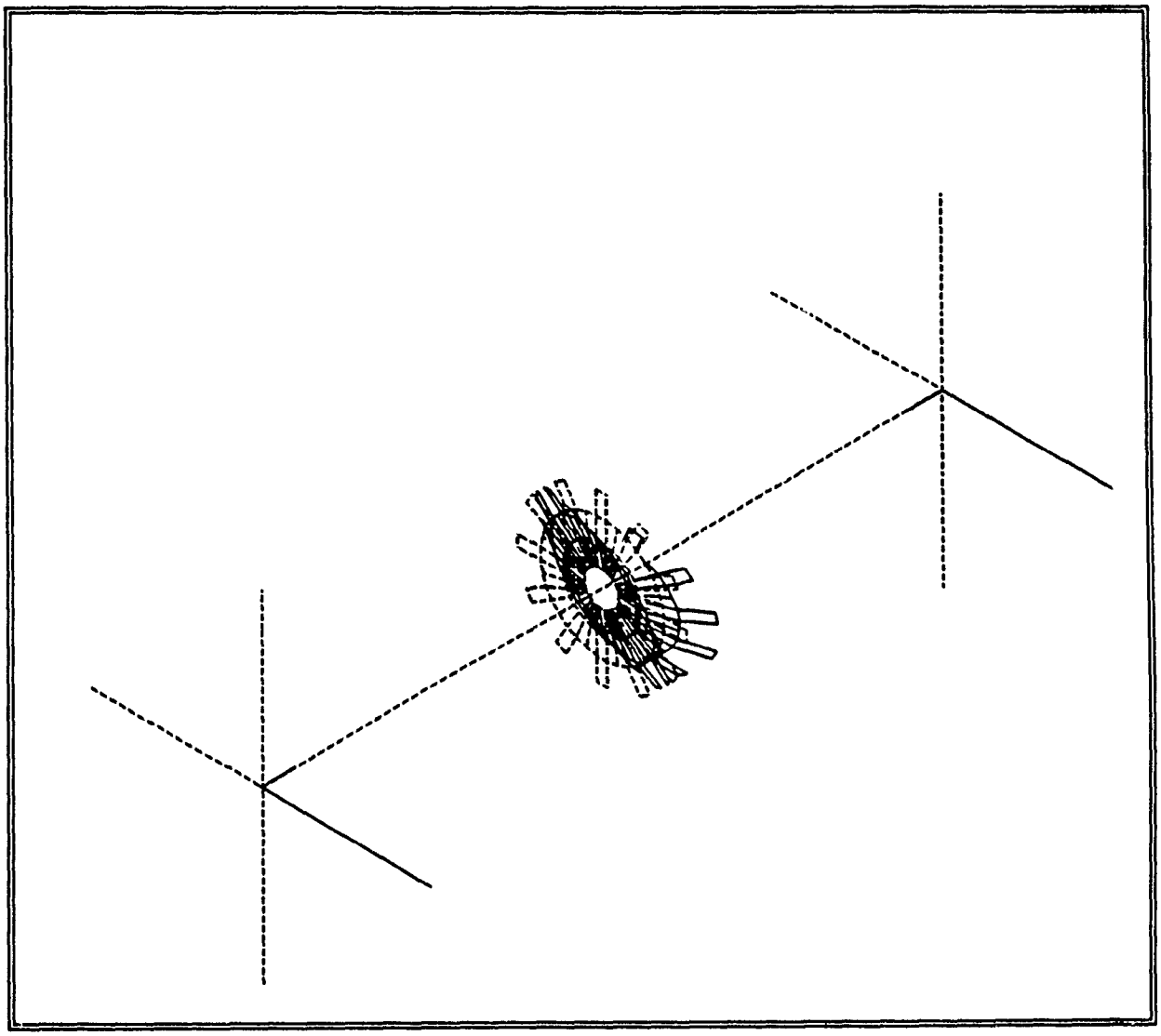

Fig. 5.11 : Mode Shape of the Turborotor Assembly (at 236.7 Hz)

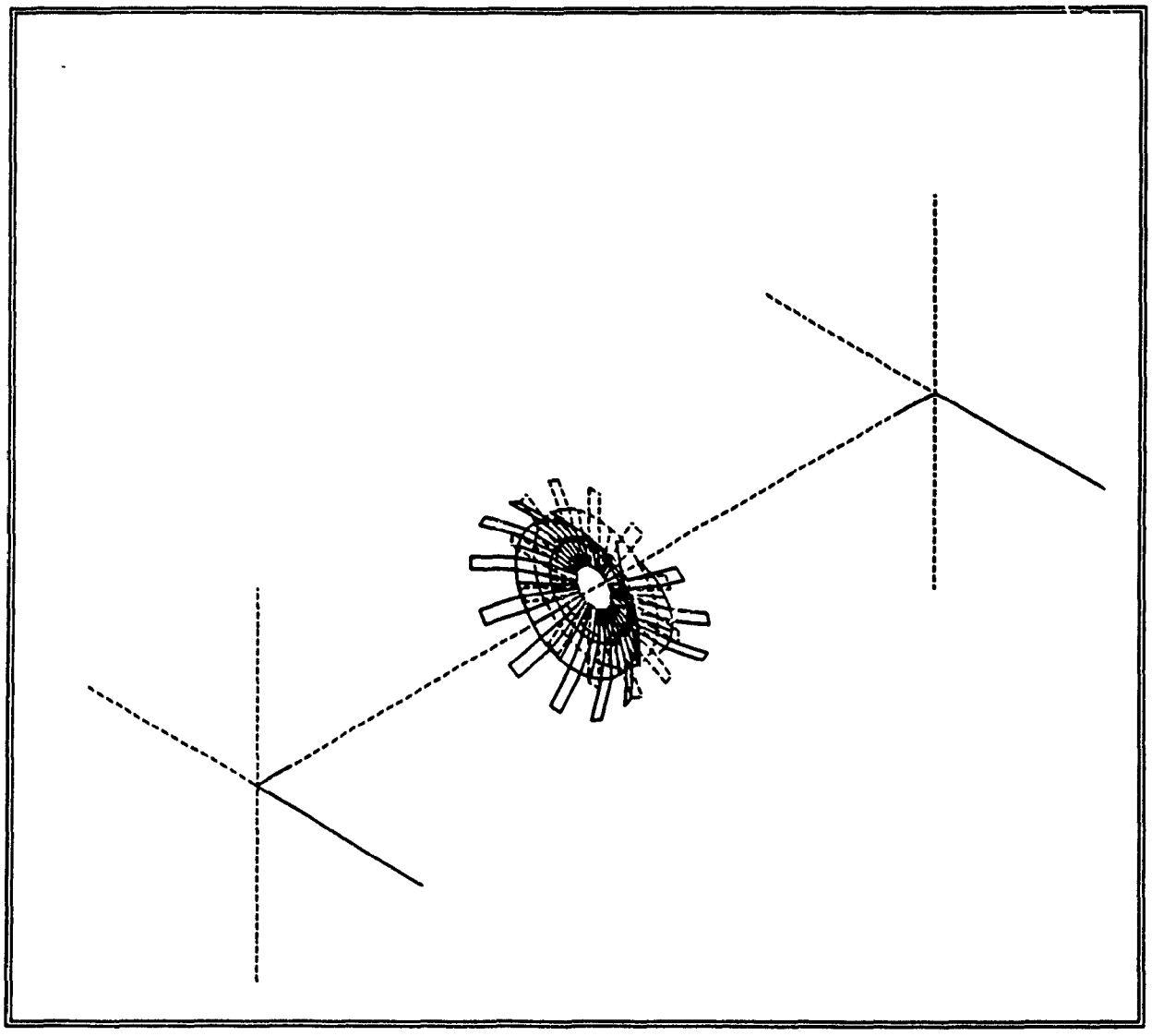

Fig. 5.12 : Mode Shape of the Turborotor assembly (at 246.7 Hz)

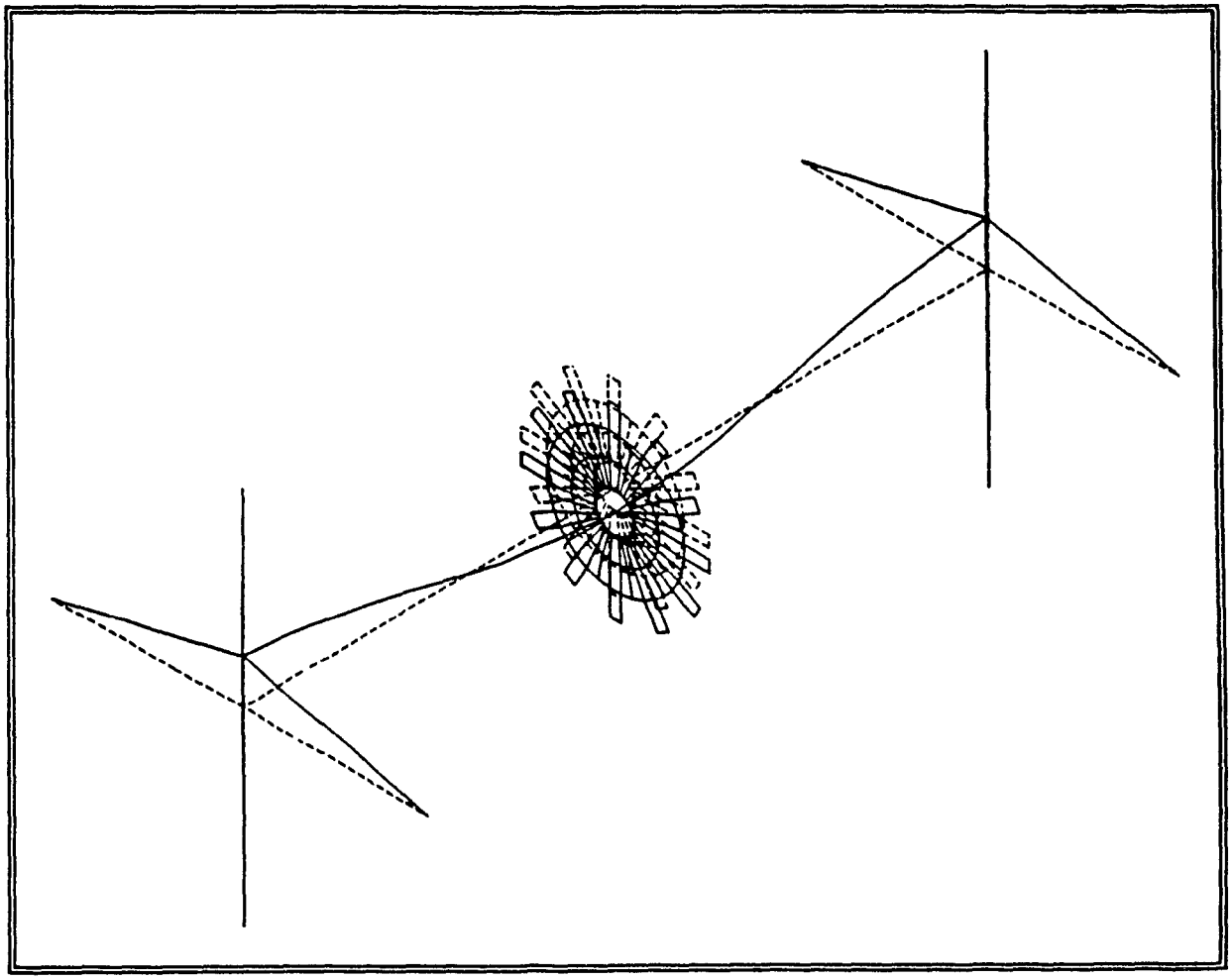

Fig. 5.13 : Mode Shape of the Turborotor Assembly
(at 261.6 Hz)

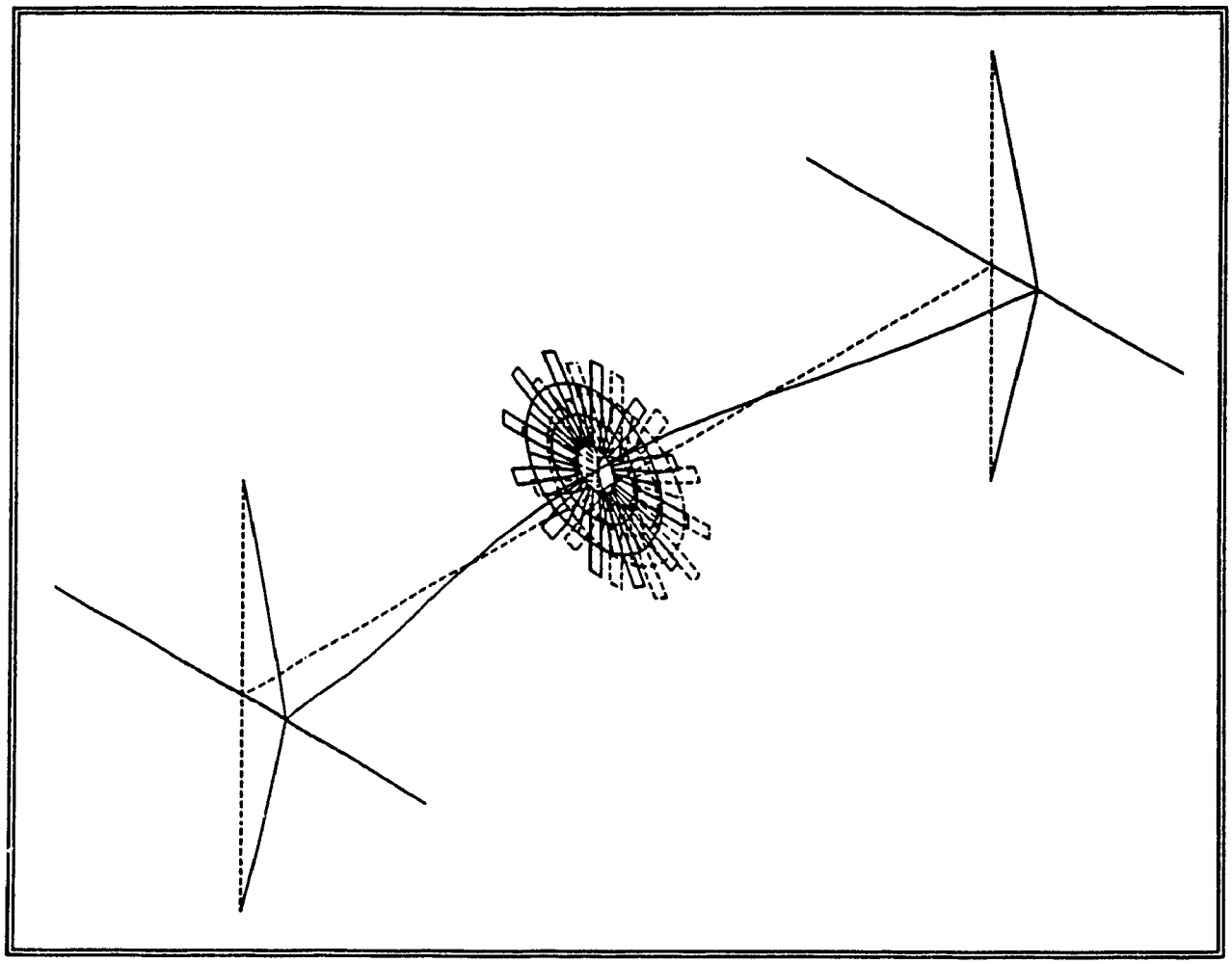

Fig. 5.14 : Mode Shape of the Turborotor Assembly
(at 261.6 Hz)

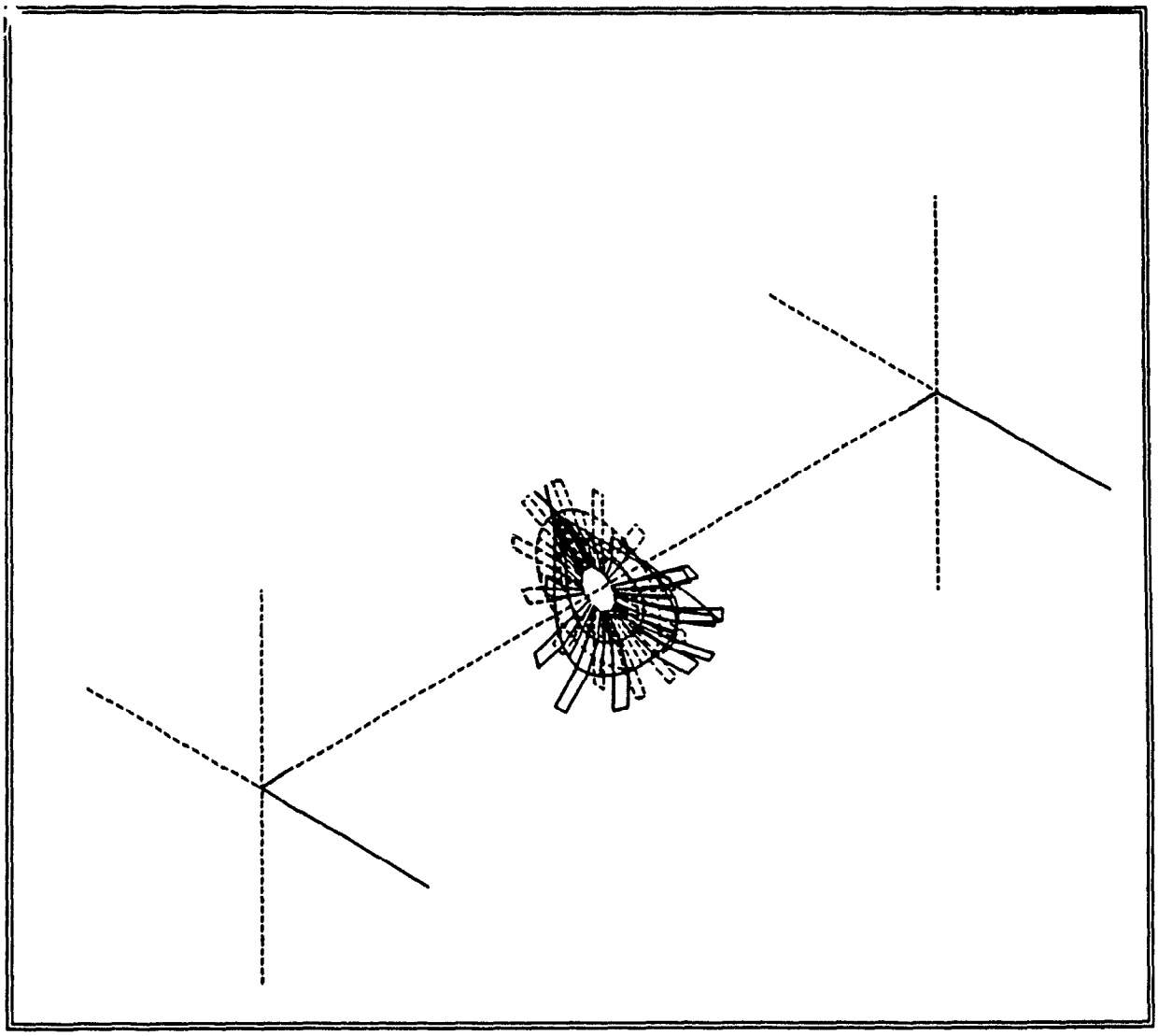

Fig. 5.15 : Mode Shape of the Turborotor Assembly
(at 269.1 Hz)

CHAPTER 6

RESPONSE ANALYSIS OF A TURBOROTOR SYSTEM

6.1 : General

The components of a turborotor system are subjected to the centrifugal forces during rotation, unbalance in a rotor, as well as loads due to the pressurized gases or fluid flowing through the blades. The components must be designed so as to withstand both the constant and the dynamic stresses they experience due to such loads.

An assembly of blades is prone to vibration in an operating system. Periodically varying pressure fields, flow distortion due to other upstream obstructions and unbalance of the rotor system are some of the principal sources of excitation that result in blade vibration response. Limiting the vibratory stresses to acceptable levels in a given design requires that the designer be able to calculate the dynamic characteristics of the assembly.

In this chapter forced vibrational behaviour of a complete turborotor system is studied using the finite element program ANSYS. The amplitude of displacement and stress contours are obtained for a turborotor system considering both harmonic and centrifugal loading.

6.2 : Finite Element Model of the Turborotor Assembly

The turborotor assembly is shown in Fig 6.1. The assembly consists of a rotating shaft mounted on linear, undamped bearings having a disk with 12 blades mounted on it. The blades have identical geometric, material and constraint properties. The disk is assumed to be at the center point of the shaft and the setting angle of the blade with the plane of rotation is 45 degrees. An actual turborotor might consist of several rows of blades, the effect of which will be a spatial distribution of the load on the rotor and also a gradual pressure variation from the first row of blades to the last row of blades. Even though a single row of blades is considered in this analysis it can be extended to incorporate several rows of blades.

The bladed disk assembly is subjected to steady sinusoidal loads due to pressurized gas flow through the blades and centrifugal loads due to rotation. The steady state sinusoidal load is applied by distributing the average load on the blade at selected node points as shown in Figures 6.2 and 6.3 . The average load on the blade due to the gas forces is calculated by considering the gas flow under pressure through the rotating blades. For illustration purposes only, the frequency band of excitation, 40-400 Hz, is selected.

As before, the bearings on which the turborotor assembly is mounted are modelled using a spring element having up to three degrees of freedom at each node. The rotating shaft is modelled using three dimensional beam elements having 6 degrees of freedom at each node : translations in the nodal X, Y, Z directions and rotations about the nodal X, Y, and Z axes. Elastic quadrilateral shell elements having 6 degrees of freedom at each node with different geometric properties are used to discretize the bladed-disk assembly. The bladed - disk assembly is mounted at the center of the shaft and is coupled to the shaft through rigid massless links. The effect of this is to couple all the motions of the shaft and the disk.

The turborotor assembly is composed of 173 nodes and 109 elements. The blade material and the disk material are taken to be orthotropic MAR-M200 DS and WASPALOY respectively.

Table 6.1 shows the dimensions and material properties that are used for the analysis of the turborotor assembly.

Table 6.1 : Turborotor Assembly Parameters

Blade Material Properties	
Modulus of Elasticity	= 1.283×10^{11} N/m^2
Density	= 8.603×10^{3} Kg/m^3
Poisson's Ratio	= 0.3
Disk Material Properties	
Modulus of Elasticity	= 2.139×10^{11} N/m^2
Density	= 8.243×10^{3} Kg/m^3
Poisson's Ratio	= 0.3
Geometric and Bearing Properties	
Disk Inner Radius (a)	= 5.08×10^{-2} m
Disk Outer Radius (b)	= 18.03×10^{-2} m
Blade Tip Radius (c)	= 25.64×10^{-2} m
Disk Thickness	= 0.635×10^{-2} m
Blade Thickness	= 0.3175×10^{-2} m
Blade Width	= 3.1475×10^{-2} m
Shaft Length	= 2.0 m
Bearing Stiffness	= 1.75×10^{7} N/m
Damping Ratio	= 1%

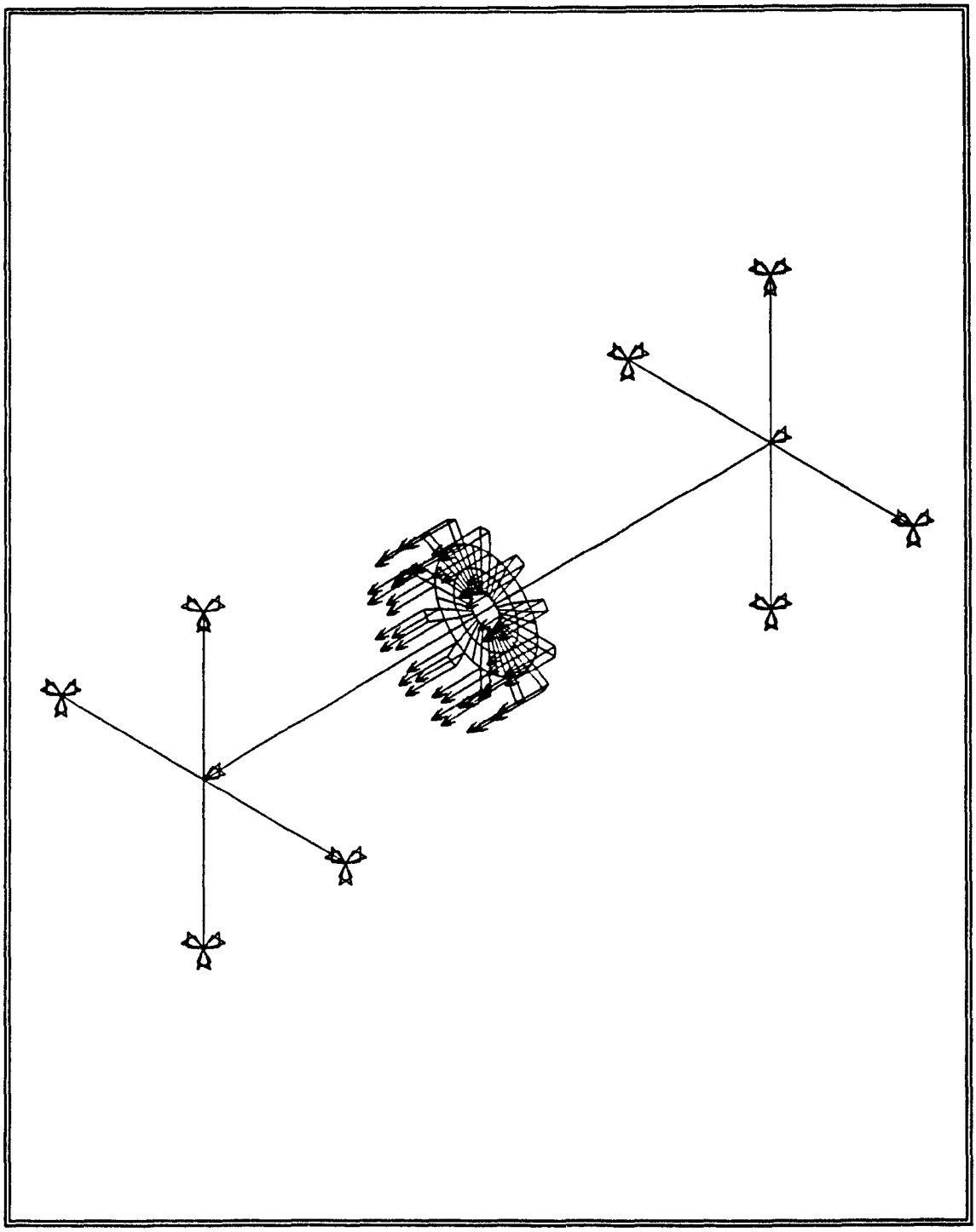

Figure 6.1 : Turborotor Assembly with Force Loading

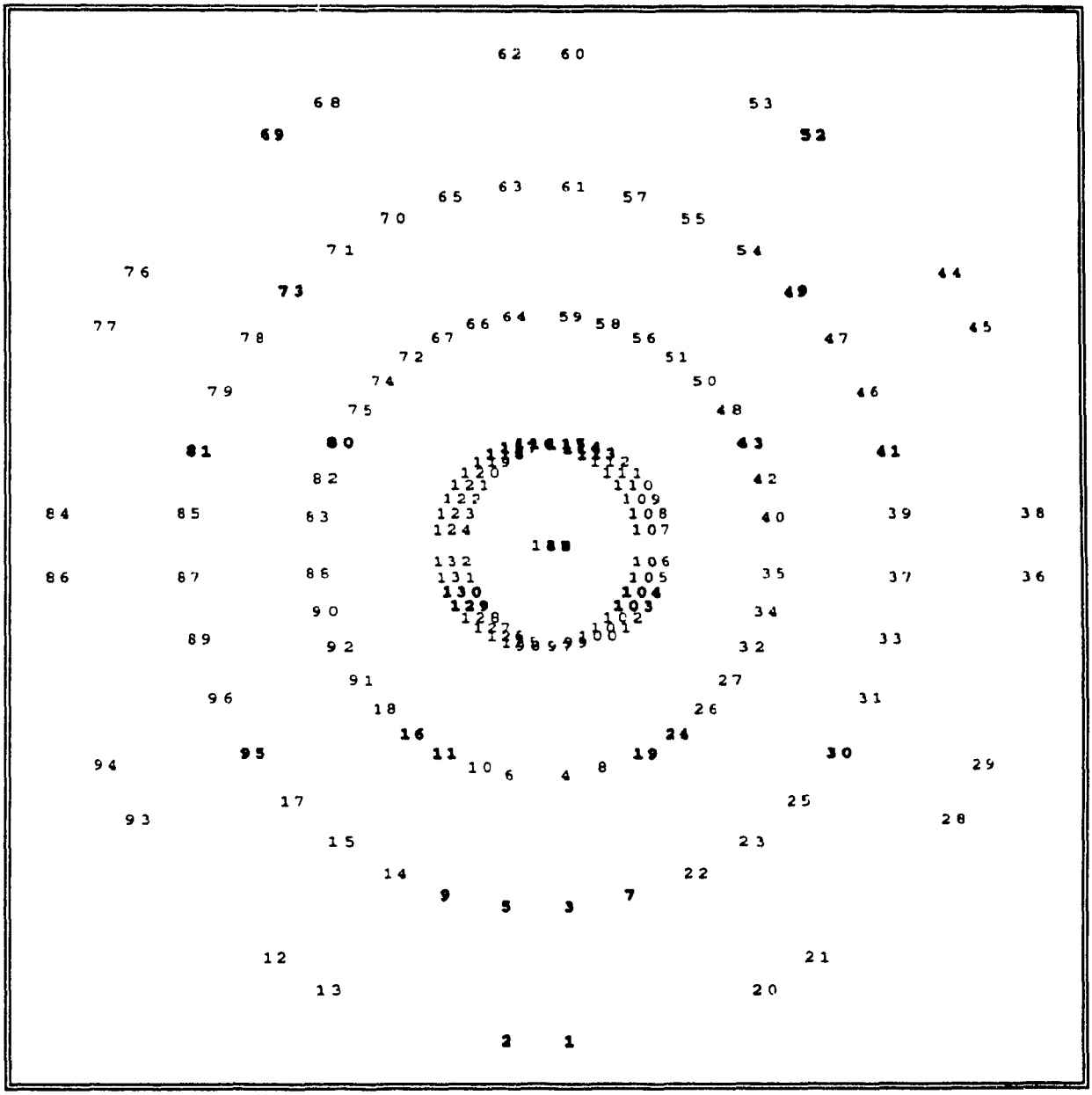

Figure 6.2 : Finite Element Model Showing the Node Numbers

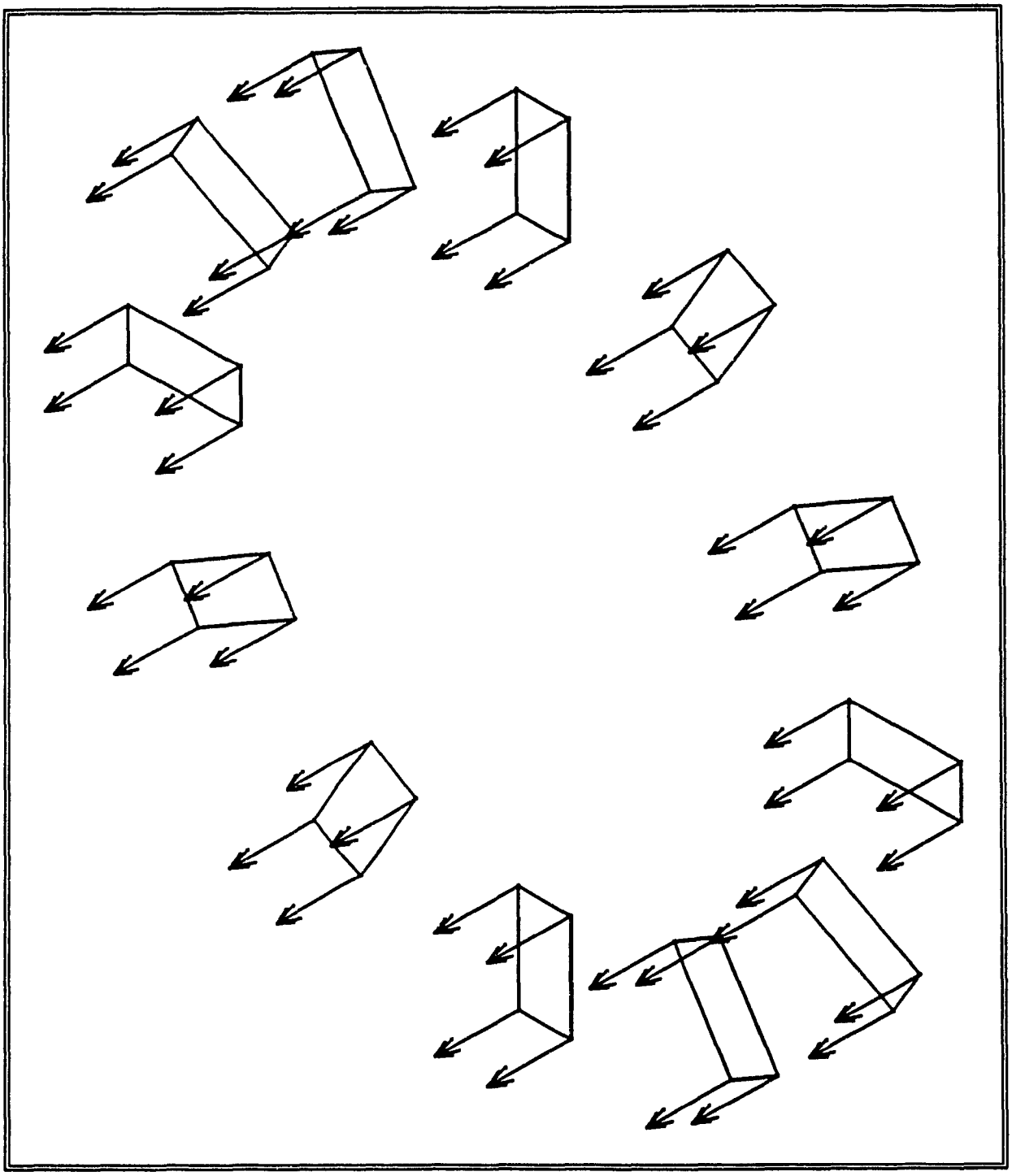

Figure 6.3 : Finite Element Model Showing the Force Loading

The governing equation for the harmonic analysis is,

$$M\ddot{u}+C\dot{u}+Ku=F(t) \tag{6.1}$$

where F(t) is a sinusoidal forcing function of known amplitude F_o and frequency p.

$$F(t)=F_o e^{i(pt+\Upsilon t)} \tag{6.2}$$

For a linear structure the displacements will also vary sinusoidally at the same frequency, resulting in,

$$(-p^2\hat{M}u+ip\hat{C}+\hat{K})\ (\hat{u}_1+i\hat{u}_2)=\hat{F}_1+i\hat{F}_2 \tag{6.3}$$

The symbol ^ is used to denote reduced matrices. $\hat{u}_1$ and F_1 represent the real part of the displacement and force vectors respectively, while $\hat{u}_2$ and F_2 represent the imaginary part. Since M, $\hat{C}$, and K matrices are assumed to be constant,

$$K_{eq}(\hat{u}_1+i\hat{u}_2)=(\hat{F}_1+i\hat{F}_2) \tag{6.4}$$

$$(\hat{u}_1+i\hat{u}_2)=K_{eq}^{-1}(\hat{F}_1+i\hat{F}_2) \tag{6.5}$$

where,

$$K_{eq} = (-p^2\hat{M} + ip\hat{C} + +\hat{K}) \qquad (6.6)$$

is the " equivalent " stiffness matrix. For any given value of p, the displacements ($\hat{u}_1 + i\hat{u}_2$) can be calculated .

If $\hat{C} = 0$ and the specified forces or displacements are not complex ($F_2 = \hat{u}_2 = 0$) , then there will be no imaginary terms in the displacement solution. i.e. The displacements are in phase with the forcing function. Otherwise the solution is complex, and can be presented in two forms, [100],

- Real and Imaginary parts, $\hat{u}_1$ and $\hat{u}_2$
- Amplitude $\hat{U}_o$ and phase angle, Y

where,

$$\hat{U}_o = \sqrt{\hat{u}_1^2 + \hat{u}_2^2} \qquad (6.7)$$

$$Y = \tan^{-1}\left(\frac{\hat{u}_2}{\hat{u}_1}\right) \qquad (6.8)$$

The displacements differ in phase (by the angle Y) from that of the forcing function.

In ANSYS the harmonic analysis requires two passes for a complete solution, the displacement pass and the stress pass. The displacement pass calculates the displacement solution at the master degrees of freedom as a function of frequency, while the stress pass is used to expand the solution to the full degrees of freedom and calculate the stresses, which are also a function of frequency. Figure 6.4 shows the solution flow chart for the harmonic analysis.

Amplitude and stress contours are obtained for a typical turborotor assembly subjected to sinusoidal and centrifugal loadings. As mentioned before, the frequency band of excitation is taken to be 40-400 Hz and the results are shown for some predetermined nodes. Stress contours are obtained for rotational speeds of 1309 rad/sec, 2618 rad/sec and 4189 rad/sec.

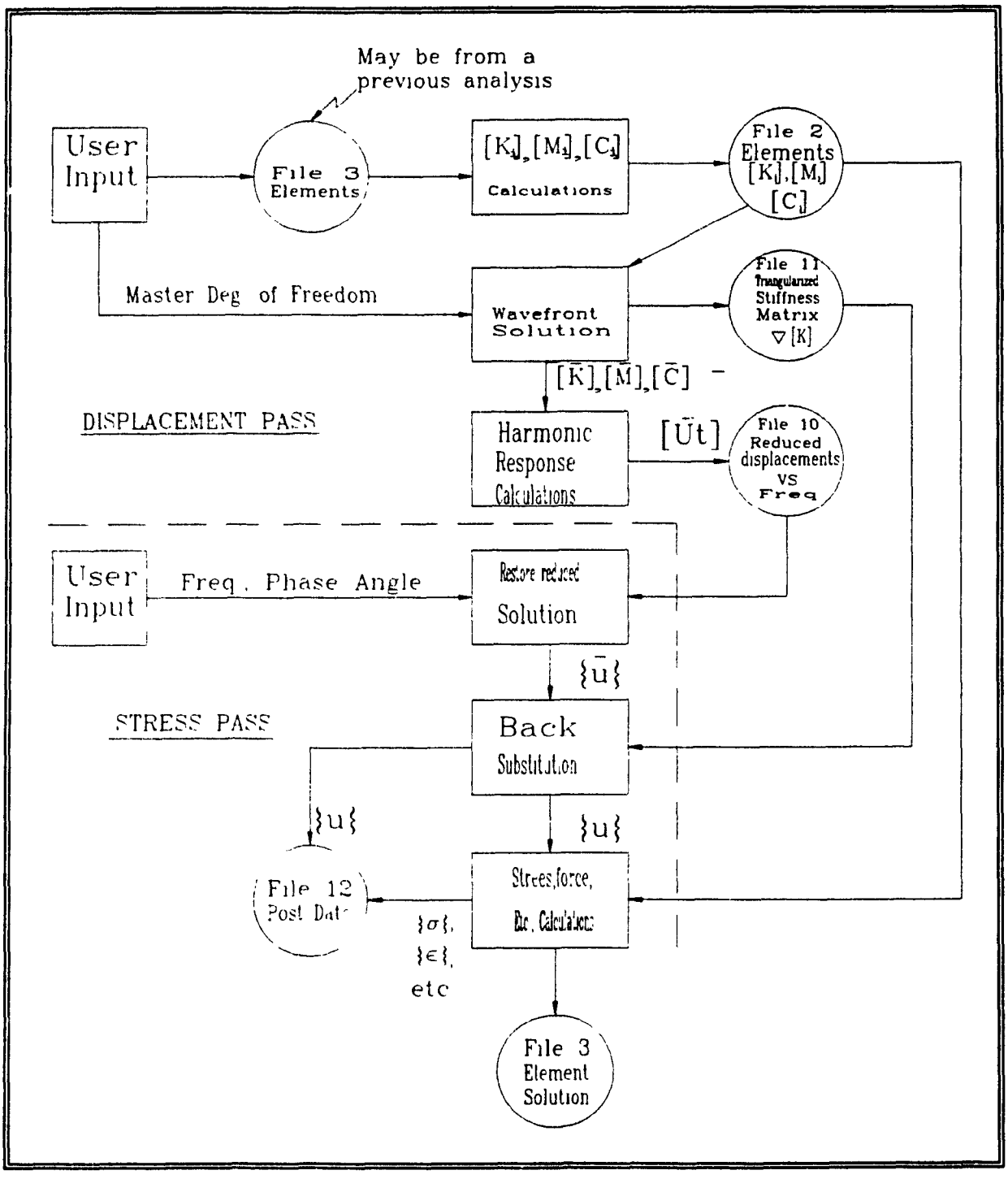

Fig. 6.4 : Harmonic Response Solution Flow Chart

6.3 : Discussion of Results

Harmonic response analysis of a turborotor system subjected to a steady sinusoidal load is studied using the finite element analyzer ANSYS. The amplitude of displacement and stress contours are obtained for predetermined critical frequencies and selected node points on the turborotor assembly. The effect due to centrifugal loading is also studied.

The amplitude of displacement is shown in Figs. 6.5 through 6.13. For presentation purposes certain node points on the blade, disk and the shaft are chosen to calculate the value of the amplitude for a frequency range of 40-400 Hz. Figures 6.5 and 6.6 show the response of the blade. From these figures it can be seen that the maximum response of the blade is approximately .018 m and .0052 m in the UZ and UX directions respectively.

Figures 6.9 through 6.11 show the amplitude of displacement for certain predetermined nodes on the disk. From these figures it can be seen that the maximum response of the disk is .018 m. The amplitude of displacement of the node points on the shaft is shown in Figs. 6.12 and 6.13. Again, it

can be observed that the maximum response of the shaft is .0027 m.

Phase angle plots of the turborotor assembly are presented in Figures 6.14 and 6.15.

The stress contours for the critical frequencies of the turborotor assembly subjected to the harmonic loading are presented in Figures 6.16 through 6.21. From Figs. 6.16 through 6.18 it can be seen that for the critical frequencies of 332 Hz, 42.8 Hz and 256 Hz the maximum stresses on the blade are 1.6×10^8 N/m^2, 9.17×10^8 N/m^2 and 2.92×10^8 N/m^2 respectively. These maximum stresses occur at the root of the blades and decrease in value towards the tip . The stresses on the disk for the same critical frequencies are presented in Figs. 6.19 through 6.21. The maximum stresses for the critical frequencies of 332 Hz, 42.8 Hz and 256 Hz are 2.46×10^9 N/m^2, 4.81×10^7 N/m^2, and 3.87×10^7 N/m^2 respectively. The maximum stresses occur at the inner periphery of the disk and decrease towards the outer periphery.

The stress contours for the blade and the disk due to centrifugal loading for different rotational speeds are shown in Figs. 6.22 through 6.27. The stress values increase with

increase in rotational speed. As it can be seen from these figures, the centrifugal loading produces significant stresses and is the major factor in determining the critical stresses for the turborotor assembly in comparison to the gas forces on the blade modelled as harmonic loading.

6.4 : Summary

The forced vibrational behaviour of a complete turborotor system is studied using the finite element program ANSYS. The amplitude of displacement and stress contours are obtained for harmonic and rotational loadings.

In the next chapter, experimental investigation to study the effect of rotation on the natural frequencies of a disk is carried out.

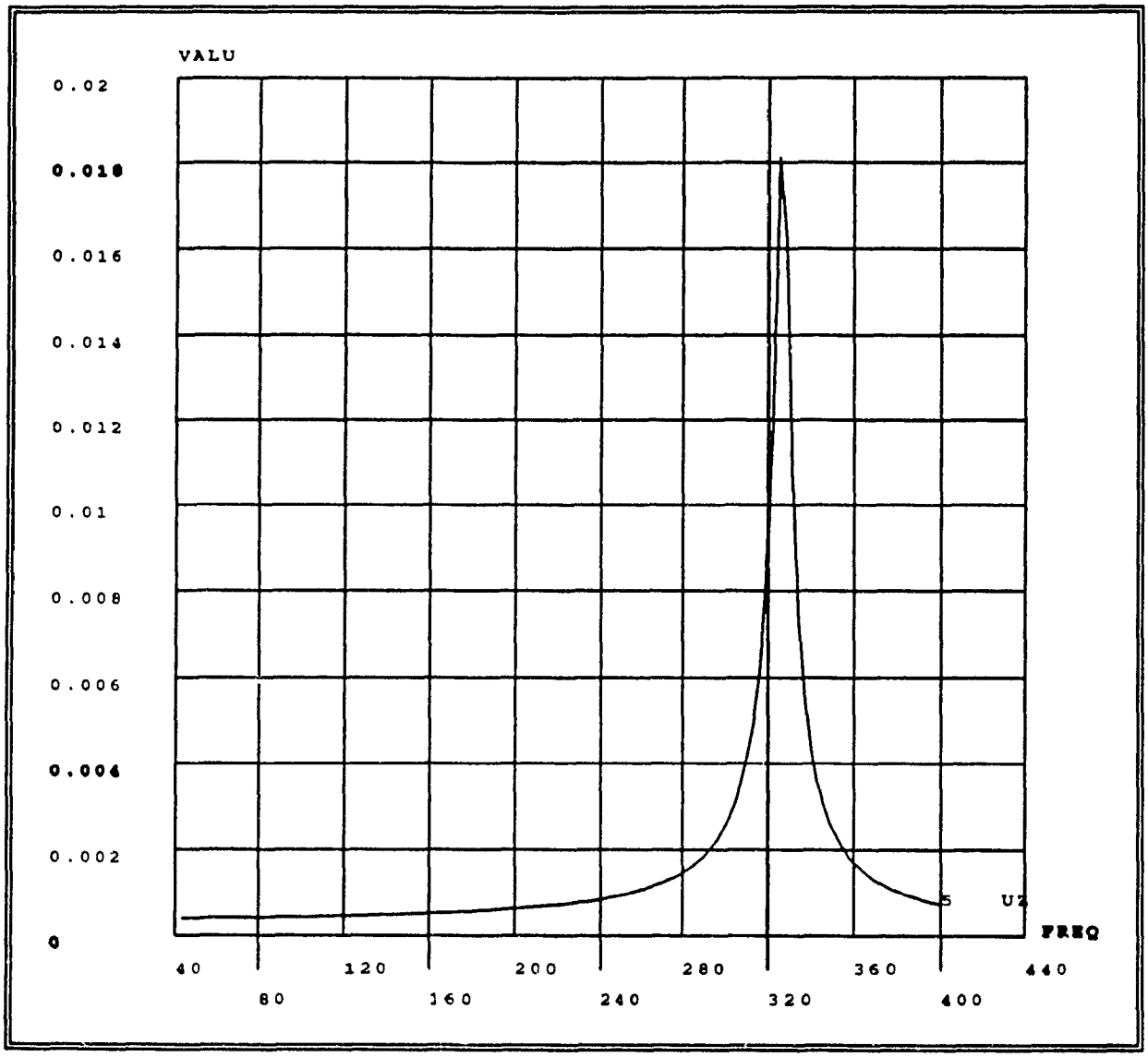

Figure 6.5 : Amplitude Plot for the Turborotor Assembly (Node 5 on the Blade UZ Direction)

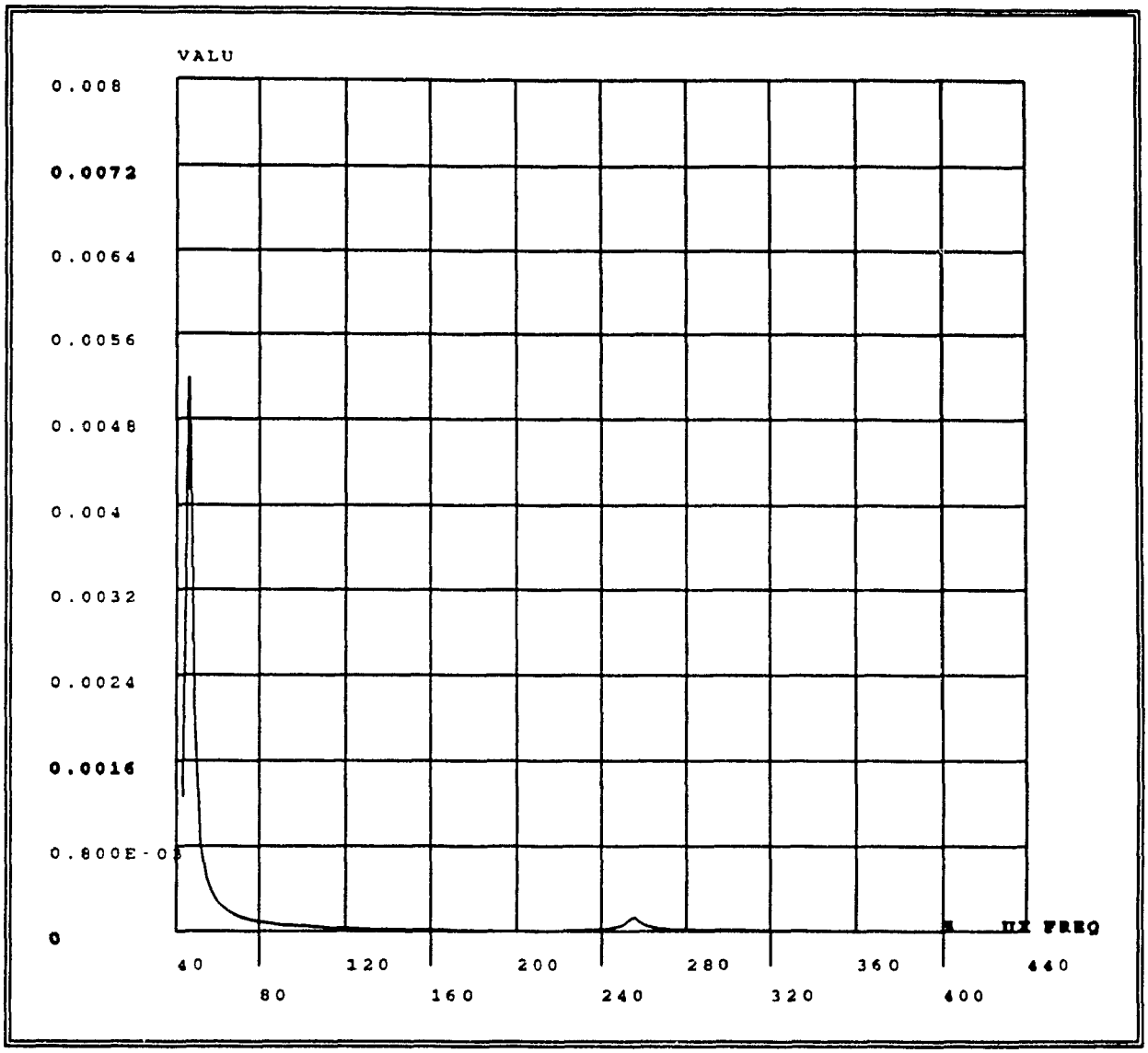

Fig. 6.6 : Amplitude Plot for the Turborotor Assembly (Node 5 on the Blade UX Direction)

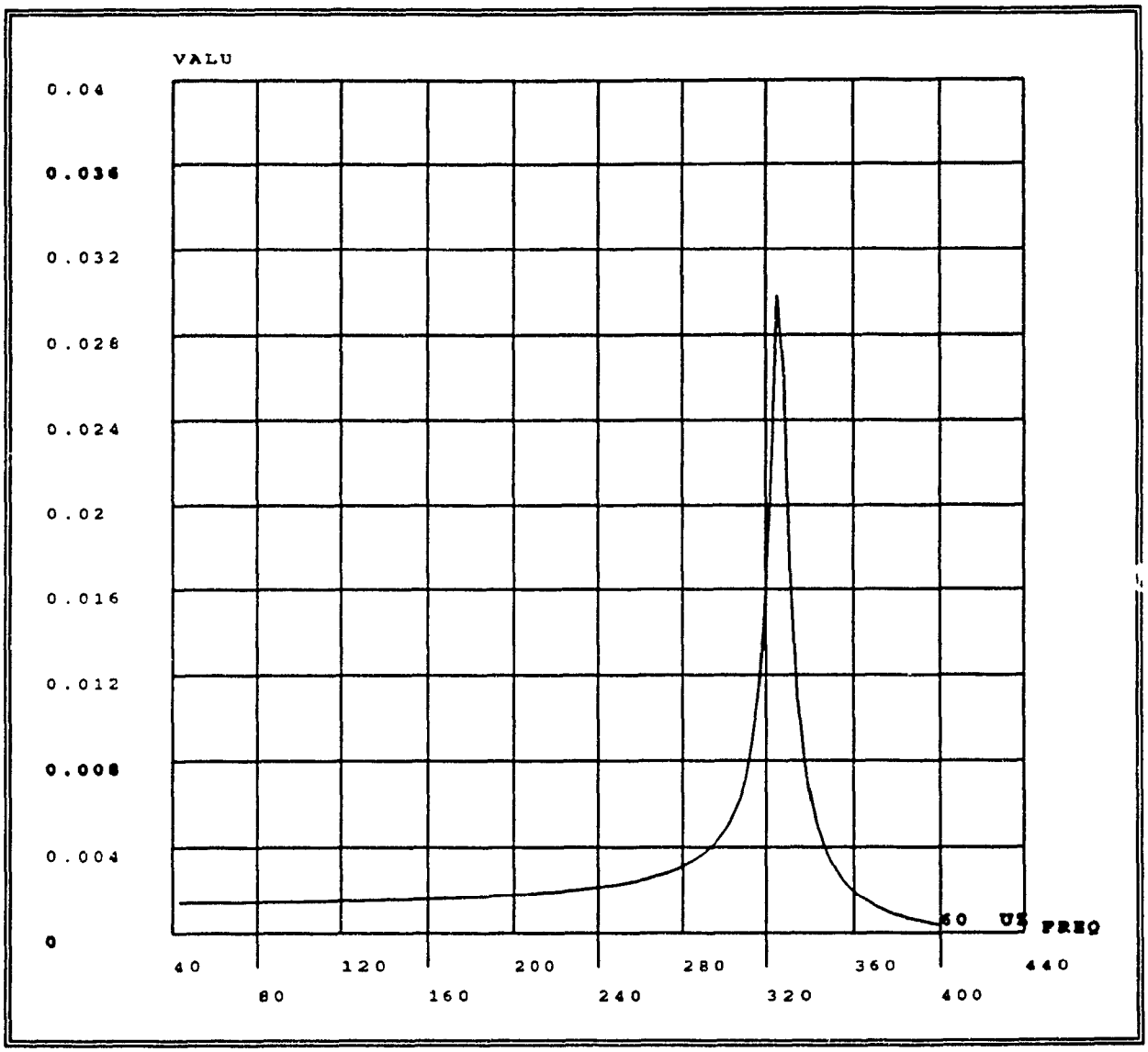

Fig. 6.7 : Amplitude Plot for the Turborotor Assembly (Node 60 on the Blade UZ Direction)

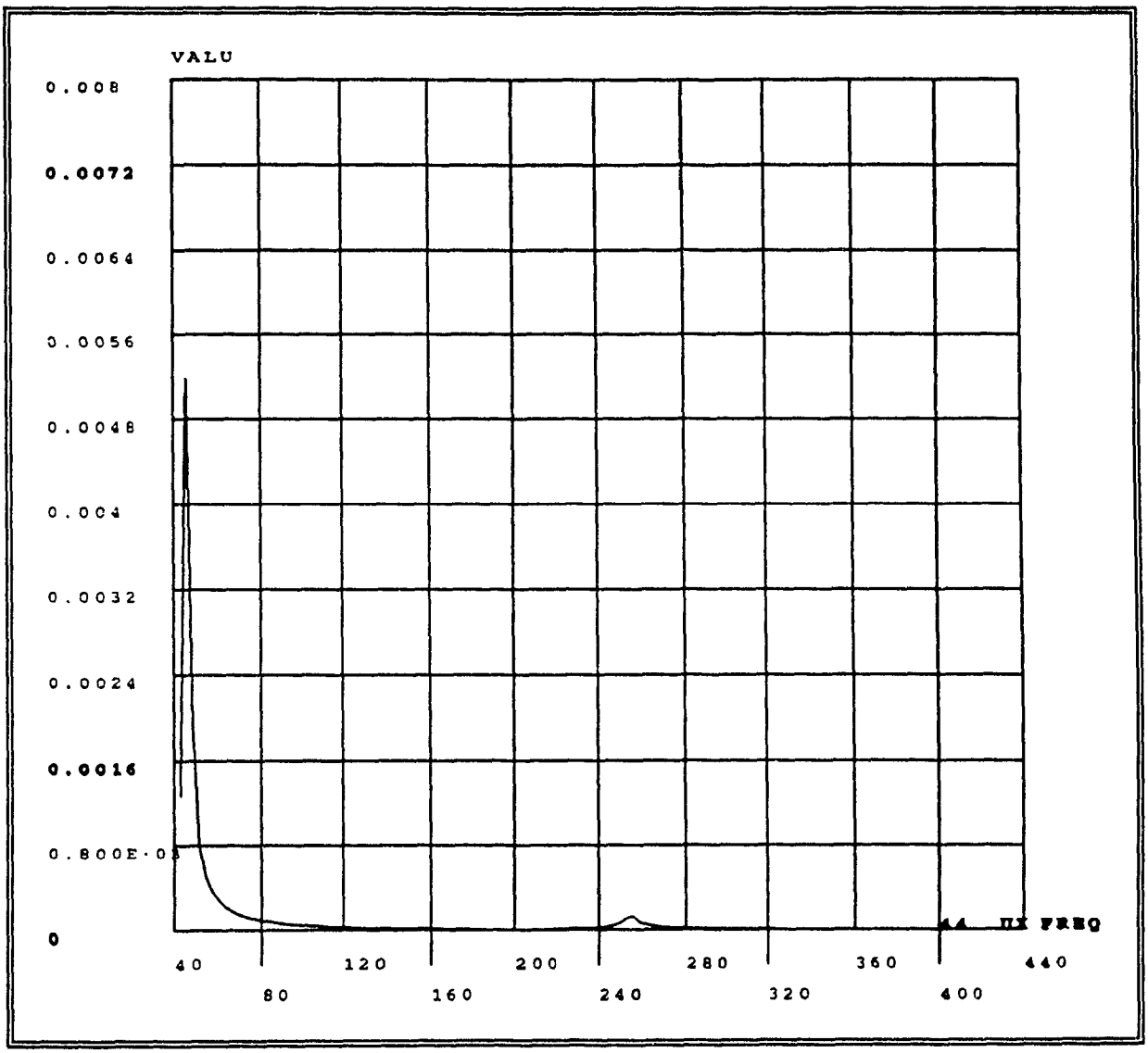

Fig. 6.8 : Amplitude Plot for the Turborotor Assembly (Node 44 on the Blade UX Direction)

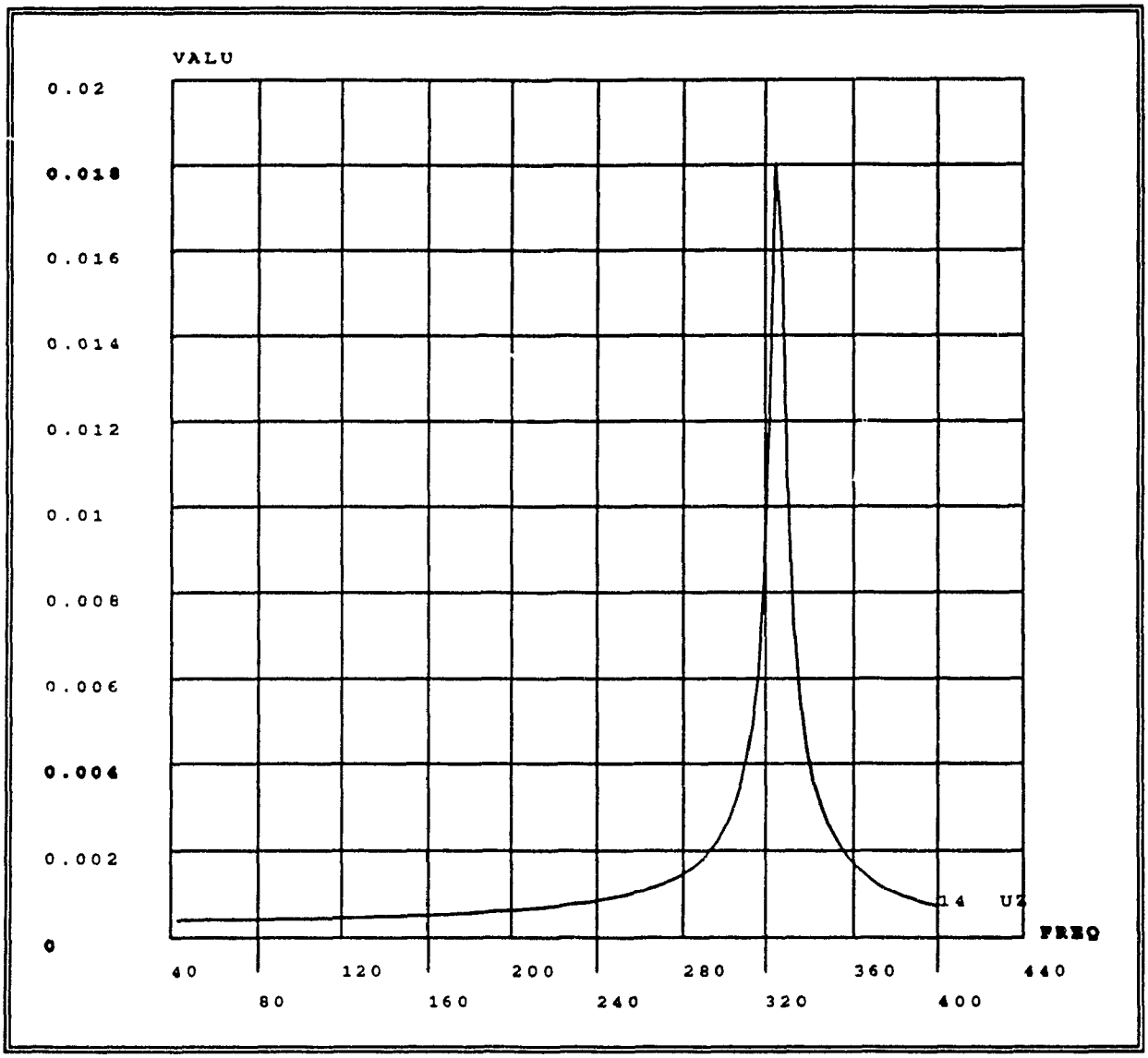

Fig. 6.9 : Amplitude Plot for the Turborotor Assembly (Node 14 on the Disk UZ direction)

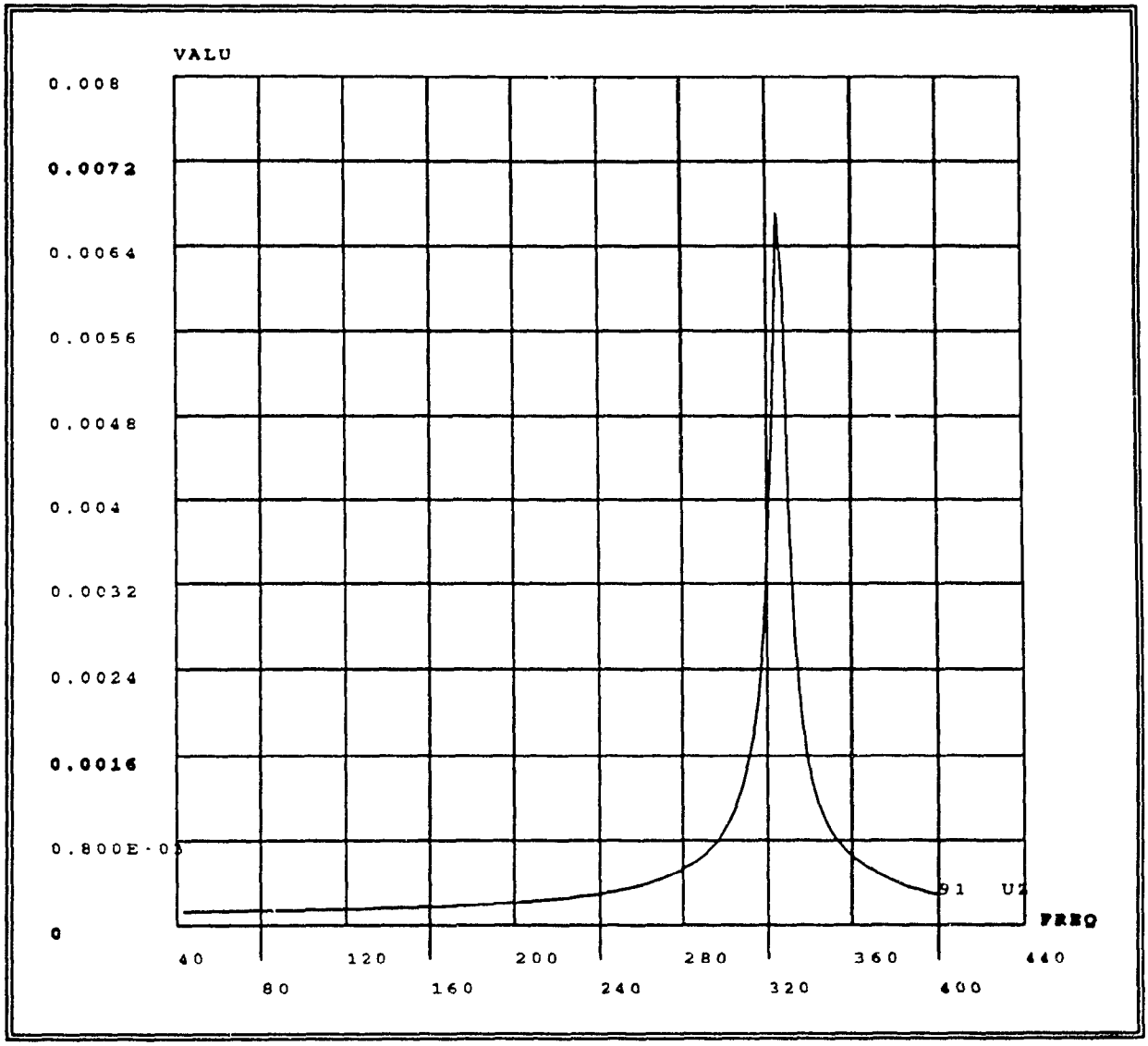

Fig. 6.10 : Amplitude Plot for the Turborotor Assembly (Node 91 on the Disk UZ Direction)

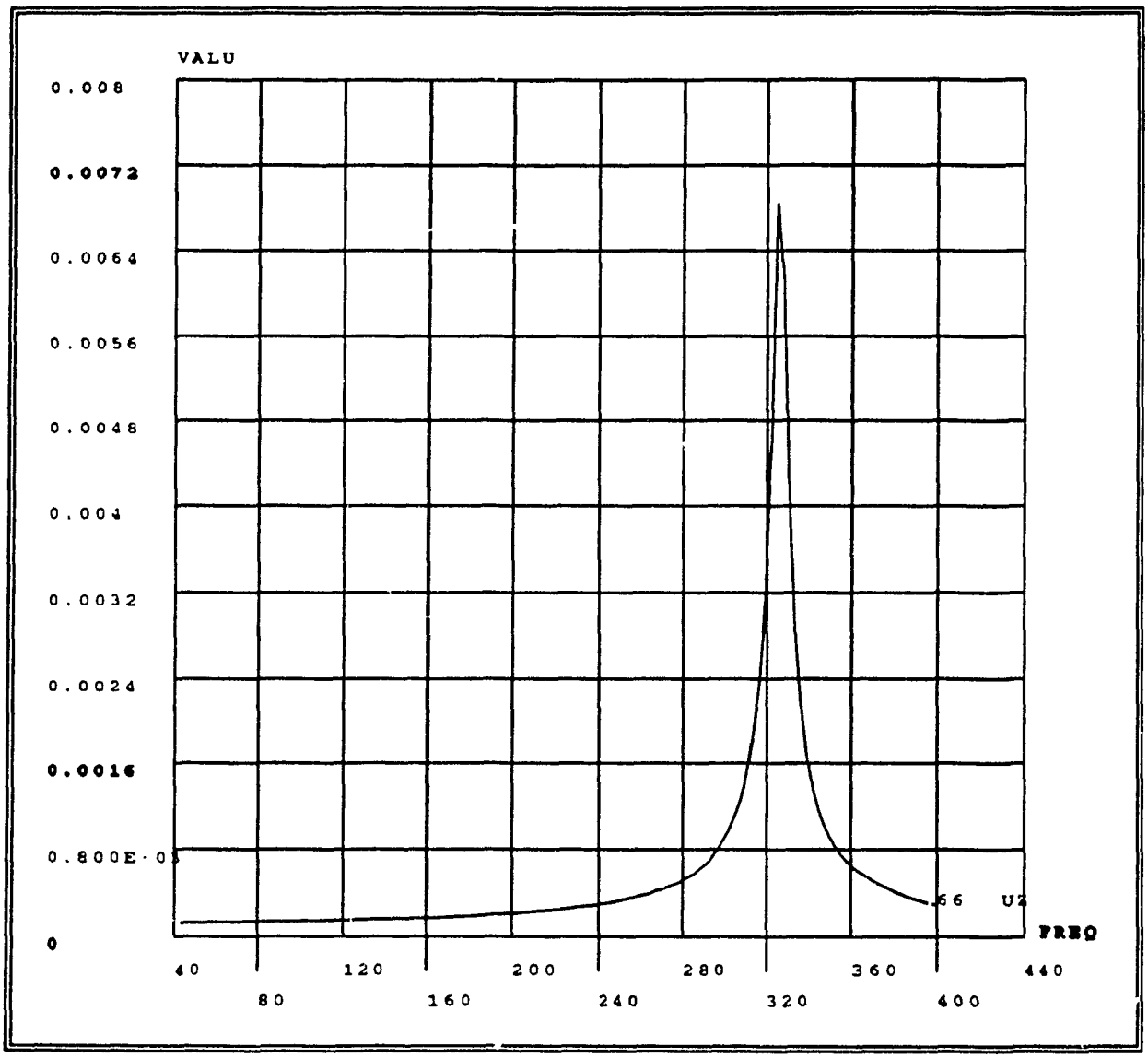

Fig 6.11 : Amplitude Plot for the Turborotor Assembly (Node 66 on the Disk UZ Direction)

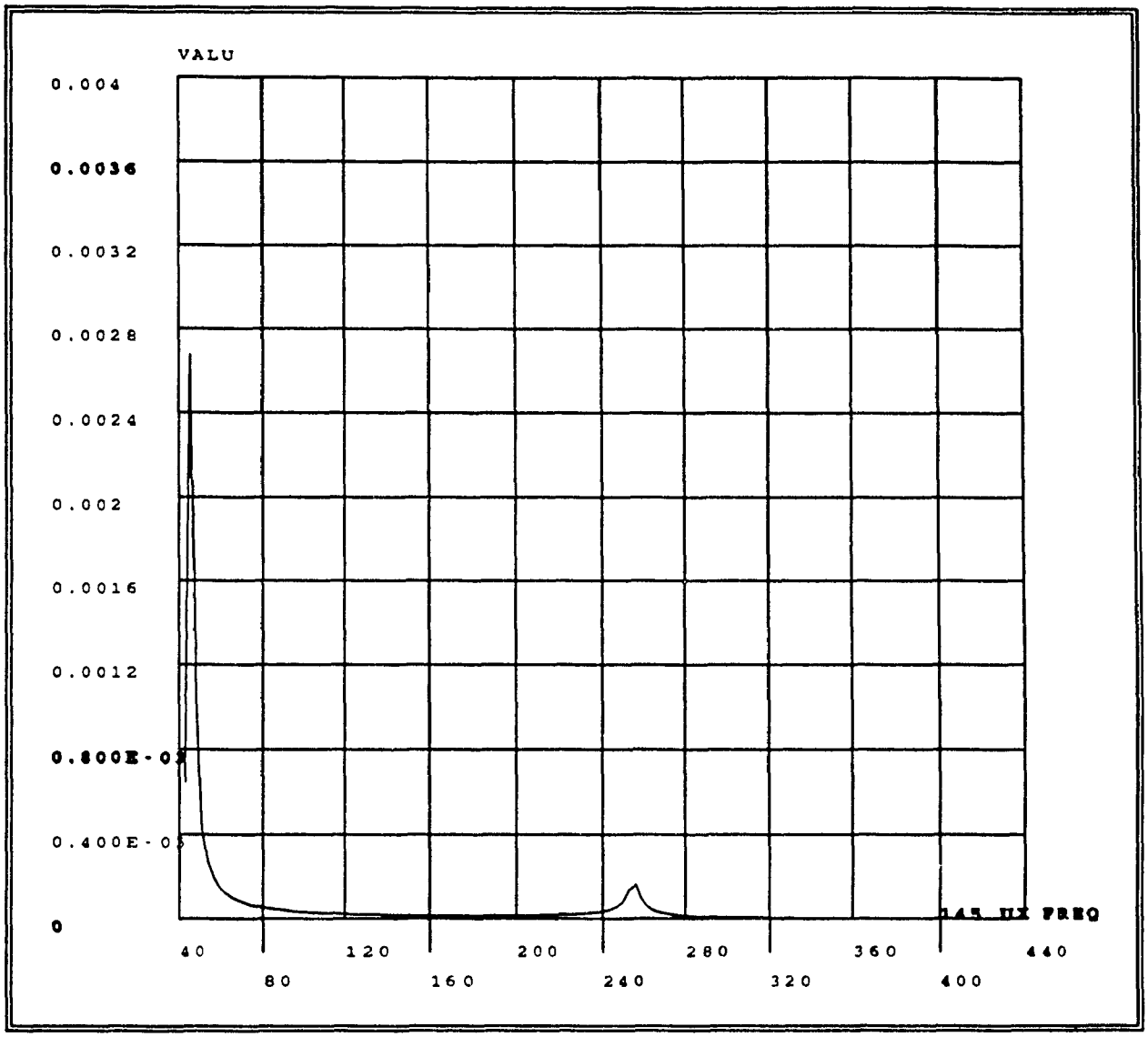

Fig. 6.12 : Amplitude Plot for the Turborotor Assembly (Node 145 on the Shaft UX Direction)

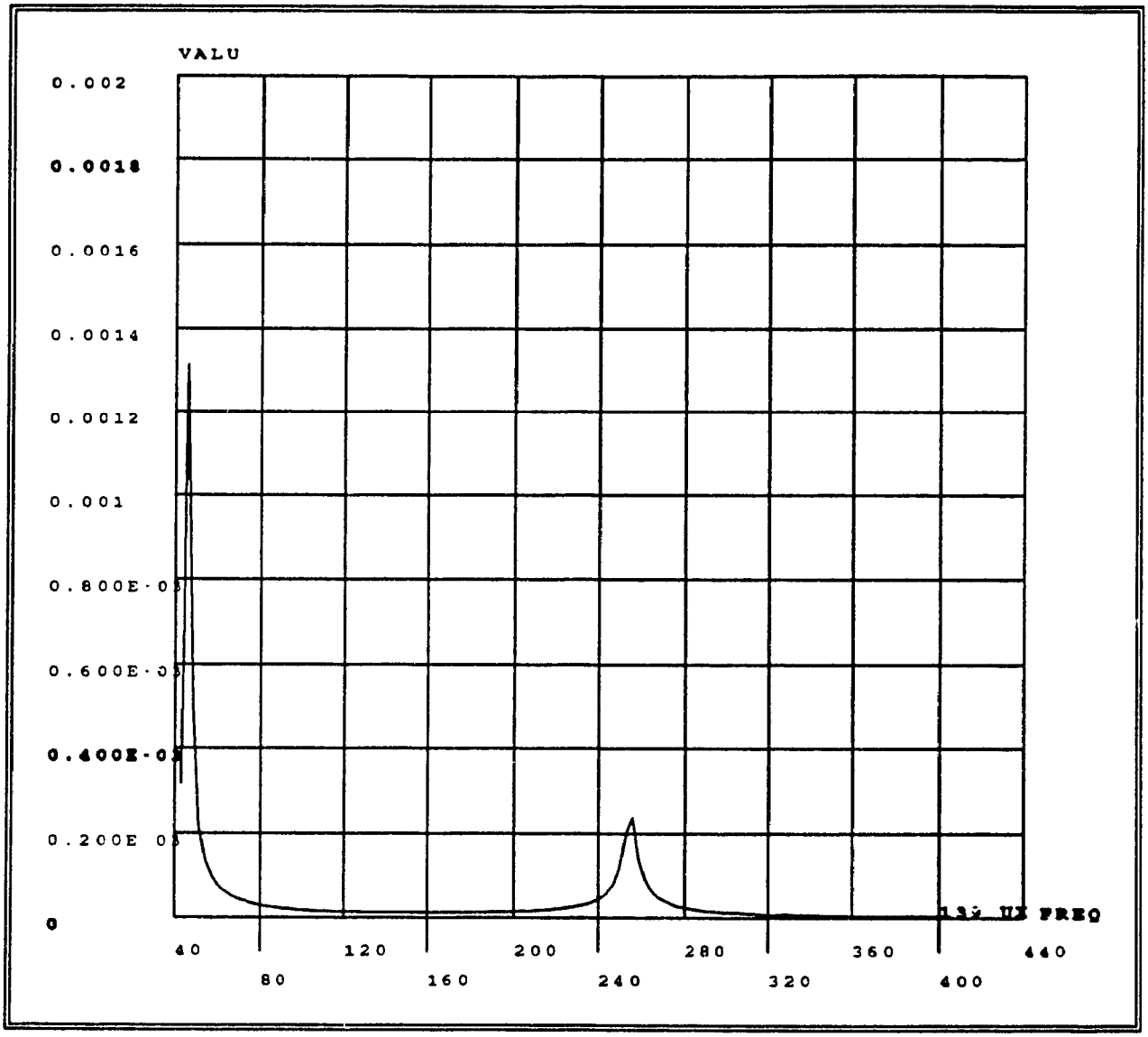

Fig 6.13 : Amplitude Plot for the Turborotor Assembly (Node 139 on the Shaft UX Direction)

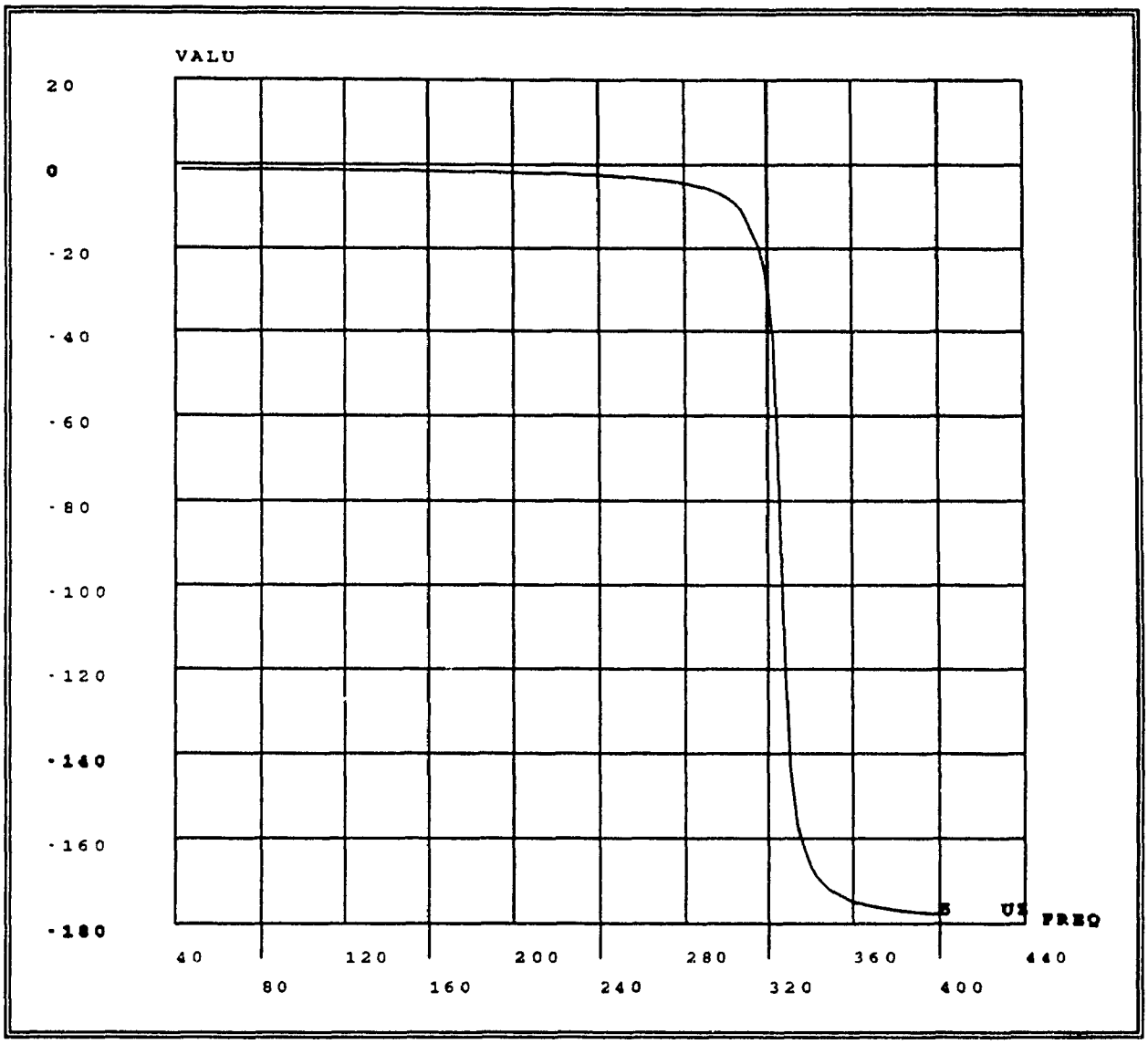

Fig. 6.14 : Phase Angle Plot for the Turborotor Assembly (Node 5 UZ Direction)

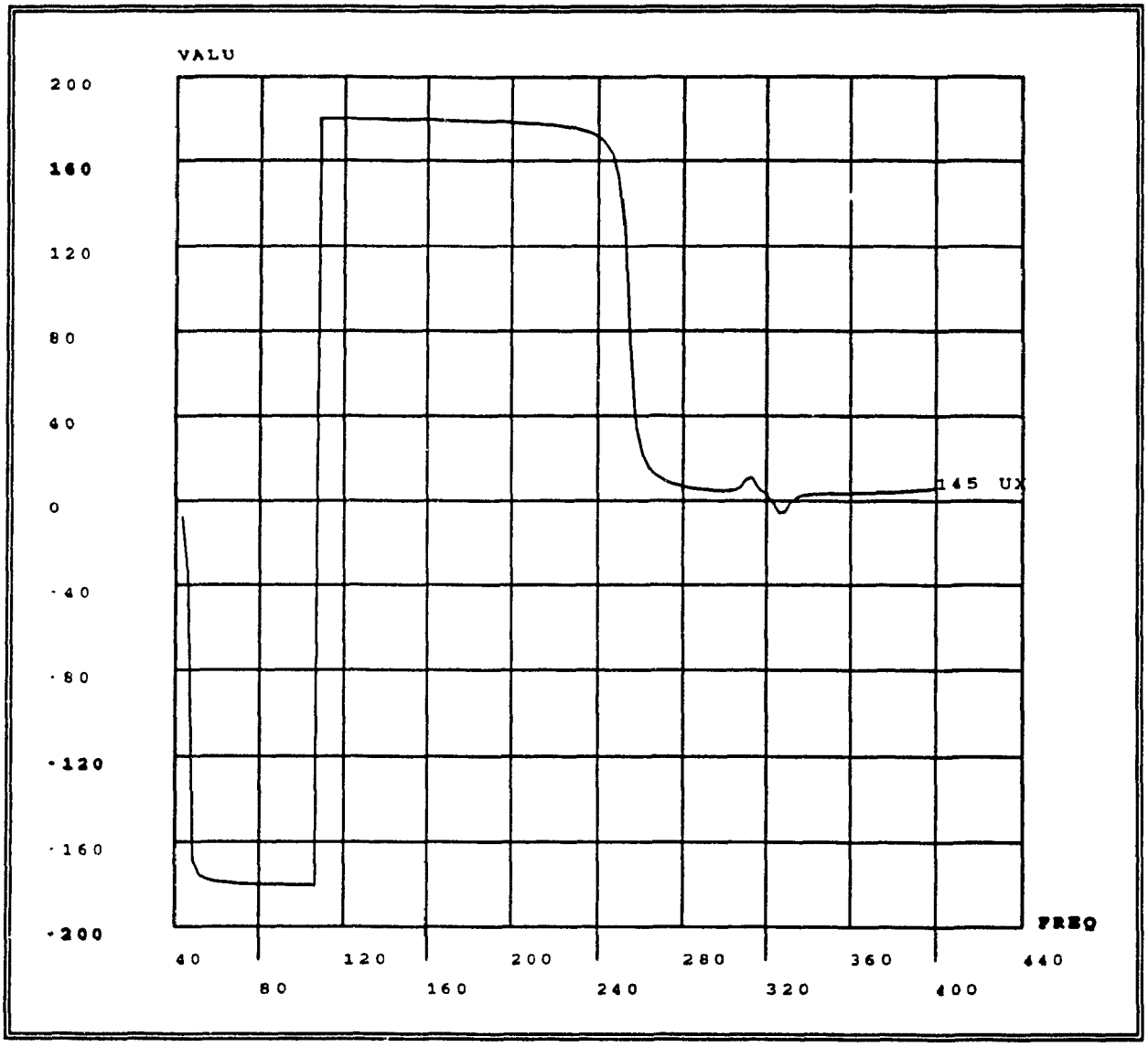

Fig. 6.15 : Phase Angle Plot for the Turborotor Assembly (Node 144 Ux Direction)

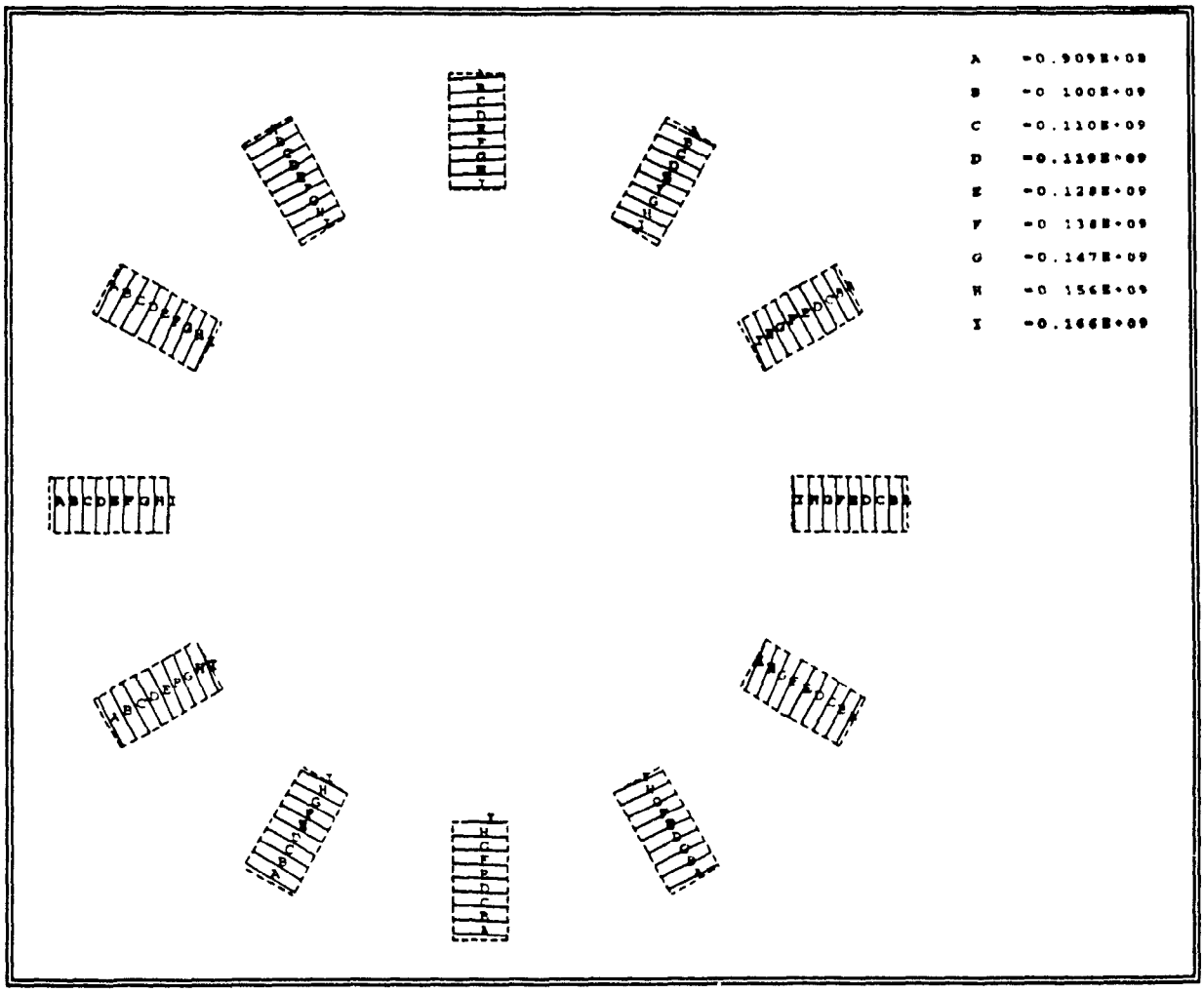

Fig. 6.16 : Average Stress Contours on the Blade (Frequency = 332 Hz)

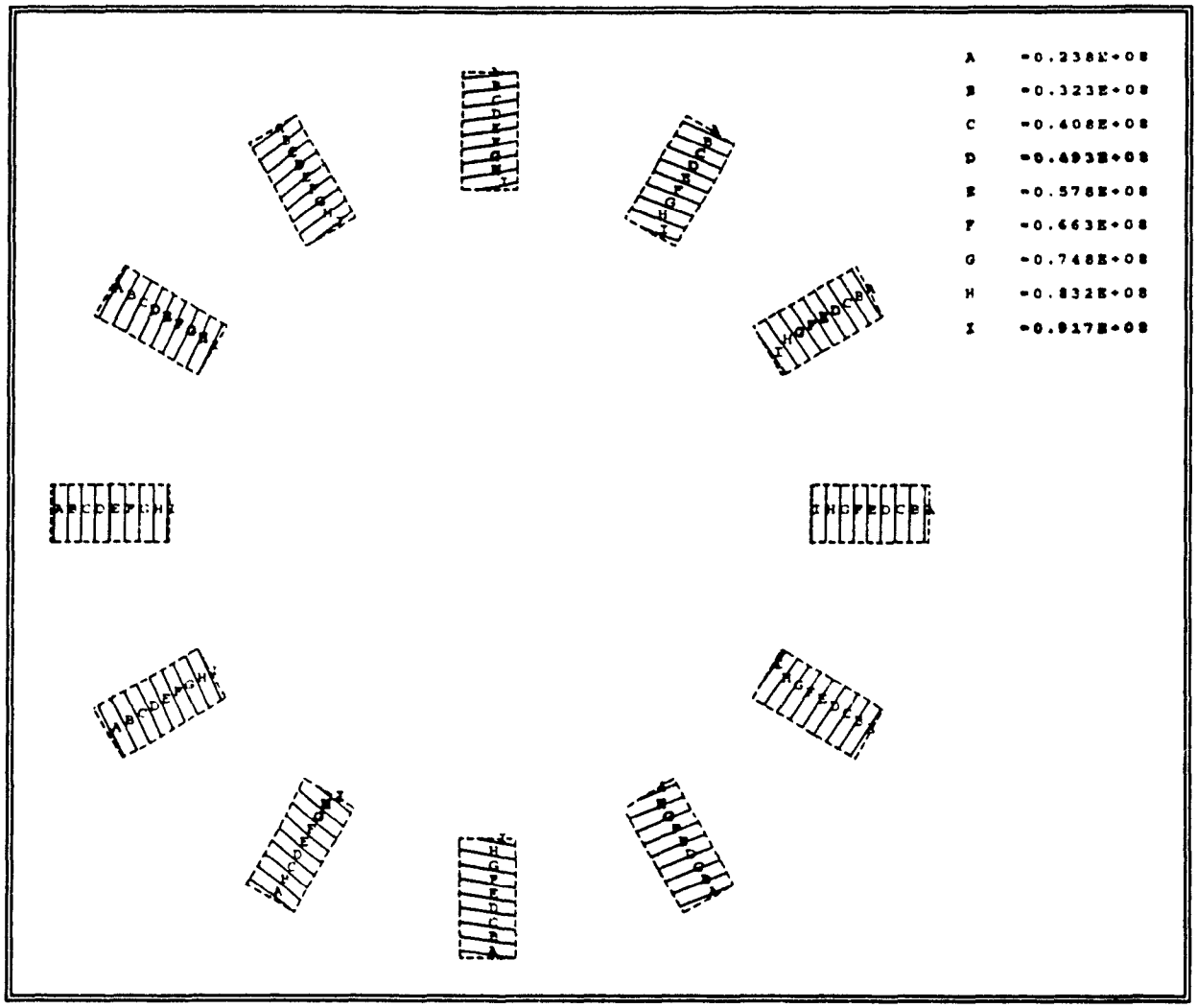

Fig. 6.17 : Average Stress Contours on the Blade (Frequency = 42.8 Hz)

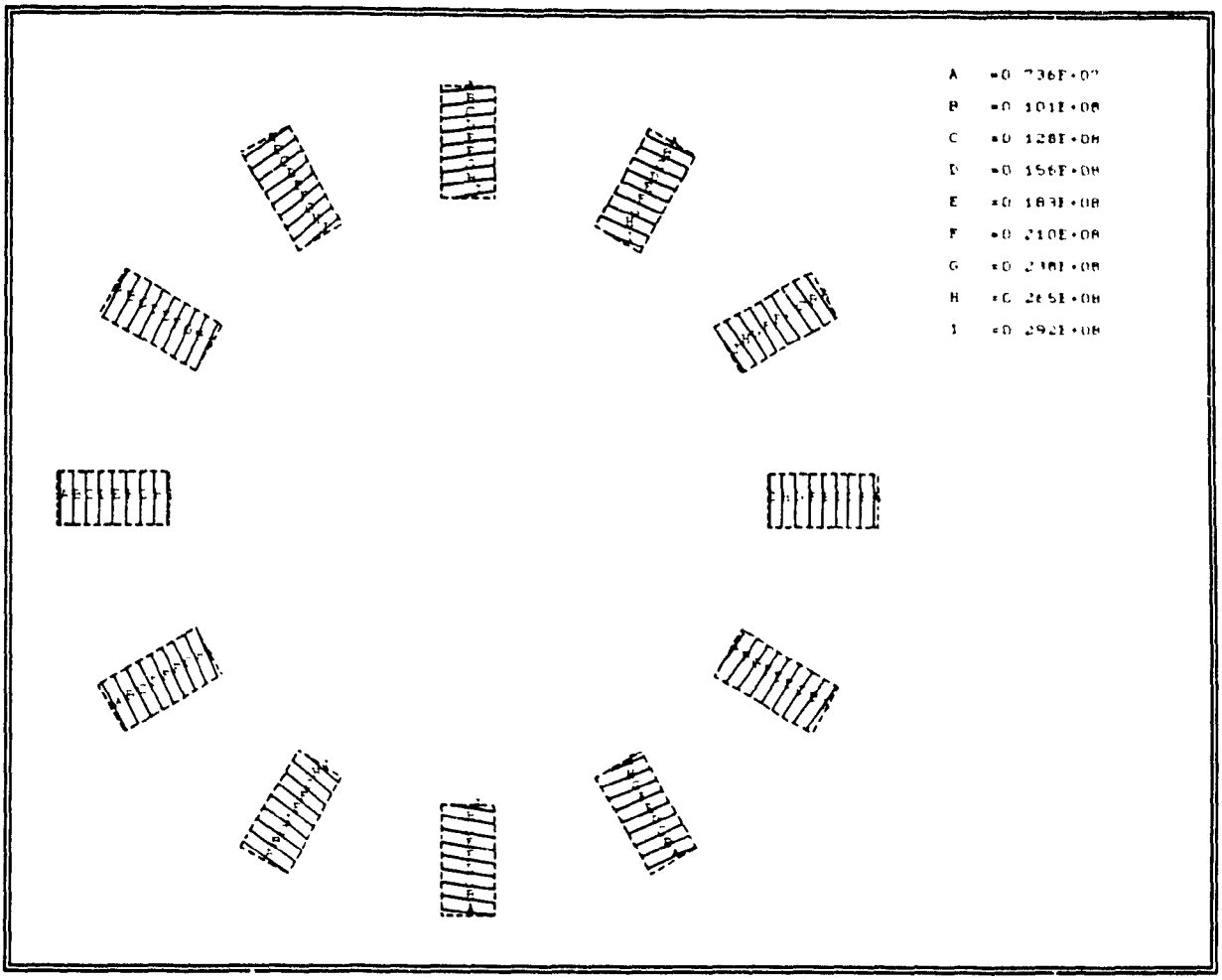

Fig. 6.18 : Average Stress Contours On the Blade (Frequency = 256 Hz)

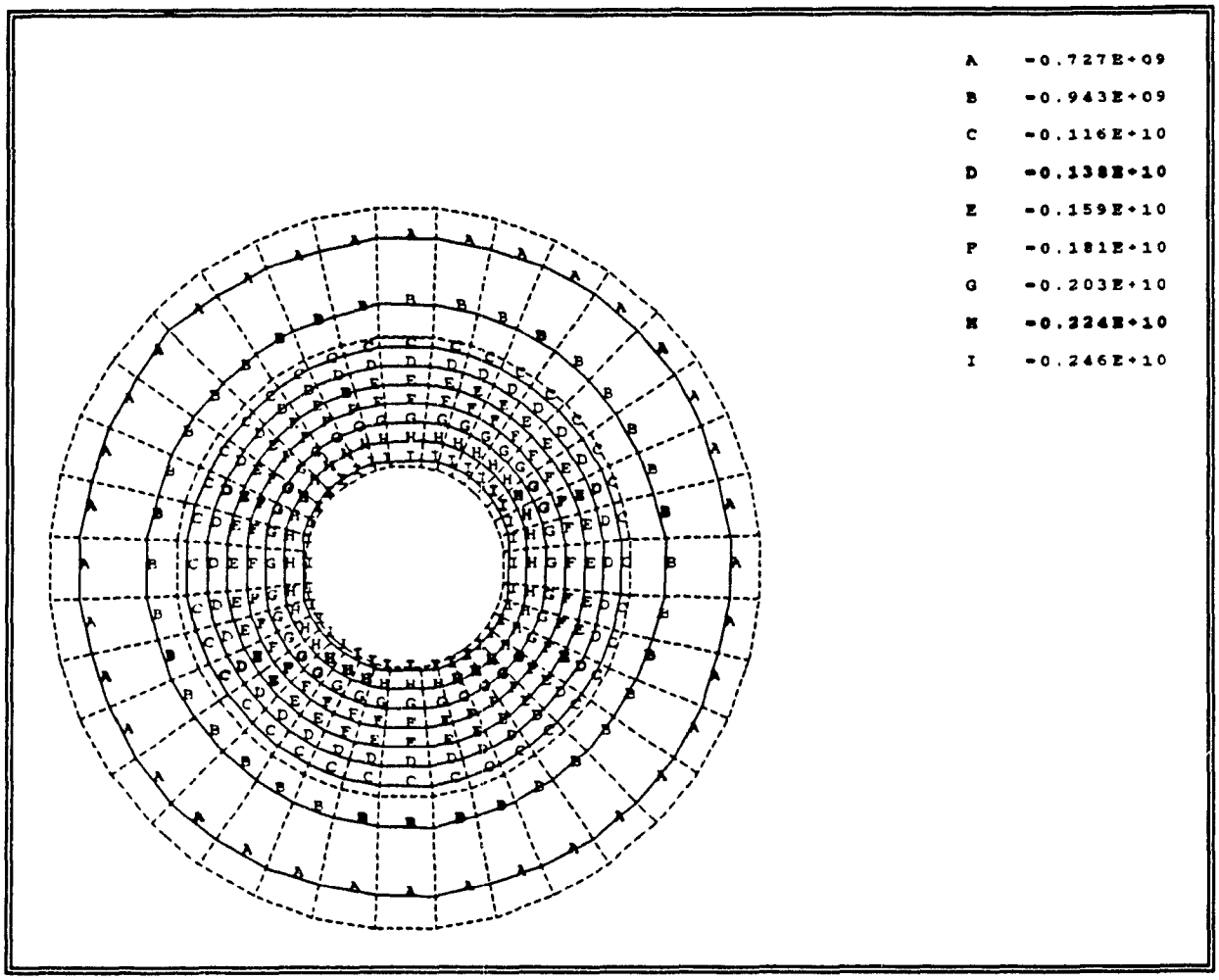

Fig. 6.19 : Average Stress Contours on the Disk (Frequency = 332 Hz)

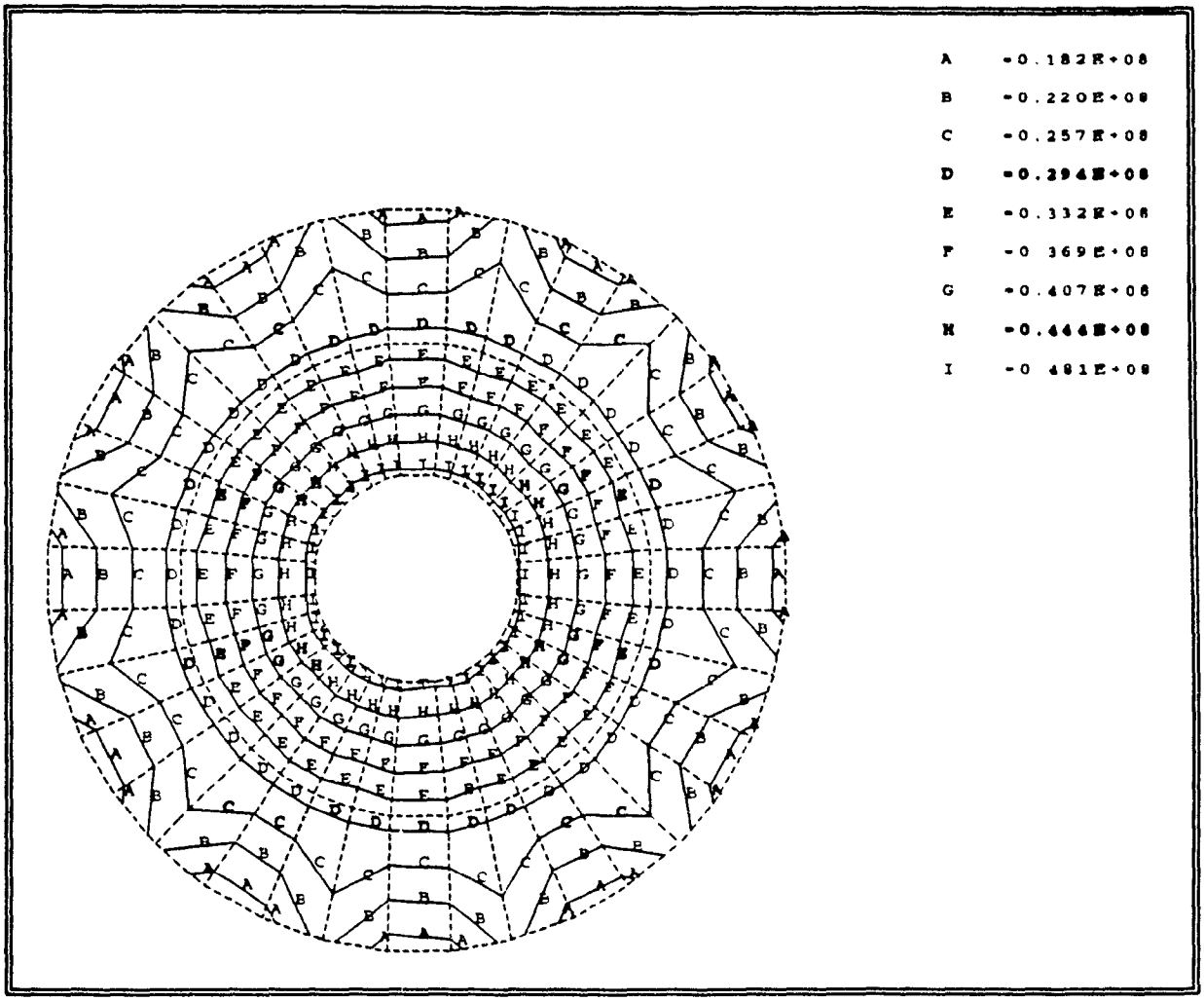

Fig. 6.20 : Average Stress Contours on the Disk (Frequency = 42.8 Hz)

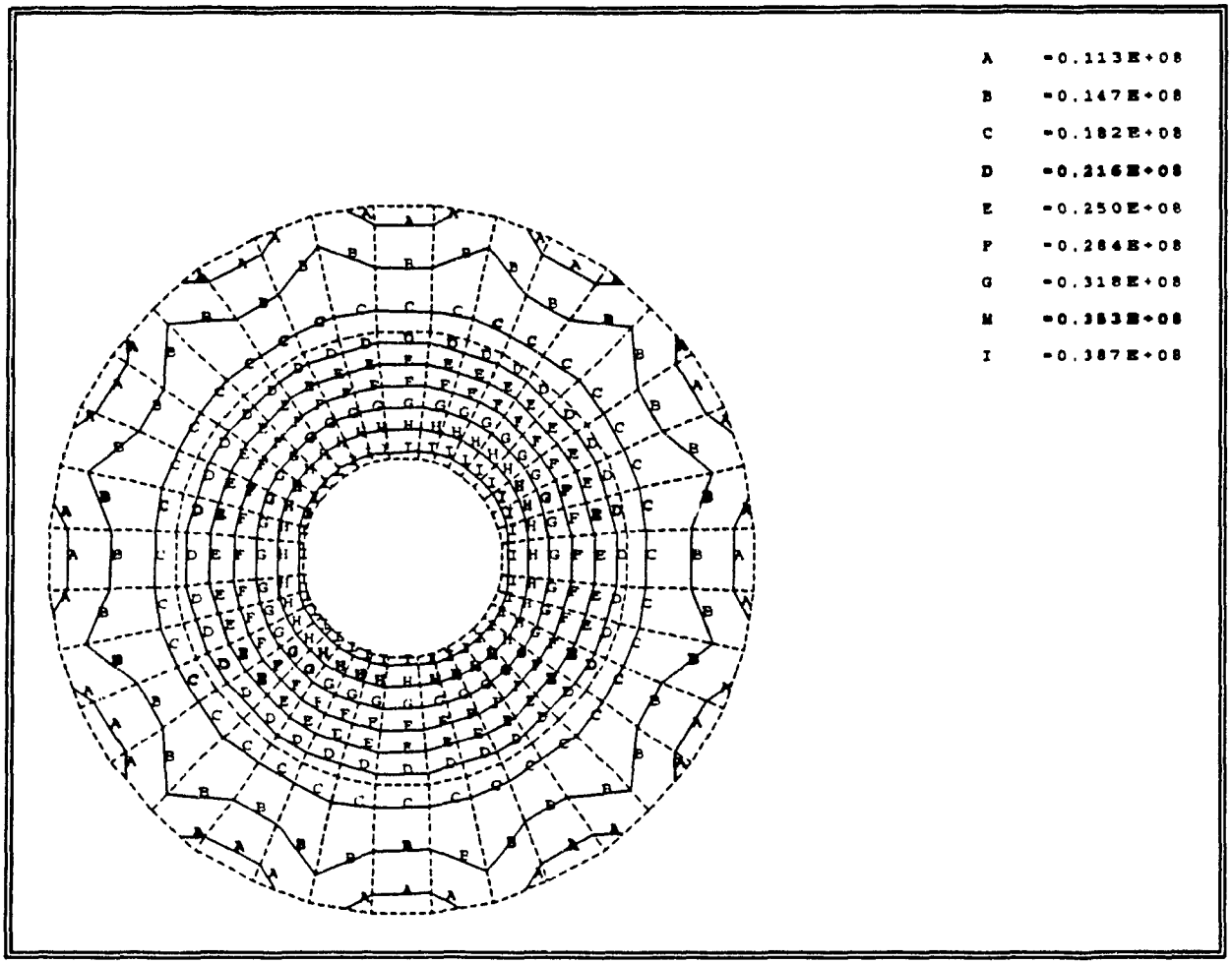

Fig. 6.21 : Average Stress Contours on the Disk (Frequency = 256 Hz)

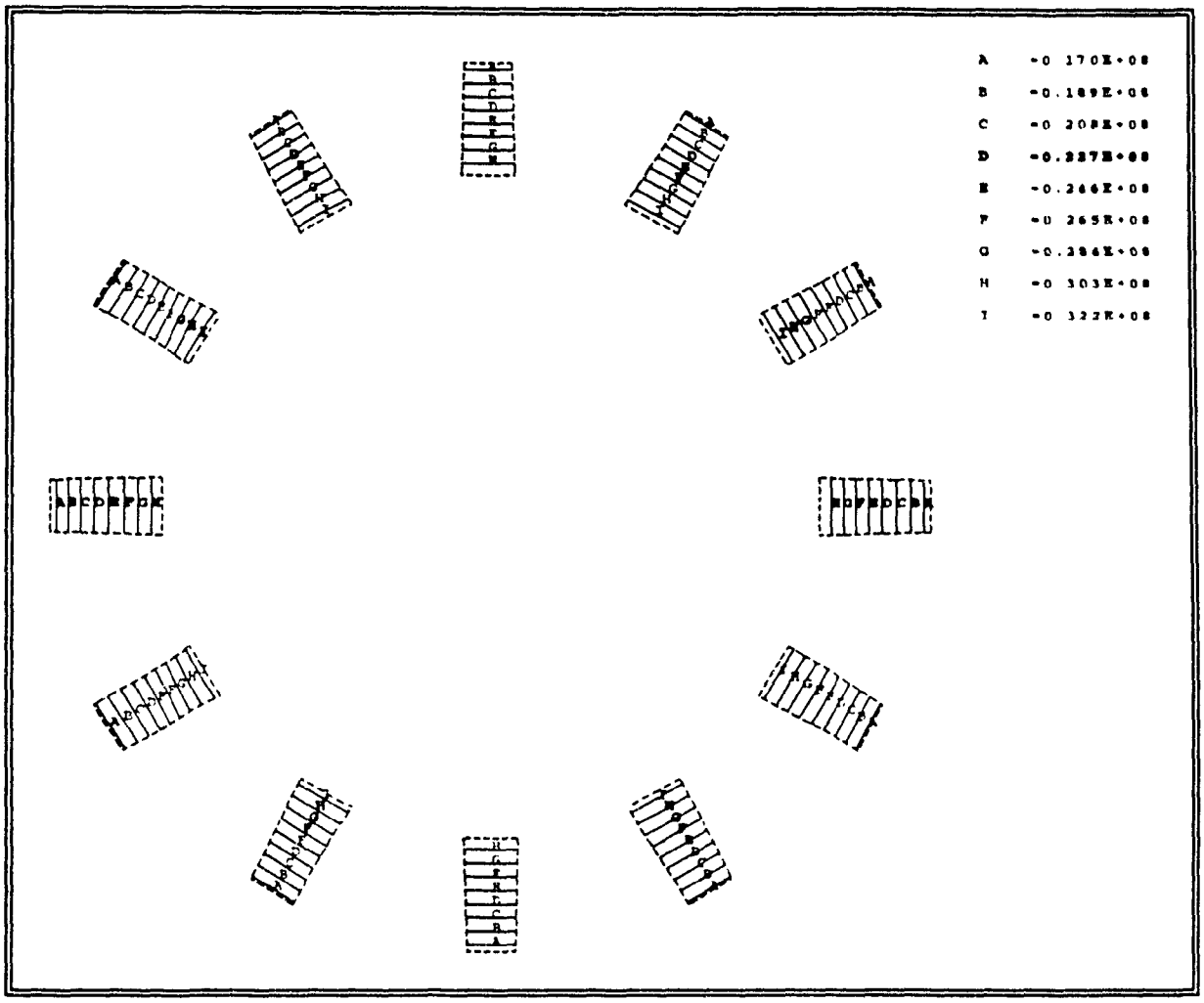

Fig. 6.22 : Average Stress Contours on the Blade (Rotational Speed = 1309 rad/sec)

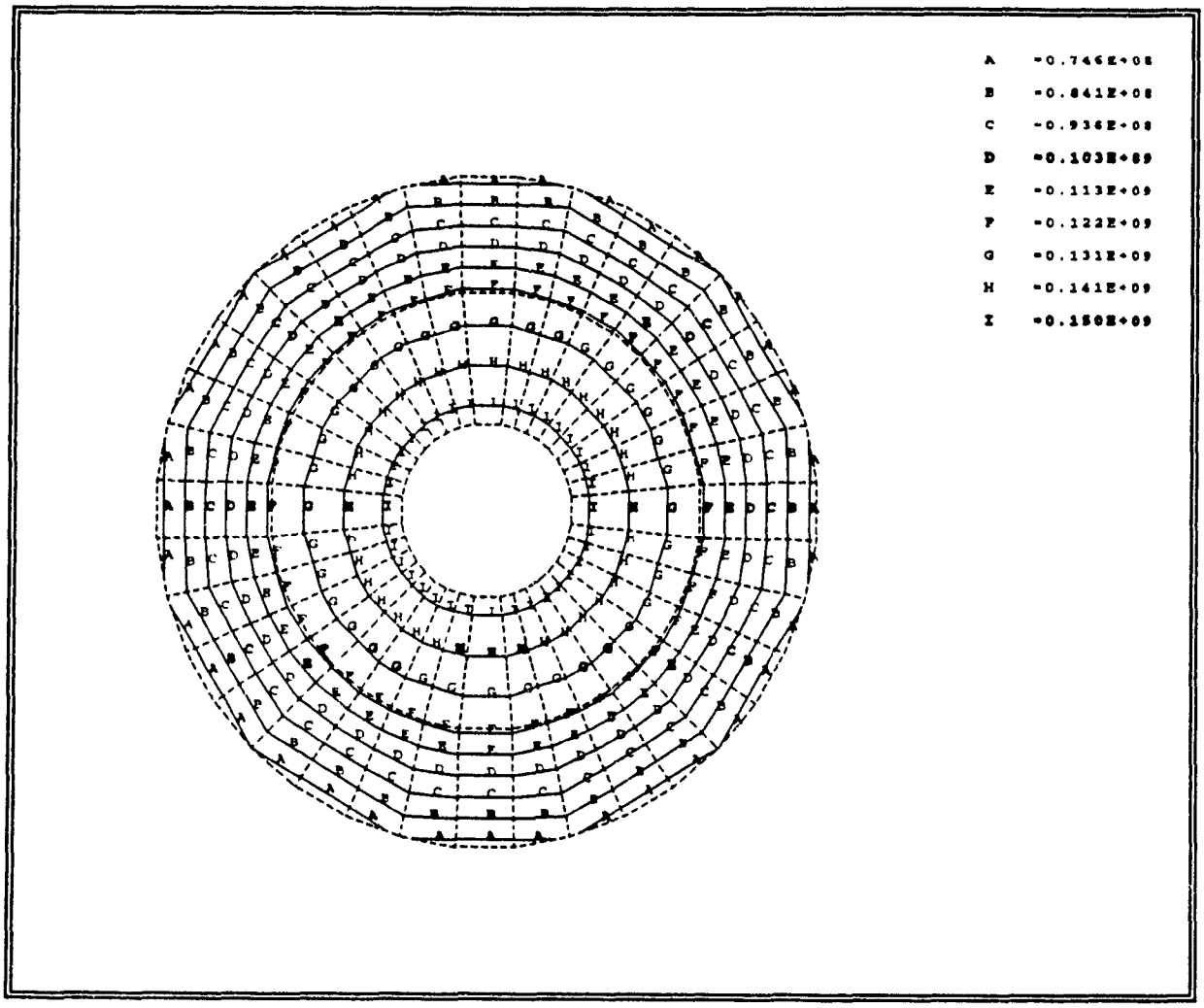

Fig. 6.23 : Average Stress Contours on the Disk (Rotational Speed = 1309 rad/sec)

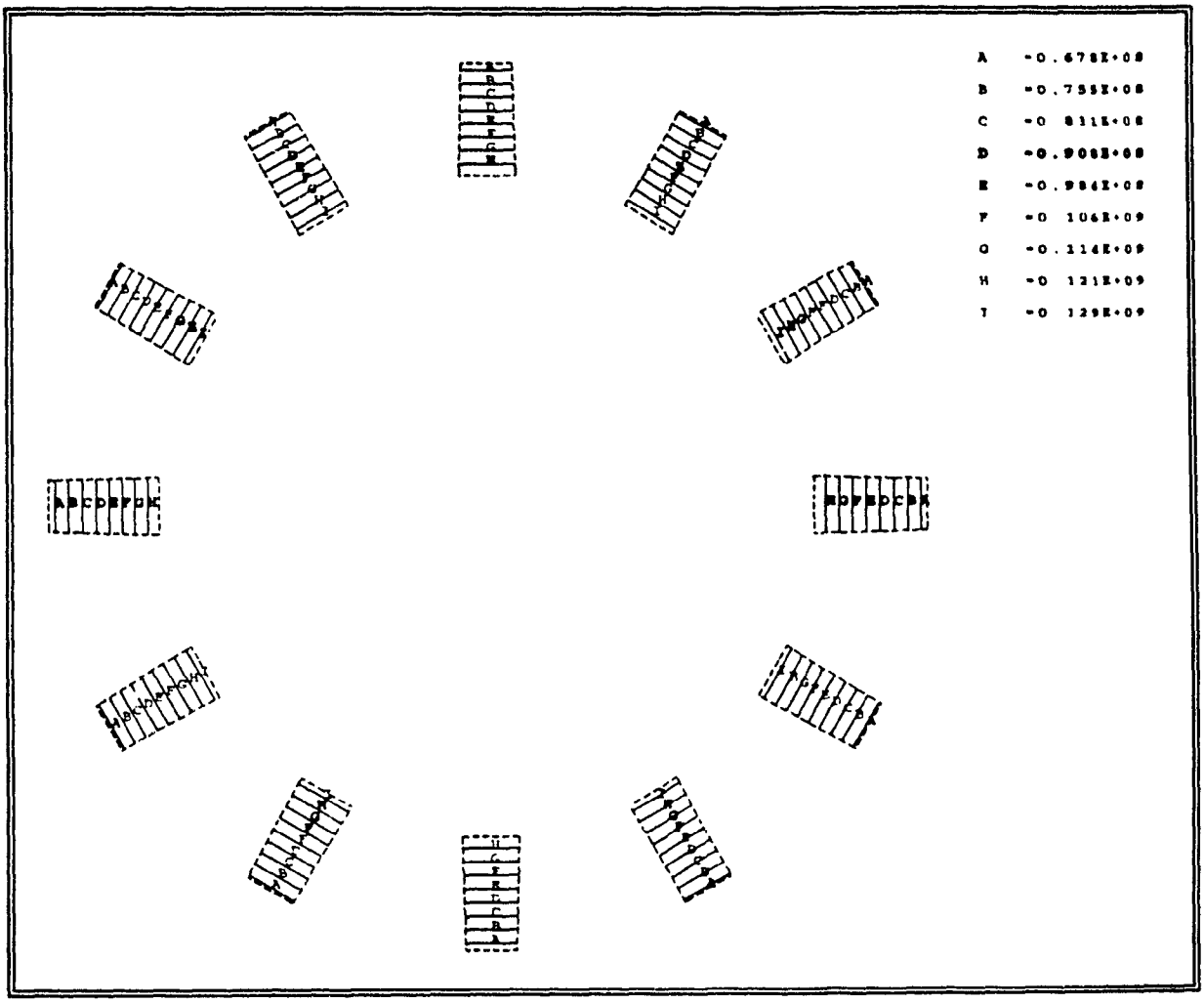

Fig. 6.24 : Average Stress Contours on the Blade (Rotational Speed = 2618 rad/sec)

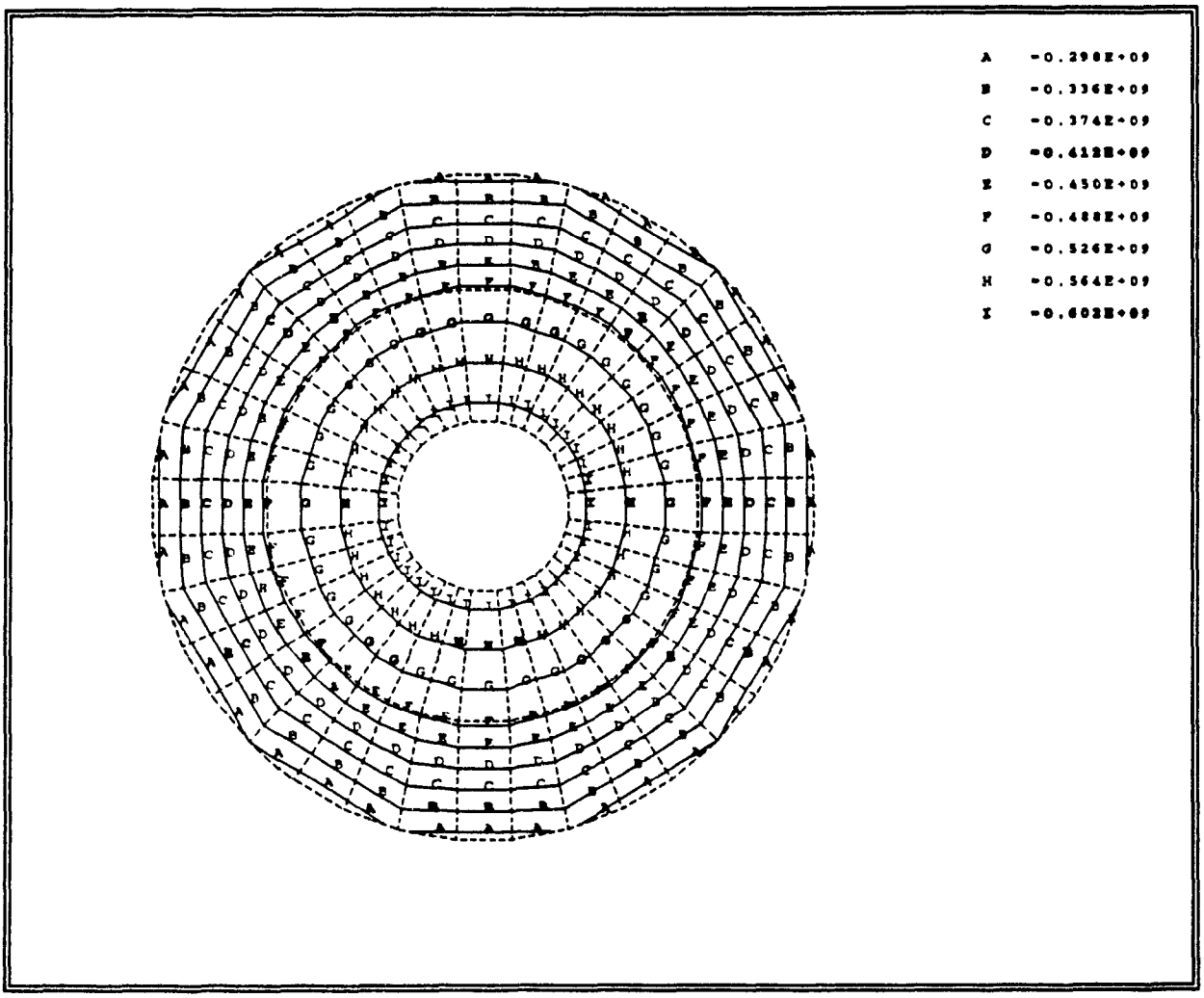

Fig. 6.25 : Average Stress Contours on the Disk (Rotational Speed = 2618 rad/sec)

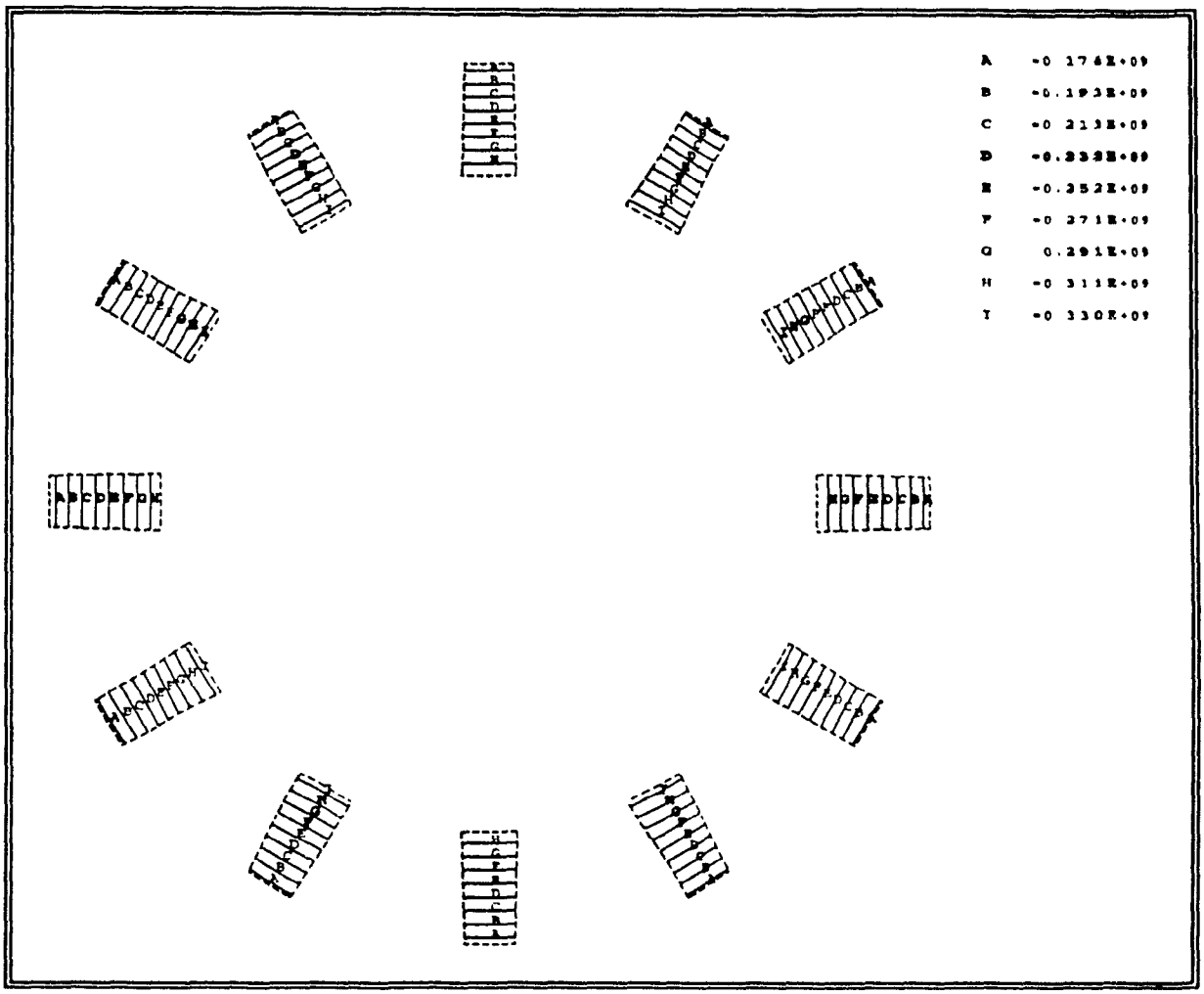

Fig.6.26 : Average Stress Contours on the Blade (Rotational Speed = 4189 rad/sec)

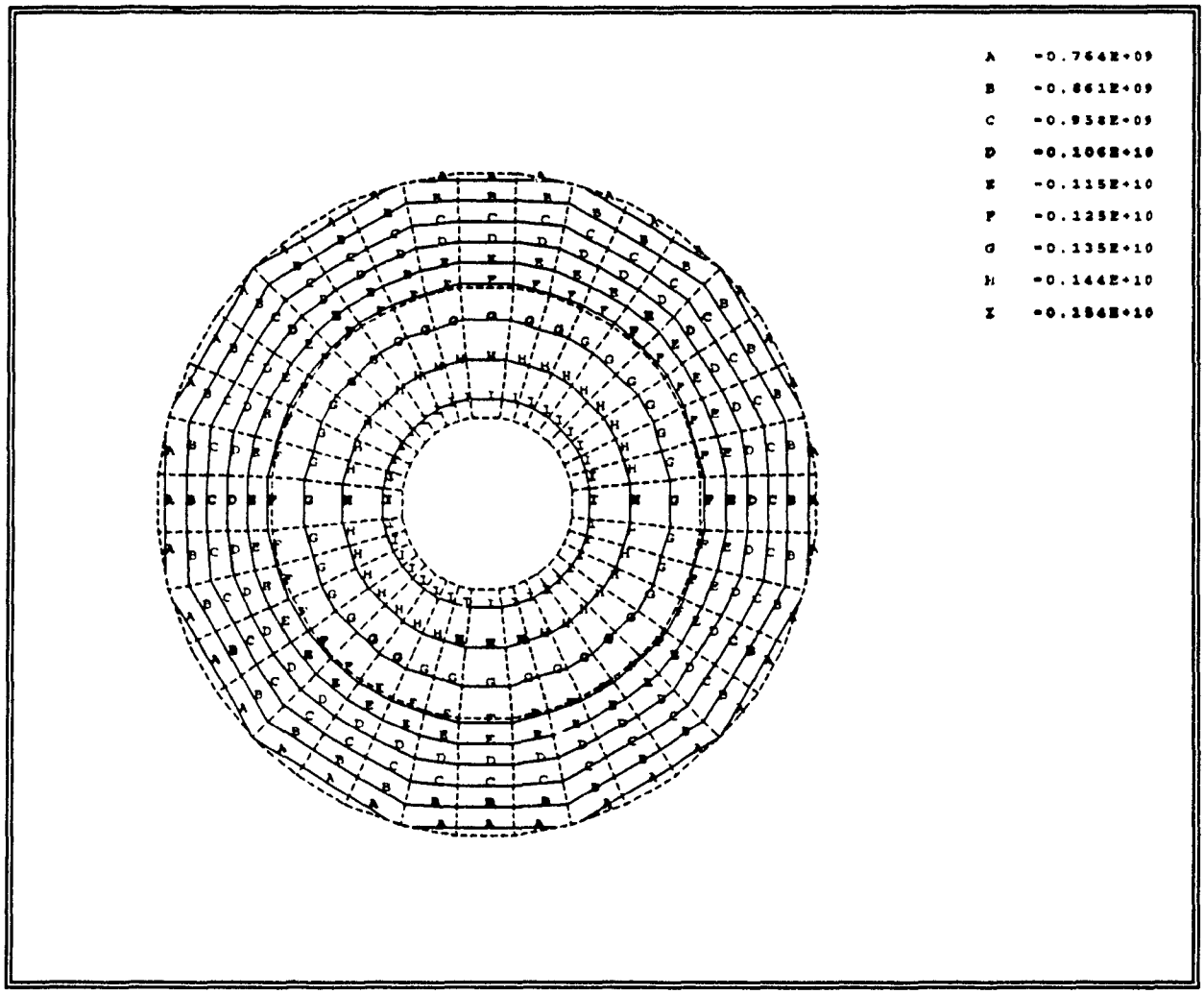

Fig. 6.27 : Average Stress Contours on the Disk (Rotational Speed = 4189 rad/sec)

CHAPTER 7

EXPERIMENTAL ANALYSIS OF A SHAFT DISK SYSTEM

7.1 : General

In the preceding chapters dynamic behaviour of a turborotor system was investigated analytically and also numerically using finite element techniques. In order to verify some of the theoretical studies an experimental set up with a rotating shaft disk system was used. The results of this investigation are presented in this chapter.

7.2 : Experimental Setup

An experimental facility was established in order to carry out a validation of some of the analytical results. The shaft disk assembly schematic and the experimental setup are shown in Figs. 7.1 through 7.5. The assembly consists of a circular shaft mounted on rolling contact bearings in cast iron pedestals. The disk is mounted at the center point of the shaft. Even though inclusion of blades on the disk would make the test structure more realistic, it would increase the complexity of the assembly in terms of the blade fixture to the disk. Since the objective of the test is to validate the analytical results on the effect of rotation on the natural frequencies , the test structure was limited to a shaft disk assembly only. The shaft is driven by a variable speed motor through gear so as to increase the speed of the shaft. The

shaft speed is measured by a digital tachometer. An accelerometer is mounted on the disk to measure the vibration level. An impulse hammer and a hydrodynamic shaker, having a force transducer to detect the magnitude of the force applied are used to apply test force at predefined points on the shaft disk system.

A slip ring arrangement was attached to one end of the shaft to transmit the response signal from the accelerometer mounted on the disk to the FFT analyzer.

Table 7.1 shows the dimensions and material properties for the shaft disk system.

7.3 : Modal Testing of the Shaft Disk System

A dynamical system can be described by either a geometrical description or modal description. In the geometrical description the system is described in terms of the mass and stiffness matrices obtained using finite element methods or lumped mass and stiffness properties. The system can also be described using properties such as natural frequencies, mode shapes, damping ratio, which is known as modal description. Modal testing is a convenient technique to obtain these system parameters.

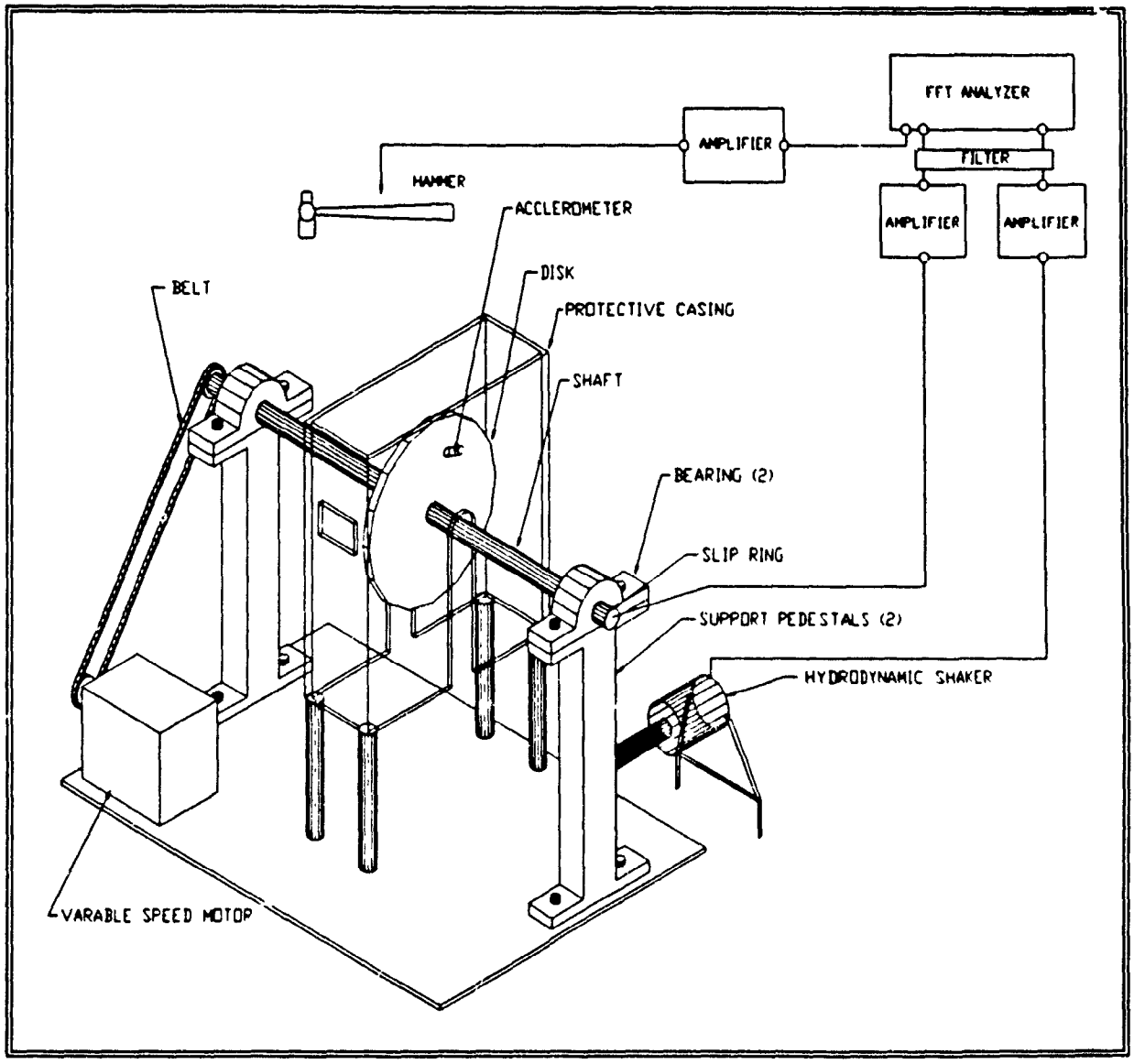

Figure 7.1 : Schematic of the Experimental Setup

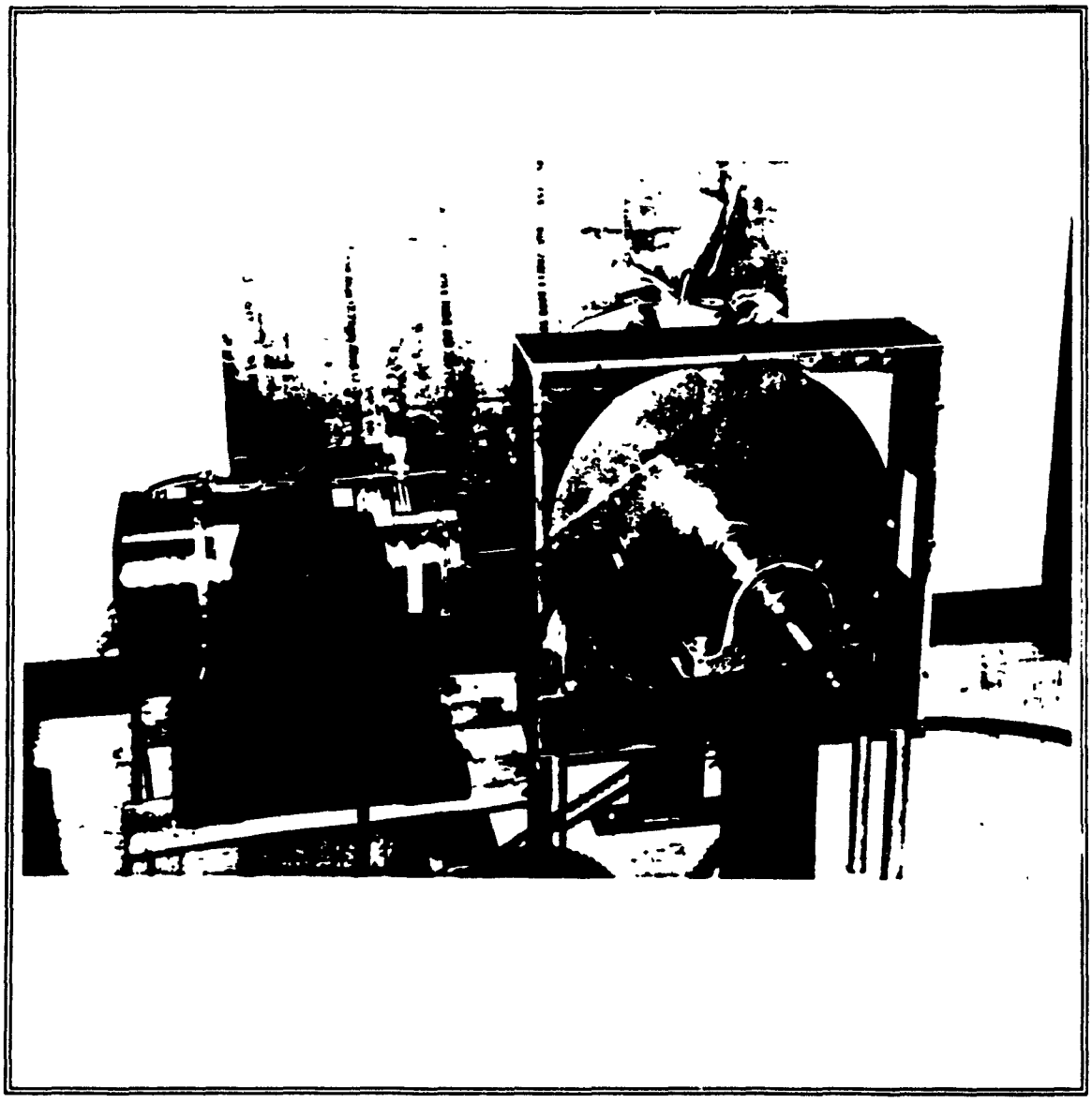

Figure 7.2 : Experimental Setup of the Shaft Disk System

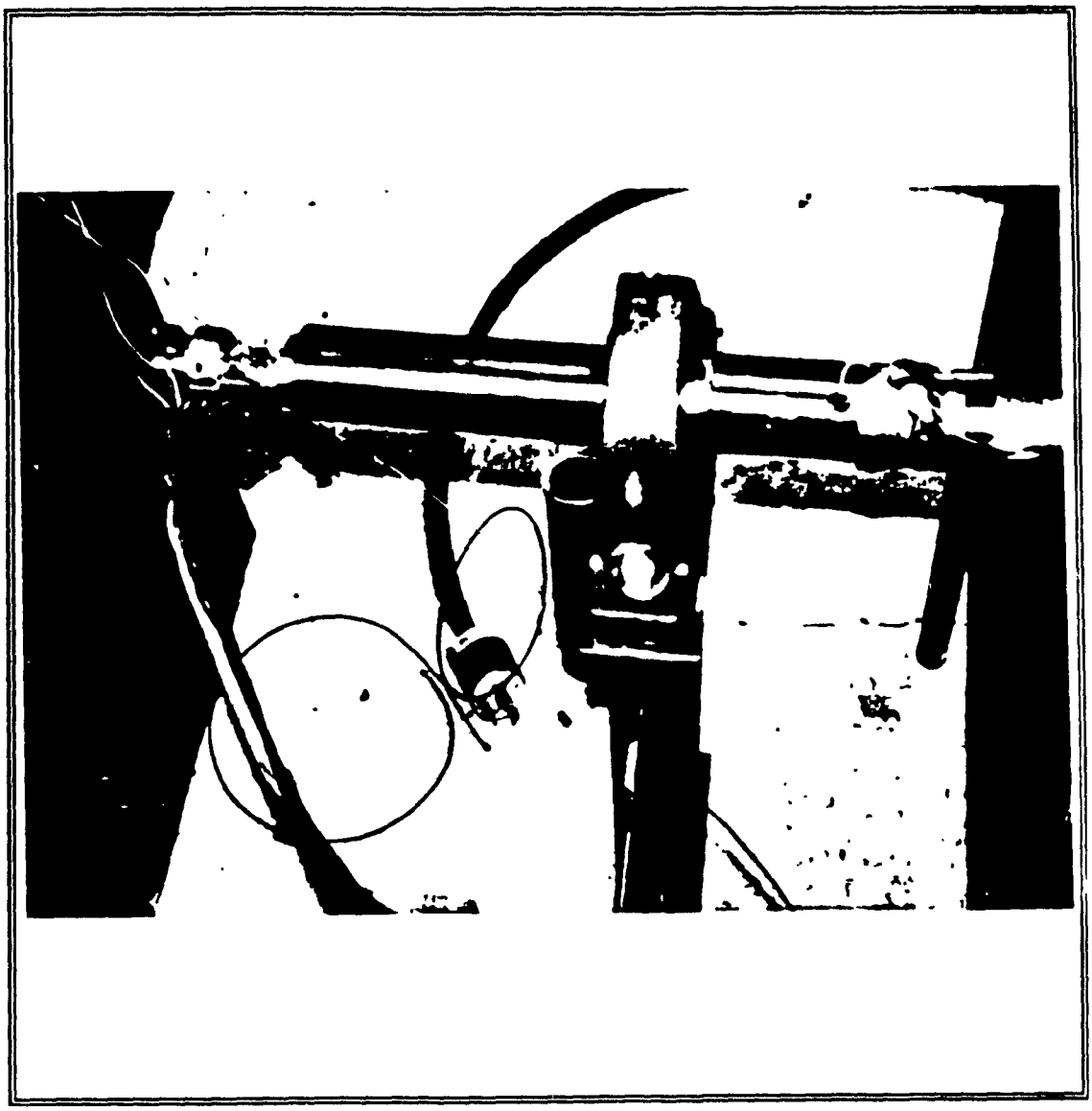

Figure 7.3 : Experimental Setup of the Shaft Disk System
(Slip Ring Arrangement)

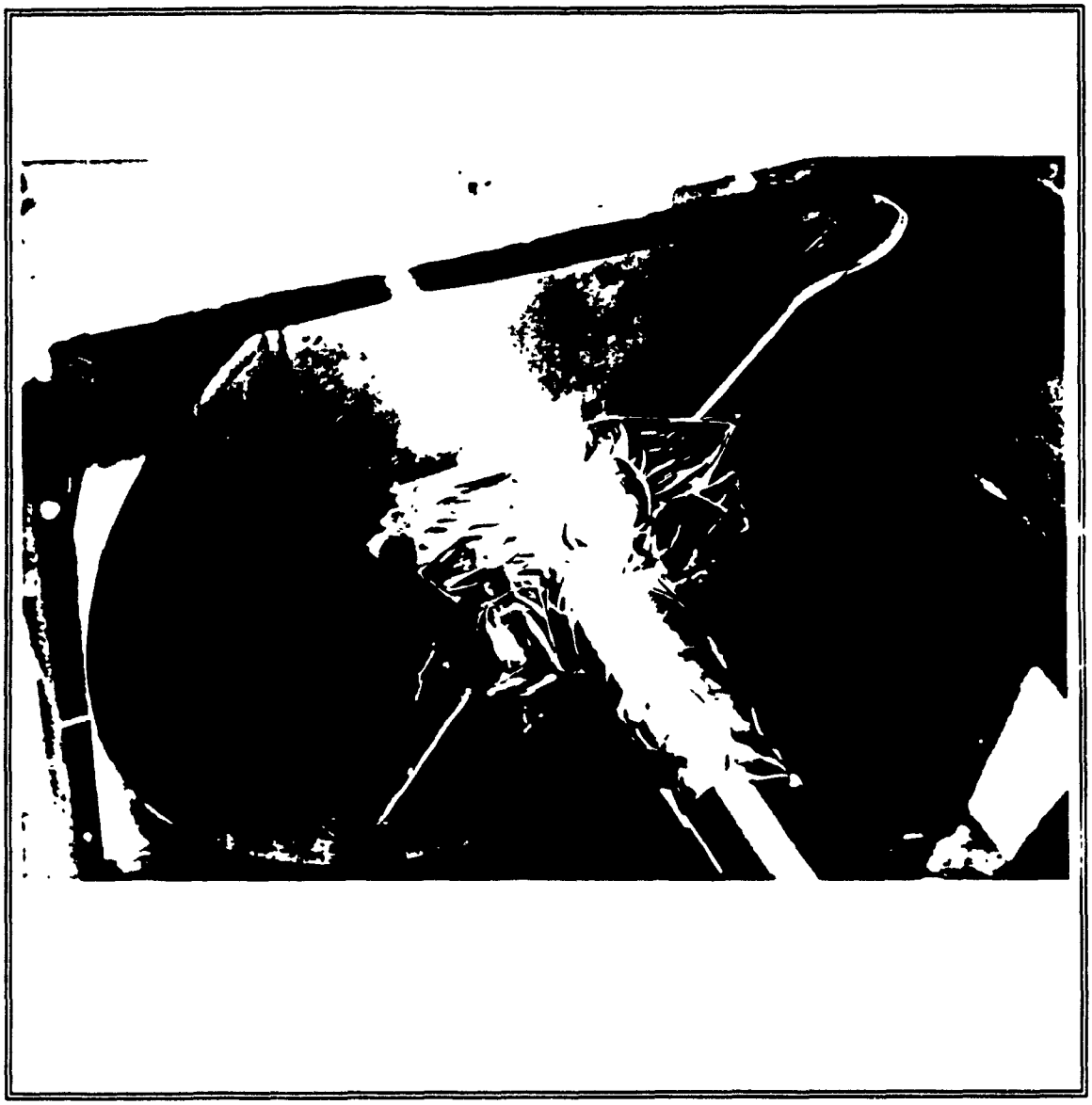

Figure 7.4 : Experimental Setup of the Shaft Disk System (Accelerometer Mounting)

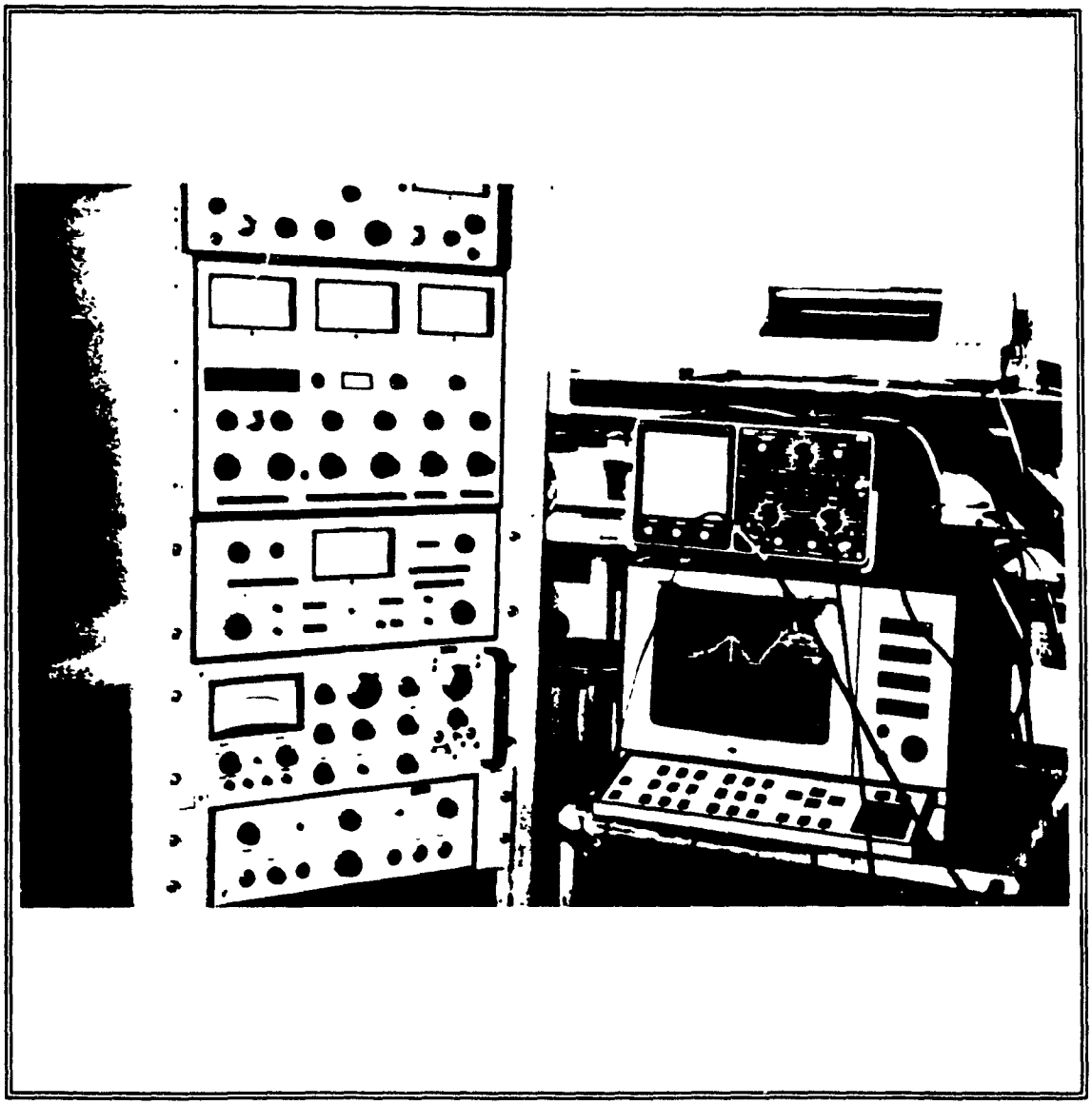

Figure 7.5 : Modal Analysis System

Table 7.1 : Details of the Experimental Setup

Motor	: GEC, 5Hp 1720 rpm (Variable Speed)
Disk Material	: Stainless Steel
Shaft Material	: Stainless Steel
Shaft Radius	= 2.54×10^{-2} m
Disk Radius	= 23.0×10^{-2} m
Disk Thickness	= 0.2×10^{-2} m
Shaft Length	= .91 m

In this study the following are investigated :

1) Determining the natural frequencies.
2) Study the effect of rotational speed on the natural frequencies and comparison with those from the theoretical model.

There are basically two steps associated with modal testing,

1) Measurement of the transfer function (Experimental stage).
2) Curve fitting of measured transfer functions and extraction of modal parameters such as natural frequencies, mode shapes, damping ratios (Numerical analysis stage).

7.4 : Frequency Response Functions

Frequency response function is described as the ratio of the amplitude of the harmonic response to that of the harmonic force input. Depending on the type of the response measured, say displacement, velocity or acceleration, it is called receptance, mobility or inertance, respectively, of the system. The determination of the frequency response functions is the first step in modal testing and is important because the modal parameters are extracted from these functions using a curve fitting procedure. Hence, the analytical evaluation of

frequency response functions for different types of systems are derived in the following.

Consider a general system with non-proportional damping. The equations of motion are given by,

$$[M]_{2Nx2N}\{\dot{U}\} + [K]_{2Nx2N}\{U\} = \{F\} \tag{7.1}$$

where,

$$[M] = \begin{bmatrix} 0 & m \\ m & c \end{bmatrix}$$

$$[K] = \begin{bmatrix} -m & 0 \\ 0 & k \end{bmatrix}$$

$$\{F\} = \begin{Bmatrix} 0 \\ f \end{Bmatrix}_{2Nx1} \quad \{U\} = \begin{Bmatrix} \dot{u} \\ u \end{Bmatrix}_{2Nx1} \tag{7.2}$$

In Eq.(7.1) the first N equations express the identity,

$$[M]\{\dot{u}\} - [M]\{\dot{u}\} = 0 \tag{7.3}$$

Transforming the physical coordinates {U} into modal coordinates {q} gives,

$$\{U\} = [\phi]\{q\} \tag{7.4}$$

where [Ø] is the modal matrix. Substituting Eq. (7.4) in Eq.(7.1) and premultiplying throughout by $[\phi]^T$, Eq. (7.1) can be rewritten as,

$$[\phi]^T[M][\phi]\{\ddot{q}\} + [\phi]^T[K][\phi]\{q\} = [\phi]^T\{F\} \tag{7.5}$$

Let,

$$[A] = [\phi]^T[M][\phi] \qquad [B] = [\phi]^T[K][\phi] \tag{7.6}$$

The complex eigen vectors [Ø] are orthogonal to each other and hence the 2N number of uncoupled system equations are obtained as follows,

$$A_i\ddot{q}_i + B_i q_i = \mathcal{F}_i = \sum_{1}^{2N} \{\phi\}^T F_i \qquad i=1,2,.....2N \tag{7.7}$$

where A_i and B_i denote diagonal elements of [A] and [B] respectively.

Consider the case of harmonic excitation at a point r, $\{F\}^T = \{0, 0, 0, \ldots . f_2, 0, \quad 0\}\ e^{j\omega t}$ where ω is the frequency of excitation. For steady state solution of the form,

$$q=\bar{Q}e^{j\omega t} \tag{7.8}$$

Eq.7.7 becomes,

$$j\omega A_i \bar{Q}_i + B_i \bar{Q}_i = \phi_{ri} f_r \tag{7.9}$$

which gives,

$$\bar{Q}_i = \frac{\phi_{ri} f_r}{(j\omega A_i + B_i)} \tag{7.10}$$

The response U_s, at point s is given by substituting Eq.(7.10) in Eq. (7.4)

$$U_s = \sum_{i=1}^{2N} \frac{\phi_{si}\phi_{ri} f_r}{(j\omega A_i + B_i)} \tag{7.11}$$

This can be written as,

$$U_s = \sum_{i=1}^{2N} \frac{\phi_{si}\phi_{ri} f_r}{A_i (j\omega - C_i)} \tag{7.12}$$

where

$$C_i = -\frac{B_i}{A_i} \tag{7.13}$$

Hence, the frequency response function H_{sr} $(j\omega)$ can be written as,

$$H_{sr} = \frac{U_s}{f_r} = \sum_{i=1}^{2N} \frac{\phi_{si}\phi_{ri}}{A_i (j\omega - C_i)} \tag{7.14}$$

However, because the eigenvalues and eigenvectors occur in complex conjugate pairs, Eq. (7.14) can be rewritten [101], for a proportionally damped system as,

$$H_{sr} = \sum_{i=1}^{2N} \frac{1}{A_i \bar{C}_i} \left[\frac{\phi_{si}\phi_{ri}}{2j (j\omega - P_i)} - \frac{\phi_{ri}^{*}\phi_{si}^{*}}{2j (j\omega - P_i^{*})} \right] \tag{7.15}$$

where,

$$\bar{C}_i = \omega_i (1 - \zeta^2)^{\frac{1}{2}} \tag{7.16}$$

The pole of the ith mode P_i is defined as,

$$P_i = -\zeta_i \omega_i + j\omega_i (1-\zeta^2)^{\frac{1}{2}} \qquad (7.17)$$

P_i^* and ϕ_i^* are complex conjugates of P_i and ϕ_i respectively.

Eq. (7.15) represents the frequency response function for a proportionally damped system. For a nonproportionally damped system the frequency response function is given by,

$$H_{sr} = \frac{U_s(j\omega)}{f_r(j\omega} = \sum_{i=1}^{2N} \left[\frac{\phi_{si}\phi_{ri}}{A_i(j\omega - P_i)} - \frac{\phi_{ri}^*\phi_{si}^*}{A_i(j\omega - P_i^*)} \right] \qquad (7.18)$$

The analytical form of the frequency response function is given by Eq. (7.15). Experimentally measured frequency response functions are fitted with this form using curve fitting procedures to extract the modal parameters.

7.5 : Obtaining the Frequency Response Function

Modal testing was carried out on the shaft disk system described in section 7.2. The system is excited using an impulse hammer when it is not rotating and an hydrodynamic

shaker when it is rotating. An accelerometer is mounted on the disk to measure the response signal. The response signal is passed through a slip ring arrangement and then along with excitation signal is fed through filters into the FFT analyzer. The modal analysis software then computes the frequency response function (FRF) from these two signals. Fig.7.6 shows a N x N matrix of frequency response functions. Measuring the response at a fixed location and exciting different test points yields one row of the FRF, which provides both the eigenvalues and eigenvectors of the system. When using the impulse hammer the magnitude of the impact can be predetermined by the mass of the hammer head and the velocity with which it is moving when it hits the structure. The magnitude of the force is adjusted by varying the mass of the hammer head. The frequency range which is effectively excited by the hammer depends on the stiffness of the contacting surfaces and the mass of the impactor head.

A typical impact force pulse and spectrum is shown in Fig 7.7. The stiffer the contacting materials, the shorter will be the duration of the pulse and the higher will be the frequency range covered by the impact. Similarly, the lighter the impactor mass, the higher the effective frequency range.

$$H_{sr}^{A}(w) = \begin{bmatrix} H_{11} & H_{12} & \cdots & H_{1r} & \cdots & H_{1N} \\ H_{21} & H_{22} & & H_{2r} & & H_{2N} \\ \vdots & & & & & \\ H_{s1} & H_{s2} & & H_{s3} & & H_{sN} \\ \vdots & \vdots & & \vdots & & \vdots \\ H_{N1} & H_{N2} & & H_{Nr} & & H_{NN} \end{bmatrix}$$

Figure 7.6 : Matrix of Frequency Response Function

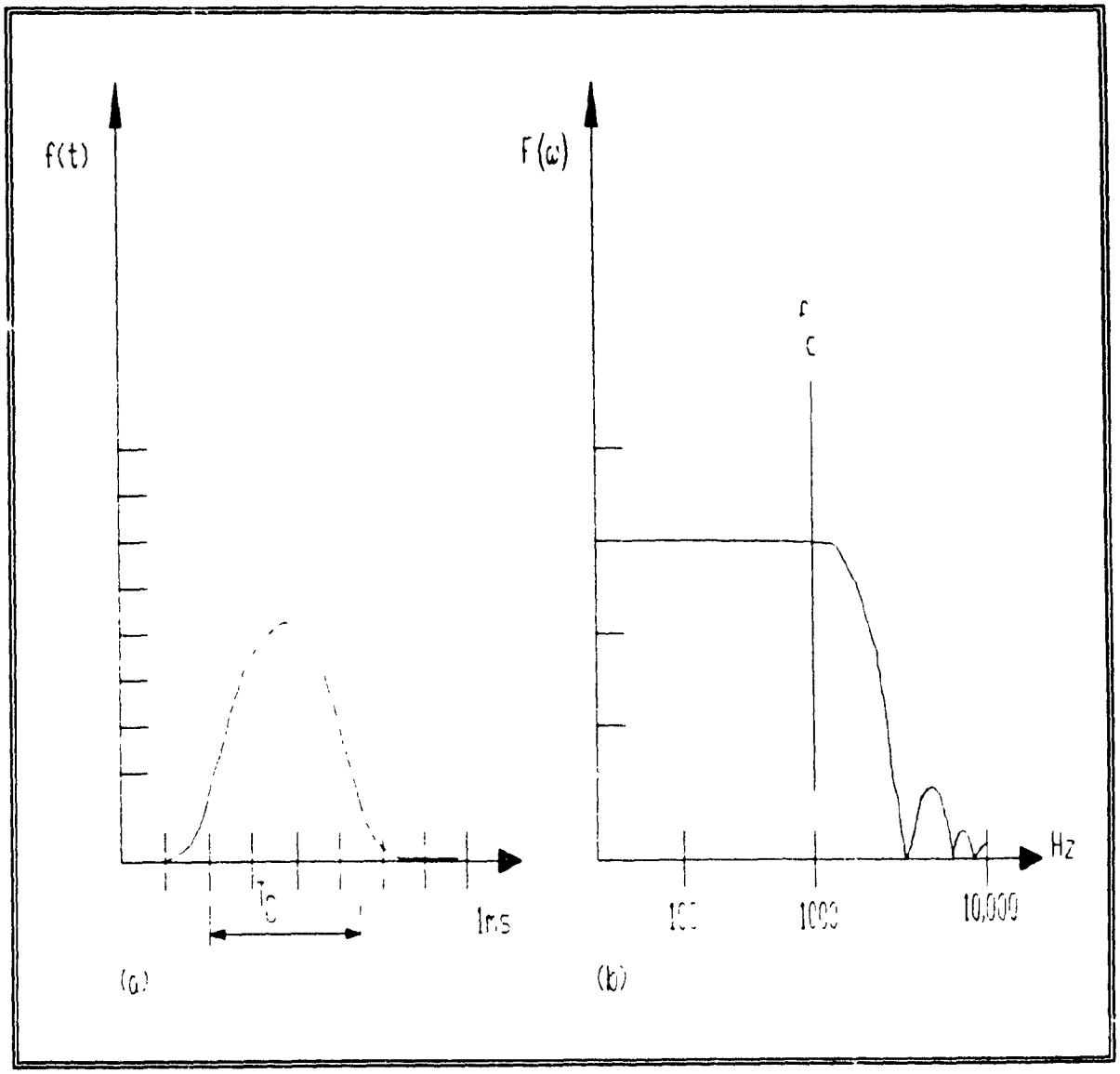

Figure 7.7 : Typical Impact Force Pulse and Spectrum [98]

(a) Time History
(b) Frequency Spectrum

Generally a soft tip is used in order to inject all the input energy into the frequency range of interest, rather than use a stiffer tip which inputs energy outside the range of interest at the expense of those inside the range.

7.6 : Discussion of results

Natural frequencies of a rotating shaft disk system are obtained using modal testing techniques.

The frequency response plots are obtained experimentally as described in section 7.5. These plots provide the natural frequencies of the system where a peak is observed in the amplitude plot and a change in the respective phase plot. Since the rotational speed has no significant effect on the natural frequencies of the shaft and the operating speed is about 2100 rpm, discussions are restricted to the first natural frequency of the disk.

The frequency response plot for the non rotating shaft disk system is shown in Fig.7.8 . The system is excited at various points on the disk using a hammer and the response is

measured in the bending direction of the disk at a fixed location. The system exhibits peaks at the natural frequencies with the first natural frequency at about 35 Hz. The first natural frequency compares quite well with the analytical model as shown in Table 7.2. The same test is carried out again but the output is measured using a microphone (rather than an accelerometer) placed close to the disk . The results are shown in Fig.7.9.

Since it is not convenient to excite the shaft disk system using a hammer while it is rotating , even though the technique was used in earlier studies on rotating structures [102], a hydrodynamic shaker is used to provide the input. The shaker is attached to one of the pedestals and a random noise excitation is given as an input signal. The system is excited using this input for various rotational speeds of the motor and the output is shown in Figs.7.10 through 7.14. From these figures it can be seen that as the rotational speed increases the natural frequency of the disk increases hence validating the analytical model.

7.8 : Summary

Modal testing was carried out on a shaft disk system. The frequency response functions were obtained and the natural frequencies identified. The effect of rotation on the first natural frequency of the disk was studied. This phenomenon was observed in the analytical model (Chapter 3).

In the next chapter, conclusions of this investigation are presented and recommendations for future work are suggested.

Table 7.2 : Comparison of the First Natural Frequency

Rotational Speed (R.P.M)	Analytical Results (rad/sec)	Experimental Results (rad/sec)
0.0	36.17	35.2
655	39.87	39.3
1055	51.31	52.7
1455	59.11	59.8
2055	67.62	65.6

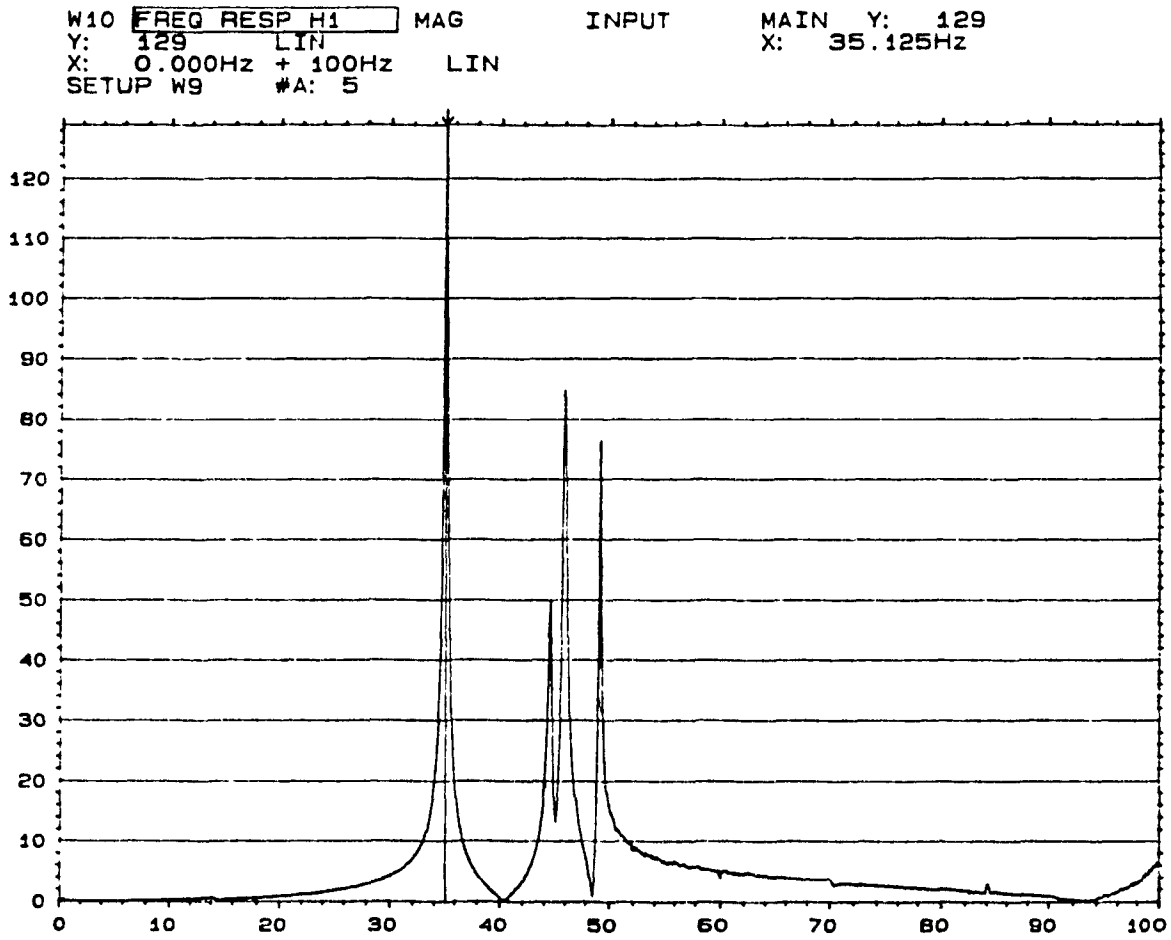

Figure 7.8 : Measured Frequency Response Function (Impulse Hammer Speed = 0 R.P.M)

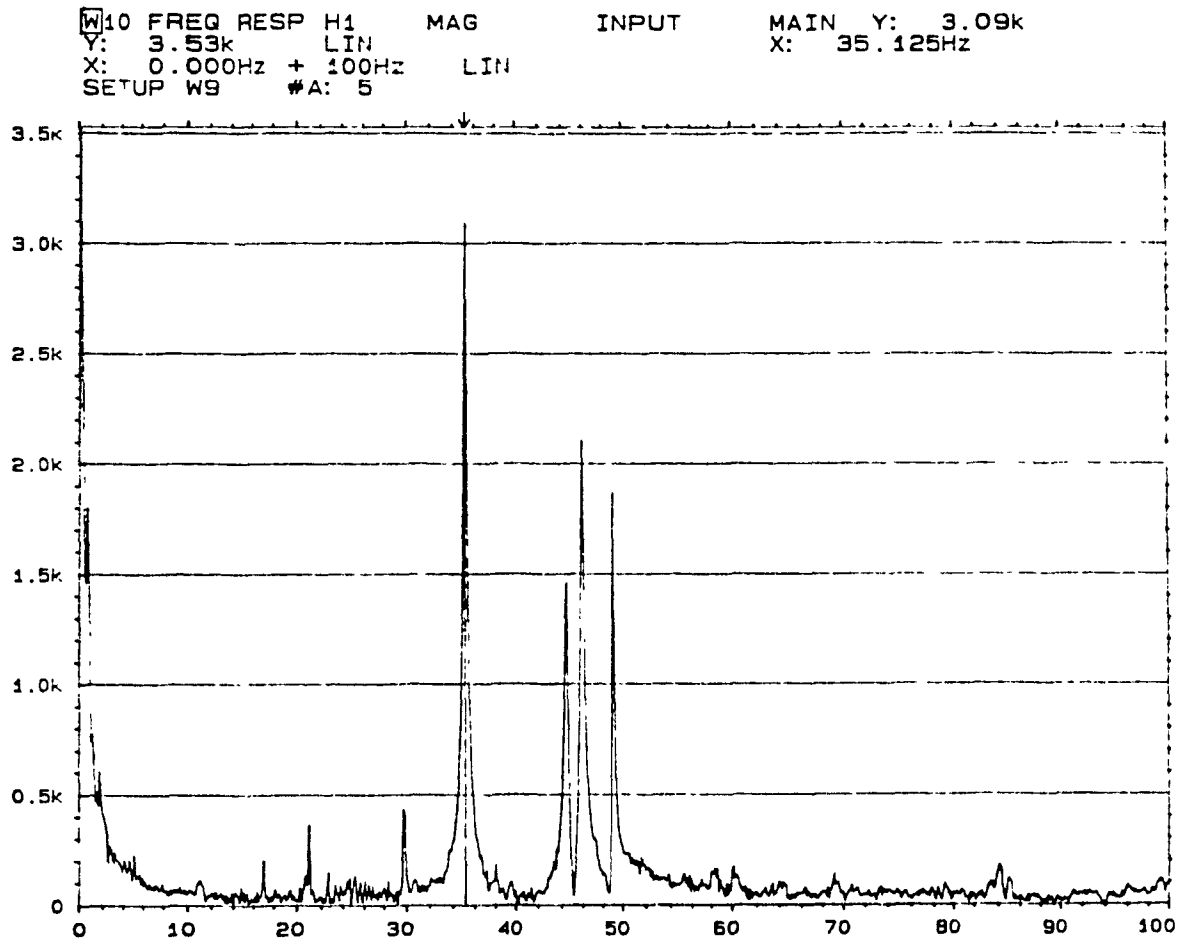

Figure 7.9 : Measured Frequency Response Function (Microphone Test Speed = 0 R.P.M)

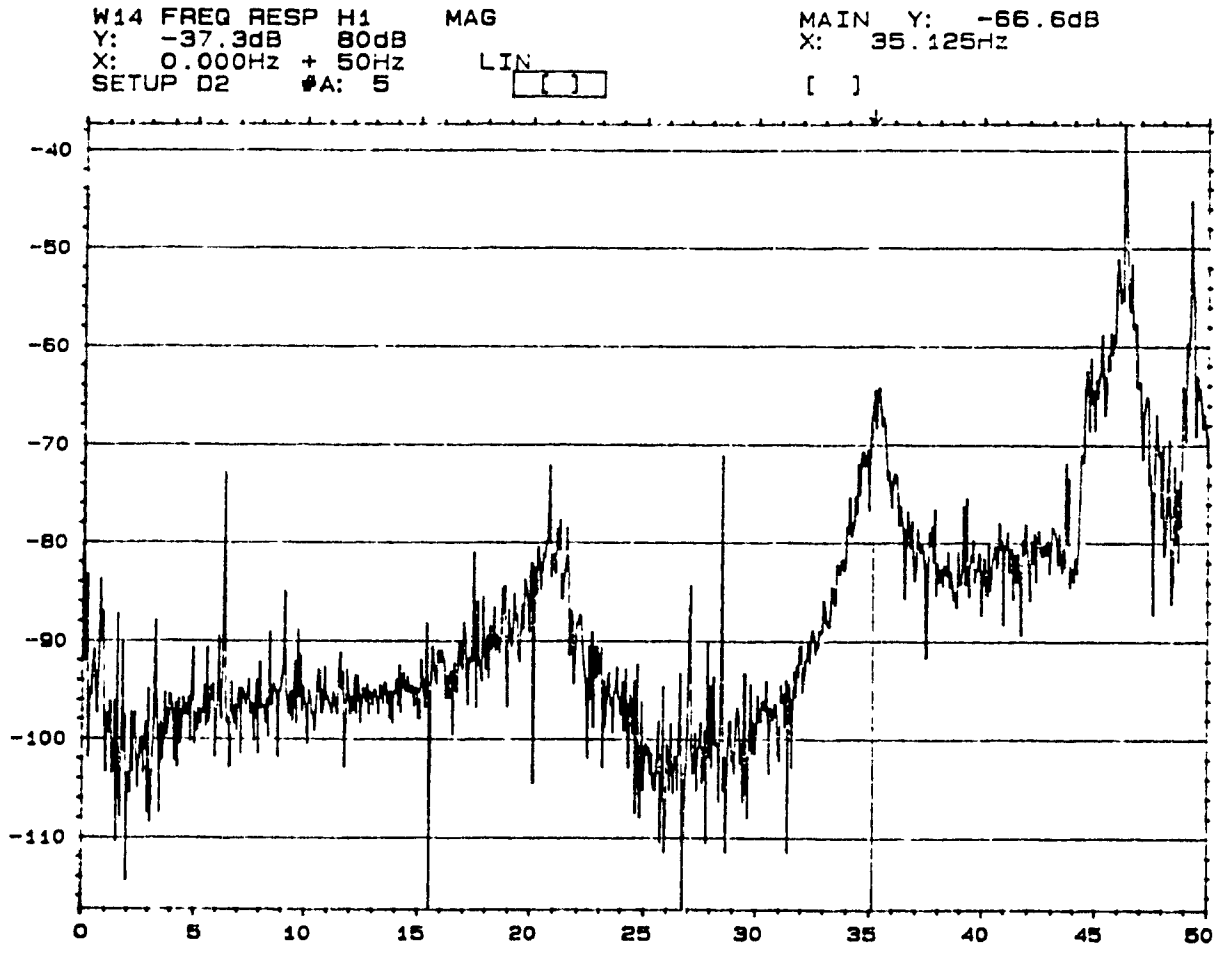

Figure 7.10 : Measured Frequency Response Function (Shaker Test Speed = 0 R.P.M)

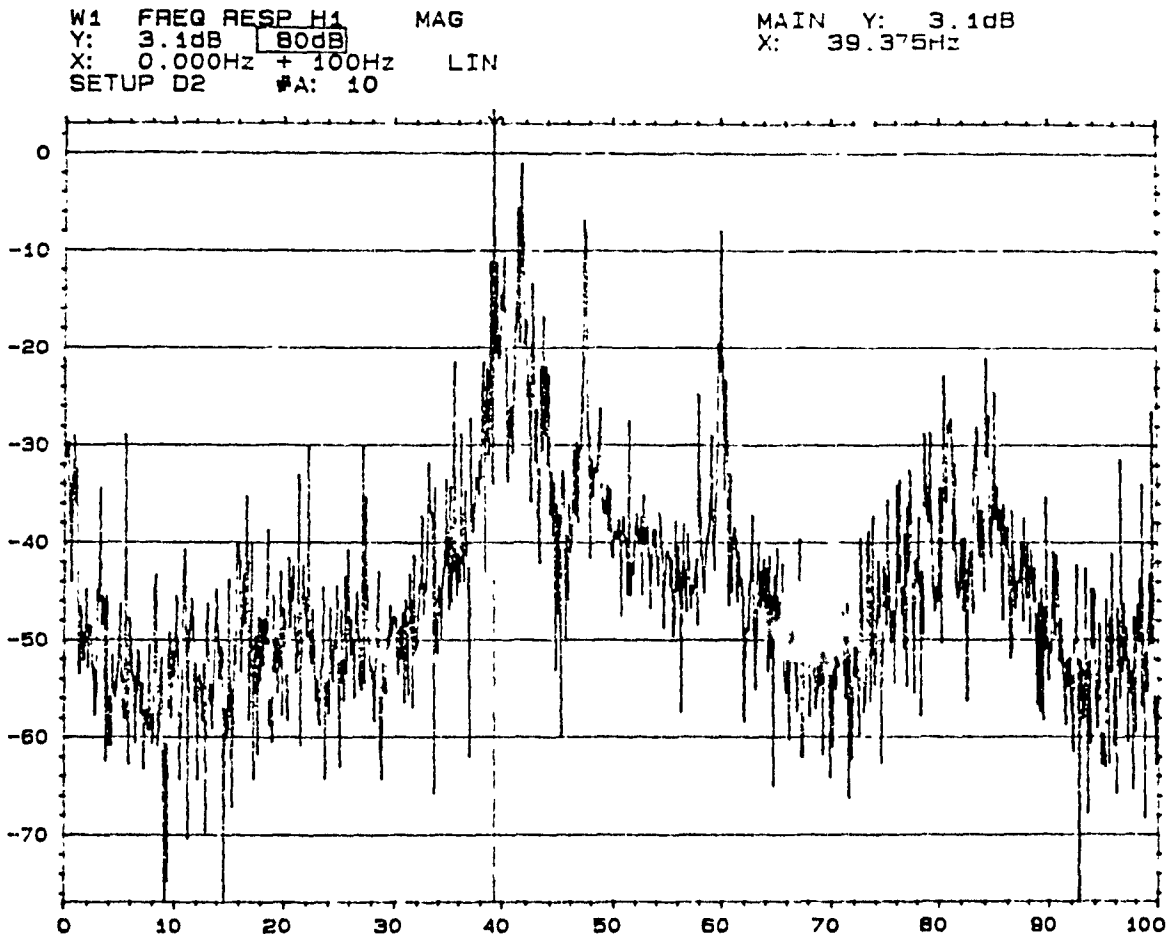

Figure 7.11 : Measured Frequency Response Function (Shaker Test Speed = 655 R.P.M)

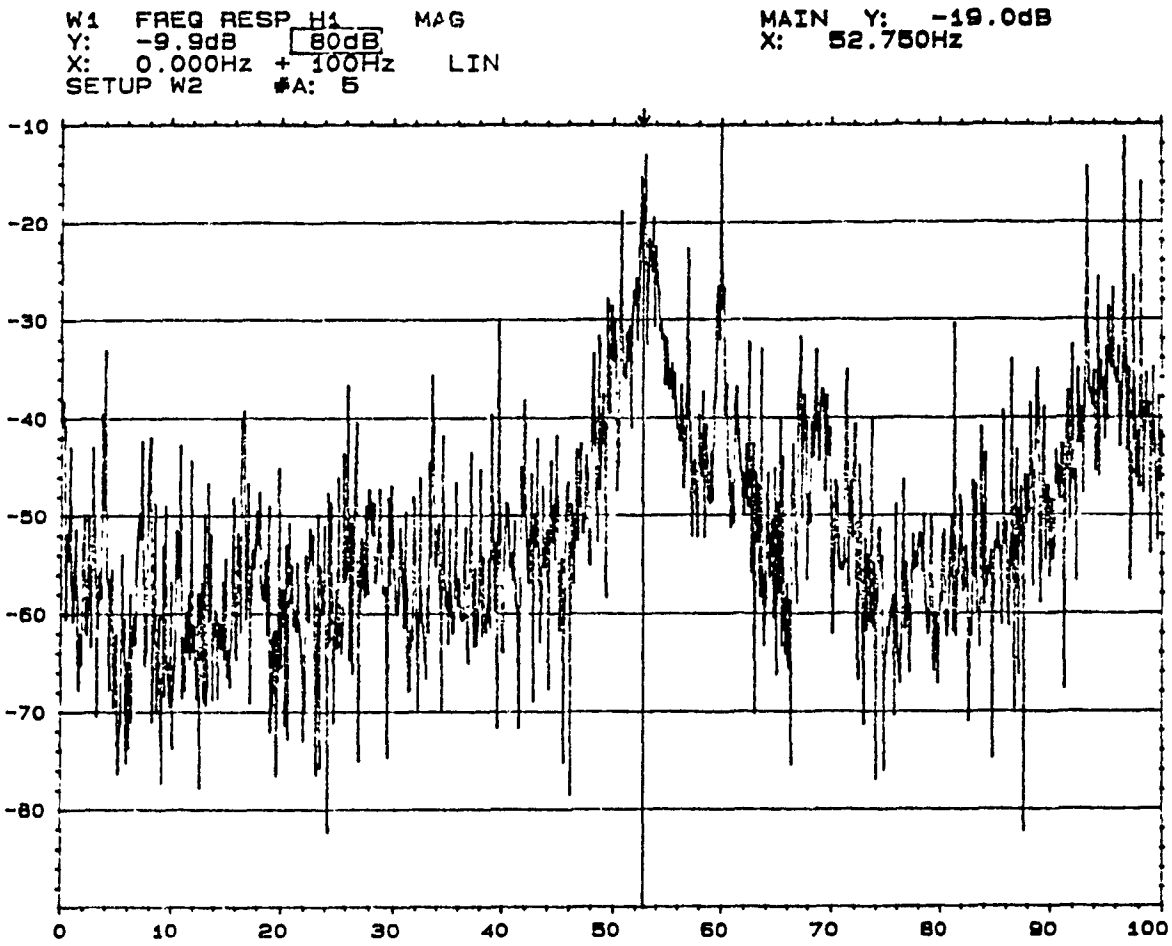

Figure 7.12 : Measured Frequency Response Function (Shaker Test Speed = 1055 R.P.M)

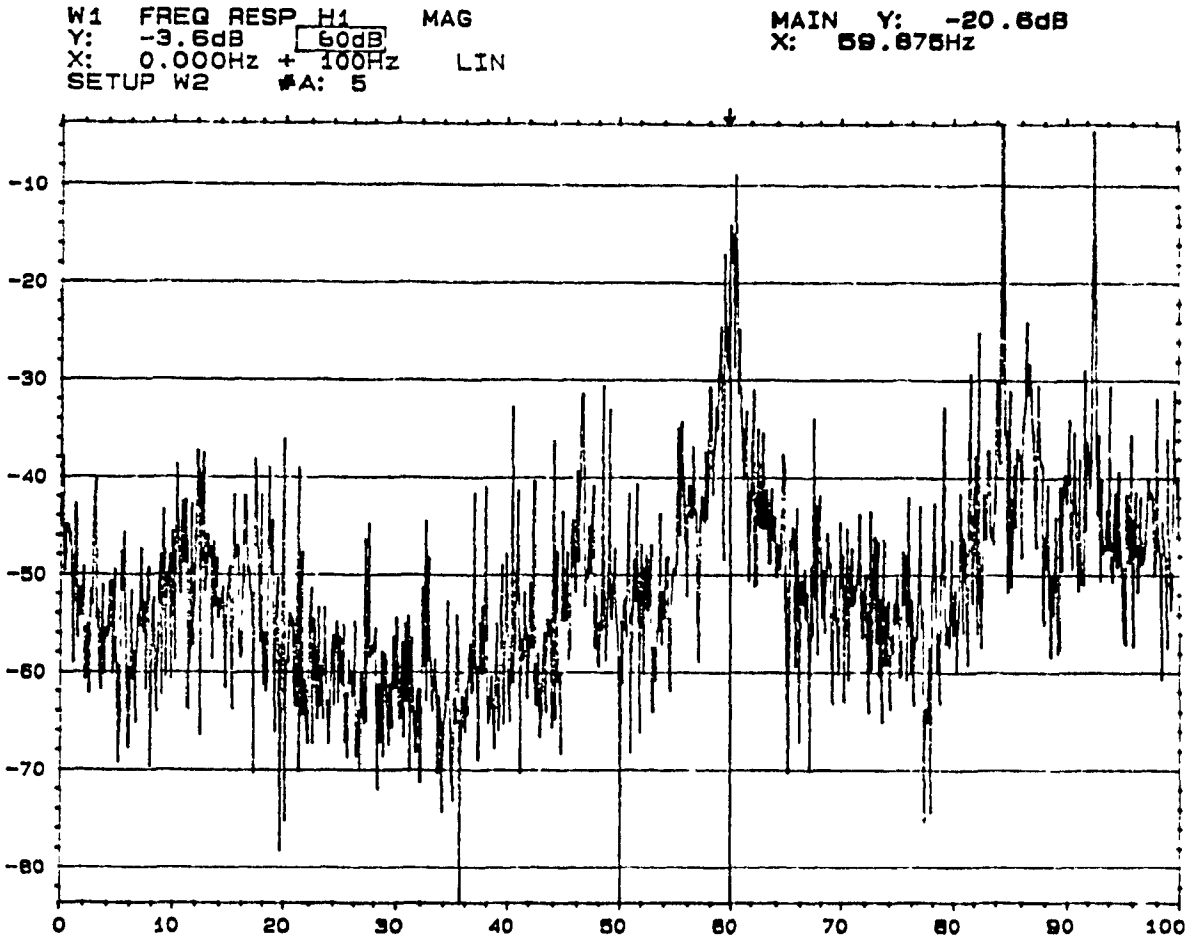

Figure 7.13 : Measured Frequency Response Function
(Shaker Test Speed = 1455 R.P.M)

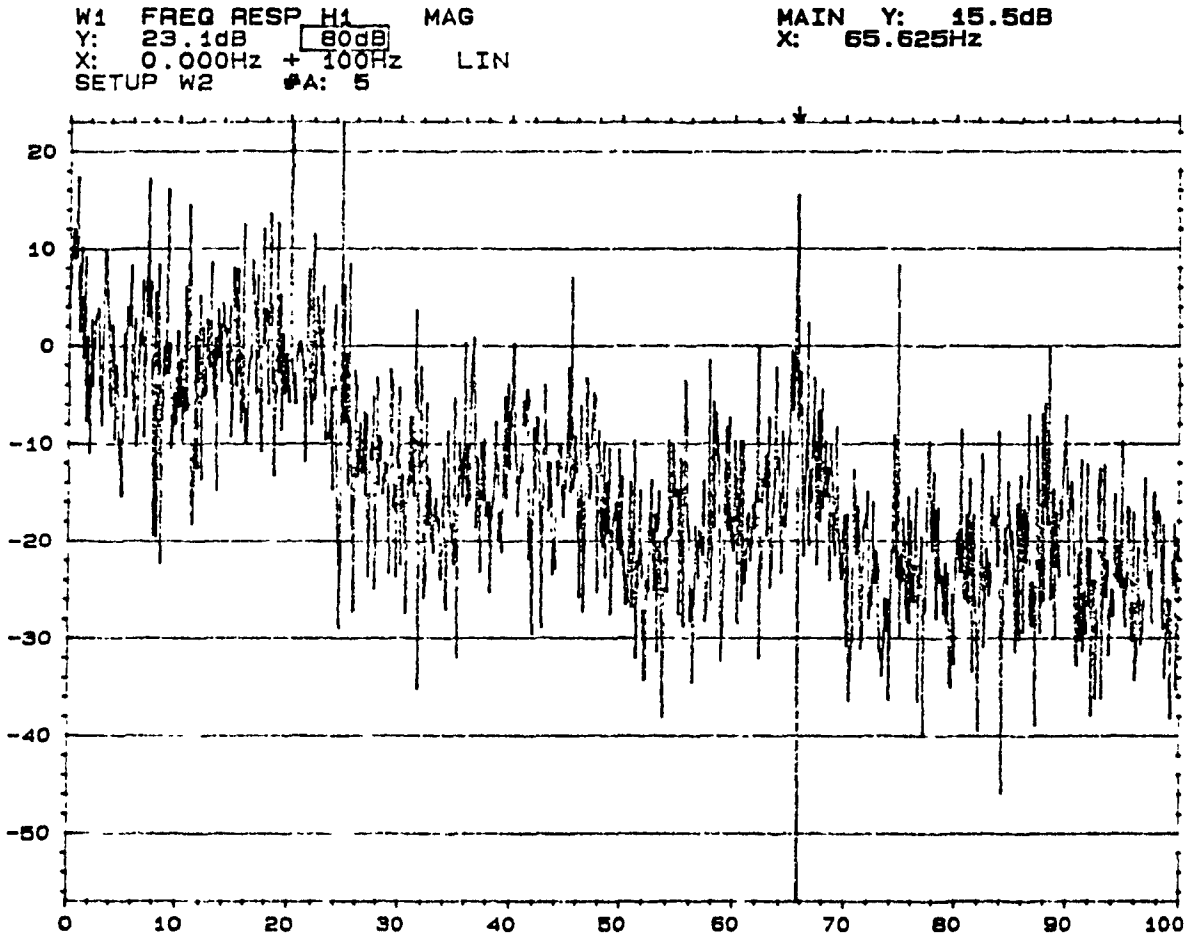

Figure 7.14 : Measured Frequency Response Function (Shaker Test Speed = 2055 R.P.M)

CHAPTER 8

CONCLUSIONS AND RECOMMENDATIONS

8.1 : General

The dynamic behaviour of a bladed disk-turborotor-bearing system was studied in this thesis.

A suitable model for each individual component of the turborotor system was developed and studied. These individual components were then assembled using the finite element technique to study the system dynamic behaviour. Natural frequencies and mode shapes were obtained. The response and stress due to harmonic and centrifugal loading was also obtained. The analytical results were compared with those obtained from experiments.

The dynamic analysis of the turborotor blade was first studied using beam characteristic orthogonal polynomials in the Rayleigh-Ritz method. The blade was idealized as a beam or a plate depending on the aspect ratio. The variation of the natural frequencies and mode shapes with speed of rotation was obtained for several combinations of the setting angle, hub radius and aspect ratio. The effects of shear deflection and rotary inertia are also studied.

Axisymmetrical and antisymmetrical vibrations of the turbine disk with varying thickness was studied and the variation of the natural frequencies with speed of rotation were obtained for several parameter combinations of the ratio of inner/outer radii and ratio of inner/outer thickness.

A complete model of the turborotor system was developed using the finite element technique and the natural frequencies and mode shapes were obtained for various rotational speeds. Finally, the response analysis of the turborotor system with the blades and the disk subjected to harmonic and centrifugal loading is carried out. The stresses and amplitudes of vibration for a typical turborotor system are obtained.

8.2 : Conclusions

The conclusions arrived on the basis of the results of this investigation in the different chapters of the thesis are summarised and given below :

8.2.1 : Beam Model

1) The natural frequencies of a rotating beam increase for higher setting angles and for any setting angle the

increase is linear at higher rotational speeds.

2) With larger values of hub radius, the natural frequencies are higher and increase faster with the rotational speed.
3) The beam tries to straighten itself as the rotational speed is increased.
4) Shear and Rotary inertia effects lower the natural frequencies of the rotating beam, such reduction being more predominant for higher modes.

8.2.2 : Plate Model

5) The natural frequencies of a rotating plate increase with higher values of the setting angle.
6) The natural frequencies increase with increase in hub radii.

8.2.3 : Disk Model

7) The natural frequencies of a rotating disk increase with increase in the inner/outer radii ratio, such increase being more predominant for higher modes.
8) The natural frequencies of a rotating disk increase with the increase in the inner/outer thickness ratio for a

rixed value of the inner/outer radii.

9) The natural frequencies of the rotating disk, having parabolic thickness variation is lower, in comparison to a disk having linear thickness variation.

10) In a fixed frame of reference, the first two modes have no critical speeds while for mode 3 its lower frequency curve decreases and intersects the lateral axis.

8.2.4 : Bladed Disk Model

11) The natural frequencies increase with increase in rotational speed.

12) The natural frequency decreases with the inclusion of the blades.

8.2.5 : Turborotor System

13) The rotational speed has no significant effect on the shaft frequencies.

14) The first natural frequency of the system corresponds to the shaft bending frequency which is significantly lower than that of the bladed disk assembly.

15) The natural frequencies increase with increase in the bearing stiffness.

16) The maximum stress occurs at the root of the blade and decreases in value towards the tip.

17) The maximum stresses occur at the inner periphery of the disk and decrease towards the outer periphery.

18) The centrifugal loading is the major factor in determining the critical stresses for the turborotor system in comparison to the gas pressure loading.

8.2.6 : Experimental

1) Vibration testing is normally performed for stationary structures in order to identify the modal parameters of the structure. For a simple shaft-disk system, this method provides the critical frequencies which are found to be close to those obtained by analysis.

2) The disk natural frequency increases with increase in rotational speed hence validating the analytical model.

8.3 : Recommendations for Future Work

Some suggestions for possible future work are given below:

- Pretwist and taper can be incorporated in the formulation of the blade models.
- The effect of shrouds and lacing wires on the natural frequencies and mode shapes can be studied.
- The effect of aerodynamic detuning on blade response can be investigated.
- Response analysis with inclusion of bearing damping and mechanical damping resulting from any rubbing action can be incorporated in the model.
- Scale model studies on the system can be carried out to see wether tests can be done on models rotating at lower speeds for prototypes which run much faster.
- The effect of anisotropic bearings on the system can be studied.
- The effect of increasing the number of bearing supports can be investigated.
- Experimental validation with the inclusion of the blades can be carried out.
- Modal testing can be carried out to determine the mode shapes of stationery and rotating turborotor system.

REFERENCES

1. Tse, S., Francois, Morse, E., Ivan, and Hinkle, T., Rolland, "Mechanical Vibrations" Allyn and Bacon Inc., Boston, Massachusetts, 1978.
2. Rao, J.S., "Natural Frequencies of Turbine Blading - a Survey", Shock and Vibration Digest, Vol.5, 1973.
3. Carnegie, W., "Vibrations of Rotating Cantilever Blading: Theoretical approaches to the Frequency problem Based on Energy Methods", Journal of Mechanical Engineering Science, Vol. 1, No. 3, 1959, pp. 235-240.
4. Schilhansl, M.J., "Bending Frequency of a Rotating Cantilever Beam", Journal of Applied Mechanics, Vol. 25, 1958, pp. 28-30.
5. Pnuelli, D., "Natural Bending Frequency Comparable to Rotational Frequency in Rotating Cantilever Beam", Journal of Applied Mechanics, Vol. 39, 1972, pp. 602-604.
6. Subrahmanyam, K.B., Kulkarni, S.V., and Rao, J.S., "Coupled Bending-Torsion Vibrations of Rotating Blades of Asymmetric Aerofoil Cross Section with Allowance for Shear Deflection and Rotary Inertia by use of the Reissner Method", Journal of Sound and Vibration, Vol. 75, No. 1, 1981, pp. 17-36.
7. Kumar, K., "Vibrations of Space Boom under Centrifugal Force Field", Transactions of C.A.S.I., Vol. 7, 1974, pp. 1-5.

8. Isabson, G., and Eisley, J.G., "Natural Frequencies in Bending of Twisted Rotating and Non-Rotating Beams", 1960, NASA TND-371.

9. Slypex, A.A., "Coupled Bending Vibrations of Pretwisted Cantilever Beams", Journal of Mechanical Engineering Science, Vol. 10, 1968, pp.365-379.

10. Wright, A.D., Smith, C.E., Thresher, R.W., and Wang, J.L.C., "Vibration Modes of Centrifugally Stiffened beams", Journal of Applied Mechanics, Vol. 49, 1982, pp 197-201.

11. Handelman, G., Boyce, W., and Cohen, H., "Vibration of a Uniform Rotating Beam with Tip Mass", Third U.S. National Congress of Applied Mechanics, Vol. 27, 1960, pp. 548-550.

12. Lo, H., Goldberg, J.E., and Bogdanoff, J.H., "Effect of Small Hub Radius Change on Bending Frequencies of a Rotating Beam", Journal of Applied Mechanics, Vol.27,1960, pp. 548-550.

13. Boyce, W.E., and Handleman, G., "Vibrations of Rotating Beams with Tip Mass", Zeitschaift fur Angewandte Mathematik and Physik, Vol. 12, 1961, pp. 369-392.

14. Wang, J.T.H., Mahrenholtz, O., and Bohm, J., "Extended Galerkins's Method for Rotating Beam Vibrations Using Legendre Polynomials", Solid Mechanics Archives, Vol. 1, 1976, pp. 341-365.

15. Kaushal, A., and Bhat., R.B., "Natural Frequencies and Mode shapes of Rotating Structures Using Improved Strain Energy Formulation in Rayleigh-Ritz Method", Proceedings of the 3rd International Modal Analysis Conference, 1985.

16. Bhat, R.B., "Transverse Vibrations of a Rotating Uniform Cantilever Beam with Tip Mass Using Beam Characteristic Orthogonal Polynomials in Rayleigh-Ritz Method", Journal of Sound and Vibration, Vol. 104, No. 3, 1985.

17. Putter, S., and Manor, H., "Natural Frequencies of Radial Rotating Beams", Journal of Sound and Vibration, Vol. 56, 1978, pp. 175-185.

18. Hoa, S.V., "Vibration of a Rotating Beam with Tip Mass", Journal of Sound and Vibration, Vol. 67, 1979, pp. 369-381.

19. Singh, V.K., and Rawtani, S., "Effect of Root Flexibility on Vibration Characteristics of Tapered Blades", Symp. Dyn. Rotors, 20th Cong. ISTAM, Paper No. 8, 1975.

20. Singh, V.K., and Rawtani, S., "Natural Frequencies and Mode Shapes of Steam Turbine Blades", Proc. BHEL Symposium Blade Design Development, Hyderabad, 1975.

21. Young, D., "Vibration of Rectangular Plates by the Ritz Method", Journal of Applied Mechanics, Vol. 17, 1950, pp. 448-453.

22. Leissa, A.W., "The Free Vibration of Rectangular Plates", Journal of Sound and Vibration, Vol. 31, 1973, pp.257-293.

23. Dickinson, S.M., "The Buckling and Frequency of Flexural Vibration of Rectangular Orthotropic Plates using Rayleigh's Method", Journal of Sound of Vibration, Vol. 61, 1978, pp. 1-8.

24. Trefftz, E., "Konvergenz und Fehterschatzung Beim Ritzchen Verfahren", Mathematische Annalen, Vol. 100, 1928, p. 503.

25. Courant, R., "Variational Methods for the Solution of Problems of Equilibrium and Vibration", Bulletin of the American Mathematical Society, N.Y., Vol. 49, 1939, pp. 1-23.

26. Collatz, L., "Eigenwertprobleme", Chelsa Publishing Company, New York, N.Y., 1948.

27. Gorman, D.J., "An Analytical Solution for the Free Vibration Analysis of Rectangular Plates Resting on Symmetrically Distributed Point Supports", Journal of Sound and Vibration, Vol. 79 (4), 1981, pp. 561-574

28. Bassily, S.F., Dickinson, S.M., "On the use of Beam Functions for Plates Involving Free Edges", Transactions of the ASME, Vol. 42, 1975, pp. 858-864.

29. Dickinson, S.M., and Li, E.K.H., "On the use of Simply Supported Plate Functions in Rayleigh's Method Applied to the Flexural Vibration of Rectangular Plates", Journal of Sound and Vibration, Vol. 80, 1982, pp. 292-297.

30. Laura, P.A.A., "Comments on the use of Simply Supported Plate Functions in the Rayleigh Ritz Method Applied to

the Flexural Vibration of Rectangular Plates", Journal of Sound and Vibration, Vol. 84, 1982, pp. 595-597.

31. Goldfracht, E., and Rosenhouse, G., "Use of Lagrange Multipliers with Polynomial Series for Dynamic Analysis of Constrained Plates", Part 1: Polynomial Series", Journal of Sound and Vibration, Vol. 92, 1984, pp. 83-93.

32 Bhat, R.B., "Natural Frequencies of Rectangular Plates Using Characteristic Orthogonal Polynomials in Rayleigh Ritz Method", Journal of Sound and Vibration, Vol. 102, No. 3, 1985.

33. Dickinson, S.M., and Blasio, A. Di "On the Use of Orthogonal Polynomials in the Rayleigh Ritz Method for the Study of the Flexural Vibration and Buckling of Isotropic and Orthotropic Rectangular Plates", Journal of Sound and Vibration, Vol. 108, 1986, pp. 51-62.

34. Leissa, A.W., Lee, J.K., Wang, A.J., "Rotating Blade Vibration Analysis", Transactions of the ASME, Vol. 104, 1982, pp. 296-302.

35. Rawtani, S., "The Effect of Camber on the Natural Frequencies of Low Aspect Ratio Turbomachinery Blades", Journal of Aeronautical Society India, Vol. 25, 1973, p 119.

36. Barten, H.G., et al., "Stress and Vibration Analysis of Inducer Blades Using Finite Element Techniques", AIAA Paper 70-630, 1970.

37. Ahmad, R., et al. "Vibration of Thick Curved Shells with Particular Reference to Turbine Blades", Journal of Strain Analysis, Vol. 5, 1970, p 200.

38. Bossak, M.A.J., and Zienkiewicz, O.C., "Free Vibrations of Initially Stressed Solids with Particular Reference to Centrifugal Force Effects in Rotating Machinery", Journal of Strain Analysis, Vol. 8, 1973, p 245.

39. Dokainish, M.A., and Rawtani, S., "Vibration Analysis of Rotating Cantilever Plates", International Journal for Numerical Methods in Engineering, Vol. 3, 1971, pp. 233-248.

40. Lalanne, M., and Henry, R., "Rotating Blade Analysis by Finite Element Method", Proc. IUTAM Symposium Dyn. Rotors, Lyngby, Denmark, 1974, p 299.

41. Mcbain, J.C., "Vibratory Behaviour of Twisted Cantilever Plates", Journal of Aircraft Engineering, Vol. 12, 1975, p 206.

42. Gupta, R.S., and Rao, S.S., "Finite Element Eigenvalue Analysis of Tapered and Twisted Timoshenko Beams", Journal of Sound and Vibration, Vol.56, 1978, pp 187-200.

43. Jumaily Al, A.M., and Faulkner, L.L., "Vibration Characteristics of Hollow Symmetric Blades Based on a Thin Shell Theory", Journal of Mechanical Design, Trans. ASME, Vol. 100 (1), 1978, p 83.

44. Gupta, K., and Rao, J.S., "Torsional Vibration of Pretwisted Cantilever Plates", Journal of Mechanical Design, Trans. ASME, Vol. 100 (3),1978, p 528.

45. Leissa, A.W., "Vibration of Plates", NASA SP-160, 1969.

46. Carrington, H., "The Frequencies of Vibration of Flat Circular Plates Fixed at the Circumference", Philosophical Magazine 50, 1925, pp. 1261-1264.

47. K., Itao, and Crandall, S.H., "Natural Modes and Natural Frequencies of Uniform, Circular, Free edge Plates", Journal of Applied Mechanics, Vol.46, 1979, pp. 448-453.

48. Leissa, A.W., and Narita, Y., "Natural Frequencies of Simply Supported Circular Plates", Journal of Sound and Vibration , Vol. 70, 1980, pp. 221-229.

49. Vogel, S.M., and Skinner, D.W.," Natural Frequencies of Transversely Vibrating Annular Plates", Journal of Applied Mechanics, Vol. 32, 1965, pp. 926-931.

50. Rao, S.S., and Prasad, A.S., "Vibration of Annular Plates Including the Effects of Rotatory Inertia and Transverse Shear Deformation", Journal of Sound and Vibration, Vol. 42, 1974, pp. 305-324.

51. Laura, P.A.A., Ficcadenti, G.M., et al., "Fundamental Frequency and Buckling Load of Circular Plates with Variable Profile and Non Uniform Boundary Conditions", Journal of Sound and Vibration, Vol. 78, 1981, pp. 147-153.

52. Raju, I.S., Rao, Prakasa B., and Rao, Venkateswara G., "Axisymmetric Vibrations of Linearly Tapered Annular Plates", Journal of Sound and Vibration, Vol. 32, 1974, pp. 507-512.

53. Soni, S.R., and Rao, Amba C.L., "Axisymmetric Vibrations of Annular Plates of Variable Thickness", Journal of Sound and Vibration, Vol. 38, 1975, pp. 465-473.

54. Gupta, U.S., and Lal, R., "Axisymmetric Vibrations of Linearly Tapered Annular Plates Under an in Plane Force", Journal of Sound and Vibration, Vol. 64, 1979, pp. 269-276.

55. Sankaranarayanan, N., Chandrasekran, K., and Ramaiyan, G., "Axisymmetric Vibrations of layered Annular Plates with Linear Variation in Thickness", Journal of Sound and Vibration, Vol. 99, 1985, pp. 351-360.

56. Gorman, D.G., "Natural Frequencies of Transverse Vibration of Polar Orthotropic Variable Thickness Annular Plates", Journal of Sound and Vibration, Vol. 86, 1983, pp. 47.

57. Lenox, T.A., and Conway, H.D., "An Exact Closed form Solution for the Flexural Vibration of a Thin Annular Plate having a Parabolic Thickness Variation", Journal of Sound and Vibration, Vol. 68, 1980, pp. 231-239.

58. Becker.,E.C.H., Conway, H.D., and Dubil, J.F., "Vibration Frequencies of Tapered Bars and Circular Plates", Journal

of Applied Mechanics, Vol. 31, 1964, pp. 329-331.

59. Southwell, R.V., and Lamb, H., "The Vibrations of a Spinning Disk", Proceedings Royal Society of London, A99, 1921, pp. 272-280.

60. Southwell, R.V., "On the Free Transverse Vibrations of a Uniform Circular Disk Clamped at its Centre; and on the Effects of Rotation", Proceedings Royal Society of London, A 101, 1922, pp. 133-153.

61. Simmonds, J.G., "The Transverse Vibrations of a Flat Spinning Membrane", Journal of Aeronautical Science, Vol. 29, 1962, pp. 16-18.

62. Eversman, W., and Dodson, R.O., "Free Vibrations of a Centrally Clamped Spinning Disk", AIAA, Vol. 7, 1969, pp. 2010-2012.

63. Barasch, S., and Chen, Y., "On the Vibration of a Rotating Disk", Journal of Mechanical Design, Trans. ASME, Vol. 39, 1972, pp. 1143-1144.

64. Mote, C.D.Jr, "Free Vibration of Initially Stressed Circular Disks", Journal of Engineering for Industry, Vol. 87, 1965, pp. 258-264.

65. Sinha, Sunil K., "Determination of Natural Frequencies of a Thick Spinning Annular Disk Using a Numerical Rayleigh-Ritz's Trial Function", Journal of Acoustical Society, Vol. 81, 1987, pp. 357-369.

66. Kirkhope, J., and Wilson, G.J., "Vibration and Stress Analysis of Thin Rotating Disks Using Annular Finite Elements", Journal of Sound and Vibration, Vol. 44, 1976, pp.461-474.

67. Kennedy, W., and Gorman, D., "Vibration Analysis of Variable Thickness disks Subjected to Centrifugal and Thermal Stresses", Journal of Sound and Vibration, Vol. 53, 1977, pp. 83-101.

68. Mote, C.D.Jr, "Stability Control Analysis of Rotating Plates by Finite Element: Emphasis on Slots and Holes ", Journal of Dynamic Systems Measurement and Control, Vol. 94, 1972, pp. 64-70.

69. Johnson, M.W., "On the Dynamics of Shallow Elastic Membranes", Proceedings of the Symposium on Thin Elastic Shells, North Holland Co., Amsterdam, 1960, pp. 281-300.

70. Eversman, W., "Transverse Vibrations of a Clamped Spinning Membrane", AIAA, Vol. 6, 1968, pp. 1395-1397.

71. Iwan, W.D., and Moeller, T.L., "The Stability of a Spinning Elastic Disk with a Transverse Load System", Journal of Applied Mechanics, ASME, Vol. 43 , 1976, pp. 485-490.

72. Chonan, S., and Sato, S., "Vibration and Stability of Rotating Free Clamped Slicing Blades", Journal of Sound and Vibration, Vol. 127 (2), 1988, pp. 245-252.

73. Benson, R.C., and Boggy, D.B, "Deflection of a Very Flexible Spinning Disk Due to a Transverse Stationery Load", Journal of Applied Mechanics, ASME, Vol. 45 , 1978, pp. 636-642.

74. Tobias, S.A., and Arnold, R.N.,"The Influence of Dynamical Imperfection on the Vibration of Rotating Disks", The Institution of Mechanical Engineers Proceedings , Vol. 171, 1957, pp.669-690.

75. Mote, C.D.Jr, "Stability of Circular Plates Subjected to Moving Loads ", Journal of Franklin Institute , Vol. 290, 1970, pp. 329-344.

76. Mote, C.D.Jr, and Neih, L.T, "Control of Circular-Disk Stability with Membrane Stresses ", Experimental Mechanics, Vol. 11, 1971, pp. 490-498.

77. Armstrong, E.K., Christie, P.I., and Hague, W.M., "Natural Frequencies of Bladed Disks", Institute of Mechanical Engineering Proceedings, Vol. 180 (31), 1966, p. 110.

78. Ewins, D.J.,"Vibration Characteristics of Bladed Disc Assemblies", Journal of Mechanical Engineering Science, Vol.15, 1973, pp.165-186.

79. Kirkhope, J., and Wilson, G.J., "Analysis of Coupled Disk Vibration in Axial Flow Turbines and Fans", Proceedings 12th AIAA/ASME Conference on Structural Dynamics, 1971.

80. Dye, R.C.F., and Henry, T.A., "Vibration Amplitudes of Compressor Blades Resulting from Scatter in Blade Natural Frequencies", Journal of Engineering for Power: Transactions ASME, Vol. 91, 1969, p. 3.

81. Green, R.B, "Gyroscopic Effects on the Critical speeds of Flexible Rotors", ASME Paper No. 48-SA-3.

82. Sann, R.I, "Dynamic Bending Stress in a Disk Type Gyroscope Rotor Under Steady Precession" ASME Paper No. 69-DE-A.

83. Dokin, J.A., and Shoup, T.E., "Rotor Resonant Speed Reduction Caused by Flexibility of Disks", Journal of Engineering for Industry, Transactions of ASME, Vol. 96, 1974, pp. 1328-1333.

84. Hagiwara, N., and Yoneyama, M., "Vibration of an Asymmetrically Mounted Rotor with Coupling of a Flexible Disk", Proceedings of the Japan National Congress for Applied Mechanics, Vol.27, 1977, pp.399-408.

85. Eshleman, R.L., and Eubanks, R.A., "On the Critical Speeds of a Continuous Shaft Disk System", Journal of Engineering for Industry, Transactions of ASME, Vol. 89 (4), 1967, pp. 645-652.

86. Hagiwara, N., et al., "Analysis of Coupled Vibration Response in a Rotating Shaft Impeller System", Journal of Mechanical Design, Transactions of ASME, Paper No. 79-DET-69.

87. Bielawa, R.L., "An Analytical Study of the Energy Dissipation of Turbomachinery Bladed Disk Assemblies Due to Inter-Shroud Segment Rubbing", ASME Paper No. 77-DET-73, 1977.

88. Srinivasan, A.V., Lionberger, S.R., and Brown, K.W., "Dynamic Analysis of an Assembly of Shrouded Blades Using Component Modes", Journal of Mechanical Design, Transactions of ASME, Vol.100 (3), 1978, pp. 520-527.

89. Rimkunas, D.A., and Frye, H.M., "Investigation of Fan Blade Shroud Mechanical Damping", Wright Patterson Air Force Base, Aero. Propulsion Lab., Report No. FR-11065, 1979.

90. Craig, R.R., and Brampton, M.C., "Coupling of Substructures for Dynamic Analyses", AIAA Journal, Vol. 6, No. 7, 1968, pp. 1313-1319.

91. Whitehead, D.S., "Effect of Mistuning on the Vibration of Turbomachine Blades Induced by Wakes", Journal of Mechanical Engineering Science, Vol. 8 (1), 1966, p.15.

92. Kaza, K.R., and Kielb, R.E., "Effect of Mistuning on Bending Torsion Flutter and Response of a Cascade in Incompressible Flow", AIAA Journal, Vol. 20 (8), 1982, pp. 1120-1127.

93. Bendiksen, O.O., "Flutter of Mistuned Turbomachinery Rotors", ASME Paper No. 83-GT-153,1983.

94. Chihara,T.S., "An Introduction to Orthogonal Polynomials", Gordon and Breach, New York, 1978.

95. Stegun, I.A., and Abramowitz, M., "Handbook of Mathematical Functions", Dover, New York 1976.

96. Kim, C.S., "The Vibration of Beams and plates Studied Using Orthogonal Polynomials", Ph.D. Thesis, The University of Western Ontario, 1988.

97. Shigley, J.E., "Mechanical Engineering Design", Mcgraw Hill Series in Mechanical Engineering, 1977.

98. Sutherland, R.L., and Goodman, L.E., "Vibrations of Prismatic Bars Including Rotary Inertia and Shear Corrections", Report N6-ORI-71 TO-6 Project NR-064-183, 1951, pp. 1-23.

99. Rao, J.S., "Flexural Vibration of Rotating Cantilever Beams", Journal of Aeronautical Society India, Vol. 22, 1970, pp. 257-261.

100. "ANSYS - Users Manual", Swanson Analysis Systems, Volume 1 and 2, 1989.

101. Klosterman, A.L., "On the Experimental Determination and Use of Modal Representations of Dynamic Characteristics", Ph.D Thesis, University of Cincinnati, 1971.

102. Subbiah, R., "Dynamic Behaviour of Rotor Systems With a Comprehensive Model for the Hydrodynamic Bearing Supports Using Modal Analysis and Testing", Ph.D. Thesis, Concordia University, 1985.